UNIVERSIDADE TÉCNICA DE LISBOA
INSTITUTO SUPERIOR TÉCNICO

Environmental based Underwater Communications

António João Freitas Gomes da Silva
(Mestre)

Dissertação para a obtenção do Grau de Doutor em
Engenharia Electrotécnica e de Computadores

Documento Provisório

Julho de 2007

Abstract

The present thesis aims at the development of an environmental-based equalizer for shallow water coherent communications. In recent years time-reversal aroused as a viable option for underwater communications since its focusing property allows for a significant signal to noise ratio enhancement and inter-symbolic interference reduction. In order to use time-reversal in an operational modem the main drawbacks were identified as the performance loss due to the source-vertical-line-array geometric mismatch (i.e. source-array relative range and depth variations) during the data transmission and the optimization concerning the multipath spread of underwater channel impulse responses in a noisy environment.

For the time-reversal environmental geometric mismatch compensation a physical model based on waveguide invariants of the acoustic channel was developed. It makes use of the frequency/range invariant and of the frequency/depth invariant. With such a physical-model in hand an environmental-based equalizer was developed.

The multipath spread that guarantees the maximum of the signal to noise ratio is given by the time-reversal overall impulse response maximum power that can be computed using channel impulse response estimates. Such optimum signal to noise ratio results in a suboptimum inter-symbolic interference compensation with, however, values close to the optimum.

In parallel with the scientific objectives, the development of a surface buoy prototype – the Acoustic Oceanographic Buoy (AOB) – was carried out. The AOB is an advanced sonobuoy with a long and dense acoustic/oceanographic vertical-line-array and with additional processing capabilities. The AOB was tested in six sea trials where its telemetry capabilities where successfully proven, and was used to acquire the real data used to test the developed environmental-based equalizer.

The time-reversal optimization concerning the multipath spread was validated with real data at 400 and 2000 bits per second, as well as the time-reversal environmental-base equalizer that showed a mean squared error gain up to 5.5 dB over the non equalized time-reversal data.

Keywords: Underwater acoustic communication, matched field processing, time-reversal, waveguide invariants, environmental-based equalizer.

Resumo

Nos sistemas de comunicações acústicos actuais a informação ambiental e espacial é quase completamente ignorada. Esta tese pretende desenvolver um equalizador ambiental para comunicações coerentes em aguas pouco profundas.

Experimentações anteriores em geometria fixa, mostraram que a focalização das técnicas baseadas no espelho acústico é estável a longo termo. Aproveitando essa propriedade de focalização foi possível desenvolver um sistema de comunicações usando o espelho acústico passivo, que faz uso de uma estimativa das respostas impulsivas do canal acústico para aumentar a relação sinal ruído e para reduzir a interferência inter-simbólica dos dados enviados posteriormente.

Para usar o espelho acústico passivo num modem acústico as principais limitações encontradas foram a optimização do operador de retro focagem em função do espalhamento temporal das respostas impulsivas do canal num ambiente ruidoso, e a perda de eficiência devido às variações da geometria fonte agregado de receptores durante a transmissão dos dados.

Para a compensação da variação geométrica da configuração fonte agregado de receptores foi desenvolvido um modelo físico baseado nos invariantes do guia de ondas. Para isso foi usado o invariante no plano frequência/distância e o invariante no plano frequência/profundidade. A partir desse modelo físico foi possível desenvolver nesta tese um equalizador ambiental.

O espalhamento temporal que garante um máximo da relação sinal ruído é dado pela máxima potência da resposta impulsiva global do operador de retro focagem passiva, e essa optimização em termos de relação sinal ruído resulta numa compensação de interferência inter-simbólica sub-óptima no entanto próxima do óptimo.

Em paralelo com os objectivos científicos foi desenvolvida a bóia de superficie – AOB, *Acoustic Oceanographic Buoy.* A AOB pretende ser uma evolução da *sonobuoy* com um agregado vertical de hidrofones e termistors e com capacidade de processamento adicional. A AOB foi testada em seis campanhas de mar em que as suas capacidades de telemetria foram demonstradas com sucesso, além disso foi usada para adquirir os dados reais usados para testar o equalizador ambiental desenvolvido.

A optimização do operador de retrofocagem em relação ao espalhamento temporal associado ao equalizador ambiental foi validado com dados reais com taxas de transmissão de 400 e 2000 bits por segundo e permitiu observar uma redução de aproximadamente 5dB no erro quadrático médio entre os símbolos transmitidos e os detectados no receptor entre o espelho acústico simples e o novo equalizador ambiental.

Palavras-chave: Comunicações acústicas submarinas, processamento por ajuste de campo, espelho acústico, invariantes do guia de ondas, equalizador ambiental.

Contents

1 Introduction 1

1.1 Rapid environmental assessment and the acoustic oceanographic buoy concept 2

1.2 Time reversal mirror and underwater communications 3

1.3 Time reversal mirror and matched-based processing 5

1.4 Communications and geometric tracking 6

1.5 Outline of the thesis 8

1.6 Contributions 9

2 The Acoustic Oceanographic Buoy Telemetry System 11

2.1 Introduction 11

2.2 System design 12

2.3 AOB main features 14

2.4 Engineering test 15

2.5 Future developments 16

3 Probe timing optimization for time-reversal underwater communications 17

3.1 Introduction 17

3.2 Theoretical background 19

  3.2.1 Digital communications with passive Time Reversal 20

  3.2.2 Autocorrelation of the noise terms 23

  3.2.3 Signal and noise power 25

3.3 The passive time-reversal output SNR and its maximum 26

3.4 Performance simulations in realistic channels 28

3.5 Experimental results 31

3.6 Conclusion and future work 34

4 Generalization of Waveguide Invariants and Application to Passive Time Reversal 37

4.1 Introduction 37

4.2 The waveguide invariants 39

  4.2.1 Approximation of the horizontal wavenumbers using waveguide invariants 39

4.2.2 Approximation of the vertical wavenumbers using waveguide invariants 42
4.3 Geometric mismatch compensation in passive time reversal 44
4.3.1 Passive Time Reversal in a stationary geometry 44
4.3.2 Passive Time Reversal with Source-Array Range Shift 45
4.3.3 Passive Time Reversal with Source Depth Shift 47
4.3.4 Passive Time Reversal with Array Depth Shift 49
4.4 Simulations with a perfect waveguide 50
4.5 Extension of geometric compensation mechanisms to realistic waveguides . 52
4.6 Geometric mismatch compensation with experimental data 55
4.7 Conclusions and future work 58

5 Environmental equalizer for underwater communications 61

5.1 Introduction 61
5.2 Passive Time Reversal applied to communications 63
5.3 Passive Time Reversal geometric mismatch compensation 64
5.4 The passive time-reversal frequency shift equalizer 66
5.5 Real Data Application 67
5.6 Conclusions and Future work 69

6 Environmental equalizer for high data rate underwater communications 71

6.1 Introduction 71
6.2 Passive Time Reversal geometric mismatch compensation 74
6.3 The passive time-reversal frequency shift equalizer 76
6.4 Time-window optimization 78
6.5 Real Data Application 79
6.6 Conclusions and Future work 84

7 Conclusion 87

7.1 Open issues 89

A 91

A.1 Deterministic and stochastic filters autocorrelation 91
A.2 Time windowed passive Time Reversal 93

B 97

B.1 Linear approximation of monotonic functions 97
B.2 Mode orthogonality in the presence of an array depth mismatch 98

Bibliography 100

List of Figures

1.1 Acoustic rapid environmental assessment network 3

2.1 AOB pre-deployment set-up, during Makai Ex. sea trial 13
2.2 AOB hardware and software block diagram 13
2.3 Base Station monitor interface, with received acoustic data during the Makai Ex. sea trial 15

3.1 Block-diagram for the application of passive time reversal to digital communications. 20
3.2 Simulated depth dependent broadband arriving pattern over a realistic scenario: start time 'o', optimum window duration '*' and maximum window duration '+'. 29
3.3 Simulated pTR output SNR for the LF case (a), and for the HF case (b). . 30
3.4 Simulated performance of the proposed optimal time-window prediction method using (3.37) and (3.40) for the LF and HF cases 31
3.5 Real data vertical array estimated impulse responses: start time '0', optimum window duration '*' and maximum window duration '+'. 32
3.6 Real data performance of the proposed optimal time-window prediction method obtained in shot 9: pTR output SNR computed by using the MSE at the slicer/detector input (a) and maxima prediction by using (3.43) (b). 33
3.7 Real data performance of the proposed optimal time-window prediction method obtained in shot 7: pTR output SNR computed by using the MSE at the slicer/detector input (a) and maxima prediction by using (3.43) (b). 33
3.8 Mean analysis over all shots for the real data performance of the proposed optimal time-window prediction method: pTR output SNR output computed by using the shot-mean MSE at the slicer/detector input (a) and shot-mean of the maxima prediction by using (3.43) (b). 34

4.1 Normalized product $\Lambda_{\beta,m}$ (4.16) (dotted line), and its least-squares approximation (4.17) for an effective number of modes $M_e = M/2$ (circles). 42
4.2 Normalized product $\Lambda_{\zeta,m}$ (4.26) (dotted line), and its least-squares approximation (4.27) for an effective number of modes $M_e = M/2$ (circles). 44

4.3 Frequency shift source-array range mismatch compensation given by the pTR acoustic field $P_{PC}(\cdot; \Delta r, \Delta\omega)$ of (4.34); (a) normalized magnitude, (b) unwrapped phase. 51
4.4 Frequency shift source depth mismatch compensation given by the pTR acoustic field $P_{PC}(\cdot; \Delta z_0, \Delta\omega)$ of (4.51); (a) normalized magnitude, (b) unwrapped phase. 52
4.5 Frequency shift array depth mismatch compensation given by the pTR acoustic field $P_{PC}(\cdot; \Delta z_i, \Delta\omega)$ of (4.57); (a) normalized magnitude, (b) unwrapped phase. 53
4.6 Arrival pattern of the non mismatch IR estimate. 56
4.7 The surface represents the normalized magnitude of $P_{pc}(\cdot; \Delta, \Delta\omega)$, when the nominal IR is at $t = 40$s and considering the IRs limited to two arriving paths. The solid line traces the maxima of the surface over time. The dashed line represents the expected behavior if there is only range mismatch. 57
4.8 Power spectrum of the slice of P_{pc} along the maximum line of Figure 4.7 (solid line), and power spectrum of the source depth time series (‘*’). 58
4.9 The same as Figure 4.7 considering the IRs limited to three arriving paths. 58

5.1 Block-diagram of the FSpTR equalizer. The blocks in the upper path represent the probe-signal IRs estimate, time windowing, and frequency shift operations. The blokes in the middle path represent data transmission and crosscorrelation with the IRs estimate obtained in the upper path. Summation over the I hydrophones gives the L pTR processor outputs $\mathbf{z}_l(t)$. The blokes path below represent the selection of $\mathbf{z}_l(t)$ with the frequency shift that best compensates for geometric mismatch between probe and data transmissions, and the transmitted symbols estimation. 67
5.2 Passive time-reversal output mean magnitude $\mathbf{z}_l(t)$ as a function of time and applied frequency shift, computed by slots of 0.5 s. The solid line traces the maximum of the surface. 69
5.3 Mean squared error between the estimated and transmitted data symbols for plain pTR (black line) and FSpTR (red dashed line). 70

6.1 Block-diagram of the FSpTR equalizer. Part (a): the blocks in the upper path represent the probe-signal IR estimate, time windowing, and frequency shift operations. The blocks in the middle path represent data transmission and crosscorrelation with the IR estimate obtained in the upper path. Summation over the I hydrophones gives the L pTR processor outputs $\mathbf{z}_l(t)$. Part (b): the blocks depicts combining of $\mathbf{z}_l(t)$ considering the frequency shift that best compensates for geometric mismatch, Doppler compensation, synchronization, and symbol estimation. 77
6.2 Mean sound speed profile during data transmission, during day 195 between 10:07h and 10:15h (local time). 80

6.3 Arrival pattern estimated by pulse compression of the chirp probe-signal of the first data packet. 80
6.4 Time-window optimization with a 16-hydrophone array (a), with a 6-hydrophone array (b). 81
6.5 Passive time-reversal output $\mathbf{z}_l(t)$ mean power as a function of time/slot-number and applied frequency shift, for the first data packet. The $\mathbf{z}_l(t)$ mean power is computed in slots of 0.25s for a 16-hydrophone array and time-window covering the first arriving paths (a), and for a 6-hydrophone array and time window covering all paths and compensation applied only to later paths (b). The solid line connects the surface maxima ('*') for each time/slot number. 82

List of Tables

6.1 MSE table for: the 16-hydrophone array with the short time-window capture of the channel IRs first arrivals and full frequency shift compensation (Case I); the 6-hydrophone array with the short time-window capture of the channel IRs first arrivals and full frequency shift compensation (Case II); the 6-hydrophone array with full window capture of the channel IRs arrivals and the frequency shift compensation applied only to later arrivals (Case III). 83
6.2 MSE table for the FSE with 16 and 6 hydrophones. 84

Chapter 1

Introduction

Evolution occurs when new solutions are found for previously identified needs that – when solved – reveal new needs, prompting a search for new solutions. That is what happens when, after underwater communications, tomographic inversion and source localization in shallow water were made possible through acoustic means, the need for Acoustic Rapid Environmental Assessment (A-REA) that motivates the development of free-drifting, light and easy to deploy acoustic Vertical Line Arrays (VLA) evolves, and in turn necessitates new solutions for computationally less demanding underwater communications algorithms and channel geometric tracking. The present work has been developed in the described context where, in order to answer the requirements of A-REA, the light "Oceanographic Acoustic Buoy (AOB)" VLA has been implemented and due to its specific characteristics a new environmental-based underwater communications algorithm has been developed. That makes the present thesis two fold: at first a technological development is proposed with the implementation of the AOB; and second a more challenging scientific objective is attained with the development of an environmental-based equalizer for underwater communications in shallow water where the waveguide approach holds.

The aim of this work is to incorporate into the receiver equipment some awareness of the environmental and spatial configuration of the acoustic link that is almost totally lacking in current underwater modems. Having these capabilities built into the receiver would be very appealing for a number of reasons. Firstly, it would provide a clear picture of the difficulties of the acoustic link involved in a given spatial configuration. Secondly, it could provide useful oceanographic information about the environment at no extra cost. Thirdly, it would provide useful localization information to be incorporated into navigation systems, e.g. of an Autonomous Underwater Vehicle (AUV).

The decision for the development of an environmental-based equalizer relies on the basic idea that although the underwater channel Impulse Responses (IRs) change quite rapidly, which makes computation requirements quite demanding for current adaptive equalizers, the non-geometric physical properties of the propagation environment change slowly. That is revealed by the medium-term stability of tomographic inversions and of Time-Reversal Mirror (TRM) experiments [34]. The robustness of TRM to the non-geometric environmental changes and its applicability to underwater communications motivate its use as the starting point for the environmental-based equalizer. The variability of the geometric parameters - source-array range, source depth and array depth - their variability should be tracked and used to compensate for the loss of performance that they impose on the Time-Reversal (TR) communications system. That is made possible by the simple physical relations given by the use of waveguide invariants that allow for the establishment of a map between the geometric variations and an appropriate frequency shift of the acoustic field.

1.1 Rapid environmental assessment and the acoustic oceanographic buoy concept

In the past few years Rapid Environment Assessment (REA) in shallow water, has become one of the most challenging topics in ocean acoustics [10], mostly because acoustic means provide a possible survey of an unknown region with minimal human intervention.

The modern REA concept involves the integration of acoustic and non-acoustic systems for collecting environmental information as well as the short notice dissemination of the acquired information to an operational command. REA has been developed in the military context where information that includes meteorology, oceanography, hydrography, geography, mine reconnaissance, and many others can be relevant in affecting the operation of marine and supported ground forces. REA methods applied to shallow water areas are also seen as promising techniques for civil and scientific environmental monitoring systems. The coastal transition zone is a very sensitive region subject to a great deal of human activity that interferes with the marine system. It is a region of significant fishing and of intense ship traffic, in particular cargo vessels and tankers. Comprehensive knowledge of the dynamics and structure of this system would have strong importance in coastal management and prevention in the case of natural or man made hazards. Such knowledge is also important for the protection of maritime structures (bridges, ports, seashore lines), and the monitoring and study of complex ocean and coastal processes such as beach erosion, sediment transport, surface and internal tide propagation and currents.

In the context of REA, the use of acoustic means is usually termed Acoustic REA (A-REA) [10] and can be applied for submarine localization, mine detection, tomographic and bottom inversion. Acoustic means also provide the necessary framework for a fast and easy deployment of an underwater communication network (see figure 1.1) where the underwater nodes (e.g. oceanographic sensors, autonomous underwater vehicles, benthic labs, telemetry buoys) communicate with each other by using acoustic modems and consequently no cables are required. The use of acoustic equipment provides an unmanned and inexpensive manner for doing high-resolution surveys, and allows for remote data collection in a large area.

Figure 1.1 shows the scenario for one of the currently most promising A-REA concepts, that is, the use of a field of air-dropped 'advanced' sonobuoys, to receive signals from controlled sound sources such as Autonomous Underwater Vehicles (AUV), or other

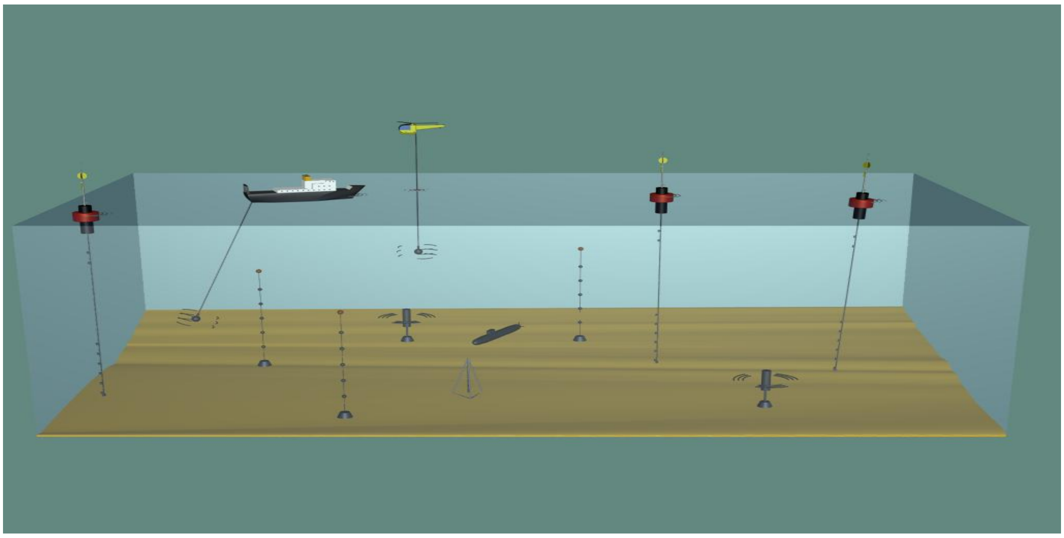

Figure 1.1: Acoustic rapid environmental assessment network

sources of opportunity. The collected information, radio transmitted to an aircraft, ship or land-based station, is processed to determine the AUV localization, water column and bottom acoustic properties. The collected information also comprises other AUV collected data e.g. imaging and mine reconnaissance. As any REA operation is likely to be performed in a crisis area – both for operational reasons and in order to have a fast uploading of the data – the collected information should be pre-processed in-situ in order to reduce the amount of data to be sent. To meet those requirements, in this work, the 'advanced' sonobuoy concept is implemented in the Oceanographic Acoustic Buoy (AOB): a telemetry buoy that meets the traditional sonobuoys characteristics of small size and weight, but with the advanced characteristics of having a sufficiently dense array of hydrophones and thermistors, a self localizing GPS system, high processing capability, a high throughput radio data link, and a large data storage capacity. The two last characteristics make it possible for REA to require a short-time presence of manned devices (helicopters, aircrafts or ships) in the operational scenario, since the AOB provides the means for the storage of the slow data acquisition and a rapid radio-link up-load. The development of such a telemetry buoy poses a significant technological challenge since usual systems with analogous capabilities are too large and too heavy (more than 300Kg). Examples of those are the ULVA/RDAS [12] and the ACDS systems (National Research Laboratory, USA).

Nevertheless the usefulness of the AOB concept depends on the development of reliable underwater communication and inversion methods suitable to be implemented on the AOB and that is the main objective of this thesis.

1.2 Time reversal mirror and underwater communications

Underwater acoustic channels exhibit time-varying severe multipath due to sound reflections on the sea surface and bottom, which is widely regarded as the dominant environmental influence on the performance of acoustic communications systems. The time variability of the multipath structure is due to the variability of the geometric characteristics of the environment (source-receiver range, source depth and receiver depth) and to the variability of the non-geometric characteristics like internal waves, internal turbulence, tidal flows, surface waves and variable sound speed profile. An experiment conduced in the south of Elba island by Kuperman et. al. in 1997 [34] revealed a great immunity of Time-Reversal (TR) to the non-geometric environment properties variation and motivated its use as the starting point of the methods to be developed in the present work.

In several recent papers [38, 26, 34, 4] TR was shown to efficiently focalize a received signal, in time and space, at the source position in the presence of an unknown environment. It makes use of a VLA that collects the signal transmitted by the source and an array of transducers collocated with the VLA that retransmits a time reversed version of the received signals. Such experiments show the capability of the acoustic channel to deconvolve itself. The same concept can be applied in a slightly different way by using only a source and a VLA. In such a case, before the signal focalization, the source must transmit a probe signal that by pulse compression will generate at the receiver an estimate of the channel Impulse Responses (IRs). The IRs estimate will then be used as a synthetic acoustic channel in order to implement the TR [50]. Such technique is termed Passive Phase Conjugation (PPC) [7] in the frequency domain or passive TR (pTR) in the time domain. The ability of pTR to produce a time focus makes it attractive for underwater communications. In fact, the time focalization property of the pTR is equivalent to the deconvolution of the severe multipath introduced by the channel and that results in a low complexity communications system. Unfortunately due to the acoustic channel variability such focalization does not hold in time, moreover acoustic focalization fluctuations are greater at higher frequencies due to the smaller focal size, where its usage is most interesting for digital communications. Recent work [62, 56] made a performance comparison between pTR and the multichannel decision-feedback equalizer (DFE) [57] concluding that for a small number of hydrophones the DFE outperforms PPC, however as the number of receivers increase, the bit error rate of both processors approaches zero. The nature of the methods is different: DFE is a signal processing method to which the nature of the channel is irrelevant; on the other hand PPC uses the physics of propagation to deconvolve the channel. One of the main differences is that the former is adaptive and the latter is not, that means that an estimation error in the DFE can be compensated as opposed to what happens in pTR. The problem can be overcome by shortening the time period between probe signals, but that will impose a serious reduction of the effective symbol rate. A second solution is to use an adaptive algorithm to track the IRs from the initial probe-signal IRs estimate: with such solution the estimated IRs are represented by a set of coefficients with given statistical properties. A third alternative is to use a low-complexity equalizer to compensate for the residual Inter-Symbolic Interference (ISI), where the equalizer coefficients represent weights to the estimated IRs. A performance comparison of the previous solutions is presented in [20]. A fourth approach, is to use a physical-based model to develop a pTR equalizer. Such approach suggests that environmental properties of the acoustic channel can be estimated jointly with the data signals. Although the physical-based equalizer has already been suggested by several authors [32, 42, 23], an effective way of carrying it out has not yet been proposed. In fact, that is the main topic of this thesis. In order to develop the basis for an environmental-based pTR equalizer the matched field methods present a framework already endowed with experience and expertise.

1.3 Time reversal mirror and matched-based processing

The key component of ocean Matched-Based Processing (MBP)[1] techniques [2] is an algorithm that generates field predictions from a set of model parameters that allow to infer physical parameters of the ocean itself. The traditional MBP approach is to compare (e.g. correlate) the acoustic field generated by the ocean (true environment data vector) with the acoustic field generated by a reliable acoustic model over all possible parameter space, and then select the one which is closer to the true environment data vector. The concept of TRM can be considered as an alternative representation of the classical MBP with the main difference that in the former the ocean is used to match with itself, while in the later the ocean is matched with a synthetic acoustic field. Despite their similarities Jesus [29], has shown that for the same amount of model mismatch, MBP will have a better performance than TR. Such result encourage the use of computational model-based methods to implement the pTR equalizer.

Unfortunately MBP with an environmental-parameters exhaustive search approach leads to an extremely large number of forward model calculations unless a reduced parameter space by a priori knowledge of the possible values of the environment parameters is used. In order to overcome that computational burden and to cope with the local minima global search methods (e.g. genetic algorithms [53] and simulated annealing [16]) are routinely employed in practical implementations. Although excellent results are attained when trying to invert tomographic parameters the convergence of the algorithms doesn't follow a steepest descendent of the mismatch error, rather it converges *somehow* statistically to the minimum by using a smaller amount of comparisons than the traditional MBP approach. That is a strong disadvantage when trying to apply MBP to communication algorithms. Recently a new approach has been proposed using a MBP adaptive formulation: the adjoint of the acoustic model. In this technique the mismatch between the model predictions and the measured observations result in a residual field – by means of adjoint modelling [23] – which is backpropagated in order to locate the model properties that need to be adjusted. Because of the non-linearity of the acoustic models, up to now the algorithms based in the adjoint model approach are developed using a local linear approximation of the gradient of the ambiguity surface. The disadvantages of global

---

[1] In the present work the term matched-based processing means the inversion of any physical parameter that influences the underwater acoustic propagation (e.g. matched-field inversion for geoacoustic parameters, matched-field tomography for water column parameters and matched-field processing for geometric parameters)

methods when compared to their local counterparts are only practical and technical, in fact the local methods are not able to "see" the large number of local extrema of the ambiguity surface, and so they require a closer to the solution starting point.

MBP has now been widely demonstrated for performing source localization, detection and tomographic inversion in ocean waveguides, but most of the processing approaches become increasingly sensitive to fluctuations or uncertainties as the frequency increases. In fact the shallow water environment is quite dynamic. In addition to the background internal wave field, rapid water temperature fluctuations generated by internal tides have a substantial impact on high frequency acoustic propagation. Recent works [25, 23, 39, 22, 61] that study the environment's influence over high frequencies and compare the results with predictions made by models attain encouraging results, but the idea that new models are required to operate MBP at high frequencies still holds [3], or at least new MBP techniques should be made as robust as possible to modelling mismatch at high frequency.

In order to compensate for the geometric mismatch between the actual and previous acoustic field a *partial*[2] acoustic model being able to track the pTR acoustic field will be developed. The proposed approach can be seen as MBP since pTR by itself is a matched-based processor where the actual acoustic field matches with an estimated version of the acoustic field at a different time. It is assumed, at least in a short time interval, that pTR is insensitive to non-geometric mismatch between the actual and the previous acoustic field.

Up to now, underwater digital communications and source localization are treated as two different topics by the scientific community. By using physics-based models and the pTR processor a different approach is proposed where the problem of performing geometric source and array tracking and communications in real time are treated as a joint problem.

1.4 Communications and geometric tracking

In this section two issues will be discussed, the first one will be a communication system based on pTR, and the second will be the tracking of the source and array locations.

One of the most challenging applications of underwater acoustics is when applied to *in situ* real-time monitoring using autonomous underwater vehicles (AUVs). In that case, a localization system is required to track the AUV survey and a high data rate acoustic communication up-loading link is required for real data transfer. In what concerns the communication system, performance constraints arise from the available SNR and ISI. SNR depends of the underwater noise power and of a compromise between the available power for communications and the increasing need for autonomy. ISI depends on the underwater acoustic channel impulse response that changes quite rapidly due to the AUV's continuous movement or drift.

One of the key components that enables the real-time exchange of data between the

---

[2] *partial* - means that the model can track the acoustic field but can not determine it.

AUV and a fixed or drifting station is a reliable up-loading high speed acoustic communication link (from the AUV to the station). In order to implement such an up-loading link and due to constraints on the AUV's power, only one AUV-projector is allowed, but an array of receivers can be placed in the receiving station. In such a configuration the pTR technique, presented in [50] can be applied, the main difference between that implementation and other pTR [7, 43] is the clear adoption of the digital modulation pulse shape as the probe signal of the channel. In fact, pTR requires a probe-signal to be transmitted ahead of the data-signal in order to estimate the channel IR (Green's function). The Green's function estimate is then used to perform a synthetic reverse channel, inside a digital signal processor. One of the most critical aspects of the pTR method is the channel IRs (Green's functions) estimate. It can be obtained from the probe-signal by simply correlating the received channel distorted probe-signal with the transmitted one, in which case the result will be an estimate of the channel impulse response. The probe-signal can be a M-sequence, a chirp, the convolution between the chirp and the pulse shape or the pulse shape adopted in the data digital modulation. The first three are high power signals with a large time bandwidth product, so, they allow for a better channel impulse response estimation; the latter is a low power signal and can be seen as a better choice when AUV power requirements are critical.

In order to be used in a digital computer, the estimated IRs must be approximated by a finite impulse response filter: that means that they must be captured in a finite time window. Typically, the onset and the duration of this time window should depend on the time dispersion of the acoustic channel which, in turn, depends on the physical channel properties and on the experiment geometry. Empirical reasoning would suggest that if a short time window fails to include all significant multipath it will result in an imperfect retrofocusing, while a too long time window will reduce the efficiency of the communication system by introducing additional noise in the pTR operation. That problem was addressed in [18, 11, 45] though no attempt for optimization has been proposed.

When there is a geometric mismatch between the probe-signal transmission and the data transmission the pTR communications system performance degrades quite rapidly. The proposed solution has to meet three requirements: first it must be simple enough to be implemented in an autonomous platform such as the AOB; second is that it must strongly reduce the number of probe signals to be sent in the pTR digital communications process in order to increase the effective data rate transfer between the source and the receiver; finally, the third requirement is that it must allow for geometric inversion, i.e., for source-array range and source and array depths estimation. The present work proposes an approach to integrate these three requirements in a single step. It consists in developing an adaptive pTR-based communication system that tracks the channel IR variability assuming that in a short time period is manly due to the geometric mismatch between the probe and data transmissions. The proposed solution is based on the Chuprov's waveguide-invariant theory [6, 21] that states that the geometric mismatches, i.e., the source-array range and the source and array depths variations result in a frequency shift of an original channel Green's function. Such system would be conceptually low complexity since only one parameter – the frequency shift – has to be tracked, it increases the effective error rate since it compensates for the channel variability, and it allows for the geometric inversion since the appropriate frequency shift is closely related with the geometric variations.

The waveguide-invariant theory has been widely used in tomographic inversion and characterization. In recent work such property has been used to change the TRM focus range [55, 33], and to increase the period of stable focusing in a non-stationary environment [32]. In weakly range dependent stratified environments, the lines of constant sound intensity lead to a constant slope between certain parameters of the waveguide [21, 35]. The invariant, denoted by β, characterizes the relation between range and frequency as

$$\delta\omega = \frac{\beta\omega}{R}\delta r, \tag{1.1}$$

where R is the horizontal range and ω is the angular frequency, δr and $\delta\omega$ denote the range and frequency shifts. At this point it is important to mention that parameter β is a weak function of frequency [9, 42], and although most of the experiments were carried up to 3.5 kHz, a similar behavior is anticipated at higher frequencies. This states the usefulness of the waveguide invariant in our narrow-band data communication application. Since β is invariant in the frequency/range plane it can be used for the compensation of the range mismatch between the probe and the data transmission in the pTR communications system. In a similar manner there exists an invariant ζ in the frequency/depth plane that can be used to compensate for the source and array depths mismatches. It results that using the waveguide invariants the channel geometric variability can be modelled by a frequency shift.

The basic idea of the TRM focal range shift approach [55] is that the focus can be placed at different ranges by increasing or decreasing the carrier frequency of the time-reversed signal to be retransmitted back into the channel. When applied to pTR the idea is slightly different, since in that case the channel that was used to estimate the IR is different from the channel that was used to transmit the data sequence. So, the requirement is to adjust the synthetic channel estimated by the probe-signal, to the actual channel during the data transmission, by means of a frequency shift. The overall system operates as a matched-filter where the actual received acoustic field matches with the frequency shifted initial channel IRs estimate, where the appropriate frequency shift is given by a waveguide invariant model.

1.5 Outline of the thesis

This thesis was divided into five main chapters where Chapters 2-6 were intensionally written as journal papers.

Chapter 2 describes the AOB system design, where the main system features will be addressed and its integration in an A-REA network is explained. In the end the operation of the AOB during the MakaiEx sea trial off Hawaii in 2005 is presented.

Chapter 3 addresses the underwater communications pTR system optimization as a function of the IRs estimate time window capture. A closed form expression for the pTR output SNR as a function of the time window is obtained. When the noise power dominates over the Inter-Symbolic Interference (ISI), it is found that the optimal time window does not depend on the noise level but only on the multipath structure of the underwater channel, and is given by a closed form expression that can be computed previously to the data arrival. Demonstrative results are presented using simulations and real data acquired during the INTIFANTE'00 sea trial off the west coast of Portugal in 2000.

Chapter 4 presents a re-interpretation of the waveguide invariant β and its application to compute an approximation of the horizontal wavenumber using the horizontal group slowness. A similar formulation is used to compute a vertical wavenumber approximation using the waveguide invariant ζ. The influence of the geometric mismatch between the probe-signal and the data transmission in the pTR operator is explained and compensation strategies using the invariants β and ζ are presented. Real data acquired during the MREA'04 sea trial are used as a demonstrative example of the effectiveness of the compensation mechanism.

Chapter 5 integrates the communication system developed in Chapter 3 and the pTR geometric mismatch compensation developed in Chapter 4 resulting in the environmental-equalizer 'Frequency Shift passive Time Reversal (FSpTR)'. Performance comparison between plain pTR and FSpTR communication systems, with low data rate signals (400 baud at 3.5 kHz band), is performed using real data acquired during the MREA'04 sea trial.

Chapter 6 applies the FSpTR environmental-equalizer to binary PSK signals at a data rate of 2000 baud with a carrier frequency of 12.5 kHz. A performance comparison between the Fractionally-Spaced Equalizer and the environmental-equalizer with real data acquired during the RADAR'07 sea trial is presented.

Chapter 7 summarizes the main results and discusses directions for future research.

1.6 Contributions

The following topics reported in this thesis represent original contributions:

1. [Chapter 3] A closed form expression for the autocorrelation of the output of a filter when the filter IR is a time limited stochastic signal and the input is a deterministic signal.
2. [Chapter 3] A closed form expression for the pTR output SNR when applied to underwater communications is derived.
3. [Chapter 3] A closed form expression for the determination of the optimum time window length for the IR estimates step of the pTR processor when applied to underwater communications is derived.
4. [Chapter 4] The waveguide invariants β and ζ are applied to the geometric mismatch compensation of the pTR processor.

5. [Chapter 5 and 6] The environmental-based equalizer is successfully applied to real data.

Chapter 2

The Acoustic Oceanographic Buoy Telemetry System

An Advanced Sonobuoy that Meets Acoustic Rapid Environmental Assessment Requirements

2.1 Introduction

In the past few years Rapid Environmental Assessment (REA), applied to shallow waters, has become one of the most challenging topics in ocean acoustics. The REA concept evolved after the cold war when the outset of regional conflicts shifted the potential operational areas from open ocean towards littoral areas, and has been identified by NATO as a new warfare requirement. REA must provide detailed and accurate information, in near real time, in order to prepare the maritime forces deployment into highly variable coastal waters that are not well known. More recently REA has become a promising technique for civil and scientific environment monitoring. Such an interest arises because the coastal transition zone is a region of significant fishing effort and of intense shiping traffic. The rapid knowledge of the dynamics and structure of coastal zones would assume strong importance in the case of natural or man made hazards. Because of the short time required for REA applications, the main topics of REA have been identified as rapid data collection, data synthesis and assessment, and dissemination of assessed products to action groups [10].

In the context of REA, the data synthesis and assessment requires the use of dynamic models for nowcast and forecast [37] that are fed with data acquired by the recording equipment. Data collection can be attained by using space/airborne sensors e.g. for marine wind, large scale currents and shallow water bathymetry; traditional oceanographic sensors like CTDs, wave height and ADCPs; passive and/or active acoustic e.g. for submarine localization, mine detection, tomography and bottom inversion. Acoustic means also provide the necessary framework for a fast and easy deployment of an underwater communication network where the underwater nodes (e.g.: oceanographic sensors, autonomous underwater vehicles, benthic labs, telemetry buoys) communicate with each other using acoustic modems and consequently no cables are required. The use of acoustic equipment is usually termed as Acoustic REA (AREA), it provides an unmanned and inexpensive manner of doing high-resolution surveys, and allows for remote data collection in a large area [10].

Currently one of the most promising AREA concepts is the use of a field of air-dropped 'advanced' sonobuoys, as an interface between an underwater wireless Acoustic Network (AcN), and an air Radio Network (RaN). The underwater AcN nodes are responsible for data collection. The air RaN nodes (satellites, aircrafts, vessels ...) are responsible for raw data storage and relay over local or world distributed data processing groups, for near real-time data synthesis and assessment. The 'advanced' sonobuoy field is responsible for the upload (from the AcN to the air RaN) of the acquired data; and for the download (from air RaN to the underwater AcN) of control and operation instructions. The 'advanced' sonobuoy field integrates simultaneously the air RaN and the underwater AcN, and that results in a single seamless network. Moreover, the 'advanced' sonobuoys can be used as an intermediate step for acquired data pre-processing and data fusion, through which data reduction can be attained. Such data reduction implies shorter data uploading, an important requisite for REA operations in a hostile area where the long time presence of air RaN nodes can compromise the mission success. Hostile area operations suggest that the 'advanced' sonobuoy field must integrate a network where nodes can be added or suppressed at any time, performing reduced operations even with a single 'advanced' sonobuoy.

The Acoustic Oceanographic Buoy (AOB) telemetry system aims to meet the 'advanced' sonobuoy characteristics. It integrates the air RaN by using a standard 'IEEE 802.11' WLAN configuration, and the underwater AcN by using a hydrophone array and an acoustic source. The first AOB prototype was tested during the Maritime Rapid Environmental Assessment sea trials in 2003 [52], and in 2004 [30]. The present version of the AOB (see figure 2.1) was tested, from 15th of September to 2nd of October 2005, during the MakaiEx sea trial off Kauai Island, Hawaii, USA, in the context of the High Frequency Initiative promoted by HLS Research Inc, San Diego, USA.

In the following, the AOB design will be described, the main system features will be addressed, the MakaiEx AOB engineering test will be presented and future developments will be pointed out.

2.2 System design

The physical characteristics of the AOB, in terms of height (1.2m), diameter (16cm), weight (40kg) and autonomy (12 hours) tend to those of a standard sonobuoy. However, the AOB presents advanced capabilities, which include: stand-alone or network operation; local data storage; dedicated signal-processing; GPS timing and localization; real-time data transmission and relaying. In this section the AOB hardware and software (see figure 2.2) is briefly presented and the main characteristics of the 'base station', an air RaN node, will be given.

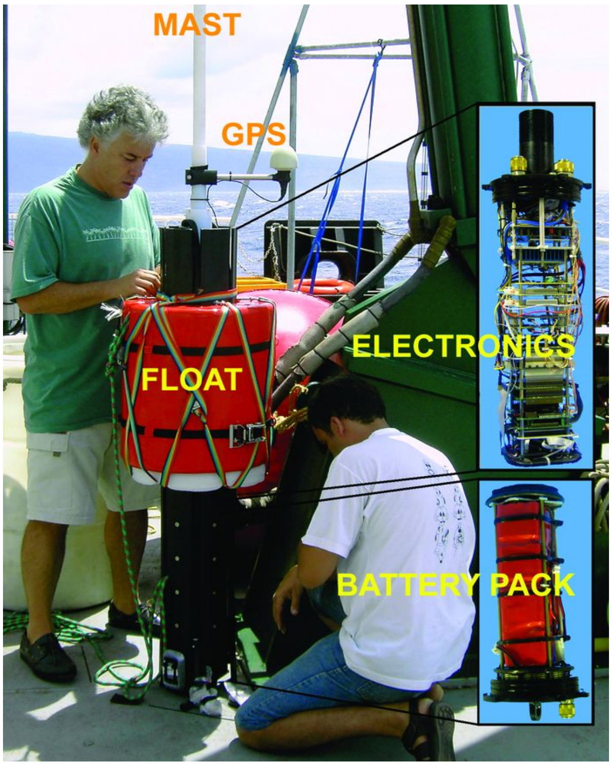

Figure 2.1: AOB pre-deployment set-up, during Makai Ex. sea trial

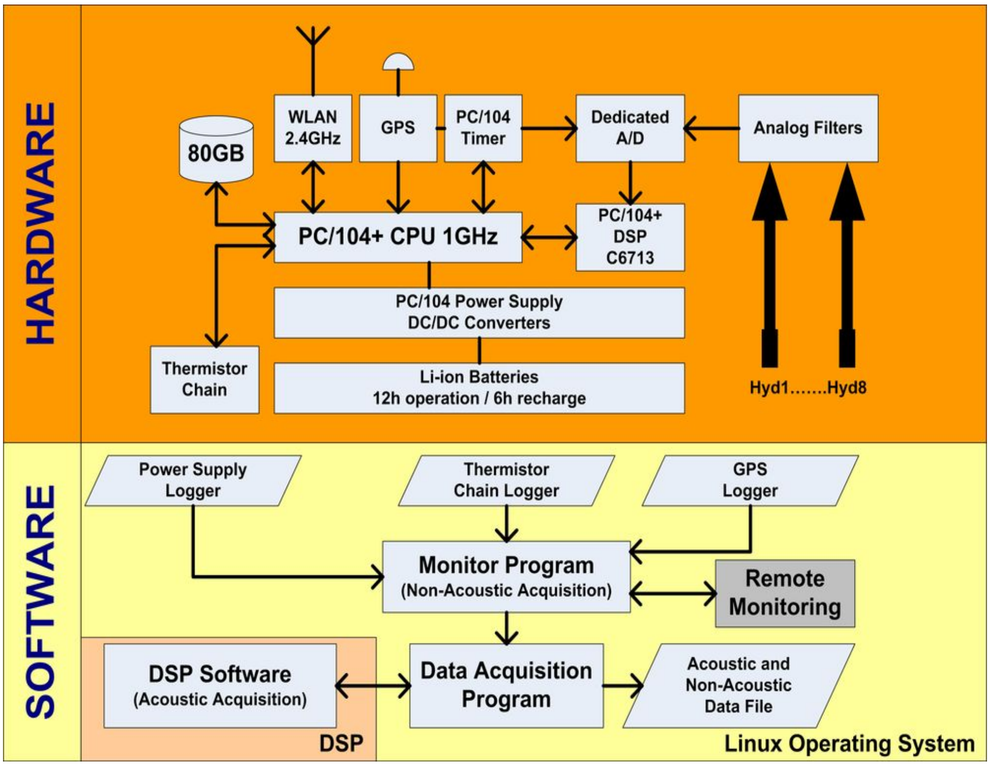

Figure 2.2: AOB hardware and software block diagram

The hardware system is contained within a PC/104 computer/electronics stack with standard purchased and inhouse developed boards. The core is a fan-less CPU board which takes care of all the system management. A 120 Gbytes hard drive allows for in situ data storage. Due to its standard WLAN transceiver the AOB is easily integrable with other similar systems to form a flexible network, and to perform online high speed data transmissions. A GPS receiver is responsible for timing and positioning information. An external data logger with 16 thermistors is responsible for the water column temperature sampling. The acoustic data acquisition system includes 8 hydrophones, 42dB pre-amplifiers, 15kHz anti-aliasing filters, signal conditioning circuitry and a dedicated acquisition board. A real time GPS synchronized timer provides the acquisition board with an accurate clock sampling signal and absolute time marking, a must for tomographic applications. The TMS320C6713 DSP board gives the AOB strong signal processing capabilities that allow for in situ data processing tasks.

All software applications were specifically developed for the AOB which runs the Linux operating system. The software is divided into various modules, each running independently. Modules include: GPS position logging; power supply control and monitoring; thermistors chain non-acoustic data acquisition; real-time remote monitoring; and the main acoustic data acquisition program which configures acquisition and stores data on the local disk. The modules exchange information through the use of TCP/IP network sockets which also allows real-time remote monitoring of buoy position and acquired data.

The 'base station' (see figure 2.3) that monitors the AOBs and manages the AOB WLAN network is portable and is comprised of a notebook and one external antenna, allowing for a reliable connection up to 10 km. The user is presented with a visual output of the 'base station' and AOB trajectories on-top of a bathymetric map, the state of the various equipments inside the buoy and the display of acquired signals. When deployed, operation requirements can be remotely modified, changes can be performed at any time and include parameters such as data acquisition rate, begin and end time for each acquisition cycle, and other options.

2.3 AOB main features

The AOB is a reusable system with reduced maintenance. Aboard, only two maintenance operations have to be performed: recharging batteries and downloading acquired data. Both are done by simply unplugging one connector, and plugging two connectors: one for recharging the batteries, and the other for external power supply and a fast ethernet link. The AOB is light enough in order to be deployed by hand from a ship, and robust enough to be deployed by air from an aircraft or to operate under rough sea conditions. At sea, the AOB is a salt-water-plug and play system designed to operate in free drifting mode, self time synchronized and locatable with great precision at all times.

Due to its DSP facility, the AOB is suitable for performing distributed digital signal processing tasks. When used in Matched Field Tomography (MFT), in the frequency

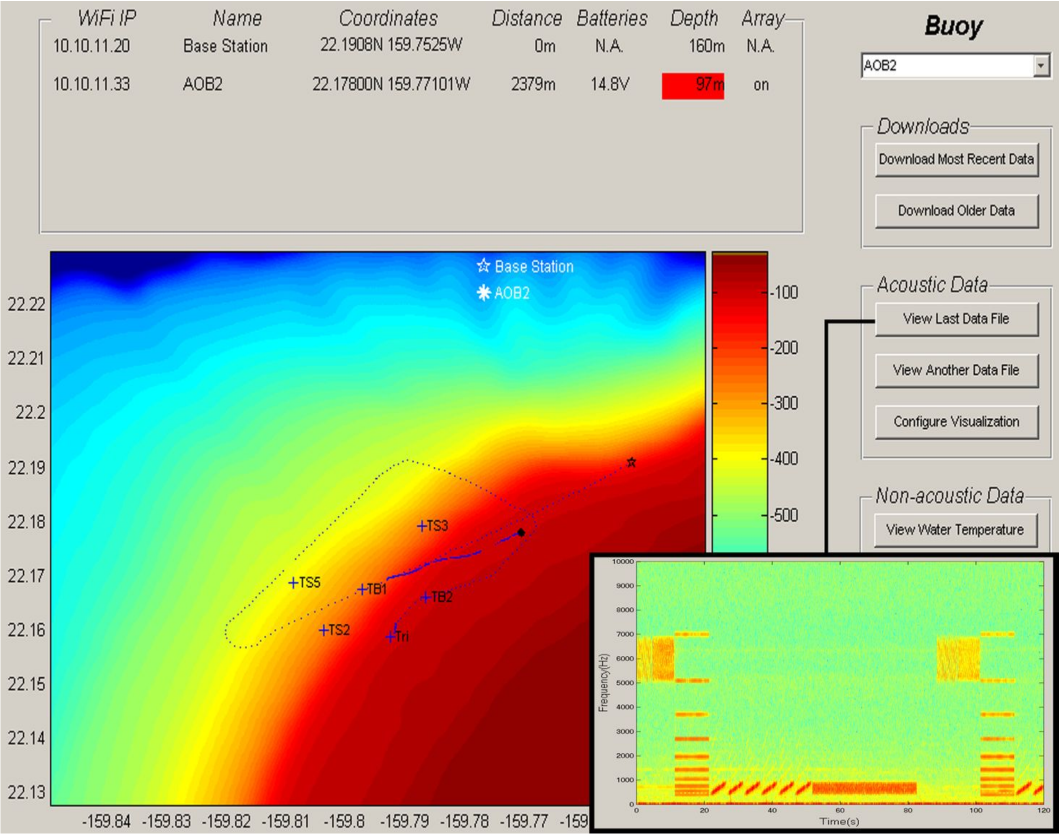

WiFi IP	Name	Coordinates	Distance	Batteries	Depth	Array
10.10.11.20	Base Station	22.1908N 159.7525W	0m	N.A.	160m	N.A.
10.10.11.33	AOB2	22.17800N 159.77101W	2379m	14.8V	97m	on

Figure 2.3: Base Station monitor interface, with received acoustic data during the Makai Ex. sea trial

domain, the AOB can pre-process the acoustic data. This can be performed by computing Fourier transforms of the acquired raw data, compute cross-covariance matrix estimates, and then just send to the base station the data concerning the frequencies of interest for posterior MFT operation. Such a distributed processing technique is advantageous when the propagated signals are either broadband or tones, in particular for the latter since only few frequency bins contain useful information. When used in non-coherent underwater acoustic data communications the DSP processing capabilities allow for the implementation of a full demodulation system. It is also suitable for the implementation of simple array processing passive localization algorithms.

2.4 Engineering test

The first engineering test of the present AOB version, in its stand-alone mode, took place during the MakaiEx sea trial [4]. Three deployments were initially planed but six were done since it was realized that the AOB was an easy system to deploy and recover. The AOB was in a free drifting configuration during five of the deployments; remote monitoring of the buoy was useful to know the status in terms of positioning and battery charge. There was one deployment where the AOB was tethered to the ship. This was not the initial planned setup and the rough sea conditions at the time showed that the AOB construction was robust and functional even when under strain. During MakaiEx the AOB participated in a wide spectrum of scientific experiments. In the first five deploys, 8-14 kHz acoustic transmissions where acquired with the main objectives of high-resolution tomography and understanding of the acoustic-environment interaction at high frequency and its influence on underwater communications. In the last deployment acoustic transmissions ranging from 500 Hz to 14 kHz where acquired in order to performs field calibration using inversion algorithms at high and low frequency.

2.5 Future developments

The AOB is now fully operational in its stand-alone mode, and the developing team is looking to future developments. A current project is the replacement of the sensor array by a robust and light array with 16 hydrophones, thermistors, pressure and other user defined sensors; and an acoustic source for control/communication operations over the underwater nodes.

An AOB network-mode engineering test, with 3 AOBs, is now under preparation and is scheduled to take place in October 2006. After that, as well as supporting the University of Algarve Signal Processing Laboratory (SiPLAB) research activities, the AOB's will be operated as a service to the international underwater research community.

Acknowledgments

The AOB system was developed under the NUACE (POSI/CPS/47824/2002) and RADAR (POCTI/CTA/47719/2002) projects supported by the FCT - Foundation for Science and Technology (Portugal). Special thanks are due to Prof. Sergio de Jesus for promoting and heading the AOB project.

Chapter 3

Probe timing optimization for time-reversal underwater communications

Abstract: Passive time reversal is one of the variants of time reversal applicable to digital underwater communications. In passive time reversal a probe-signal is transmitted ahead of the data-signal in order to estimate the channel impulse response for later use as a replica signal in a time reversal mirror fashion. In practice the received probe-signal must be captured in a time-window and, after correlation with the transmitted probe-signal, give a noisy estimation of the channel impulse response. Therefore, the output signal to noise ratio (SNR) and the detection rate of passive time reversal will strongly depend on the starting time and duration of such time-window. Typically the beginning and the duration of that time-window should depend on the travel time and the dispersion of the acoustic channel. Heuristic reasoning would suggest that if a short time-window fails to include all significant multipath it will result in imperfect focusing, while a too long time-window will reduce the efficiency of the communication system by introducing additional noise in the passive time reversal system. That problem clearly calls for an optimization. In order to bring the time reversal capabilities to a practical modem the time-window automatic optimization engineering problem must be solved. In this paper, the maximization of the passive time reversal output SNR relative to the probe time-window is derived in closed form. Theoretical results are found to be in full agreement with simulations and with results obtained on experimental data taken during the INTIFANTE'00 sea trial.

3.1 Introduction

In the past few years coherent modulation techniques for fast and reliable shallow water acoustic communication have triggered a number of theoretic developments, simulations and field experiments. To that end multichannel adaptive equalization methods [57], although quite computationally demanding, currently provide the most popular framework. Recently, active and passive Time Reversal (a-pTR) [26, 7] appeared as a viable alternative for simple and robust underwater coherent communications [50, 18, 43]. Active Time Reversal (aTR) takes advantage of the acoustic channel mode orthogonality and reciprocity properties and matches the ocean response with itself in a much similar way to Matched Field Processing (MFP)[29]. Like aTR, passive Time Reversal (pTR) relies on mode orthogonality but instead of the reciprocity property, uses an estimate of the underwater channel Green's function to perform a virtual ocean response match inside the computer, in a MFP fashion. Despite its simplicity, a-pTR applied to high frequency underwater communications presents a lower performance than multichannel equalization [45, 62, 56]. That is due to the Time Reversal Mirror (TRM) requirement for a long and dense array [34], without which residual Inter-Symbol Interference (ISI) is always present due to poor sampling of the high-order modes and subsequent orthogonality property violation.

One of the most critical aspects of the a-pTR methods is the channel Green's function estimation, which is typically obtained by simply correlating the received channel distorted probe-signal with the transmitted one, resulting in a noisy version of the channel Impulse Response (IR). In practice the probe-signal can be a M-sequence, a chirp, or the pulse shape adopted in the data digital modulation. In any case, and since the underwater channel is quite time variable, probe-signals must be frequently transmitted in order to maintain the a-pTR performance at an acceptable level. A significantly different technique is to adaptively estimate the channel Green's function by using the data communication signal [19], in a similar manner to that used in the multichannel equalizer [57] with, however, the difference that the IR must be estimated instead of its inverse. As in the multichannel equalizer, such technique is computationally very demanding when compared with the probe-signal based Green's function estimation which in turns presents the major drawback of losing validity due to channel fading.

Figure 3.1 shows a block diagram of the pTR application adopted in the sequel, where the received probe-signal $f_i'(t)$ is the channel IR estimate that is simply obtained as the channel noise contaminated response to a dirac impulse (upper path in the block diagram). For later use the estimated IR must be approximated by a FIR filter, which means that it must be captured in a finite time-window (see Figure 3.1). The time windowed estimated IR, $g_{i,t0,\tau}(t)$, is them used as a matched filter with the received data signal $v_i(t)$ (lower path in the block diagram). Typically, the start time and the duration of such time-window should depend on the time dispersion of the acoustic channel which, in turn, depends on the physical channel properties and on the experiment geometry. Heuristic reasoning would suggest that if a short time-window fails to include all significant multipath it will result in an imperfect retrofocusing, while a too long time-window will reduce the efficiency of the communication system and introduce additional noise in the pTR operation [18, 45, 11]. In a pTR communications system that adaptively estimates the channel IRs [19, 47] the *a priori* time-window optimization is also relevant since it anticipates the optimum number of coefficients that should be used to track the channel IRs.

The time-window probe-signal capture optimization is an important issue since it will affect the pTR communications system performance, its output Signal-to-Noise Ratio (SNR) and thus the detection error rate. For a well designed pTR Vertical Line Array

(VLA) [1] that is able to reduce the residual ISI to an acceptable level, the time-window optimization can be transformed in to a problem of pTR output SNR maximization, that can be solved after establishing signal and noise power time-window dependence. The a-pTR output SNR have been addressed by several authors [56, 4], including heuristic characterizations of time-window dependence [18, 45, 11] though optimization was not attempted.

It will be shown that the optimal pTR output SNR occurs when the time-windowed pTR overall IR has maximum power, while the optimal time-window for ISI tends to occur when the full length of the pTR overall IR is considered. Since in shallow water the IRs can extend over hundreds of milliseconds it turns out that the time-window for ISI optimization can be made impractical. Moreover, it will be shown that the time-window that gives an optimum Mean Square Error (MSE), between the transmitted and estimated symbols sequence, can be predicted by the pTR output SNR when in presence of a low input SNR, and by the ISI when in presence of a high input SNR.

In Section 3.2 signal and noise terms of the pTR communication system are identified and their means, autocorrelations and powers are derived. In Section 3.3 a closed form expression for the pTR output SNR as a function of the time-window is obtained and strategies for its optimization are proposed. In particular, it is found that the optimal time-window does not depend on the input noise level but only on the multipath structure of the underwater acoustic channel. Section 3.4 presents the results obtained in simulation using realistic underwater acoustic propagation models. In Section 3.5 the proposed optimization method will be applied to real data acquired during the INTIFANTE'00 sea trial. Conclusions and future work are presented in Section 3.6

3.2 Theoretical background

The objective of this Section is to set up the theoretical background for analysing the implications of probe-signal windowing operation in pTR performance when applied to digital communications in the presence of acoustic noise. An 'ideal' pTR where the TRM basic principle associated assumptions [2] are fulfilled will be considered.

The pTR communications system in the presence of a noisy environment involves the filtering of deterministic or stochastic signals by deterministic or stochastic IRs resulting in noise terms whose output statistical characteristics are required for the computation of the pTR output SNR. In Appendix A.1 the autocorrelation of those noise terms is derived in closed form. In Appendix A.2, for a perfect waveguide the time-window operation mode-filtering relation will be established and applied to time-windowed pTR.

---

[1] i.e., with a sufficiently large number of hydrophones spanning almost whole the water column

[2] *i.e.*, that there is a sufficiently large number of hydrophones, the vertical array is spanning the whole water column and the propagation environment is time-invariant.

3.2.1 Digital communications with passive Time Reversal

Figure 3.1 shows the baseband equivalent of the source-channel-receiver representation of the pTR processor for one hydrophone. In a first step (upper path in Figure 3.1) a duly time windowed and phase conjugated channel IR estimate is computed. In a second step (lower path in Figure 3.1) the deconvolution of the transmitted data sequence a_n distorted by the underwater channel is accomplished using the estimated channel IR computed in the first step. In that figure, the transmitting and receiving filter, $p(t)$, is a fourth-root raised cosine pulse [3]. In the sequel

$$p_m(t) = \underbrace{p(t) * ... * p(t)}_{\text{m times}}, \tag{3.1}$$

represents the m-times self-convolution of $p(t)$ such that $p_4(t)$ is the raised-cosine pulse shape function. In the IR estimation step, $p_2(t)$ is used as a narrowband filter resulting in a square-root raised cosine shape. In the second step $p(t)$ is used as the transmitting pulse shape for the data sequence that, in conjunction with $p(t)$ in the receiver side, results in a received data sequence square-root raised cosine pulse shaped, distorted with the baseband equivalent channel IR $h_i(t)$. With such configuration, in presence of a non-distortive channel (that is $h_i(t) = h_i'(t) = \delta(t)$) and with a sufficiently large time-window, one can guarantee a raised cosine pulse shape for the data sequence in the pTR output signal $z(t)$.

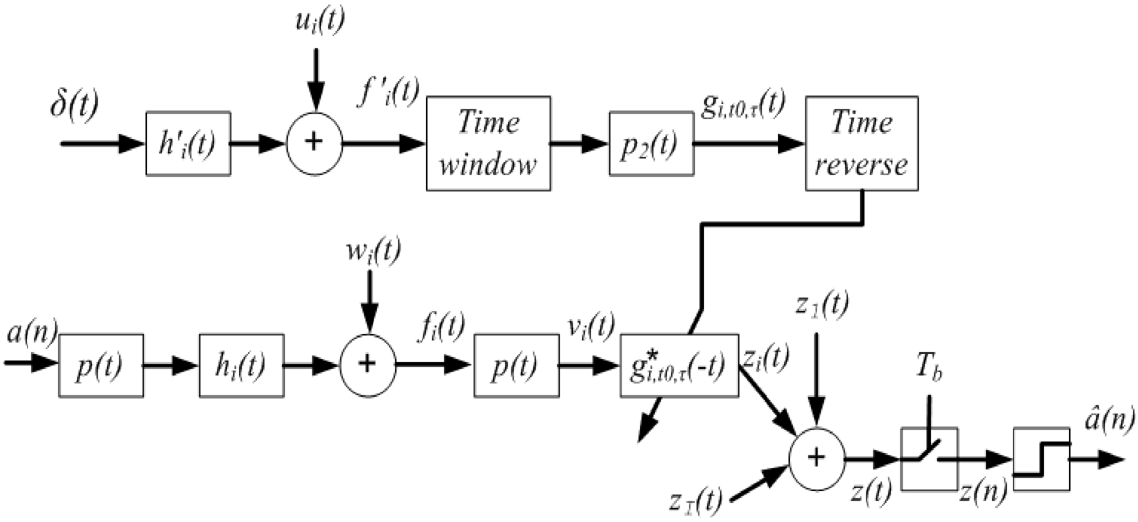

Figure 3.1: Block-diagram for the application of passive time reversal to digital communications.

Let us assume that the transmitted signal is Pulse Amplitude Modulated (PAM) written as

$$s(t) = a(t) * p(t), \tag{3.2}$$

---

[3] for notation convenience it is assumed that $p(t)$ is the inverse Fourier transform of $\sqrt[4]{P_4(f)}$, where $P_4(f)$ is a raised cosine pulse in the frequency domain.

with

$$a(t) = \sum_{n=-\infty}^{+\infty} a_n \delta(t - nT_b), \tag{3.3}$$

where a_n is a zero mean symbol sequence assumed to be white with power σ_a^2, and T_b is the symbol duration.

Assuming the acoustic channel as a time-invariant linear system with impulse response $h_i(t)$, the received data-signal at hydrophone i is given by

$$v_i(t) = h_i(t) * a(t) * p_2(t) + w_i(t) * p(t), \tag{3.4}$$

where $w_i(t)$ is an additive zero mean white noise with power σ_w^2, assumed to be uncorrelated with the signal and from sensor to sensor. When the probe-signal is a dirac impulse the received probe (upper path in Figure 3.1) is written as

$$f_i'(t) = h_i'(t) + u_i(t) \tag{3.5}$$

where $u_i(t)$ is the channel additive noise sequence with the same properties as $w_i(t)$ and independent from it, $h_i'(t)$ is the same channel impulse response as $h_i(t)$ (no environment/geometry mismatch case) and the $'$ denotes that there is an unspecified time delay between the two impulse responses (IRs).

The time-window operator multiplies the input signal with a unit-gate function of length τ and starting point t_0 (A3), thus

$$f'_{i,t_0,\tau}(t) = \begin{cases} f_i'(t) & t \in [t_0, t_0 + \tau] \\ 0 & \text{elsewhere} \end{cases}. \tag{3.6}$$

The narrowband time-limited IR estimate is then obtained as

$$g_{i,t_0,\tau}(t) = f'_{i,t_0,\tau}(t) * p_2(t). \tag{3.7}$$

Finally, the time limited IR estimation is phase conjugated or, equivalently in the time domain, time-reversed and conjugated. The pTR output for channel i is therefore

$$z_i(t) = g^*_{i,t_0,\tau}(-t) * v_i(t) \tag{3.8}$$

where $v_i(t)$ is given by (3.4). Replacing (3.3), (3.4) and (3.7) in (3.8) and summing over the hydrophone index i, the pTR output signal can be written as

$$z(t) = y(t) + x1(t) + x2(t) + x3(t), \tag{3.9}$$

where $y(t)$ contains the desired data-signal contaminated with ISI and the other three terms are noise disturbances, defined as

$$\begin{aligned}
y(t) &= \sum_{n=-\infty}^{+\infty} a_n c(t-nT_b) \\
x1(t) &= \sum_{n=-\infty}^{+\infty} a_n e(t-nT_b) \\
x2(t) &= p_3(t) * \sum_{i=1}^{I} h^*_{i,t0,\tau}(-t) * w_i(t) \\
x3(t) &= p_3(t) * \sum_{i=1}^{I} u^*_{i,t0,\tau}(-t) * w_i(t),
\end{aligned} \tag{3.10}$$

where

$$\begin{aligned}
c(t) &= p_4(t) * \sum_{i=1}^{I} h_i(t) * h^*_{i,t0,\tau}(-t) \\
e(t) &= p_4(t) * \sum_{i=1}^{I} h_i(t) * u^*_{i,t0,\tau}(-t).
\end{aligned} \tag{3.11}$$

The next logic step will be to derive the pTR output SNR using (3.9) and proceed to its maximization relative to the time-window parameters t_0 and τ, respectively start time and duration. Before doing so, and in order to motivate this optimization procedure, Figures 3.2 and 3.5 anticipate the results obtained, respectively in simulation (Section 3.4) and with real data (Section 3.5). Figures 3.2 and 3.5 shows the depth dependent IRs for a reduced time scale where the sign 'o' indicates the time-window starting instant t_0, sign '*' indicates the optimum time-window duration, the one that guarantees the pTR best performance $t_0 + \tau_{opt}$ as derived from the optimization of the output SNR, and sign '+' indicate the maximum time-window duration considered in the analysis, $t_0 + \tau_{max}$. Close inspection in Figure 3.5, for the real data noise contaminated IR estimates, reveals that as the time-window increases, more IR paths are included in $h_{i,t_0,\tau}(t)$ and simultaneously more noise power is included in $u_{i,t_0,\tau}(t)$. Those two factors will affect the pTR performance in opposite directions, resulting in an optimum time-window that does not include all the arriving paths ('*' signs). It should be noted however that, in order for the system to operate as a pTR, the time windowing operation must contain at least the main arrivals of the channel IRs. When operating with a vertical line array this can be done by using the same time-window for all hydrophones since at long ranges, greater than a few water depths, the main arrivals approximate plane waves. Under those conditions t_0 must be set before the main arrivals and τ must include the first arriving paths. In order to proceed to the output SNR maximization one needs to first derive the various noise cross terms that will appear in the SNR expression denominator.

3.2.2 Autocorrelation of the noise terms

In order to obtain a closed form expression for the pTR SNR output it is important to characterize each noise disturbance $x1\dots3$ individually, namely by determining their mean and variance. Their mean is easily calculated since the additive noise is zero mean, then $E\{x1\dots3(t)\} = 0$. The variance can be obtained as the value of the autocorrelation function at the origin after demonstrating that the noise terms are zero-mean Wide Sense Stationary (WSS).

The autocorrelation function of $x3(t)$ can be obtained considering that the autocorrelation of the convolution is equal to the convolution of the autocorrelations and that the autocorrelation of a sum is the sum of the autocorrelation plus the cross correlated terms that will be zero for independent summation terms. Assuming the independence of noise from sensor to sensor, and (A7), the autocorrelation of $x3$ will be

$$\begin{aligned} R_{x3}(t+t',t) &= E\{x3(t+t')x3(t)\} \\ &= r_{p_3}(t') * \sigma_w^2\sigma_u^2\tau I r_\delta(t') \\ &= r_{p_3}(t')\sigma_w^2\sigma_u^2\tau I \\ &= R_{x3}(t'), \end{aligned} \tag{3.12}$$

where σ_w^2 and σ_u^2 are the noise variances of $w(t)$ and $u(t)$ respectively, τ is the window length, I is the number of hydrophones, $r_{p_3}(t')$ is the autocorrelation of $p_3(t)$ and $r_\delta(t')$ is the autocorrelation of $\delta(t)$. In order to compute its variance it is important to note that $x3(t)$ is a WSS stochastic signal.

For $x2(t)$ the autocorrelation can be computed considering (A7) and (A11) for each hydrophone i,

$$\begin{aligned} R_{x2,i}(t+t',t) &= E\{x2_i(t+t')x2_i(t)\} \\ &= r_{p_3}(t') * r_{h,i,t_0,\tau}(t') * \sigma_w^2\delta(t') \\ &= r_{p_3}(t') * r_{h,i,t_0,\tau}(t')\sigma_w^2 \\ &= R_{x2,i}(t'). \end{aligned} \tag{3.13}$$

Thus, since the autocorrelation of the sum over the entire array is the sum of the autocorrelations given by (3.13) plus the cross-correlation terms that are null due to the noise independence from sensor to sensor, the autocorrelation of $x2(t)$ is given by

$$R_{x2}(t') = r_{p_3}(t') * \sigma_w^2 \sum_{i=1}^{I} r_{h,i,t_0,\tau}(t'). \tag{3.14}$$

This equation can be further simplified considering that for a well positioned time-window that covers the main arrival paths of $h_i(t)$, according to the TRM basic principle associated assumptions, and considering (A10)

$$\sum_{i=1}^{I} r_{h,i,t_0,\tau}(t') \approx C_{x2}(t_0,\tau)\delta(t'), \tag{3.15}$$

with the time-window dependent coefficient

$$C_{x2}(t_0, \tau) \approx \sum_{i=1}^{I} \int_{t_0}^{t_0+\tau} h_i(t) h_i^*(t) dt, \tag{3.16}$$

where $C_{x2}(\cdot)$ is a baseband version of C' from (A23).

Thus the autocorrelation of $x2(t)$ is approximately equal to

$$\begin{aligned} R_{x2}(t') &\approx r_{p_3}(t') * \sigma_w^2 C_{x2}(t_0, \tau) \delta(t') \\ &\approx r_{p_3}(t') \sigma_w^2 C_{x2}(t_0, \tau), \end{aligned} \tag{3.17}$$

which means that $x2$ is also a WSS stochastic signal.

In (3.15) it was considered that IRs bandwidth is large enough in order to attain convergence of the *sinc* function to an impulse (see Appendix A.2). Nevertheless such assumption can be relaxed since in (3.17) the *sinc* convolution with $r_{p_3}(t')$ behaves as an identity in the signal bandwidth. In the following, with no loss of generality, the *sinc* will be ignored when similar operations to (3.15) appear.

For the autocorrelation of $x1(t)$, the signal will be considered as the convolution of two continuous stochastic signals

$$x1(t) = a(t) * e(t), \tag{3.18}$$

where $a(t)$ and $e(t)$ are respectively given in (3.3) and (3.11). The autocorrelation of $e(t)$ is obtained by applying (A18) to the summation terms $h_i(t) * u_{i,t0,\tau}^*(-t)$, and by applying (A2)

$$\begin{aligned} R_e(t + t', t) &= \int \int r_{p_4}(t' - \gamma) \sigma_u^2 C_{x1}(\gamma, \nu, \tau) d\nu d\gamma \\ &= \sigma_u^2 \int r_{p_4}(t' - \gamma) \int C_{x1}(\gamma, \nu, \tau) d\nu d\gamma, \end{aligned} \tag{3.19}$$

where $C_{x1}(\cdot, \cdot, \cdot)$ is a summation of terms analogous to $A_\tau(\cdot, \cdot, z = 0)$ given in (A17), that is

$$C_{x1}(t', t, \tau) = \sum_{i=1}^{I} \int_{t-\tau}^{t} h_i(\lambda + t') h_i^*(\lambda) d\lambda. \tag{3.20}$$

In (3.19) the integral of (3.20) is given by

$$\begin{aligned} \int_{-\infty}^{+\infty} C_{x1}(t', t, \tau) dt &= \int_{-\infty}^{+\infty} \sum_{i=1}^{I} \int_{t-\tau}^{t} h_i(\alpha + t') h_i(\alpha) d\alpha dt \\ &= \sum_{i=1}^{I} \int_{-\infty}^{+\infty} \int_{-\infty}^{+\infty} h_i(\alpha + t') h_i(\alpha) \Pi_{t-\tau,\tau}(\alpha) d\alpha dt \\ &= \sum_{i=1}^{I} \int_{-\infty}^{+\infty} h_i(\alpha + t') h_i(\alpha) \int_{-\infty}^{+\infty} \Pi_{t-\tau,\tau}(\alpha) dt d\alpha \\ &= \tau \sum_{i=1}^{I} \int_{-\infty}^{+\infty} h_i(\alpha + t') h_i(\alpha) d\alpha \\ &\approx \tau C_h \delta(t'), \end{aligned} \tag{3.21}$$

where $\Pi_{t-\tau,\tau}(\alpha)$ is an unit-gate sliding window, similar to (A3) with constant area equal to τ, and

$$C_h = \sum_{i=1}^{I} \int h_i(t) h_i^*(t) dt, \tag{3.22}$$

considering analogous assumptions as those for $x2(t)$. In (3.22) C_h is a baseband version of C in (A21). The autocorrelation of $e(t)$ will be given by

$$R_e(t+t', t) = R_e(t') = r_{p_4}(t')\sigma_u^2 \tau C_h, \tag{3.23}$$

where $e(t)$ becomes a WSS stochastic signal.

The PAM signal $a(t)$ is a cyclostationary signal [36, 41] given by (3.3), but here the strategy used in [36] will be adopted whereby $a(t)$ is changed to $a(t) = \sum_{n=-\infty}^{+\infty} a_n \delta(t + \Theta - nT_b)$, where Θ is an unknown timing phase that reflects the fact that the origin of the time axis is arbitrary. By considering that Θ is uniformly distributed over the interval $[0, T_b[$, $a(t)$ becomes WSS with autocorrelation given by

$$R_a(t') = \frac{\sigma_a^2}{T_b} r_\delta(t'), \tag{3.24}$$

where $r_\delta(t')$ is the autocorrelation of the dirac impulse. Finally, the autocorrelation of $x_1(t)$ can be seen as the convolution of the autocorrelations of $e(t)$ and $a(t)$, and is given by

$$R_{x1}(t') = r_{p_4}(t') \frac{\sigma_a^2}{T_b} \sigma_u^2 C_h \tau, \tag{3.25}$$

where one can see that $x_1(t)$ is also WSS.

3.2.3 Signal and noise power

In order to compute the pTR output SNR (SNR_{out}) the signal and the noise terms power must be obtained. Since we have already computed the noise terms autocorrelation and shown that they are zero mean WSS processes, their power can be easily computed by considering its variance equal to the autocorrelation at the origin

$$\sigma_{x3}^2(\tau) = R_{x3}(0) = r_{p_3}(0)\sigma_w^2 \sigma_u^2 \tau I, \tag{3.26}$$

$$\sigma_{x2}^2(t_0, \tau) = R_{x2}(0) = r_{p_3}(0)\sigma_w^2 C_{x2}(t_0, \tau), \tag{3.27}$$

$$\sigma_{x1}^2(\tau) = R_{x1}(0) = r_{p_4}(0) \frac{\sigma_a^2}{T_b} \sigma_u^2 C_h \tau. \tag{3.28}$$

In (3.9) the PAM data-signal has pulse shape $c(t)$ given by (3.11), and considering similar assumptions to those underlying (3.24) its power is

$$\sigma_y^2(t_0, \tau) = \frac{\sigma_a^2}{T_b} [C_y(t_0, \tau)]^2 r_{p_4}(0), \tag{3.29}$$

where $C_y(t_0,\tau)$ is computed in a similar manner to $C_{x2}(t_0,\tau)$ and becomes

$$\begin{aligned} C_y(t_0,\tau)\delta(t') &\approx \sum_{i=1}^{I}\int_{-\infty}^{\infty} h_i(t+t')h^*_{i,t_0,\tau}(t)dt \\ &\approx \sum_{i=1}^{I}\int_{t_0}^{t_0+\tau} h_i(t+t')h^*_i(t)dt. \end{aligned} \tag{3.30}$$

Under those conditions $[C_y(t_0,\tau)]^2$ is the autocorrelation at the origin of $C_y(t_0,\tau)\delta(t')$, and $C_y(.)$ is a baseband version of C'' in (A25).

In the above equations the time-window dependent factors $C_.(.)$ that affects the signal and noise power terms are equivalent to TRM gains at the focal point for different configurations of the channel IRs (limited and/or unlimited). These constants are related with each other and it is important to note that when TRM associated assumptions are fulfilled C_{x2} is equal to C_y and as τ increases they both converge to C_h.

3.3 The passive time-reversal output SNR and its maximum

The pTR communication system firstly recombines energy as a matched filter, whose function is to maximize the SNR in each hydrophone and then sums all z_i signals (see Figure 3.1) to further reduce SNR and to reduce the ISI [56]. Considering that the array structure is adapted to the propagation environment such that the residual ISI is considered negligible the time-windowing optimization can be obtained from a closed form expression for the pTR output SNR.

The pTR communication system signal and noise power terms have already been found in (3.26), (3.27), (3.28) and (3.29). Since $x1$, $x2$ and $x3$ are zero mean independent random terms the variance of the sum is simply the sum of the variances and the pTR output SNR will be given by

$$SNR_{o,ideal}(t_0,\tau) = \frac{\sigma_y^2(t_0,\tau)}{\sigma_{x3}^2(\tau)+\sigma_{x2}^2(t_0,\tau)+\sigma_{x1}^2(\tau)}, \tag{3.31}$$

where its dependence on the window length, τ, and starting time t_0 is perfectly clear. Such pTR output SNR is ideal in the sense that it considers that there is no residual ISI.

After the pTR, the data frame detection can be made, as in Figure 3.1, in two steps: by sampling the pTR output signal $z(t)$ at the symbol period, T_b, that will result in the sampled signal $z(nT_b)$ corrupted by noise and ISI, followed by a slicer/detector that estimates the transmitted symbols. The full elimination of the ISI can only be attained if the pTR associated assumptions are fulfilled and, as deduced in Appendix A.2, can be attained even for a short time window. In a real scenario the array does not densely cover the entire water column and the overall pTR IR becomes a dirac-pulse corrupted with residual multipath that in the pTR communication system results in residual ISI.

For digital communications purpose the residual ISI should be considered as a corruption term similar to a noise term and can be incorporated in the SNR_{out} of (3.31) in a similar manner of equation (33) of [56]. Despite the influence of the residual multipath over the noise terms the pTR output SNR in presence of ISI can be approximated by

$$SNR_{o,isi}(t_0,\tau) \approx \frac{\sigma_y^2(t_0,\tau)}{\sigma_y^2(t_0,\tau)[ISI(t_0,\tau)] + \sigma_{x3}^2(\tau) + \sigma_{x2}^2(t_0,\tau) + \sigma_{x1}^2(\tau)}, \tag{3.32}$$

where the ISI is given by the ratio between the power of the multipath spread of the pTR overall IR at the symbol rate and its main path power,

$$ISI(t_0,\tau) = \frac{\sum_{n\neq 0} |p_{TR}(nT_b,t_0,\tau)^2|}{|p_{TR}(0,t_0,\tau)^2|} \tag{3.33}$$

where

$$p_{TR}(nT_b,t_0,\tau) = \sum_{i=1}^{I} [h_i^*(-t,t_0,\tau) * h_i(t)] * p_4(t)\bigg|_{t=nT_b} \tag{3.34}$$

is the baseband version of the pTR IR (A24) affected by the time window operation and sampled at the symbol rate $1/T_b$.

The pTR output SNR in presence of ISI given by (3.32) can also be computed considering the MSE between the transmitted symbols and the detector input $\overline{|a(n) - z(n)|^2}$ (see Figure 3.1) as in [56, 41]

$$SNR_{o,mse}(t_0,\tau) = \frac{1}{MSE(t_0,\tau)} - 1. \tag{3.35}$$

When the noise power dominates over the ISI $SNR_{o,mse}(t_0,\tau) \approx SNR_{o,ideal}(t_0,\tau)$, but when ISI dominates $SNR_{o,mse}(t_0,\tau) \approx ISI^{-1}(t_0,\tau)$ while the $SNR_{o,ideal}$ increases as the input noise power decreases. In spite of the differences between the $SNR_{o,ideal}$ given in (3.31) and $SNR_{o,mse}$ given in (3.35), when in presence of a well designed array that ensures $ISI^{-1} > SNR_{o,ideal}$ at the pTR output, their maxima occur for the same time-window duration, which will be clarified in Section 3.4. Window parameters for optimal detection can therefore be predicted from the pTR output SNR given in (3.31).

Equation (3.31) can be simplified since in (3.27) and (3.28) $C_{x2}(t_0,\tau) \ll \tau C_h$, $\sigma_w^2 = \sigma_u^2$, $\sigma_a^2/T_b \gg 1$, and $r_{p_4}(0) > r_{p_3}(0)$, such that $\sigma_{x2}^2(t_0,\tau) \ll \sigma_{x1}^2(t_0,\tau)$. Then (3.31) reduces to

$$SNR_{o,ideal}(t_0,\tau) \approx \frac{\sigma_y^2(t_0,\tau)}{\sigma_{x3}^2(\tau) + \sigma_{x1}^2(\tau)}, \tag{3.36}$$

and the approximation improves as τ increases, and more channel IR paths are included in the time-window.

For values of $\tau > 0$ one can define

$$\Phi(t_0,\tau) = \frac{C_y(t_0,\tau)}{\tau^{\frac{1}{2}}}, \tag{3.37}$$

where $C_y(t_0,\tau)$ can be computed from (3.30) as

$$C_y(t_0,\tau) = \sum_{i=1}^{I} \int_{t_0}^{t_0+\tau} |h_i(t)|^2 dt, \tag{3.38}$$

that is the summation of the energy cumulative functions of the channels IRs at all hydrophones. Using (3.37) in (3.36) it results that

$$\frac{SNR_{out}(t_0,\tau)}{\Phi^2(t_0,\tau)} = \frac{(\sigma_a^2/T_b)r_{p4}(0)}{\sigma_w^2\sigma_u^2 I r_{p3}(0) + (\sigma_a^2/T_b)\sigma_u^2 C_h r_{p4}(0)}. \tag{3.39}$$

Since the right term of the equation is constant with τ, $SNR_{out}(t_0,\tau)$ and $|\Phi(t_0,\tau)|^2$ have the same shape and the optimum τ that yields the global maximum for $SNR_{out}(t_0,\tau)$ is given by

$$\tau_{opt} = \arg\max(\Phi(t_0,\tau)). \tag{3.40}$$

where, with no loss of generality, the time-window starting point t_0 was considered to be chosen arbitrarily before the main path arrivals of the $h_i(t)$ IRs. Equations (3.37) and (3.40) state the remarkable result that the time-window that ensure the pTR maximum output SNR does not depend on the input noise power, and that it only depends on the channel IRs (see (3.38)). Since $C_y(t_0,\tau)$ can be seen as the overall pTR IR, $\Phi^2(t_0,\tau)$ represents its power and τ_{opt} the time-window length that guarantees an higher power of the pTR operator.

In a real situation $C_y(t_0,\tau)$ is not available since only a noisy version of $h_i(t)$ can be estimated in the pTR processor. An estimate of $\hat{C}_y(t_0,\tau)$ can be computed as

$$\begin{aligned}\hat{C}_y(t_0,\tau) &= \sum_{i=1}^{I}\int_{t_0}^{t_0+\tau} E\{|h_i(t)+u_i(t)|^2\}dt \\ &= C_y(t_0,\tau) + \sigma_u^2 I\tau, \end{aligned} \tag{3.41}$$

it results that

$$C_y(t_0,\tau) = \hat{C}_y(t_0,\tau) - \sigma_u^2 I\tau \tag{3.42}$$

where here $h_i(t) + u_i(t)$ is considered to be a narrowband estimate of the channel IRs. Replacing (3.42) in (3.37) yields an estimate of the optimal τ for real data

$$\begin{aligned}\hat{\Phi}(t_0,\tau) &= \frac{\hat{C}_y(t_0,\tau) - \sigma_u^2 I\tau}{\tau^{\frac{1}{2}}} \\ \hat{\tau}_{opt} &= \arg\max\hat{\Phi}(t_0,\tau) \end{aligned} \tag{3.43}$$

A good estimate of $\hat{C}_y(t_0,\tau)$ should be used in (3.42) if good results using real data are expected. It will be seen in Section 3.5 that when estimating $\hat{C}_y(t_0,\tau)$ with a single realization the estimate $\hat{\Phi}(t_0,\tau)$ becomes sensitive to noise, but using an average of (3.42) realizations improves the quality of results.

3.4 Performance simulations in realistic channels

The simulation scenario comprises a range independent acoustic channel with 100 m depth, over a 1.5 m thick silt sub-bottom and a gravel like bottom. The arrival pattern computed with the Bellhop ray/beam model [27], for a source depth of 60m and a source-array range of 1.5km, can be seen in Figure 3.2, where the multipath spans over 100 ms, as usual with a higher concentration of energy in the first arrivals. The beginning of the time-window was chosen manually just before the first arriving path, and is represented by a vertical line of 'o' in Figure 3.2 where the '+' indicates the maximum time-window length considered in the analysis, and '*' the optimum time-window length for pTR output SNR optimization as described below.

Two cases were considered:

1. The Low Frequency (LF) case that comprises a 16-hydrophone-4-meter-spaced VLA with the first hydrophone placed at 30m, the transmitted data signal is a 2-PSK PAM signal with a 50% rolloff fourth-root raised-cosine pulse shape, the carrier frequency is of 1600Hz, and the data rate is 300 bits/s.

2. The High Frequency (HF) case that comprises a 8-hydrophone-8-meter-spaced Vertical Line Array (VLA) with the first hydrophone placed at 30m, the transmitted data signal is a 2-PSK PAM signal with a 50% rolloff fourth-root raised-cosine pulse shape, the carrier frequency is of 10kHz, and the data rate is 2000 bits/s.

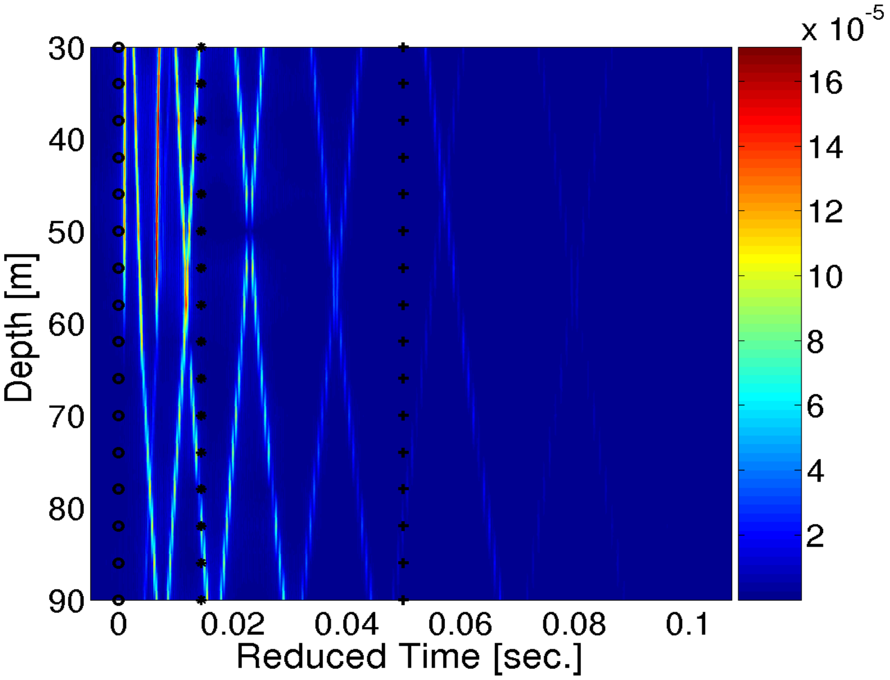

Figure 3.2: Simulated depth dependent broadband arriving pattern over a realistic scenario: start time 'o', optimum window duration '*' and maximum window duration '+'.

For the LF case a low pTR residual ISI is expected due to the low symbol rate and the high number of hydrophones. In opposition an high pTR residual ISI will be expected in the HF case. For each of the two cases Monte Carlo runs under low and high input SNR will be conducted.

Figure 3.3 shows the pTR output SNR (in dB) as a function of window length parameterized by the input SNR ($\mathrm{SNR_{in}}$), for the LF case (a) and the HF case (b). In each case, pTR output SNR results are shown via Monte-Carlo simulation with the MSE-based form (3.35) ('□'), using the ideal pTR closed form expression (3.31) ('∇'), and for the residual ISI given by the inverse of (3.32) ('o').

For low residual ISI in LF case Figure 3.3(a) shows that for a $SNR_{in} \approx -25$ dB good agreement is obtained between the ideal pTR and MSE curves. For high $SNR_{in} \approx -10$ dB the residual ISI of the TR operator becomes dominant and leads to saturation of SNR_{mse}. For high residual ISI, in the HF case, Figure 3.3(b) shows that for a low $SNR_{in} \approx -25$ dB good agreement in shape is obtained between the ideal pTR and MSE curves a better agreement would be obtained if instead of the SNR_{out} given by (3.31) the SNR_{out} given by (3.32) was used, nevertheless the agreement in shape its enough for the optimum time window length prediction. For high $SNR_{in} \approx -10$ dB the residual ISI of the TR operator becomes dominant and leads to saturation of SNR_{mse}.

The overall SNR gain of the pTR is given by the array number of elements that is approximately 12dB (for 16-hydrophone, LF case) and 9dB (for 8-hydrophone, HF case), the time-window length SNR and ISI improvement. In what concerns the ISI as the time-window includes more paths its tendency is to reduce as it can be observed in the enhancement of the $SNR_{o,isi} = ISI^{-1}$ curve of Figure 3.3(b), nevertheless in Figure 3.3(a) shows that the ISI^{-1} curve present a local maximum at 6ms and the global maximum at 30ms revealing that such tendency behave nonlinearly with the time-windowed multipath structure of the channel.

As previously mentioned for the low SNR_{in} case the optimum time-window is ruled by the $SNR_{o,ideal} \approx SNR_{o,mse}$ curves, their maxima reveal that the optimum time-window length would be 15ms, approximately 5 symbols for the LF case, and 13.5ms, approximately 27 symbols for the HF case. In the high SNR_{in} case the optimum time-window is ruled by the ISI and the $SNR_{o,mse}$ curve is maximum when the $SNR_{o,isi}$ is maximum.

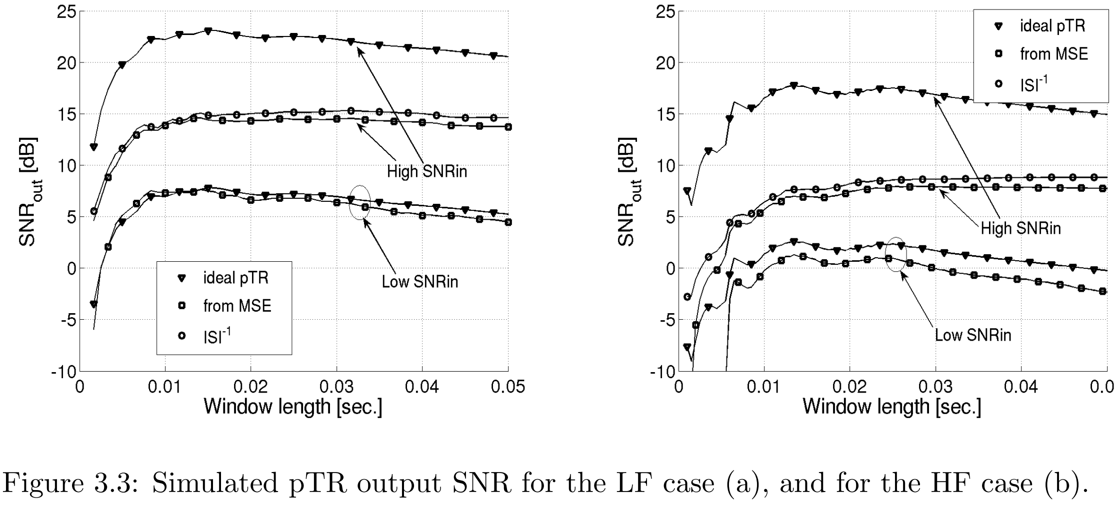
(a)

(b)

Figure 3.3: Simulated pTR output SNR for the LF case (a), and for the HF case (b).

Figure 3.4 shows the behavior of $\Phi(t_0, \tau)$ (3.37) versus time-window length for the LF and the HF cases. It can be seen that, as predicted by the theoretical derivation, the maxima clearly coincide with those of $SNR_{o,ideal}$ in Figure 3.3 both for the LF case with $\tau_{opt} = 15$ms and the HF case with $\tau_{opt} = 13.5$ms. More than detecting the optimum time window when the SNR dominates over the ISI the $\Phi(t_0, \tau)$ curve shape agrees well with the $SNR_{o,ideal}$ and $SNR_{o,mse}$ curves shape.

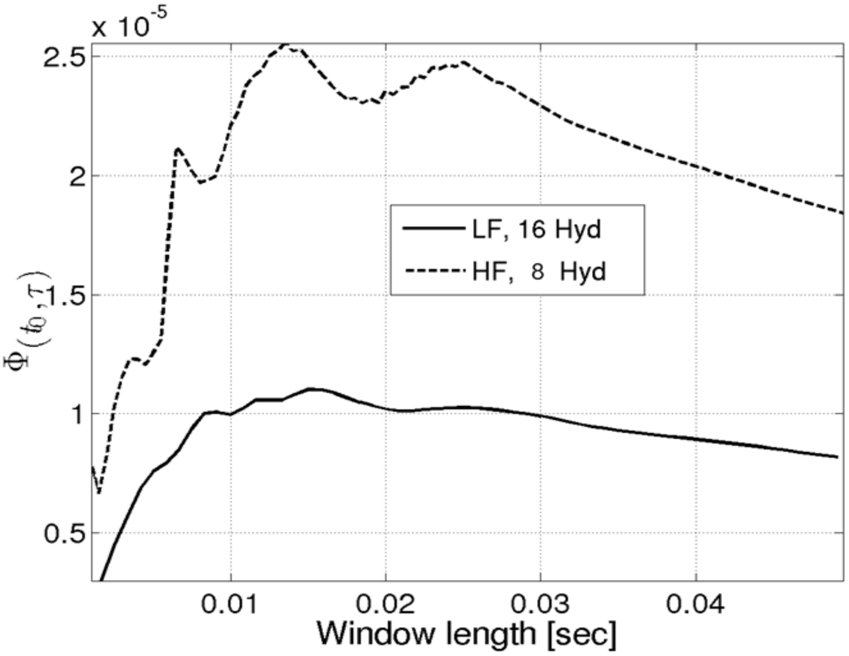

Figure 3.4: Simulated performance of the proposed optimal time-window prediction method using (3.37) and (3.40) for the LF and HF cases

3.5 Experimental results

The experimental data were acquired during the INTIFANTE'00 sea trial that took place off the town of Setúbal, approximately 50km south of Lisbon (Portugal) in October 2000 [28]. This paper concentrates on the Binary Phase Shift Keying data collection. The scenario was similar to that used in Section 3.4 with the main differences being that with real data there are noise corruption and geometric/environment mismatch between the probe-signal and the data transmissions. The acoustic source was suspended from the free drifting oceanographic vessel - NRP D. Carlos I - at a nominal depth of 60 m. The receiver was a surface suspended 16-equispaced-hydrophone vertical line array spanning nominal depths between 31 an 91 m. The source range distance was approximately 1420 m ± 100 m. Nine sequential transmissions (in the following referred to as shot 1 to 9) will be considered, each one composed of a probe-signal transmitted 0.5 seconds before a 5 second PSK data stream, with a repetition rate of 7 seconds.

During the INTIFANTE'00 sea trial the pTR based data communications system was similar to that of Figure 3.1, with the $p_2(t)$ narrowband filter of the IR estimation operation (path above in Figure 3.1) distributed between the transmitter and the receiver, i.e., the transmitted probe-signal was a fourth-root raised-cosine pulse, $p_1(t)$, and IR estimates were obtained by pulse compression at the receiver side (see [45] for details).

The estimated arrival pattern for shot 9 can be seen in Figure 3.5. This Figure shows a number of arrival paths that are not as well defined as in the simulations due to noise corruption. Such noise corruption will, obviously, affect the proposed time-window optimization method given by equation (3.43) since $\hat{C}_y(t_0, \tau)$ in (3.41) has to be computed from a single realization of $|h_i(t) + u_i(t)|^2$. In (3.43) the noise variance σ_u^2 was calculated considering the mean noise variance for all hydrophones.

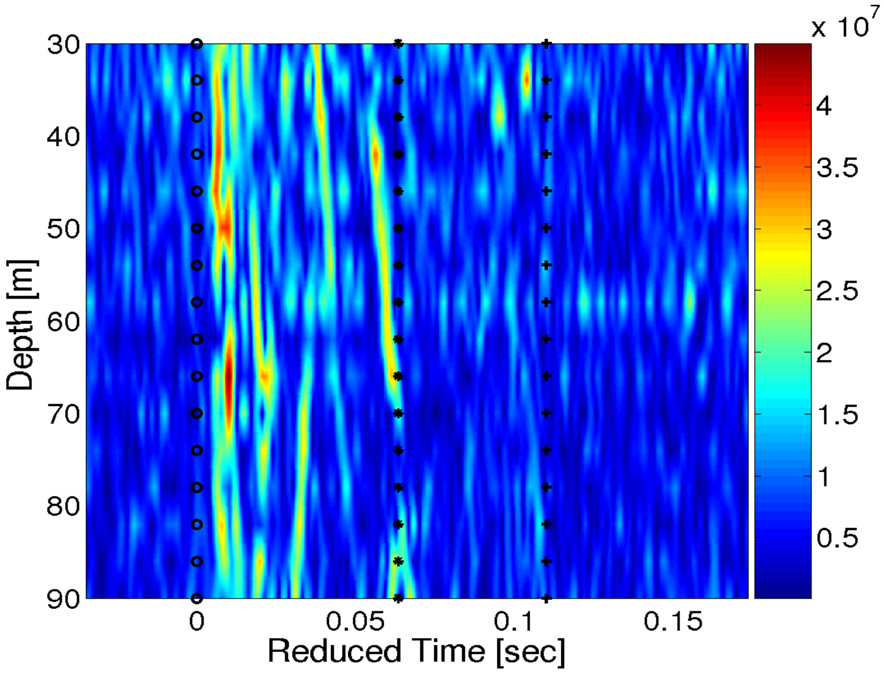

Figure 3.5: Real data vertical array estimated impulse responses: start time '0', optimum window duration '*' and maximum window duration '+'.

Figure 3.6(a) shows the pTR output SNR computed via the MSE at the detector input with (3.35), for the first 3 seconds of data during shot 9. One can see a progressive degradation in performance due to geometric/environmental mismatch in IRs between the probe-signal and data-signal transmissions. Such loss of performance affects primarily larger time windows since those include the later arrivals that are usually considered more prone to fading. Despite this channel variability, Figure 3.6(b) shows that the predicted pTR output SNR maxima, given by the local maxima of $\hat{\Phi}(t_0, \tau)$, are in a good agrement with the true local maxima in the first-second curve of Figure 3.6(a). Although the maxima location are well predicted the first and the second maxima are interchanged.

Figure 3.7 shows analogous results for shot 7. Figure 3.7(a) shows that, although this case presents a pTR output SNR maxima location almost constant during the three seconds of data only the first maximum is clearly predicted by the $\hat{\Phi}(t_0, \tau)$ curve in Figure 3.7(b).

Figures 3.6 and 3.7 present two extreme cases in the pTR output SNR maxima detec-

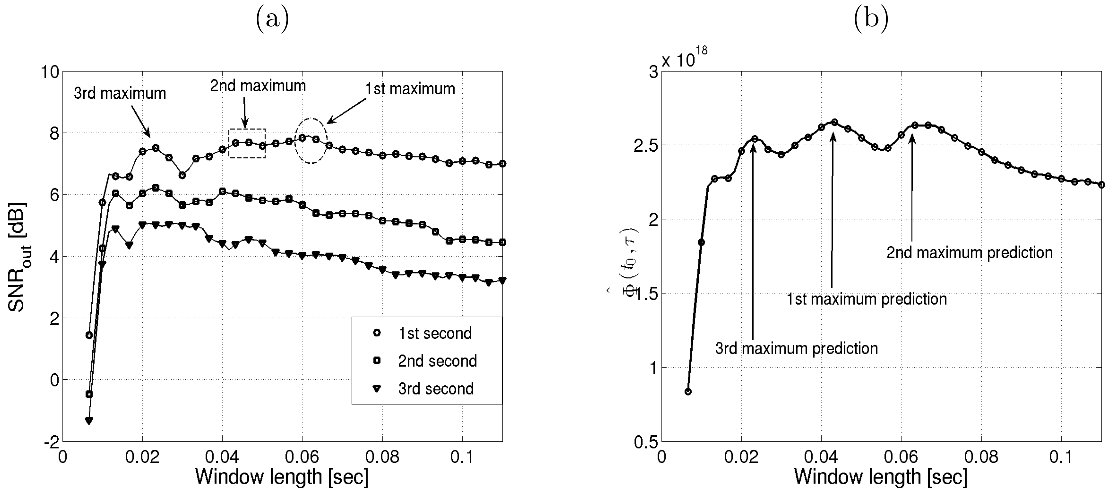
(a) (b)

Figure 3.6: Real data performance of the proposed optimal time-window prediction method obtained in shot 9: pTR output SNR computed by using the MSE at the slicer/detector input (a) and maxima prediction by using (3.43) (b).

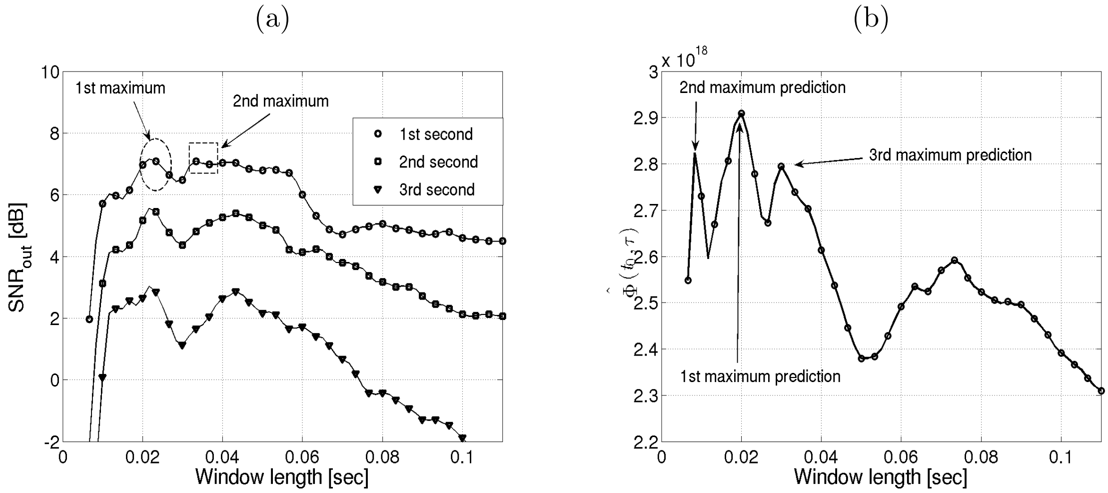
(a) (b)

Figure 3.7: Real data performance of the proposed optimal time-window prediction method obtained in shot 7: pTR output SNR computed by using the MSE at the slicer/detector input (a) and maxima prediction by using (3.43) (b).

tion: in the former the global maximum is predicted to be the second true maximum but a reasonable shape agreement is observed between $\hat{\Phi}(t_0, \tau)$ and the first-second SNR_{out} curves; while in the latter the global maxima is well predicted but a different shape are observed for the two curves. Typically the other shots present an intermediate behavior between shot 7 and 9.

To verify the robustness of the proposed optimization technique a mean analysis over the first second of data using all nine shots is presented in Figure 3.8. The continuous line shows the mean pTR SNR_{out} that partially eliminates the fake (noise-induced) paths and the later path arrivals that are more sensitive to fading. The dashed line shows the mean of $\hat{\Phi}(t_0, \tau)$ over all shots. One can see that these two curves are in excellent agreement and display an almost constant ratio, such that the same maxima locations are predicted. That suggests that pTR performance optimization is affected by channel noise that will introduce a fake path structure. The problem can be overcome by enhanced IR estimation using large time-bandwidth product probe-signal or by averaging a number of closely time spaced probe-signals sent before the data stream.

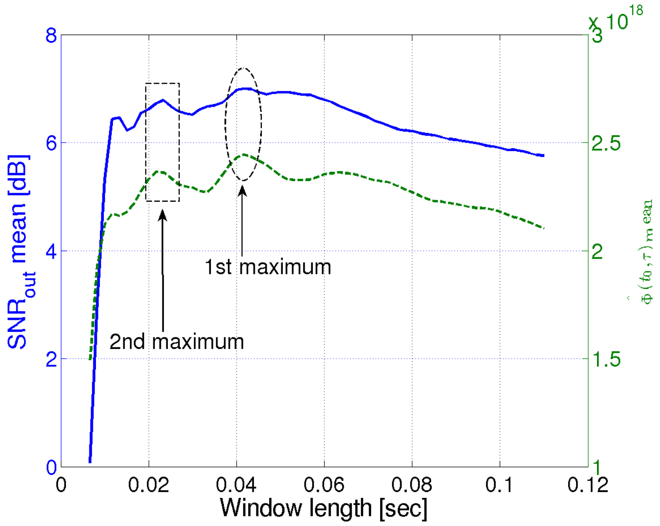

Figure 3.8: Mean analysis over all shots for the real data performance of the proposed optimal time-window prediction method: pTR output SNR output computed by using the shot-mean MSE at the slicer/detector input (a) and shot-mean of the maxima prediction by using (3.43) (b).

Due to the good agrement between the $\hat{\Phi}(t_0, \tau)$ and $SNR_{o,mse}$ curves one can state that the VLA used during the experiment is well design for the ISI reduction required to satisfy the condition that the pTR output SNR dominates over the ISI.

3.6 Conclusion and future work

The problem of time-window optimization when operating a pTR with a VLA for underwater communications was considered. It was found that the optimum time-window simultaneously guarantees higher pTR output SNR and lower MSE at the slicer/detector input, concerning the use of a well design VLA for the environmental conditions to provide a sufficiently low ISI at the pTR output, in order to satisfy the condition that the pTR output SNR should dominate over the ISI. Time window optimization was made possible by the derivation of a closed-form expression for the pTR output SNR (3.31). Such expression allowed the derivation of (3.40) that clearly states that the optimum time-window depends only on the channel IRs and is not dependent on the data signal or noise level. Simulation results confirm and gauge for the theoretic foresight.

When applied to real data the channel IRs are not available and noisy estimates must be used. Even with heavily noise corrupted IRs the developed technique presents a good fit with the pTR output SNR and its global maximum being closely predicted in most of the shots. Noise-related problems in IRs estimation are mainly due (in real data) to the use of low power probe-signals (fourth-root raised cosine pulse). The usage of high power probe-signals such as chirp signals or M-sequences should be addressed in future experiments. Despite its quality, it was found that the optimum time-window loses validity after only a few seconds due to geometric/environment variability. Future developments should address the problem of using the proposed time-window optimization with adaptive pTR-based equalizers.

Although it was developed for pTR, the time-window optimization method can also be applied to aTR by considering that in the latter case the noise term $x3$ does not exist and $x2$ and $x1$ (3.10) are slightly different (see [18]).

Acknowledgments

The authors would like to thank the NATO Undersea Research Centre (NURC) for the loan of the acoustic sound source, the support of Enrico Muzzi and the NRP D. Carlos I crew during the INTIFANTE'00 sea trial. This work was financed by FCT, Portugal, under NUACE project, contract POSI/CPS/47824/2002, ATOMS project, contract POCTI/P/MAR/15296/1999, and the Portuguese Ministry of Defense under the LOCAPASS project.

Chapter 4

Generalization of Waveguide Invariants and Application to Passive Time Reversal

Abstract: In most underwater acoustic experiments acoustic sources and hydrophone arrays are moored so as to provide a geometry as controllable as possible. A more operational approach is to use moving sources and drifting acoustic receivers in which case the data exhibits continuous phase and amplitude changes due to depth and range shifts. This may be problematic when the processing of the collected acoustic data requires the use of correlation between successive received signals, e.g., in passive time reversal where a probe-signal is sent ahead of the data for post crosscorrelation. This paper demonstrates that in the passive time reversal context the source-array range, the array and source depth mismatches that occurs during data transmission can be compensated using an appropriate frequency shift of the received probe-signal pressure field. Acoustic simulations and real data collected during the MREA'04 experiment show that the frequency translation required for the geometric mismatch compensation can be computed using invariant properties of the waveguide, and thus provide a potential for substantial processing signal to noise ratio gain in underwater communications between moving platforms.

4.1 Introduction

Active Time reversal (aTR) has been shown to produce temporally and spatially focused acoustic signals in a stationary environment. Such focusing capabilities are a consequence of the time reversal invariance of the linear lossless wave equation describing acoustic propagation in the ocean environment [34] and one of its major goals is the development of underwater coherent communication techniques since focusing is similar to undoing the multipath structure of the channel [17, 11]. Passive Time Reversal (pTR), originally referred to as Passive Phase Conjugation (PPC) [8], is a synthetic version of aTR where a probe-signal is transmitted ahead of the data-signal in order to provide an estimate of the underwater channel Impulse Responses (IRs). Time focusing is then performed at the array side by simply convolving a time reversed version of the estimated IRs with the incoming data-signal [50, 24, 43]. In the presence of a moving source and a free drifting array, there exist three major sources of mismatch: the source-array range shift, the source depth shift and the array depth shift. Due to those geometric mismatches pTR rapidly loses its time focusing capability [29, 45] and up to now there has been no attempt to incorporate a geometric tracking in pTR in order to attain long-term focusing.

For aTR, previous work by Song el al. [55] addresses the focal spot range shift problem using a frequency translation of the array received acoustic field. The technique can be readily applied in pTR, making it possible to perform source-array range tracking. It is based on the β waveguide invariant [21] and only accounts for shifting in range of the focal spot intensity. In what concerns the focal spot depth shift in aTR a different strategy was proposed by Walker [60]. In Walker's work a depth shift of the focal spot has been achieved, but contrarily to the source-array range shift proposed by Song it is not based in simple waveguide invariant properties, and its implementation for the pTR source depth shift compensation in real time does not look straightforward.

In [46] the authors presented preliminary simulations and real data results suggesting that similarly to source-array range shift compensation, source depth shift and array depth shift compensation could be performed by a frequency shift of the acoustic field. It was found that for narrowband signals with a center frequency of 3.6 kHz, frequency shift compensation performs well in the vicinity of the geometric canonical values. Moreover, it was found that associated with the intensity geometric mismatch compensation there is an approximately linear phase. In the present paper the theoretical proof for such compensation capability is given for the source-array range shift, for the array depth and source depth shifts.

The source-array range compensation depends on the waveguide invariant β that relates the modal horizontal phase velocity with the horizontal group velocity. The invariant β summarizes in a single parameter the dispersive characteristics of the acoustic field in a waveguide. In fact, it has been shown by Chuprov [6, 21] that the lines of constant sound intensity, constant rate of change of the phase velocity along the waveguide, and constant envelope group delay have constant slope β in the frequency/range plane. In this paper by using a perfect waveguide a different interpretation of the invariant is given in order to explicitly derive an approximation of the horizontal wavenumber by using the group slowness. Such reinterpretation of β is then used for range shift compensation of the pressure field in intensity and phase by simply using an appropriate frequency shift. Using a similar approach it was found that the vertical wave number can also be approximated by considering a frequency invariant ζ that relates the vertical phase velocity with the horizontal group velocity, which allows for the compensation of source and array depth shifts in pTR applications. The invariants β and ζ has been originally derived by Chuprov [6] taking in consideration only the sound pressure field intensity. The reinterpretation presented in this work allows for the use of the invariants for pressure field intensity and phase compensation when using pTR in a geometric mismatch environment.

When applied to underwater communications the proposed geometric mismatch compensation method provides a longer stability of a pTR communications system by increasing the elapsed time between probe-signal transmissions, but also makes it possible to estimate source and receiving array depth oscillations, and source-receiver range variations, under the form of an environmental equalizer [47].

Section 4.2 explains how the invariant β and ζ can be used to compute an approximation to the horizontal and vertical wave numbers respectively, using the horizontal group slowness. Section 4.3 explains the influence of the geometric mismatch over the pTR in a perfect waveguide and finds compensation strategies using a frequency shift that can be computed with the invariants β and ζ. Section 4.5 heuristically extends the findings to realistic environments, by taking into consideration the WKB approximation and the Pekeris waveguide. Section 4.6 uses real data, narrowband signals centered at 3.6 kHz, with geometric mismatch to demonstrate the usefulness of the new findings, and shows that longer stability of the pTR processor can be attained at least up to a range mismatch of 25 m, and a source depth mismatch and an array depth mismatch of about 0.7 m. Section 4.7 summarizes the compensation procedure and describes possible applications.

4.2 The waveguide invariants

In this section it will be shown that the horizontal wavenumber k_m and the vertical wavenumber γ_m can be computed by a linear approximation of the horizontal group slowness and that such approximation is made possible by the frequency invariants β and ζ, respectively. These results will be obtained for the perfect waveguide and extended heuristically to the Pekeris waveguide and to the WKB approximation in Section 4.5

The derivation draws upon generic results proposed in Appendix B.1, where it is shown that one monotonic function Φ can be linearly approximated by another monotonic function Π using a least-squares approximation or by setting one point of the two functions to the same position and then rotating one of the functions until it fits the other at a different point. The later provides a connection with the current waveguide invariant theory and the former becomes more useful in the context of the pTR geometric mismatch compensation proposed in this paper. The former strategy is a particular case of the latter and ensures smaller approximation error.

4.2.1 Approximation of the horizontal wavenumbers using waveguide invariants

The two strategies of Appendix B.1 can be applied to the approximation of horizontal wavenumbers by their reciprocals by setting $\Phi_m = k_m$ and $\Pi_m = k_m^{-1}$. Using (B4) it results that k_m can be approximated by k'_m with

$$k'_m = -\beta'_{\mu,\nu} k_m^{-1} + \rho'_{\beta,\mu,\nu}, \tag{4.1}$$

where $m=\mu$ and $m=\nu$ are the modes where k_m and k'_m coincide,

$$\beta'_{\mu,\nu} = -\frac{k_\mu - k_\nu}{\frac{1}{k_\mu} - \frac{1}{k_\nu}}, \tag{4.2}$$

and

$$\rho'_{\beta,\mu,\nu} = k_\nu + \beta'_{\mu,\nu}\frac{1}{k_\nu}. \tag{4.3}$$

In a perfect waveguide the horizontal wavenumber is given by

$$k_m = \sqrt{\frac{\omega^2}{c^2} - \gamma_m^2}, \tag{4.4}$$

where γ_m is the vertical wavenumber (which, in a range independent waveguide, is frequency independent). Using (4.4) the horizontal group slowness becomes

$$\frac{1}{u_{h,m}} = \frac{dk_m}{d\omega} = \frac{\omega}{c^2}\frac{1}{k_m}, \tag{4.5}$$

and the horizontal phase slowness

$$\frac{1}{v_{h,m}} = \frac{k_m}{\omega}. \tag{4.6}$$

Multiplying and dividing the fist term of the right hand side of (4.1) by $(\omega/c)^2$, multiplying and dividing the second term by ω, and considering the phase and the group slowness equations for the perfect waveguide (4.5) and (4.6), respectively, it results

$$k'_m = -\beta_{\mu,\nu}\omega\frac{dk_m}{d\omega} + \omega\rho_{\beta,\mu,\nu}, \tag{4.7}$$

where

$$\beta_{\mu,\nu} = -\frac{\frac{k_\mu}{\omega} - \frac{k_\nu}{\omega}}{\frac{\omega}{c^2}\frac{1}{k_\mu} - \frac{\omega}{c^2}\frac{1}{k_\nu}} = -\frac{\frac{1}{v_{h,\mu}} - \frac{1}{v_{h,\nu}}}{\frac{1}{u_{h,\mu}} - \frac{1}{u_{h,\nu}}}, \tag{4.8}$$

and

$$\rho_{\beta,\mu,\nu} = \frac{1}{v_{h,\nu}} + \beta_{\mu,\nu}\frac{1}{u_{h,\mu}}. \tag{4.9}$$

Since (4.7) can be rewritten as

$$\frac{k_m}{\omega} \approx -\beta_{\mu,\nu}\frac{dk_m}{d\omega} + \rho_{\beta,\mu,\nu}, \tag{4.10}$$

it corresponds to linearly approximate the horizontal phase slowness using the horizontal group slowness [35] [1], and $\beta_{\mu,\nu}$ is usually termed waveguide invariant [21] [6]. Here it will be re-termed as horizontal waveguide invariant since it relates the horizontal phase slowness with the horizontal group slowness.

In a similar manner the approximation can be done considering the least-squares form (B1), that can be applied by considering all modes or just a subset M_e of the propagating modes M, resulting in

$$k'_m = -\beta_e\omega\frac{dk_m}{d\omega} + \omega\rho_{\beta,e}, \tag{4.11}$$

---

[1] Figure 1 of reference [35] shows that there is an approximately linear relation between phase speed and group speed. A case with two groups of modes that result in a dual slope linear relation is presented.

where

$$\beta_e = -\frac{\overline{k_m k_m^{-1}} - \overline{k_m}\;\overline{k_m^{-1}}}{\overline{(k_m^{-1})^2} - \overline{k_m^{-1}}^2}\;\frac{c^2}{\omega^2}, \tag{4.12}$$

and

$$\rho_{\beta,e} = \overline{\frac{1}{v_{h,m}}} + \beta_e \overline{\frac{1}{u_{h,m}}}, \tag{4.13}$$

where the bar represents the mean over the assumed subset of modes M_e

Since (4.7) represents a set of linear approximations to k_m it is expected that the approximation in the least-squares error sense (4.11) equals or is close to one of them. In other words, there should exist an effective number of modes M_e and a pair (μ, ν) where $\beta_e \approx \beta_{\mu,\nu}$ and $\rho_{\beta,e} \approx \rho_{\beta,\mu,\nu}$. The approximation using an effective number of modes $M_e < M$ is plausible since in a real situation the waveguide itself filters the higher order modes or, at least, strongly attenuates them. Such filtering corresponds, in the ray mode analogy, to eliminating rays with steeper angles.

In order to develop signal processing techniques that make use of the horizontal wavenumber approximation k'_m it is important to demonstrate the frequency invariance of β_e and $\rho_{\beta,e}$. To establish that property the following auxiliary normalized product will be used

$$\Gamma_{\beta,m} = \frac{k_m k_m}{\gamma_m^2 + k_m^2}, \tag{4.14}$$

where $(\gamma_m^2 + k_m^2) = (\omega/c)^2$ is the wavenumber absolute value.

In the ray mode analogy it is considered by Tolstoy ([58] pp. 102) that the ray solution to the wave equation defines an infinite number of angles corresponding to the angles of incidence. The mode solution defines a finite number of angles that correspond to the rays that reinforce each other. So, in a perfect waveguide each mode is associated to an angle from the horizontal $\pm\theta_m$ that corresponds to an angle of incidence $\left(\frac{\pi}{2} - \theta_m\right)$. In such context the horizontal and the vertical wavenumbers can be defined as

$$\begin{aligned} k_m &= \frac{\omega}{c}\cos\theta_m, \\ \gamma_m &= \frac{\omega}{c}\sin\theta_m, \end{aligned} \tag{4.15}$$

where c represents the waveguide sound speed (assumed isovelocity). By using (4.15), product (4.14) becomes

$$\Gamma_{\beta,m} = \Gamma_\beta(\theta_m) = \cos^2(\theta_m) \tag{4.16}$$

where $\theta_m \in]0, \pi/2[$. Figure 4.1 shows the product $\Gamma_{\beta,m}$ as a function of θ_m (dotted curve). As the frequency increases the angles θ_m shift to the left and new angles, that correspond to new modes/rays, are included every $\omega_{0,m} = (c/D)m\pi$ ([58] pp. 99), where $\omega_{0,m}$ is the mode m cutoff frequency. Although θ_m changes with frequency, for a sufficiently high number of propagating modes M the shape of $\Gamma_{\beta,m}$ remains unchanged, in particular for small values of m where θ_m is densely populated. That means that the shape of $\Gamma_{\beta,m}$ becomes invariant with increasing frequency.

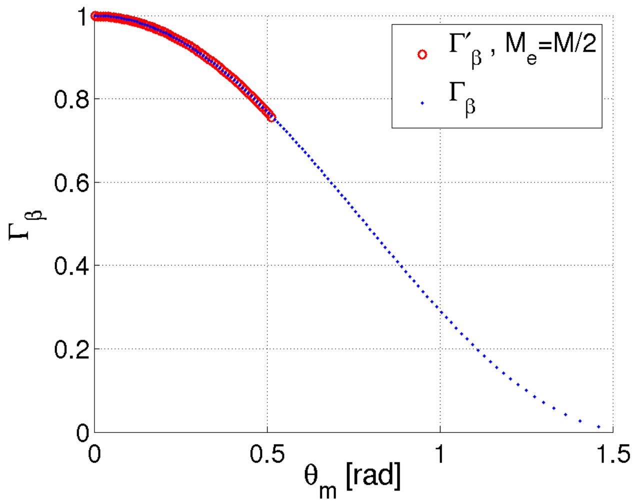

Figure 4.1: Normalized product $\Lambda_{\beta,m}$ (4.16) (dotted line), and its least-squares approximation (4.17) for an effective number of modes $M_e = M/2$ (circles).

Product (4.14) can be approximated by $\Gamma'_{\beta,m}$ with

$$\begin{aligned} \Gamma'_{\beta,m} &= \frac{k'_m k_m}{\gamma_m^2 + k_m^2}, \\ \Gamma'_\beta(\theta_m) &= -\beta_e + \rho_{\beta,e}\, c \cos\theta_m, \end{aligned} \tag{4.17}$$

where k'_m is given by (4.11). This is shown by the circles in Figure 4.1 for $M_e = M/2$ corresponding to $\theta_m \in]0, \pi/6[$. Since the $\Gamma_{\beta,m}$ shape is invariant with frequency its approximation $\Gamma'_\beta(\theta_m)$ will be almost invariant, and that makes β_e and $\rho_{\beta,e}$ also almost frequency invariant. In fact as the frequency increases M_e increases and β_e and $\rho_{\beta,e}$ oscillate around a frequency independent mean value with an amplitude that decreases with frequency.

4.2.2 Approximation of the vertical wavenumbers using waveguide invariants

The approximation of the vertical wavenumber using the horizontal wavenumber inverse is analogous to the approximation of the horizontal wavenumber of Section 4.2.1 and is straightforward considering the two linear approximation strategies of Appendix B.1 with $\Phi_m = \gamma_m$ and $\Pi_m = k_m^{-1}$.

Considering the vertical phase slowness

$$\frac{1}{v_{v,m}} = \frac{\gamma_m}{\omega}, \tag{4.18}$$

and the horizontal group slowness for the perfect waveguide (4.5), it results that γ_m can be approximated by γ'_m

$$\gamma'_m = -\zeta_{\mu,\nu}\omega\frac{dk_m}{d\omega} + \omega\rho_{\zeta,\mu,\nu}, \tag{4.19}$$

where

$$\zeta_{\mu,\nu} = -\frac{\frac{\gamma_\mu}{\omega} - \frac{\gamma_\nu}{\omega}}{\frac{\omega}{c^2}\frac{1}{k_\mu} - \frac{\omega}{c^2}\frac{1}{k_\nu}} = -\frac{\frac{1}{v_{v,\mu}} - \frac{1}{v_{v,\nu}}}{\frac{1}{u_{h,\mu}} - \frac{1}{u_{h,\nu}}}, \tag{4.20}$$

and

$$\rho_{\zeta,\mu,\nu} = \frac{1}{v_{v,\nu}} + \zeta_{\mu,\nu}\frac{1}{u_{h,\mu}}, \tag{4.21}$$

where (4.20) defines a constant that will be called vertical waveguide invariant and its invariance with the frequency will be shown at the end of this section.

Similarly to the k_m approximation in the least-squares sense, the approximation can be done considering the least-squares form (B1), yielding

$$\gamma'_m = -\zeta_e \omega \frac{dk_m}{d\omega} + \omega \rho_{\zeta,e}, \tag{4.22}$$

where

$$\zeta_e = -\frac{\overline{\gamma_m k_m^{-1}} - \overline{\gamma_m}\;\overline{k_m^{-1}}}{\overline{(k_m^{-1})^2} - \overline{k_m^{-1}}^2}\,\frac{c^2}{\omega^2}, \tag{4.23}$$

and

$$\rho_{\zeta,e} = \overline{\frac{1}{v_{v,m}}} + \zeta_e \overline{\frac{1}{u_{h,m}}}. \tag{4.24}$$

Since (4.19) represents a set of linear approximations to γ_m it is expected that the approximation in the least-squares sense (4.22) will be close to one of them, that is, there is an effective number of modes M_e and one pair (μ, ν) such that $\zeta_e \approx \zeta_{\mu,\nu}$ and $\rho_{\zeta,e} \approx \rho_{\zeta,\mu,\nu}$.

In order to develop signal processing techniques that make use of the horizontal wavenumber approximation γ'_m with wideband signals it is important to demonstrate the frequency invariance of ζ_e and $\rho_{\zeta,e}$. Such frequency invariance is better understood by considering the normalized product

$$\Gamma_{\zeta,m} = \frac{\gamma_m k_m}{\gamma_m^2 + k_m^2}. \tag{4.25}$$

Considering the ray mode analogy ([58] pp. 102) and k_m and γ_m given by (4.15), product (4.25) becomes

$$\Gamma_{\zeta,m} = \Gamma_\zeta(\theta_m) = \frac{1}{2}\sin(2\theta_m), \tag{4.26}$$

where $\theta_m \in]0, \pi/2[$. It can be approximated by $\Gamma'_{\zeta,m}$, defined as

$$\begin{aligned} \Gamma'_{\zeta,m} &= \frac{\gamma'_m k_m}{\gamma_m^2 + k_m^2} \\ \Gamma'_\zeta(\theta_m) &= -\zeta_e + \rho_{\zeta,e}\; c\cos\theta_m. \end{aligned} \tag{4.27}$$

Figure 4.2 shows the product $\Gamma_{\zeta,m}$ as a function of θ_m (dotted line). The maximum of Γ_ζ is always at $M/\sqrt{2}$ that corresponds to $\theta_{M/\sqrt{(2)}} \approx \pi/4$. In Figure 4.2 the circles represent the approximation to Γ_ζ with $M_e = M/2$ that correspond to $\theta_m \in]0, \pi/6[$.

It is clear from Figures 4.1 and 4.2 that the approximation γ'_m is poorer than k'_m, nevertheless in both cases the approximation quality can be enhanced by applying the

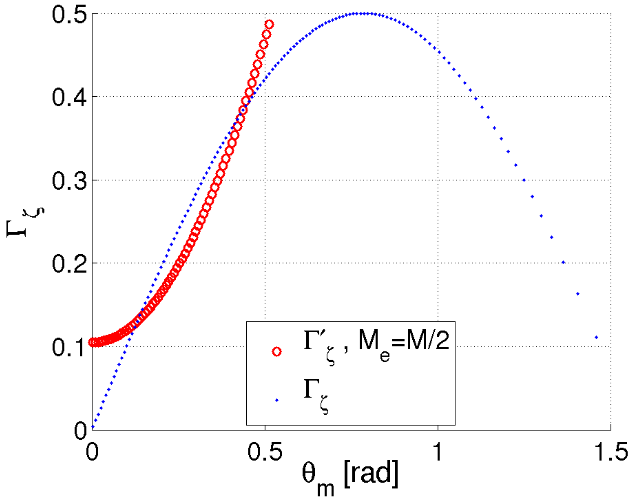

Figure 4.2: Normalized product $\Lambda_{\zeta,m}$ (4.26) (dotted line), and its least-squares approximation (4.27) for an effective number of modes $M_e = M/2$ (circles).

approximation to a small number of modes M_e or by applying the approximation in small sets of modes, resulting in different values of the waveguide invariants for each set. Still similar arguments as those used in Figure 4.1 demonstrate that ζ_e and $\rho_{\zeta,e}$ are also nearly invariant with frequency.

4.3 Geometric mismatch compensation in passive time reversal

This section establishes how the geometric mismatch (source-array range, source depth and array depth mismatch) and the frequency shift affect the pTR output in a perfect waveguide. The usefulness of the approximations to k_m and γ_m developed in Section 4.2 for geometric mismatch compensation will then arise naturally.

4.3.1 Passive Time Reversal in a stationary geometry

The behavior of pTR in a stationary environment was originally defined in [26] and refined by several authors, and it will be repeated here only for the definition of terms and for further formal understanding of how geometric mismatch affects pTR performance.

The pressure field received by each hydrophone of a Vertical Line Array (VLA) from a monochromatic point source is given by the *Green's* function

$$G_\omega(R, z_0, z_i) = \frac{-j}{\rho\sqrt{8\pi R}} e^{-j\frac{\pi}{4}} \sum_{m=1}^{M} \frac{Z_m(z_i)Z_m(z_0)}{\sqrt{k_m}} e^{ik_m R}, \tag{4.28}$$

where R represents the range between the source and the VLA, z_0 the source depth, z_i the array hydrophones depth, ρ the water density considered to be unitary constant over the water column, Z_m is the depth dependent mode shape and k_m is the horizontal wavenumber.

When the pTR processor is implemented in a stationary environment a first signal (index m) is sent from the source to the array and then the received pressure field is correlated with a second transmission (index n). The resulting pressure field in the frequency domain is given by

$$\begin{aligned} P_{pc}(R, z_0, z_i, \omega) &= \sum_{i=1}^{I} G_\omega(R, z_0, z_i) G_\omega^*(R, z_0, z_i) \\ &= \frac{1}{\rho^2 8\pi R} \sum_{m=1}^{M} \sum_{n=1}^{M} \frac{Z_m(z_0) Z_n(z_0)}{\sqrt{k_m k_n}} \Psi(m, n) e^{j(k_m R - k_n R)}, \end{aligned} \tag{4.29}$$

where, according to the basic assumptions of aTR [2], the mode orthogonality property can be applied, such that

$$\Psi(m, n) = \sum_{i=1}^{I} Z_m(z_i) Z_n(z_i) \approx \delta_{m,n}. \tag{4.30}$$

Due to (4.30) the two summations in (4.29) can be replaced by a single one, the exponential vanishes, and the pTR pressure field in the frequency domain becomes approximately constant

$$P_{pc}(\cdot) = \frac{1}{\rho^2 8\pi R} \sum_{m=1}^{M} \frac{|Z_m(z_0)|^2}{|k_m|}. \tag{4.31}$$

In the following the problem of performance loss of pTR with variable geometry will be addressed and compensation strategies will be proposed. Since pTR performs the crosscorrelation between the first and a second received signal, it will be considered that the geometric mismatch affects the second received signal (index n) while the compensation strategies will be implemented in the first received signal (index m).

4.3.2 Passive Time Reversal with Source-Array Range Shift

If there is a source-array range shift $\Delta r = r - R$ (where r is the new range) between the first and the second transmissions the resulting pTR pressure field is given by

$$\begin{aligned} P_{pc}(\cdot; \Delta r) &= \sum_{i} G_\omega(R + \Delta r, z_0, z_i) G_\omega^*(R, z_0, z_i) \\ &= \frac{1}{\rho^2 8\pi R} \sum_{m=1}^{M} \frac{|Z_m(z_0)|^2}{|k_m|} e^{j(k_m(R+\Delta r) - k_m R)}, \end{aligned} \tag{4.32}$$

where Δr is small enough in order to be considered negligible in the denominator. The argument of the complex exponential in (4.32) is no longer null and this is responsible for a loss of performance of pTR.

---

[2] *i.e.*, that there is a sufficiently large number of hydrophones, the vertical array is spanning the whole water column and the propagation environment is time-invariant.

Song et al [55] developed a waveguide invariant based method [21] to perform range shift of the aTR focal spot whose application to pTR range shift compensation is straightforward. As originally proposed this method only emphasizes the pressure field intensity, and a different interpretation of the compensation mechanism is given here to account for the phase effect over the frequency domain pressure field, that results in a delay in the time domain. According to [55] the source-array range distortion over the pTR can be compensated by applying a frequency shift $\Delta\omega$ to the first received pressure field (index m) in (4.32), i.e.,

$$G_{\omega+\Delta\omega}(R, z_0, z_i) = \frac{-j}{\rho\sqrt{8\pi R}} e^{-j\frac{\pi}{4}} \sum_{m=1}^{M} \frac{Z_m(z_i)Z_m(z_0)}{\sqrt{k_m}} e^{ik_m(\omega+\Delta\omega)R}, \tag{4.33}$$

where under the adiabatic condition the only quantity that is considered to be frequency dependent is the horizontal wavenumber k_m in the argument of the complex exponential (the frequency shift in the k_m placed in the denominator is negligible). Using (4.33) in (4.32) results in

$$\begin{aligned} P_{pc}(\cdot; \Delta r, \Delta\omega) &= \sum_i G_\omega(R + \Delta r, z_0, z_i) G^*_{\omega+\Delta\omega}(R, z_0, z_i) \\ &= \frac{1}{\rho^2 8\pi R} \sum_{m=1}^{M} \frac{|Z_m(z_0)|^2}{|k_m|} e^{j(k_m(R+\Delta r) - k^\dagger_m R)}, \end{aligned} \tag{4.34}$$

where $k^\dagger_m = k_m(\omega + \Delta\omega)$. Considering the first order Taylor approximation for the frequency shift horizontal wavenumber

$$\begin{aligned} k^\dagger_m &= k_m + \frac{dk_m}{d\omega}\Delta\omega \\ &= k_m + \frac{1}{u_m(\omega)}\Delta\omega, \end{aligned} \tag{4.35}$$

where u_m is the horizontal group velocity. Replacing (4.35) in (4.34) yields

$$P_{pc}(\cdot; \Delta r, \Delta\omega) = \frac{1}{\rho^2 8\pi R} \sum_{m=1}^{M} \frac{|Z_m(z_0)|^2}{|k_m|} e^{jk_m\Delta r} e^{-j\frac{dk_m}{d\omega}\Delta\omega R}. \tag{4.36}$$

The frequency shift $\Delta\omega$ used in [55] to perform a range shift of the aTR focal spot can be adapted here to compensate for the pTR range shift Δr, and is given by

$$\Delta\omega = -\frac{\omega}{R}\Delta r\beta. \tag{4.37}$$

where β is the horizontal waveguide invariant that can be chosen from a set of possible values (4.8) or given by (4.12). In the following the second option will be considered.

As previously mentioned, in [55] only the aTR focal spot intensity was considered, and no attempt was made to understand the range shift influence over the aTR focal spot phase. When applying the same strategy to compensate for pTR range mismatch, namely for underwater communications, the argument of the exponential term in (4.34) should be approximately linear with frequency and range shift (to avoid signal distortion). That is made possible by using (4.11) and (4.37) in the exponential term (4.36)

$$k_m \Delta r + \frac{dk_m}{d\omega} \omega \beta_e \Delta r \approx \omega \rho_{\beta,e} \Delta r, \tag{4.38}$$

where β_e and $\rho_{\beta,e}$ are given by (4.12) and (4.13) respectively. Finally replacing (4.38) in (4.36) results in

$$P_{pc}(\cdot; \Delta r, \Delta\omega) \approx \frac{e^{j\rho_{\beta,e}\omega\Delta r}}{\rho^2 8\pi R} \sum_{m=1}^{M} \frac{|Z_m(z_0)|^2}{|k_m|}. \tag{4.39}$$

When compared with (4.31), it is clear that, except for a harmless linear phase term, the source-array range mismatch has been compensated in (4.39).

4.3.3 Passive Time Reversal with Source Depth Shift

If there is a source depth shift Δz_0 between the first and second transmissions the pTR pressure field becomes

$$\begin{aligned} P_{pc}(.; \Delta z_0) &= \sum_{i}^{I} G_\omega(R, z_0 + \Delta z_0, z_i) G^*_\omega(R, z_0, z_i) \\ &= \frac{1}{8\pi R} \sum_{m=1}^{M} \sum_{n=1}^{M} \frac{Z_m(z_0) Z_n(z_0 + \Delta z_0)}{\rho} \sum_i \frac{Z_n(z_i) Z_m(z_i)}{\rho} \frac{e^{j(k_m R - k_n R)}}{\sqrt{k_m k_n}} \\ &= \frac{1}{\rho 8\pi R} \sum_{m=1}^{M} \left[\frac{Z_m(z_0) Z_m(z_0 + \Delta z_0)}{\rho} \right] \frac{1}{|k_m|}, \end{aligned} \tag{4.40}$$

where the term in $[\cdot]$ is responsible for a loss of performance of pTR.

In a perfect waveguide with no source depth mismatch, $\rho = 1$, and considering the full set of modes,

$$\sum_{m=1}^{M} \frac{Z_m(z_0) Z_m(z)}{\rho} \approx \begin{cases} \frac{D}{2} \frac{M}{2} & \text{if } z = z_0 \\ 0 & \text{if } z \neq z_0 \end{cases}, \tag{4.41}$$

which means that even with a small depth mismatch $\Delta z_0 = z - z_0$ the pTR performance strongly degrades, since (4.41) results in a weighted dirac in depth [3].

Applying to pTR the basic idea of Walker [60] for aTR focal spot depth shift, the term in $[\cdot]$ can be written as

$$\sum_{m=1}^{M} \left[\frac{Z_m(z_0) Z_m(z_0 + \Delta z_0)}{\rho} \right] = \sum_{m=1}^{M} \left[\frac{Z_m(z_0) Z_m(z_0)}{\rho} \left\{ \frac{Z_m(z_0 + \Delta z_0)}{Z_m(z_0)} \right\} \right]. \tag{4.42}$$

This implies that a compensation of the source depth shift can be achieved by applying the inverse of the term in $\{\cdot\}$ to (4.40). The method proposed in [60] requires the explicit computation of $Z_m(z)$ using, e.g., the data-based mode extraction method proposed in

---

[3] it should be mentioned that in a real scenario the weighted dirac is replaced by a pulse with a main lobe, that originates a slower performance degradation with the depth mismatch, when compared with the theoretical case.

[59] that requires the collection of data at several ranges. Although the basic idea is the same, the compensation method presented here does not require the explicit computation of Z_m; instead, by using a frequency shift of the acoustic field, an approximation to the inverse of the term in $\{\cdot\}$ is computed implicitly.

It was found that in a perfect waveguide the source depth mismatch compensation can be partially achieved multiplying by $\cos(\gamma_m \Delta z_0)$ the left term of (4.42) [4], that is

$$\sum_{m=1}^{M} Z_m(z_0) Z_m(z_0 + \Delta z_0) \cos(\gamma_m \Delta z_0). \tag{4.43}$$

For the perfect waveguide mode shape (4.43) can be rewritten as

$$\frac{D}{2} \sum_{m=1}^{M} \sin(\gamma_m z_0) \sin(\gamma_m z_0 + \gamma_m \Delta z_0) \cos(\gamma_m \Delta z_0), \tag{4.44}$$

that, by trivial trigonometric manipulation, becomes

$$\frac{D}{2} \sum_{m=1}^{M} \frac{1}{4} \left[1 + \cos(2\gamma_m \Delta z_0) - \cos(2\gamma_m z_0) - \cos(2\gamma_m z_0 + 2\gamma_m \Delta z_0)\right]. \tag{4.45}$$

The sum of oscillating terms in (4.45) is approximately zero except for $\Delta z_0 = 0$ due to $\cos(2\gamma_m \Delta z_0)$, and the term 1 is responsible for the compensation. It results that

$$\sum_{m=1}^{M} Z_m(z_0) Z_m(z_0 + \Delta z_0) \cos(\gamma_m \Delta z_0) \approx \begin{cases} \frac{D}{2}\frac{M}{2} & \text{if } \Delta z_0 = 0 \\ \frac{D}{2}\frac{M}{4} & \text{if } \Delta z_0 \neq 0 \end{cases}. \tag{4.46}$$

Comparing (4.41) and (4.46) it is clear that under depth mismatch the compensation can restore half the magnitude of (4.41). Similarly $\exp(j\gamma_m \Delta z_0)$ (the negative exponential is also a viable choice) can be used for compensation instead of $\cos(\gamma_m \Delta z_0)$, in which case one must consider an additional imaginary component that will be responsible for the presence of a linear phase[5] with Δz_0

$$\sum_{m=1}^{M} Z_m(z_0) Z_m(z_0 + \Delta z_0) e^{j\gamma_m \Delta z_0} \approx \sum_{m=1}^{M} Z_m(z_0) Z_m(z_0) \frac{V(\Delta z_0)}{2}, \tag{4.47}$$

where $|V(\Delta z_0)| \approx 2$ for $\Delta z_0 = 0$ and $|V(\Delta z_0)| \approx 1$ for $\Delta z_0 \neq 0$.

In [34] it is considered that for aTR (4.41) can be applied approximately by assuming that the k_m's are nearly constant over the interval of the contributing modes and can be replaced by their mean $\overline{|k_m|}$. Here, in a similar manner (4.47) is used for the compensated pTR and results in the source depth shift compensated pTR pressure field given by

$$P_{pc}^{comp}(\cdot; \Delta z_0) \approx \frac{1}{\rho^2 8\pi R} \sum_{m=1}^{M} \frac{|Z_m(z_0)|^2}{\overline{|k_m|}} \frac{V(\Delta z_0)}{2}. \tag{4.48}$$

---

[4] the choice of $\cos(\gamma_m \Delta z_0)$ was made in aTR context and further adapted to pTR by considering an analogy with the demodulation of a single-side-band modulation using a double-side-band demodulator.

[5] in a real scenario due to the previously mentioned replacement of the weighted dirac in (4.41) by a pulse with a main lobe, it results that the linear phase with Δz_0 becomes a dual-slope linear phase (one inside the lobe and the other outside), that can be observed in Figure 4.4 for simulated data.

As previously, a frequency shift is used to implicitly perform the compensation based on the product by $\exp(j\gamma_m \Delta z_0)$. Considering the approximation to the vertical wavenumber using the horizontal group slowness (4.22), in a similar manner to the compensation of the source-array range mismatch (4.38) one can write

$$\gamma_m \Delta z_0 \approx -\frac{dk_m}{d\omega}\omega\zeta_0 \Delta z_0 + \rho_{\zeta,0}\omega\Delta z_0, \tag{4.49}$$

where ζ_0 is given by (4.23) and $\rho_{\zeta,0}$ is given by (4.24). Taking

$$\Delta\omega = \frac{\omega}{R}\Delta z_0 \zeta_0, \tag{4.50}$$

in the first-order Taylor expansion (4.35), results in the compensated field

$$\begin{aligned} P_{pc}(\cdot; \Delta z_0, \Delta\omega) &= \sum_i G_\omega(R, z_0 + \Delta z_0, z_i) G^*_{\omega+\Delta\omega}(R, z_0, z_i) \\ &= \frac{1}{\rho^2 8\pi R} \sum_{m=1}^{M} \frac{Z_m(z_0 + \Delta z_0) Z_m(z_0)}{|k_m|} e^{-j\frac{dk_m}{d\omega}\Delta\omega R} \\ &\approx \frac{V(\Delta z_0)}{2} \frac{e^{-j\rho_{\zeta,0}\omega\Delta z_0}}{\rho^2 8\pi R} \sum_{m=1}^{M} \frac{|Z_m(z_0)|^2}{|k_m|}. \end{aligned} \tag{4.51}$$

When compared with (4.31) it is clear that, at the cost of an attenuation and a harmless linear phase term the source depth mismatch pTR acoustic field becomes partially compensated.

4.3.4 Passive Time Reversal with Array Depth Shift

If there is an array depth shift Δz_i between the first and the second transmissions the mismatched pTR pressure field becomes

$$\begin{aligned} P_{pc}(.; \Delta z_i) &= \sum_i^I G_\omega(R, z_0, z_i + \Delta z_i) G^*_\omega(R, z_0, z_i) \\ &= \frac{1}{\rho^2 8\pi R} \sum_{m=1}^{M} \sum_{n=1}^{M} \frac{Z_m(z_0) Z_n(z_0)}{\sqrt{k_m k_n}} \sum_i Z_n(z_i + \Delta z_i) Z_m(z_i) e^{j(k_m R - k_n R)} \\ &= \frac{1}{\rho^2 8\pi R} \sum_{m=1}^{M} \sum_{n=1}^{M} \frac{Z_m(z_0) Z_n(z_0)}{\sqrt{k_m k_n}} \Psi(m, n, \Delta z_i) e^{j(k_m R - k_n R)}. \end{aligned} \tag{4.52}$$

Unlike $\Psi(m, n)$ in (4.29) and (4.30) in (4.52) $\Psi(m, n, \Delta z_i)$, is no longer an impulse and the two summations $\sum_{m=1}^{M}\sum_{n=1}^{M}(.)$ cannot be replaced by a single one. Instead they must be replaced by $\sum_{m=n}^{M}(.) + \sum_{m\neq n}^{M}(.)$, where the cross terms will be responsible for a loss of performance of the pTR processor.

Appendix B.2 studies the effect of the array depth mismatch over the mode orthogonality property, and proposes a compensation strategy that partially recovers it in the presence of array depth mismatch. It results that partial compensation can be achieved using (B22) in (4.52)

$$
\begin{aligned}
P_{pc}^{comp}(.;\Delta z_i) &\approx \frac{1}{\rho^2 8\pi R}\sum_{m=1}^{M}\sum_{n=1}^{M}\frac{Z_m(z_0)Z_n(z_0)}{\sqrt{k_m k_n}}\Psi(m,n,\Delta z_i)e^{j\gamma_m\Delta z_i}e^{j(k_m R-k_n R)} \\
&\approx \frac{1}{\rho^2 8\pi R}\sum_{m=1}^{M}\sum_{n=1}^{M}\frac{Z_m(z_0)Z_n(z_0)}{\sqrt{k_m k_n}}\Psi(m,n)\frac{W(m,\Delta z_i)}{2}e^{j(k_m R-k_n R)} \qquad (4.53)
\end{aligned}
$$

In (4.53) the summation $\sum_{m=1}^{M}\sum_{n=1}^{M}(.)$ can be replaced by $\sum_{m=n}^{M}[W(m,\Delta z_i),(.)]$, and the resulting pTR pressure field will be given by

$$
P_{pc}^{comp}(.;\Delta z_i) \approx \frac{1}{\rho^2 8\pi R}\sum_{m=1}^{M}\frac{|Z_m(z_0)|^2}{|k_m|}\frac{W(m,\Delta z_i)}{2}. \qquad (4.54)
$$

As in (4.48) a frequency shift implicitly introduces the required factor $\exp(j\gamma_m\Delta z_i)$ (note that $\exp(-j\gamma_m\Delta z_i)$ is also a viable choice since in appendix B.2 the compensation is originally attained by $\cos(\gamma_m\Delta z_i)$). Considering the approximation to the vertical wavenumber using the horizontal group slowness (4.22), one can write, similarly to (4.49),

$$
\gamma_m\Delta z_0 \approx -\frac{dk_m}{d\omega}\omega\zeta_i\Delta z_i + \rho_{\zeta,i}\omega\Delta z_i, \qquad (4.55)
$$

where ζ_i is given by (4.23) and $\rho_{\zeta,i}$ is given by (4.24). Considering the first order Taylor expansion (4.35) and

$$
\Delta\omega = \frac{\omega}{R}\Delta z_i\zeta_i, \qquad (4.56)
$$

yields the compensated field

$$
\begin{aligned}
P_{pc}(\cdot;\Delta z_i,\Delta\omega) &= \sum_i G_\omega(R,z_0,z_i+\Delta z_i)G^*_{\omega+\Delta\omega}(R,z_0,z_i) \\
&= \frac{1}{\rho^2 8\pi R}\sum_{m=1}^{M}\frac{|Z_m(z_0)|^2}{|k_m|}\Psi(m,n,\Delta z_i)e^{-j\frac{dk_m}{d\omega}\Delta\omega R} \\
&\approx \frac{e^{-j\rho_{\zeta,i}\omega\Delta z_i}}{\rho^2 8\pi R}\sum_{m=1}^{M}\frac{|Z_m(z_0)|^2}{|k_m|}\frac{W(m,\Delta z_i)}{2}, \qquad (4.57)
\end{aligned}
$$

that resembles (4.51), and similar comments apply.

4.4 Simulations with a perfect waveguide

In order to illustrate the behavior of the geometric mismatch frequency shift compensation mechanism, simulations were conducted for a perfect waveguide with $D = 100$m water column depth, $c = 1500$m/s, frequency $f = 1$kHz, nominal source-array range $R = 1$km, nominal source depth $z_0 = 50$m and a vertical line array of 81 hydrophones, 1m spaced, centered in the water column.

Results for the source-array range mismatch compensation given by the pTR acoustic field $P_{PC}(\cdot;\Delta r,\Delta\omega)$ of (4.34), source depth mismatch compensation given by $P_{PC}(\cdot;\Delta z_0,\Delta\omega)$

of (4.51), and array depth mismatch compensation given by $P_{PC}(\cdot; \Delta z_i, \Delta\omega)$ of (4.57), are shown in Figures 4.3, 4.4 and 4.5, respectively. The blue dashed line shows the behavior of pTR under the geometric mismatch $\Delta \equiv (\Delta r, \Delta z_0, \Delta z_i)$ with no compensation, $\Delta\omega = 0$ where $\Delta\omega = 2\pi\Delta f$. The continuous line shows the maxima of the surface $|P_{PC}(\cdot; \Delta, \Delta\omega)|$ in (a) and the respective phase in (b). The red dot-dashed line represents the pTR acoustic field with the proposed compensation mechanism given by (4.37), (4.50) and (4.56) for source-array range, source depth and array depth mismatches, respectively. In all three cases the waveguide invariants β_e, $\zeta_{e,0}$, $\zeta_{e,i}$, $\rho_{\beta,e}$, $\rho_{\zeta,e,0}$ and $\rho_{\zeta,e,i}$ were computed for an effective number of modes $M_e = M/2$.

Figure 4.3(a) shows the pTR acoustic field magnitude $|P_{PC}(\cdot; \Delta r, \Delta\omega)|$ of (4.34) where it is clear that the compensation $\Delta\omega$ behaves linearly with the mismatch Δr with an invariant $\beta_e \approx 0.88$ given by (4.12). For each Δr the frequency shift for which the maximum magnitude is attained almost equals (4.37), and provides a strong gain when compared with the no compensation case given by the dashed line. Figure 4.3(b) shows the unwrapped phase of (4.36) for the three cases described before. Except for the max(P_{PC}) case the others exhibit a linear trend with Δr that, for the proposed frequency shift compensation mechanism, is controlled by $\rho_{\beta,e}$ given by (4.13).

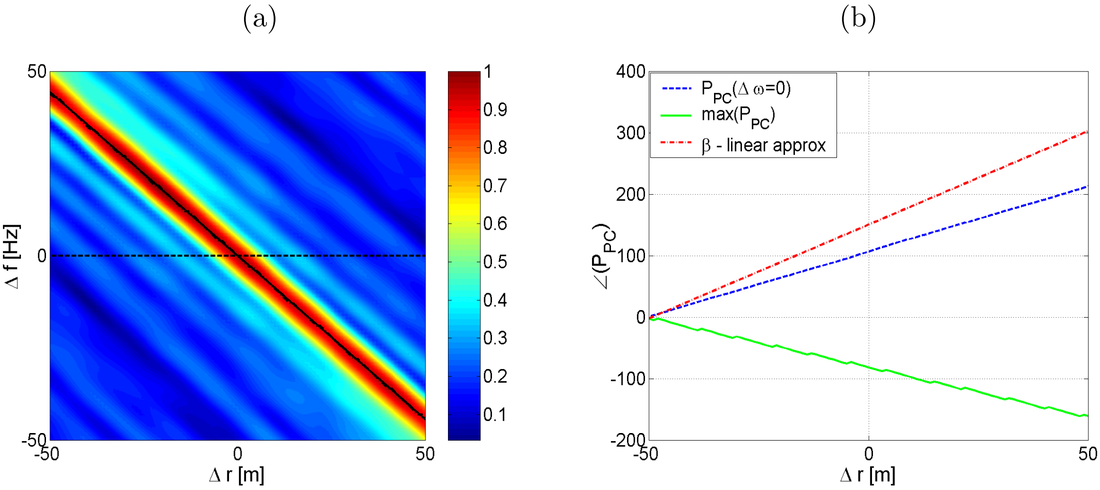

Figure 4.3: Frequency shift source-array range mismatch compensation given by the pTR acoustic field $P_{PC}(\cdot; \Delta r, \Delta\omega)$ of (4.34); (a) normalized magnitude, (b) unwrapped phase.

Figure 4.4(a) shows the magnitude of (4.51) where an almost symmetric behavior with Δf is observed since the compensation can be done either with $\exp(j\gamma_m\Delta z_0)$ or $\exp(-j\gamma_m\Delta z_0)$ (recall that compensation is originally attained using $\cos(\gamma_m\Delta z_0)$ and that the positive and the negative exponentials are both easy to implement alternative choices). This near symmetry causes the maximum to toggle between positive and negative values of the frequency shift. Considering only one side of the symmetry it can be observed that the compensation $\Delta\omega$ behaves almost linearly with the mismatch Δz_0 with a invariant $\zeta_{e,0} \approx 3.14$ given by (4.23) (such linearity becomes a weaker approximation for high frequencies and high source depth mismatches). Figure 4.4(a) shows that the frequency shift compensation maximum ($\max(P_{PC})$) attain a stronger magnitude than the non-compensated case ($P_{PC}(\Delta\omega = 0)$) when the main lobe, which can be seen in the center of the figure, reaches one half of the maximum value given for $\Delta z_0 = 0$ as predicted by (4.46).

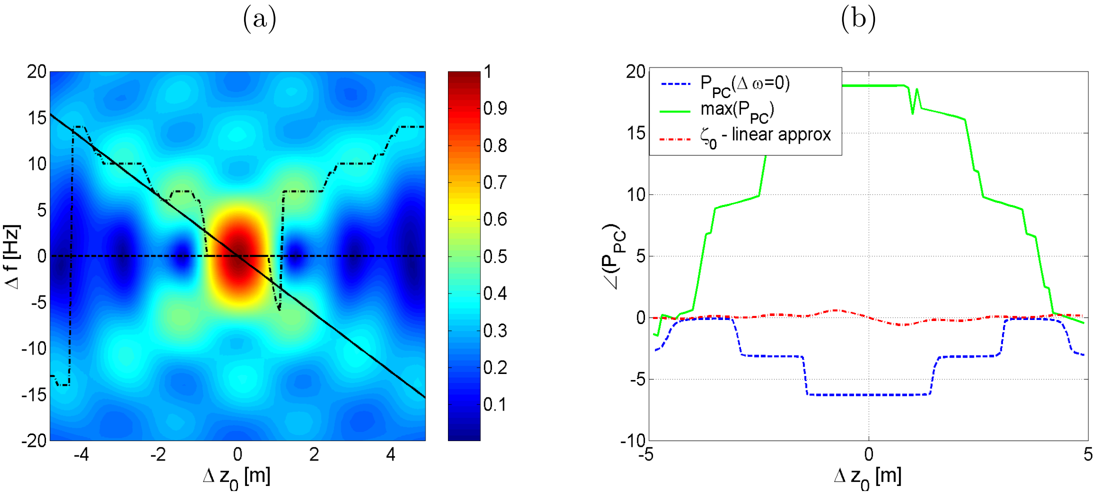

Figure 4.4: Frequency shift source depth mismatch compensation given by the pTR acoustic field $P_{PC}(\cdot; \Delta z_0, \Delta\omega)$ of (4.51); (a) normalized magnitude, (b) unwrapped phase.

Figure 4.4(b) shows the phase of (4.51) for the three cases described above. An almost linear trend with Δz_0 is observed only for the proposed compensation mechanism (dot-dashed line) that is controlled by $\rho_{\zeta,e}$ and the phase of $V(\Delta z_0)$ as given by (4.51) (in fact a detailed observation shows a tenuous two slope linear phase with one slope inside the $|P_{PC}(\cdot; \Delta z_0, \Delta\omega)|$ main lobe and a different one outside).

Figure 4.5 shows the simulation behavior of the array depth mismatch frequency shift compensation mechanism for a perfect waveguide similar to the one used for Figures 4.3 and 4.4. The behavior is quite similar to the one observed for the source depth mismatch compensation case and similar comments apply, with the main difference being that now $W(m, \Delta z_i)$ plays the role of $V(\Delta z_0)$. Note that the invariant $\zeta_{e,i} = \zeta_{e,0} \approx 3.14$ are both given by (4.23) and are equal due to the fact that the Sound Speed Profile (SSP) is constant over the water column, which makes the vertical wavenumber γ_m depth independent. Additional comments when in the presence of a depth dependent SSP will be given in Sections 4.5 and 4.6.

4.5 Extension of geometric compensation mechanisms to realistic waveguides

The intrinsic behavior of the geometric mismatch compensation mechanism in a perfect waveguide can be further extended to more realistic waveguides by considering the Pekeris waveguide and the WKB approximation. In a Pekeris waveguide the high order modes become leaky due to the presence of the half space and at sufficiently larger range they have

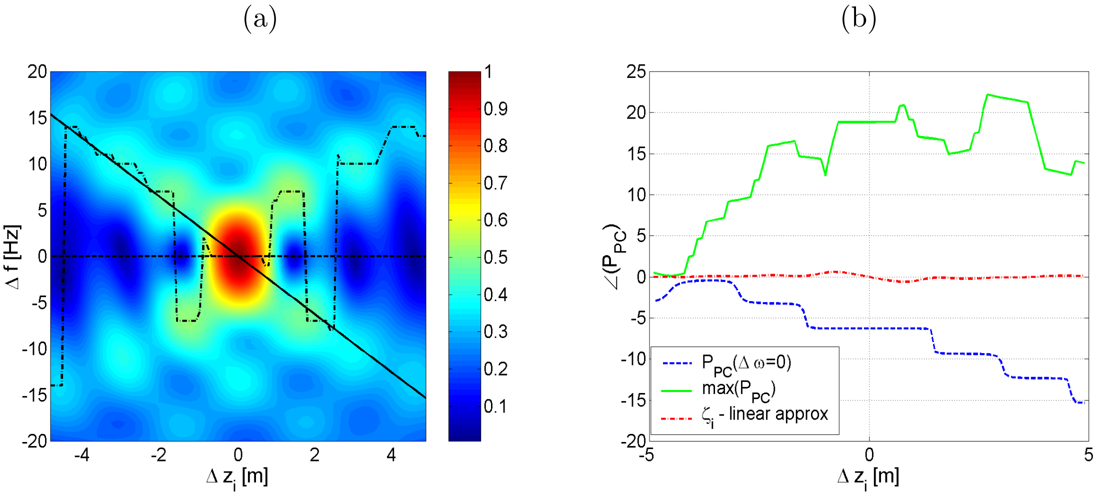

Figure 4.5: Frequency shift array depth mismatch compensation given by the pTR acoustic field $P_{PC}(\cdot;\Delta z_i,\Delta\omega)$ of (4.57); (a) normalized magnitude, (b) unwrapped phase.

no contribution to the received acoustic field [27]. That means that in a real waveguide the mode limitation required to improve the k'_m to k_m approximation (4.11) and γ'_m to γ_m approximation (4.22) is performed up to a certain point by the waveguide itself.

Although the WKB approximation is usually applied in deep water, some insight into the behavior of the modes in a waveguide with a depth-dependent SSP can be obtained. In [5] it is shown that under the WKB approximation the group slowness is given by

$$\frac{dk_m}{d\omega} = \frac{\omega}{k_m}\frac{\int \frac{1}{\rho(z)c^2(z)} Z_m^2(z)dz}{\int \frac{1}{\rho(z)} Z_m^2(z)dz} \tag{4.58}$$

where $\rho(z)$ and $c(z)$ are the depth-dependent water density and SSP, respectively, and the ratio of integrals in the right hand side is a constant. Using the WKB horizontal group slowness (4.58) instead of the perfect waveguide horizontal group slowness (4.5) the approximations (4.11) and (4.22) are still valid. Heuristically, this suggests that the genesis of the range shift compensation mechanism under the WKB approximation with a depth-dependent SSP remains unchanged.

Regarding the use of $\exp(\pm j\gamma_m\Delta z)$ to compensate for the source depth shift and array depth shift, the following should be considered. The WKB approximation reveals that in the presence of a ducted SSP [58, 5] the mode shape is no longer ruled by a constant vertical wavenumber, γ_m, but by a depth-dependent $\gamma_m(z)$. Under the WKB approximation the mode shape between the points where it vanishes, that is, between the ray turning points in the ray mode analogy, is given by

$$Z_m(z) = A_m(z)\sin\Upsilon_m(z), \tag{4.59}$$

where $A_m(z)$ is a slowly-varying amplitude

$$A_m(z) = \gamma_m^{-1/2}(z) = \left[\frac{\omega^2}{c^2(z)} - k_m^2\right]^{-1/4}, \tag{4.60}$$

the WKB phase is

$$\Upsilon_m(z) = \Upsilon_a + \int_a^z \gamma_m(z')dz', \tag{4.61}$$

where a is the upper mode vanishing depth (or the equivalent ray turning depth) and the depth dependent vertical wavenumber is

$$\gamma_m^2(z) = \frac{\omega^2}{c^2(z)} - k_m^2, \tag{4.62}$$

where k_m is the depth-independent horizontal wavenumber. In presence of a depth shift Δz one can compute the new vertical wavenumber $\gamma_m(z+\Delta z)$ using the nominal $\gamma_m(z)$ and the sound speed at z and $z+\Delta z$

$$\gamma_m^2(z+\Delta z) = \frac{\omega^2}{c^2(z)}\sigma_c(z,\Delta z) + \gamma_m^2(z), \tag{4.63}$$

where

$$\sigma_c(z,\Delta z) = \frac{c^2(z) - c^2(z+\Delta z)}{c^2(z+\Delta z)}. \tag{4.64}$$

Replacing (4.62) in (4.63) results in

$$\gamma_m^2(z+\Delta z) = \frac{\omega^2}{c^2(z)}(\sigma_c(z,\Delta z)+1) - k_m^2, \tag{4.65}$$

where $\sigma_c(z,\Delta z) \approx 0$ and $\gamma_m^2(z+\Delta z) \approx \gamma_m^2(z)$ if the sound speed varies slowly with depth. In the presence of a depth shift Δz the WKB phase (4.61) becomes

$$\Upsilon_m(z+\Delta z) = \Upsilon_a + \int_a^z \gamma_m(z')dz' + \int_z^{z+\Delta z} \gamma_m(z')dz', \tag{4.66}$$

and, since $\sigma_c(z,\Delta z)+1 \approx 1$ for a slowly-varying SSP , with small Δz, the third term of (4.66) becomes

$$\int_z^{z+\Delta z} \gamma_m(z')dz' \approx \gamma_m(z)\Delta z, \tag{4.67}$$

and the mode shape $Z_m(z)$ becomes

$$Z_m(z+\Delta z) \approx A_m(z)\sin\left[\Upsilon_m(z) + \gamma_m(z)\Delta z\right]. \tag{4.68}$$

Note the similarity to the mode shape in a perfect waveguide, given by $Z_m(z+\Delta z) = \sin(\gamma_m z + \gamma_m \Delta z)$.

Considering now that a real waveguide is a Pekeris waveguide with a WKB approximation such that the mode shape in the water column is given by the WKB approximation, but near the boundaries the mode vanishing locations (ray turning points) are given by the boundaries of the waveguide as in the Pekeris waveguide, the $\Psi(m,n,\Delta z_i)$ function of (B11) becomes

$$\Psi(m,n,\Delta z_i) = \Xi \int_0^D \sin[\Upsilon_m(z) + \gamma_m(z)\Delta z_i)]\sin(\Upsilon_n(z))dz, \tag{4.69}$$

where the assumed constant Ξ is a function of water depth D and $A_m(z)$ of (4.60). The latter is a slowly-varying function of z and assumed constant within the water column.

Comparing (B11) for the perfect waveguide with (4.69) for the more realistic case based on the Pekeris waveguide with the WKB approximation, one can see that the distortion is similar, the main difference being that for (4.69) the vertical wavenumber is depth dependent. Such dependence suggests that a short array placed in the middle of the water column must be used in order to consider $\gamma_m(z) \approx \overline{\gamma_m(z)}$, or that for large vertical arrays the compensation should be applied in small array sections.

4.6 Geometric mismatch compensation with experimental data

The experimental data were collected during the MREA'04 sea trial that took place off the town of Setúbal, approximately 50km from Lisbon (Portugal) in April 2004. The acoustic source was suspended from the NRV Alliance at a nominal depth of 70m, the receiving VLA was surface-suspended from the free-drifting Acoustic Oceanographic Buoy (AOB) [30] and comprised two sections. The upper section with two hydrophones at nominal depths of 10 and 15m and the lower section with six hydrophones at nominal depths of 55, 60, 65, 70, 75 and 80m (in the following only the lower section will be used). The pTR experiment data processed in this section were acquired at a close range between 0.6 and 0.8km to the south of the acoustic source in a constant up slope region with a water column depth varying between 90 and 110m, at an almost constant source-array relative speed of about 0.6m/s. The environment was characterized by a thermocline of approximately 20m over a downward refracting SSP over a 1.5m silt bottom and a gravel sub-bottom. The surface-suspended AOB was affected by a wave height of approximately 0.63m with frequency between 0.43 and 0.4Hz, as measured with a costal monitoring buoy placed in the area of the experiment. The source depth was measured at a sampling rate of 1 second with 10cm resolution and oscillates between 71.64 and 72.24m. The power spectral density of the source depth data reveals the presence of one main component at 0.1Hz.

The transmission set processed here corresponds to modulated data at a carrier frequency of 3.6kHz, using a 400 baud symbol rate with 2-PSK constellation and fourth-root raised cosine signaling pulses with 100% roll-off, such that the signal bandwidth is 800Hz. Each individual transmission comprises a single PAM signaling pulse acting as a channel probe with symmetric guard intervals and a total duration of 1s, followed by a 20s data packet. The source transmits four packets with a total duration of 84s.

Before any geometric mismatch compensation the data were synchronized, Doppler compensated and channel identification was performed independently for each hydrophone using the exponentially-windowed RLS algorithm (see [19] and [20] for details). Each data packet provides a set of 400 IR estimates at intervals of 0.05s, where the first 9 estimates were rejected. The proposed pTR geometric mismatch compensation is then applied to

78.2s of data (collected during 83s) that corresponds to 1564 IR estimates with the IR estimate number 782 being used as the nominal IR. This results in a setup where the source-array range mismatch $\Delta r = r - R$ starts at negative values and then gradually increases up to the 1564 IR estimate.

Figure 4.6 shows the arriving pattern of the lower sections of the array for the middle IR estimate where four relevant paths are clearly identified.

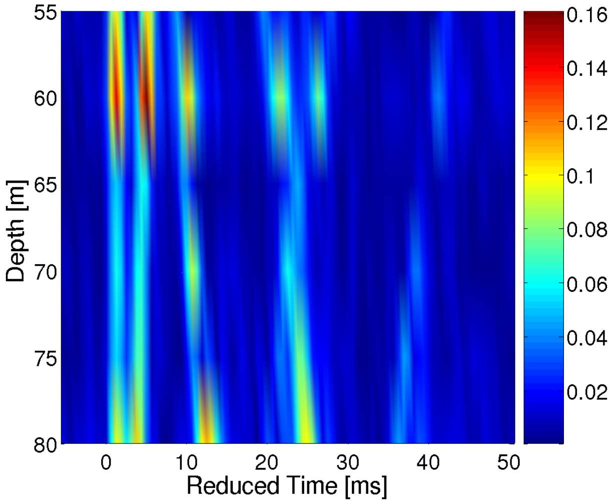

Figure 4.6: Arrival pattern of the non mismatch IR estimate.

Applying the proposed frequency shift geometric mismatch compensation strategy to the pTR operator, with only the first two paths of Figure 4.6, the surface of Figure 4.7 is obtained. Since the range mismatch changes from negative to positive values, crossing zero at about $40s$ (that corresponds to the nominal IR), it is expected that the frequency shift which compensates for the range mismatch varies from positive to negative values as in Figure 4.3(a) for the simulation in a perfect waveguide. This is confirmed in Figure 4.7 that shows a patch of pTR maxima ranging from a frequency shift mean value of about -90 up to 90Hz. The dashed line represents the expected frequency shift obtained with (4.37) by considering the range shift obtained from the NRV Alliance and AOB real-time GPS data, the data carrier frequency ($f_c = 3.6$kHz) and a horizontal waveguide invariant $\beta = 0.81$. The β value was computed from an approximation for constant slope range-dependent environments with constant sound speed derived by D'Spain [9]. In such conditions the invariant β depends of the water column depths at the source and receiver location and varies slowly with the source-receiver range. Originally, β was proposed to be the ratio between the source and the array position water-column depths, $\beta \approx D(S)/D(VLA)$. When applied in the present context (with the compensation mechanism applied in the reversed field) it should be considered that pTR implements a synthetic aTR with a virtual transmitting/receiving array at the VLA location and a virtual receiver at the source location. It results that the β invariant as a function of range is approximately given by

$$\beta \approx \frac{D(VLA)}{D(S)}. \tag{4.70}$$

Although the dashed line is just an approximation, Figure 4.7 confirms that (4.37) produces a good fit to the actual path of maximum magnitude (solid line). This similarity suggests that the frequency shift compensation is dominated by the range mismatch.

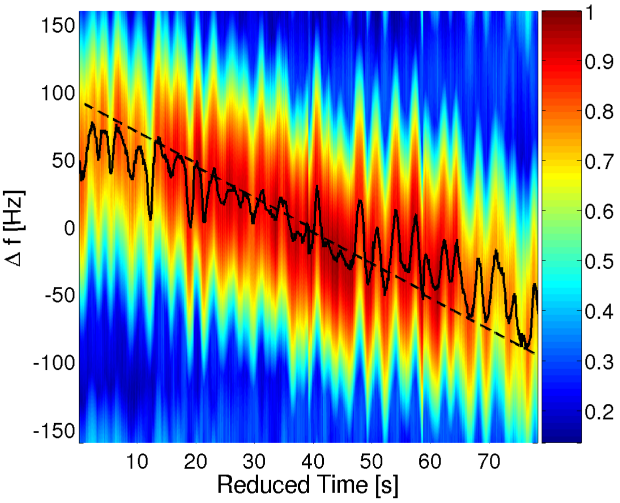

Figure 4.7: The surface represents the normalized magnitude of $P_{pc}(\cdot;\Delta,\Delta\omega)$, when the nominal IR is at $t = 40$s and considering the IRs limited to two arriving paths. The solid line traces the maxima of the surface over time. The dashed line represents the expected behavior if there is only range mismatch.

Figure 4.8 shows the power spectral density of the slice of $P_{pc}(\cdot;\Delta,\Delta\omega)$ along the maximum line of Figure 4.7, where three main components are identifiable at approximately 0.21, 0.3 and 0.4Hz (the first maximum at 0.012Hz is due to the 83s data packet length). Superimposed on the $P_{pc}(\cdot;\Delta,\Delta\omega)$ along the maximum line power spectrum, with '*', one can see the power spectrum of the source depth time series during the same data packet. Both curves display a similar behavior, despite a displacement in frequency. This fact, together with the array depth oscillation induced by the 0.4Hz surface waves allow us to speculate that the swing of the $P_{pc}(\cdot;\Delta,\Delta\omega)$ along the maximum line curve in Figure 4.7 is due to source and array depth oscillations. Nevertheless, no definitive conclusions can be attained since no accurate *in situ* source and array depth measurements with fast enough sampling rate are available.

It is interesting to observe that the symmetric ducts of the source and array depth compensations in the ideal waveguide of Figures 4.4(a) and 4.5(a) vanish in Figure 4.7. That is due to the presence of a depth-dependent SSP that causes the vertical wavenumber $\gamma_m(z)$ to become depth dependent as well.

Figure 4.9 is similar to Figure 4.7, but was computed with the first three paths of Figure 4.6. The main difference between these two figures is the appearance of two more P_{PC} maximum patches almost parallel to the original one. Those patches do not have

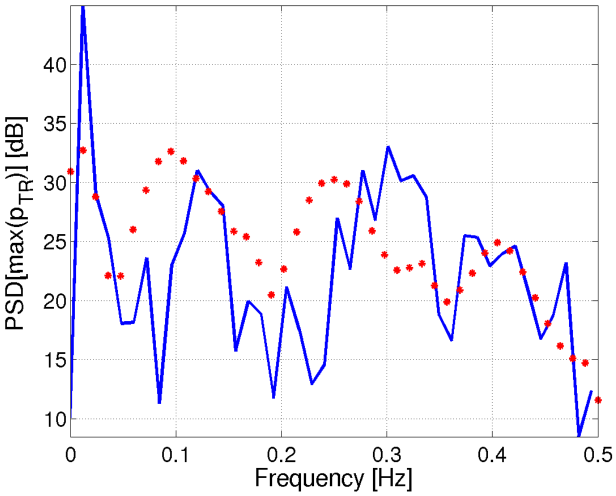

Figure 4.8: Power spectrum of the slice of P_{pc} along the maximum line of Figure 4.7 (solid line), and power spectrum of the source depth time series ('*').

the same nature as the symmetric patches of the source and array depth compensations in an ideal waveguide (see Figures 4.4 and 4.5). They originate from aliasing due to poor spatial sampling of the high-order modes in the 5m spaced hydrophone array.

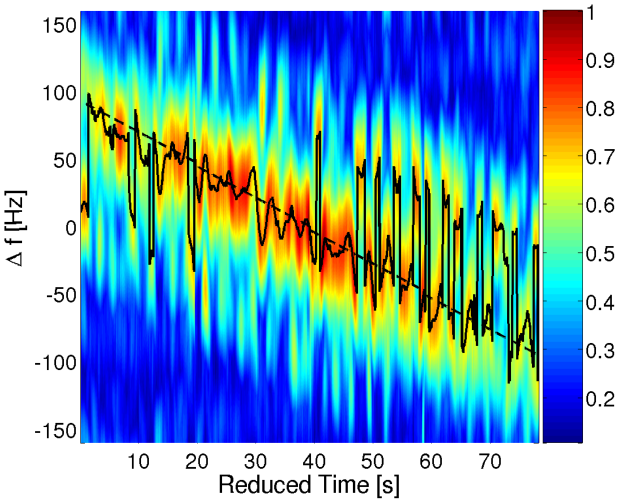

Figure 4.9: The same as Figure 4.7 considering the IRs limited to three arriving paths.

4.7 Conclusions and future work

An analytical model based waveguide invariant approach has been developed for pTR geometric mismatch compensation in shallow water. It was found that the horizontal waveguide invariant β can be used to approximate the horizontal wavenumber using the group slowness, and that the waveguide invariant ζ can be used to approximate the vertical wavenumber. By analogy with the invariance of β in the frequency/range plane, ζ would be invariant in the frequency/depth plane. After theoretically establishing the effect of geometric mismatch over the pTR operation for a perfect waveguide, it was found that an appropriate frequency shift calculated using the invariants can then be used for compensation during the pTR operation. The compensation method was extended heuristically to realistic waveguides and its usefulness was shown with real data.

In the present paper the invariance of ζ in the frequency/depth plane was not completely demonstrated, mainly due to the absence of appropriate real data. Future experiments should be designed in order to overcome this problem, by providing sufficiently high sample rate measurements of the source and array depths.

The proposed compensation method is potentially useful, e.g., in underwater communication systems based on pTR, where the presence of uncompensated geometric mismatch between the probe-signal and actual data transmissions degrades the performance. In fact, an underwater communication system, based on the developed geometric mismatch compensation, is proposed in [47]. It results in a environmental equalizer that uses a relatively small number of coefficients to deconvolve the cannel multipath, unlike most current equalizers.

Acknowledgments

This work was supported by Fundação para a Ciência e a Tecnologia under programs POCI, POCTI and POSI. The authors would like to thank the NATO Undersea Research Centre for the organization of MREA'04 sea trial, NRV Alliance master and personnel and the scientist in charge Emanuel F. Coelho, and to Orlando C. Rodrigez for the useful conversations about the waveguide invariants.

Chapter 5

Environmental equalizer for underwater communications

Abstract: This paper presents an environmental-based equalization algorithm for underwater communications. This algorithm is based on the passive time-reversal (pTR) and waveguide invariant properties of ocean channels. Passive time-reversal allows for the implementation of a simple communications system, but it loses performance in the presence of geometric mismatch between the probe-signal and the actual data symbols transmission. The waveguide invariant properties state that geometric mismatches, both in depth and range, can be partially compensated by applying an appropriate frequency shift in the passive time-reversal operator. Results with binary PSK data at a carrier frequency of 3.6 kHz, collected during the MREA'04 sea trial, show that the Mean Square Error (MSE) between the transmitted and the received data symbols remains stable at least to a range mismatch of about 37.5 m in the presence of source depth and an array depth oscillations of approximately 0.7 m. In such conditions, when comparing the proposed pTR equalizer with plain pTR, an overall gain of approximately 4.11 dB in output MSE is achieved.

5.1 Introduction

In recent years Time Reversal (TR) has received particular attention from the scientific community. After practical demonstration of its spatial-temporal focusing capabilities in the ocean [34] several applications of active TR (aTR), from tomography to communications, were suggested [34, 26]. Passive TR uses a receive-only array, and a probe-signal is transmitted ahead of the data for channel Impulse Response (IR) estimation. The IR estimate is then used as a synthetic channel for temporal focusing of the data signal, which is equivalent to the deconvolution of the multipath generated by the real channel.

When applied to underwater coherent communications the achieved TR focus is not perfect due to errors on the IR estimate and the time variability of the channel, resulting in uncompensated intersymbol interference (ISI) [45]. That problem is even more relevant in communications with a moving source and/or receiver. In that case it is intuitive that a rapid degradation of passive TR temporal focusing will occur due to the increasing mismatch between the assumed and actual channels. In order to guarantee longer stability of the focal spot, three solutions are usually proposed: one is to transmit probe-signals more frequently; another is to use an adaptive algorithm to track the IR from the initial probe signal IR estimation; and finally a third alternative is to use a low-complexity equalizer with only one coefficient per channel. A performance comparison between those adaptive pTR variants is presented in [20]. The major inconvenient of the first method is that frequent transmission of probe-signals reduces the overall transmission rate. In the second the channel estimates are represented by a large number of coefficients that have to be adapted. The third case seems to be the best compromise between complexity and efficiency. In this paper a different approach is proposed by considering that the environment mismatch between the probe-signal and data transmission is mainly due to the geometric properties (source-array range, source depth and array depth), and that the knowledge of such mismatch can be used to compensate for the overall pTR IR mismatch between the probe-signal and actual data transmissions.

A physics-based algorithm for pTR equalization based on the waveguide invariant properties of the shallow water channel is proposed. The waveguide invariant property β [6, 21] has been applied to change the aTR range focus in [55], and to interpret a model for performance prediction of a time-reversal communication system [42]. In [48] the waveguide invariant ζ in conjunction with β, allows for the compensation of pTR geometric mismatch. Through those waveguide invariants, changes on geometric features of the acoustic channel, such as source-receiver range, source depth and array depth, can be compensated by a frequency shift in the estimated IRs during probe-signal transmission. The resulting Frequency Shift pTR (FSpTR) equalizer will increase the pTR output power, resulting in lower MSE. A physics-based equalizer for underwater communications that is able to detect the transmitted data sequence and to simultaneously estimate the source-array range, source depth and array depth is thus obtained.

The reliability of the physics-based waveguide invariant pTR equalizer is demonstrated using experimental data obtained during the MREA'04 sea trial, where binary PSK signals at a data rate of 400 bits per second were transmitted with a carrier frequency of 3.6 kHz. Results obtained with FSpTR, after Doppler compensation of the received signals, show a long-term compensation of channel mismatch, with the MSE remaining stable up to a source-array range mismatch of about 37.5 m in the presence of source depth variations between 71.6 m and 72.3 m and array depth oscillations of approximately 0.63 m. In such conditions, when comparing FSpTR with plain pTR, an overall gain of approximately 4.11 dB in output MSE is achieved.

The paper is organized as follows: Section 5.2 recalls the use of pTR in underwater communications; in Section 5.3 the pTR geometric mismatch compensation using frequency shifts is presented; Section 5.4 develops the FSpTR equalizer, which is applied to real data in section 5.5; Section 5.6 summarizes the main results, draws some conclusions, and suggests future research.

5.2 Passive Time Reversal applied to communications

The basic setup for applying pTR to communications consists in a point source that sends information to a Vertical Line Array (VLA). The procedure starts by sending a short probe-signal, waiting for the channel to clear of multipath arrivals, and then sending the data stream. Considering the noiseless case, the received probe and the data are processed in a TR fashion and it results that the pTR output, in its baseband version [49], is given by

$$y(t) = [a(t) * p_4(t)] * p_{TR}(t, \Delta), \tag{5.1}$$

where $*$ represents convolution, $[a(t) * p_4(t)]$ is the transmitted signal with raised-cosine shaped symbols; $p_{TR}(t, \Delta)$ is the resulting pTR IR acoustic field given by

$$p_{TR}(t, \Delta) = \sum_{i=1}^{I} h_i(t, \Delta) * h_i'^{*}(-t), \tag{5.2}$$

where the upper $*$ represents conjugation, i is the hydrophones index, $h_i'(t)$ represents the channel IRs during probe transmission, $h_i(t, \Delta)$ is the channel IRs during data transmission, and Δ represents a possible mismatch between h_i' and h_i.

In a shallow water waveguide and at a range greater than a few water depths the acoustic field generated by a monochromatic point source at the i^{th} hydrophone of a VLA is given by the so-called *Green's* function

$$G_\omega(r, z_0, z_i) = \frac{-j}{\rho\sqrt{8\pi R}} e^{-j\frac{\pi}{4}} \sum_{n=1}^{M} \frac{Z_m(z_i) Z_m(z_0)}{\sqrt{k_m}} e^{jk_m R}, \tag{5.3}$$

where m is the mode number, M is the total number of propagating modes, ρ is the (constant) water density, R is the source-array range, Z_m is the m^{th} mode shape, z_0 is the source depth, z_i is the i-hydrophone depth, and k_m is the m^{th} mode horizontal wavenumber. In a range independent environment and under the adiabatic condition k_m and M are the only quantities in (5.3) that depend on frequency ω. In the frequency domain the synthetic pTR IR acoustic field (5.2) in a stationary environment (considering Δ to be negligible) is given by [44]

$$\begin{aligned} P_{pc}(R, z_0, z_i, \omega) &= \sum_{i=1}^{I} G_\omega(R, z_0, z_i) G_\omega^*(R, z_0, z_i) \\ &= \frac{1}{\rho^2 8\pi R} \sum_{m=1}^{M} \sum_{n=1}^{M} \frac{Z_m(z_0) Z_n(z_0)}{\sqrt{k_m k_n}} \sum_{i=1}^{I} Z_m(z_i) Z_n(z_i) e^{j(k_m R - k_n R)} \\ &= \frac{1}{\rho^2 8\pi R} \sum_{m=1}^{M} \frac{|Z_m(z_0)|^2}{|k_m|}, \end{aligned} \tag{5.4}$$

where, for simplicity, it was considered that $Z_m(\cdot)$ and k_m are real quantities, which amounts to ignoring the leaky modes and considering the loss mechanisms to be negligible [27]. Additionally, in (5.4) it was considered that the array spans the entire water column and that hydrophones depth sampling is sufficiently dense to fulfil the modal orthogonality property.

Since k_m in the denominator of (5.4) is a weak function of frequency, $P_{pc}(\cdot)$ is approximately constant. Thus the in time domain $p_{TR}(\cdot)$ given by (5.2) can be approximated by a dirac pulse under convolution with the bandlimited transmitted sequence.

5.3 Passive Time Reversal geometric mismatch compensation

When there is a geometric mismatch Δ (Δr for source-array range, Δz_0 for source depth, Δz_i for array depth, or any combination of those) between the probe and data transmissions it can be shown [48] that the mismatch in one of them can be compensated by applying a frequency shift $\Delta\omega$ to the other, and (5.4) becomes

$$\begin{aligned} P_{pc}(\cdot,\Delta\omega;\Delta r,\Delta z_0,\Delta z_i) &= \sum_i^I G_\omega(R+\Delta r, z_0+\Delta z_0, z_i+\Delta z_i)G^*_{\omega+\Delta\omega}(R,z_0,z_i) \\ &= \frac{1}{\rho^2 8\pi R}\sum_{m=1}^M\sum_{n=1}^M \frac{Z_m(z_0)Z_n(z_0+\Delta z_0)}{\sqrt{k_m k_n}}\sum Z_m(z_i)Z_n(z_i+\Delta z_i) \\ &\quad e^{j(k_m^\dagger R - k_n(R+\Delta r))}, \end{aligned} \tag{5.5}$$

where $k_m^\dagger = k_m(\omega+\Delta\omega)$, the influence of the frequency shift on the horizontal wavenumber k_m placed in the denominator of (5.5) is neglected and the range shift is considered to be small enough so that $R \approx \sqrt{R(R+\Delta r)}$ in the denominator. In (5.5) it is relevant that the source-array range shift Δr perturbs the exponential term, the array depth shift Δz_i perturbs the modes orthogonality and the source depth shift Δz_0 perturbs the gain that is related with the focal spot depth in aTR (see [48] for details). A full discussion of this perturbation mechanism is presented in [48] and [46]. From this discussion it turns out that the frequency shift $\Delta\omega$ used in (5.5) can be computed as

$$\Delta\omega = \frac{\omega}{R}(-\Delta r\beta + \Delta z_i\zeta_i + \Delta z_0\zeta_0), \tag{5.6}$$

and is applied in (5.5) by considering the first order Taylor expansion

$$k_m(\omega+\Delta\omega) \approx k_m(\omega) + \frac{dk_m(\omega)}{d\omega}\Delta\omega, \tag{5.7}$$

where the derivative of k_m with respect to ω represents the horizontal group slowness. In (5.6) β, ζ_i and ζ_0 are the waveguide invariants related to Δr, Δz_i and Δz_0, respectively. Since ζ_i and ζ_0 have a similar nature, in the following ζ will be used to represent both.

The invariant β is a well-known invariant in the frequency/range plane [6, 21] and is selected from a set of values

$$\beta_{mn} = \frac{\frac{1}{v_{h,n}} - \frac{1}{v_{h,m}}}{\frac{1}{u_{h,n}} - \frac{1}{u_{h,m}}}, \tag{5.8}$$

where $v_{h,m} = \omega/k_m$ is the horizontal phase velocity and $u_{h,m}$ is the horizontal group velocity of mode m. The selection of β from the β_{mn} set must take in consideration the best linear approximation in the least-squares sense of the horizontal wavenumber k_m using the horizontal group slowness for a limited number of of modes $M_e < M$, that is,

$$k_m \approx -\frac{dk_m}{d\omega}\omega\beta + \omega\rho_\beta, \tag{5.9}$$

where β represents the slope of the approximation and ρ_β its offset. The invariant ρ_β is closely related with β and is selected in a set of values

$$\rho_{\beta,mn} = \frac{1}{v_{h,m}} + \beta_{mn}\frac{1}{u_{h,m}}. \tag{5.10}$$

With the approximation of k_m (5.9) the compensation of the range mismatch is straightforward since the range mismatch Δr and the frequency shift compensation $\Delta\omega$ given by (5.6) both affect (5.5) in the exponential term. Such compensation can be applied to narrowband signals since β and ρ_β are invariant with frequency, in a similar manner to the focal intensity range shift for aTR proposed in [55].

The ζ waveguide invariants used for source depth Δz_0 and array depth Δz_i compensation have been used in [48] in a similar manner to β, but for the approximation of the vertical wavenumber γ_m using the horizontal group slowness

$$\gamma_m \approx -\frac{dk_m}{d\omega}\omega\zeta + \omega\rho_\zeta, \tag{5.11}$$

ζ is selected from a set of values

$$\zeta_{mn} = \frac{\frac{1}{v_{v,n}} - \frac{1}{v_{v,m}}}{\frac{1}{u_{h,n}} - \frac{1}{u_{h,m}}}, \tag{5.12}$$

where $v_{v,m} = \omega/\gamma_m$ is the vertical phase velocity, and ρ_ζ is selected in the set

$$\rho_{\zeta,mn} = \frac{1}{v_{v,m}} + \zeta_{mn}\frac{1}{u_{h,m}}. \tag{5.13}$$

The application of (5.11) in (5.5) for the source depth mismatch Δz_0 and array depth mismatch Δz_i compensation was made possible after establishing that they can be partially compensated using $\exp(j\gamma_m\Delta z_0)$ and $\exp(j\gamma_m\Delta z_i)$ respectively (see [48] for details). That is, for source depth mismatch Δz_0 compensation

$$\sum_{m=1}^{M} Z_m(z_0)Z_m(z_0+\Delta z_0)e^{j\gamma_m\Delta z_0} \approx \sum_{m=1}^{M} Z_m(z_0)Z_m(z_0)\frac{V(\Delta z_0)}{2}, \tag{5.14}$$

where $|V(\Delta z_0)| \approx 2$ for small values of Δz_0 and $|V(\Delta z_0)| \approx 1$ for higher values of Δz_0. For the array depth mismatch Δz_i compensation

$$\sum_{i=1}^{I} Z_m(z_i)Z_n(z_i+\Delta z_i)e^{j\gamma_m\Delta z_i} \approx \sum_{i=1}^{I} Z_m(z_i)Z_n(z_i)\frac{W(m,\Delta z_i)}{2}, \tag{5.15}$$

where $|W(m, \Delta z_i)| \approx 2$ for small values of Δz_i and $|W(m, \Delta z_i)|$ oscillates around 1 for higher values of Δz_i.

With the approximation of γ_m (5.11) and the compensation mechanisms (5.14) and (5.15) the compensation of the source and array depth mismatches is straightforward since the mismatch can be compensated by a complex exponential of γ_m and the frequency shift compensation $\Delta\omega$, given by (5.6), affects (5.5) in an exponential factor. Such compensation can be applied to narrowband signals since ζ and ρ_ζ are invariant with frequency.

As previously suggested for the invariant β, the ζ compensation mechanism has better performance when considering an effective number of modes $M_e < M$. The selection of β in (5.8) and ζ in (5.12) for optimal compensation depends on M_e. Such dependence suggests that the compensation mechanism can be further optimized by considering its application to smaller groups of modes instead of a single group of modes from $m = 1, .., M_e$, resulting in different values of β and ζ for each group. That was previously proposed in [55] and [35] for the waveguide invariant β.

In a waveguide with a depth-dependent sound-speed profile the vertical wavenumber as well as phase velocity become depth dependent. In the present paper it is assumed that such dependence is small enough so that ζ_i can be calculated from the mean phase velocity, $\overline{v_{v,m}(z_i)}$, over the array. Since ζ_0 is computed for the nominal source depth z_0 in a real situation it will be expected that $\zeta_i \neq \zeta_0$.

5.4 The passive time-reversal frequency shift equalizer

Figure 5.1 shows the pTR system adapted to incorporate a frequency shift that compensates for the geometric mismatch Δ between the IR for probe-signal transmission $h'(t)$ and the IR during data transmission $h(t)$. It behaves as a matched filter (to the IR) demodulator with a set of L frequency shifts being applied to the channel IR $h'(t)$ estimate after time windowing, where the optimal frequency shift is selected based on the "Maximum power selection" block with the $\mathsf{z}_l(t)$ power being computed in time slots. In Figure 5.1 the pTR output signal can be written as

$$\mathsf{z}_l(t) = y_l(t) + x1_l(t) + x2_l(t) + x3_l(t), \tag{5.16}$$

where index l designates frequency shift $\Delta\omega_l$, $y_l(t)$ contains the desired data-signal contaminated with ISI and the other three terms are noise disturbances (see [49] for definitions and details).

The overall Signal to Noise Ratio (SNR) is the ratio between the power of the signal term $y_l(t)$ and a sum of the variances of the noise disturbances $x1_l(t)$, $x2_l(t)$ and $x3_l(t)$. Considering the signal and noise powers given by (3.26-29) of [49] it can be shown that the effect of the frequency shift compensation on the channel IR $h'(t)$ estimate is higher on the signal variance term than on the noise variances, contributing to SNR enhancement. Therefore, tracking the maximum power of the pTR output $\mathsf{z}_l(t)$ gives a clear indicator of the best frequency shift taking into account the actual environmental/geometric conditions

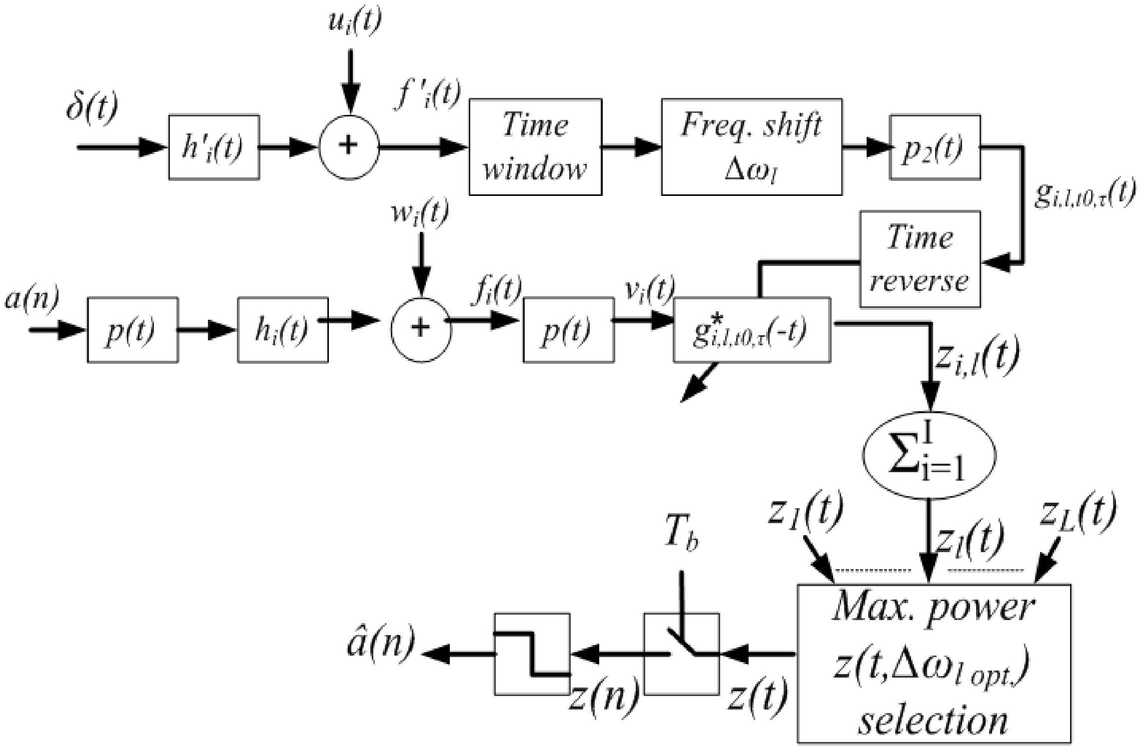

Figure 5.1: Block-diagram of the FSpTR equalizer. The blocks in the upper path represent the probe-signal IRs estimate, time windowing, and frequency shift operations. The blokes in the middle path represent data transmission and crosscorrelation with the IRs estimate obtained in the upper path. Summation over the I hydrophones gives the L pTR processor outputs $\mathsf{z}_l(t)$. The blokes path below represent the selection of $\mathsf{z}_l(t)$ with the frequency shift that best compensates for geometric mismatch between probe and data transmissions, and the transmitted symbols estimation.

of the signals being received. That results in the FSpTR system that equalizes the real pTR IR $\sum_{i=1}^{I} h_i(t) * h'^{*}_{i,t_0,\tau}(-t)$ (where the $'$ indicates that there is a geometric mismatch Δ between h_i and $h'^{*}_{i,t_0,\tau}$) with the non mismatched pTR IR $\sum_{i=1}^{I} h_i(t) * h^{*}_{i,t_0,\tau}(-t)$, where t_0 and τ are the starting time and duration of the time window, respectively.

5.5 Real Data Application

The experimental data were acquired during the MREA'04 sea trial that took place off the town of Setúbal, approximately 50km south of Lisbon (Portugal), in April 2004. The pTR experiment started at a close range of 0.6km to the south of the receiving array (in a gently up sloping region) and the source progressively opened range to the southeast up to 2km (with a progressive slope reduction up to range independence). The environment was characterized by a water column depth ranging between 90 to 110 m over a 1.5 m silt bottom and gravel layer. The receiving array was free drifting in a surface suspended Acoustic Oceanographic Buoy (AOB) [51], which was found to oscillate vertically due to the surface waves with amplitude of approximately 0.63m and frequency between 0.43 and

0.4Hz, as measured by a wave rider buoy placed in the area of the experiment. The acoustic source was suspended from the NRV Alliance, its depth was measured at a sampling rate of 1 s with a 10 cm resolution depth sensor. In the data set processed in this paper it oscillates with a main component of 0.1 Hz, between 71.64 and 72.24 m.

During the MREA'04 sea trial the pTR based data communications conceptual system was similar to that of Figure 5.1, with the $p_2(t)$ narrowband filter of the IR estimation operation (path above in Figure 5.1) distributed between the transmitter and the receiver, i.e., the transmitted probe-signal was a fourth-root raised-cosine pulse and IR estimates were obtained by correlating the received probe-signal with the transmitted one (see [45] for details).

This paper analyzes modulated data at a carrier frequency of 3.6 kHz, using a symbol rate of 400 baud and 2-PSK constellation. Fourth-root raised cosine signaling pulses with 100% roll-off were used such that the signal bandwidth is 800 Hz. Each individual transmission comprises a single truncated PAM signaling pulse acting as a channel probe with symmetric guard intervals for a total duration of 1 s, followed by a 20 s data packet. The source sequentially transmits 4 packets for a total duration of 84 s. In order to demonstrate the long-term stability of the proposed FSpTR compensation mechanism only the third channel probe pulse was used in the pTR operation of Figure 5.1 to estimate the transmitted symbols in the four data packets. The data was preprocessed using the Doppler compensation method as proposed in [20].

Since the sound speed profile is composed of a thermocline of approximately 20 m and 1512 m/s over a down refracting sound speed up to approximately 1505 m/s near the bottom two different modal structures have been observed by the top two hydrophones and by the six bottom hydrophones [35] [48]. Those two modal structures are expected to have different invariants [35], and for the purpose of showing the usefulness of the waveguide invariant frequency shift in underwater communications with pTR in a geometric variable environment, only the six hydrophones below the thermocline were considered.

The system of Figure 5.1 requires the use of a time window whose optimum length τ_{opt}, in a non geometric mismatch case, has been found in [49]. The time window initial point t_0 is set to an arbitrary point before the first arrival and the time window length τ is set to a value higher that the optimum in order to allow for a better behavior of the compensation mechanism in presence of geometric mismatch. In the ray mode analogy [58] later arrivals are related with higher modes, making the time window operate as a mode filter.

By considering the same frequency shift $\Delta\omega_l$ to be applied to all modes captured in the time window (t_0, τ) in the system of Figure 5.1 the surface of Figure 5.2 results. The surface represents the pTR output power $\sigma_z^2(t)$, computed in time slots of 0.5 s, as a function of time and frequency shift and the blank spaces represent the the elapsed time between the data slots. The solid line traces the maximum of the surface as a function of time, and the '*' indicates the time instant where the channel probe used in the pTR processor was received. GPS data, acquired during the experiment, shows that during the 80 s of data transmission the source-array range increases by about 50 m, which can be clearly seen in Figure 5.2 as a mean decrement of optimal frequency shift from about 150 Hz to about -50 Hz with 0 Hz at the channel probe location. Oscillations around the mean increment seem to be mainly due to the other geometric mismatches (array depth and source depth), but no definitive conclusions can be drawn since there is no ground truth information about array or source depth variations.

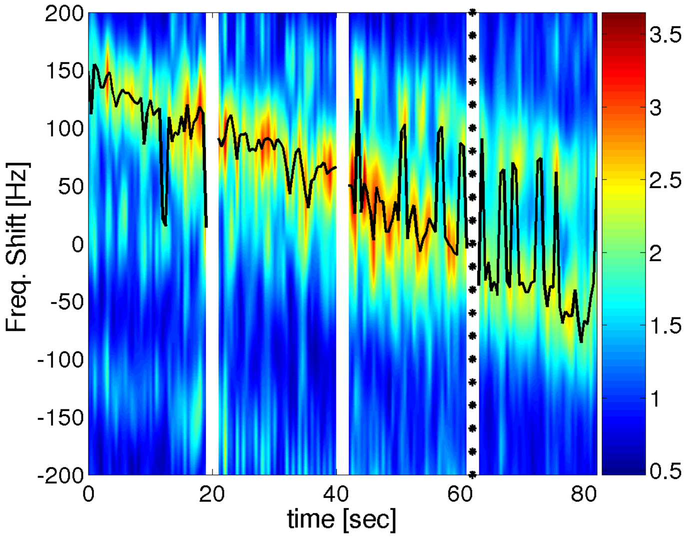

Figure 5.2: Passive time-reversal output mean magnitude $\mathbf{z}_l(t)$ as a function of time and applied frequency shift, computed by slots of 0.5 s. The solid line traces the maximum of the surface.

Figure 5.3 shows the MSE between the estimated and transmitted bit sequences, computed in slots of 0.5 seconds, for plain pTR with no compensation (solid line) and for pTR with compensation (red dashed line). The solid line initially shows a strong degradation in the uncompensated pTR that progressively reduces when approaching $t = 60$ s. Compensated results (red dashed line) maintain the MSE at approximately the same level, resulting in a strong gain. In the first 20 s that gain is about 5.55 dB, in the second 20 s it is about 5.7 dB, in the third 20 s is about it 1.64 dB and in last 20 s it is about 1.53 dB, for an overall gain of about 4.11 dB. It is remarkable that such results were obtained with a range mismatch up to about 37.5 m with source depth varying between 71.6 m and 72.3 m and an array depth oscillation of approximately 0.63 m.

5.6 Conclusions and Future work

Experimental results were given for time-reversed demodulation of 3.6 kHz binary PSK data collected during the MREA'04 experiment. Two receiving architectures were compared: plain pTR and pTR with frequency shift for geometric mismatch compensation - FSpTR. By itself, pTR suffers a significant performance penalty due to geometric mismatch during data transmission, resulting in acceptable results only in a 20 s window

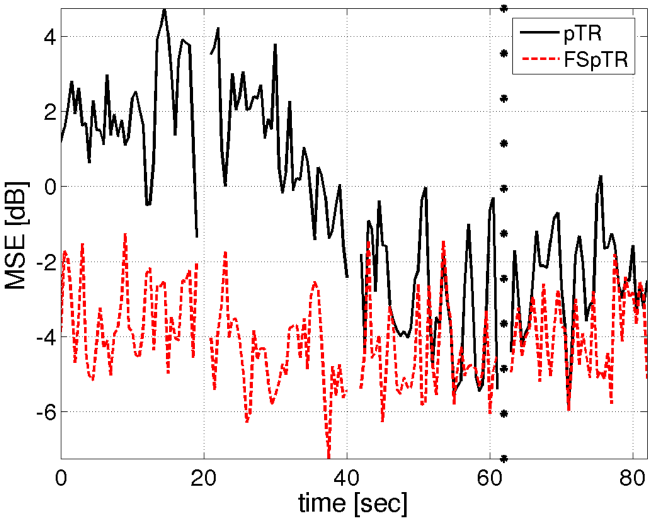

Figure 5.3: Mean squared error between the estimated and transmitted data symbols for plain pTR (black line) and FSpTR (red dashed line).

around the channel probe location. FSpTR presents a longer stability that was shown to be effective for up to 60 s from the channel probe location. Moreover, FSpTR presents a gain of 1.5 dB over pTR even for short-term mismatch. Future work should address a comparison between FSpTR and other adaptive pTR systems [20].

Due to its environmental based nature, FSpTR can be used not only to attain reliable underwater communications, but also to track the geometric variations during data transmission considering a previous estimation of the waveguide invariants β, ζ_i and ζ_0. Future experiments should be planned in order to explore such possibility.

In the present paper the Doppler compensation has been performed off-line prior to the equalization process. Future work should address its inclusion in the equalizer processor. In what concerns symbol synchronization, an heuristic method that chooses the minimal spread of the constellation prior to the slicing, was adopted.

Acknowledgments

This work was supported by Fundação para a Ciência e a Tecnologia under programs POCI, POCTI and POSI. The authors would like to thank the NATO Undersea Research Centre for the organization of MREA'04 sea trial, NRV Alliance master and personnel and the scientist in charge Emanuel F. Coelho.

Chapter 6

Environmental equalizer for high data rate underwater communications

---

Abstract: Equalizers are used in underwater coherent communications to track channel impulse responses and compensate for intersymbol interference due to multipath. Such equalizers are based on black-box channel models which conceptually ignore the fact that IR variability is caused by fluctuations of environmental parameters. Environmental-based equalization as presented in this work is based on passive time-reversal and waveguide invariant properties of ocean channels. Passive time-reversal allows for the implementation of a simplified communication system, but its primary cause of performance degradation is the presence of geometric mismatch between the probe-signal and the actual data transmission. This problem is addressed here through waveguide invariance, which states that geometric mismatches, both in depth and range, can be partially compensated by applying an appropriate frequency shift in the passive time-reversal operator. Results with 2000 baud binary PSK signaling at a carrier frequency of 12.5 kHz, collected during the RADAR'07 sea trial with a moving source and a free drifting receiver array, show that the Mean-Square Error (MSE) between transmitted and estimated data symbols reduces to -4 and -8 dB in the presence of strong and mild multipath, respectively.

6.1 Introduction

Underwater acoustic communication channels present serious limitations for attaining even modest data rates that are trivially achieved in terrestrial wireless radio channels. Common causes are the significant delay spread that induces multipath and hence strong frequency selectivity; the available bandwidth is limited and increasing the frequency also increases the attenuation; and the low propagation speed of sound causes significant Doppler even with low source-receiver relative speeds.

In order to overcome such drawbacks the most widely-used solutions for coherent communications are based on equalizers similar to those adopted in terrestrial communications. Operational difficulties, such as problems of convergence of adaptive algorithms, occur due to specific characteristics of the underwater channel (high variability of the channel Impulse Responses (IRs), high number of coefficients that depend on the channel delay spread and can vary from a few to hundreds of symbols, strong Doppler).

Despite the high spread and high variability of underwater channel IRs it is well known, from tomographic and inversion experiments, that the physical characteristics of the environment vary quite slowly [1]. This suggests that an equalizer based on environmental change tracking and matched-field processing (i.e. a full inversion equalizer) would be more robust and stable than standard equalizers. Unfortunately, the strong nonlinearity of inversion and tomographic methods and their high computational load (when compared with the required speed for high data-rate acoustic communication) makes full inversion equalization impractical.

Considering that a communication system usually transmits information in packets whose duration does not exceeds a few tens of seconds, it is possible to identify geometric environmental characteristics[1], as being those that have first order impact on the variability of IRs during packet transmission. Chuprov's work [6] on the invariant properties of layered media establishes a linear relation between group and phase velocities in the vicinity of a canonic point, from which local frequency/range and frequency/depth invariants follow.

The first attempts at underwater communication using environmental information [17, 50, 24, 43] relied on basic properties of Time-Reversal (TR) in underwater channels [38, 26, 8, 34, 13]. A particular type of TR — passive Time-Reversal (pTR), also termed Passive Phase Conjugation (PPC) [26] in the frequency domain —, uses a receive-only array, with a probe-signal transmitted ahead of the data for IR estimation. The received probes are then used as a synthetic channel for temporal focusing of the data, which effectively deconvolves the multipath generated by the real channel.

When applied to field data, the achieved TR focus is not perfect due to errors in IR estimates and the time variability of the channel, resulting in uncompensated intersymbol interference (ISI) [45]. That problem is even more relevant in communications with a moving source and/or receiver, in which case one would expect a rapid degradation of pTR temporal focusing due to the increasing mismatch between assumed and actual channels. In order to ensure longer stability of the focal spot, three solutions have been proposed in the literature: one is to use an adaptive algorithm to track the IRs throughout data packets [14]; another solution is to use a single-channel equalizer after TR [54]; and finally a third alternative is to use a low-complexity equalizer with only one coefficient per channel [20]. A performance comparison between adaptive pTR variants is presented in [20]. In the first method, channel estimates are represented by a large number of coefficients that need to be adapted, thus leading to relatively complex equalizers. The second and third methods offer a better compromise between complexity and efficiency. The approach taken in this work

---

[1] geometric characteristics are source-receiver range, as well as source, receiver and water column depths. Non-geometric characteristics include sound-speed profile, sediment and bottom properties, salinity, and water density.

stems from those but goes one step further by considering that the environment mismatch between the probe-signal and data transmissions is mainly due to geometric disparities, knowledge of which can then be used to compensate for the overall IR mismatch.

A physics-based algorithm for pTR equalization based on waveguide invariants of shallow water channels is proposed. The waveguide invariant β [6, 21] has been previously applied to change the range focus in active time reversal (aTR) [55], and to develop a model for performance prediction of a time-reversal communication system [42]. In [48] the waveguide invariant allowed for the compensation of pTR geometric mismatch, as it was shown that the impact of changes on geometric features can be compensated by a simple frequency shift of estimated IRs acquired during probe-signal transmission. In [47] such mismatch compensation method was applied to underwater communications in the 3.5 kHz frequency band. The resulting environmental equalizer, termed Frequency Shift pTR (FSpTR), increased the pTR output power and reduced the Mean-Square Error (MSE).

In this work the FSpTR equalizer is applied in a frequency band around 12.5 kHz. Signal propagation is substantially different from the one reported in [47], with a significant number of undersampled high order modes resulting in strong modal aliasing, while a strategy to overcome this effect is proposed. Moreover, the environmental equalizer does not require symbol decisions to be fed back to the processing structure, as the performance criterion is based on output power. This has the added benefit of allowing simple Doppler compensation methods to be used at the equalizer output.

Probe timing optimization is another important issue in pTR-based communications. Heuristic reasoning suggests that if the observation window fails to include all significant multipaths, pTR operation will result in imperfect retrofocusing, while an overly long window will degrade the performance by introducing undesired noise [18, 45, 11]. In [49] it was shown that a metric can be defined in order to optimize the pTR communications system with respect to the time-window length. In this work it will be shown that the same approach can be extended to the pTR environmental equalizer.

The reliability of the physics-based waveguide invariant pTR equalizer is demonstrated using experimental data obtained during the RADAR'07 sea trial, where binary PSK signals at a data rate of 2000 bits per second were transmitted with a carrier frequency of 12.5 kHz. FSpTR features long-term compensation of channel mismatch (up to 50 seconds), its output MSE remaining stable even in the presence of geometric mismatches. Results show that the environmental equalizer achieves almost error-free decoding, with -4 dB of MSE using a short array of 6 hydrophones, and -8 dB using 16 hydrophones.

A performance comparison between the Fractionally-Spaced Equalizer (FSE) and the environmental equalizer is presented. It is found that the FSE outperforms the environmental equalizer. Nevertheless, it should be stressed that for proper operation the FSE requires crucial human intervention for selecting the number of coefficients and forgetting factor, while the probe timing optimization of pTR environmental equalizers depends on well-defined metrics that can possibly be used for unsupervised operation.

This work is organized as follows: section 6.2 recalls the use of pTR in underwater communications and the geometric mismatch compensation of pTR using frequency shifts; section 6.3 presents the FSpTR equalizer and describes its operation; section 6.4 addresses probe timing optimization; the FSpTR is applied to real data in section 6.5; section 6.6 summarizes the main results, draws some conclusions, and suggests future research.

6.2 Passive Time Reversal geometric mismatch compensation

The basic setup for applying pTR to communications consists in a point source that sends information to a Vertical Line Array (VLA). The procedure starts by sending a short probe-signal, waiting for the channel to clear of multipath arrivals, and then sending the data stream. In the noiseless case, the pTR output after the received probe and data are processed is given by [49]

$$y(t) = [a(t) * p_4(t)] * p_{TR}(t, \Delta), \tag{6.1}$$

where $*$ represents convolution, $[a(t) * p_4(t)]$ is the transmitted amplitude/phase-modulated signal with raised-cosine shaped symbols; $p_{TR}(t, \Delta)$ is the resulting pTR IR acoustic field given by

$$p_{TR}(t, \Delta) = \sum_{i=1}^{I} h_i(t, \Delta) * h_i'^{*}(-t), \tag{6.2}$$

where the superscript $*$ denotes complex conjugation, i is the hydrophone index, $h_i'(t)$ represents the channel IR during probe transmission, $h_i(t, \Delta)$ is the IR during data transmission, and $\Delta \equiv (\Delta r, \Delta z_i, \Delta z_0)$ represents a possible mismatch between h_i' and h_i (where Δr is the source-array range mismatch, Δz_i is the array depth mismatch, and Δz_0 the source depth mismatch). If there is no mismatch and the array densely samples the whole water column the overall time domain pTR IR given by (6.2) for $\Delta \equiv 0$ can be approximated by a bandlimited sinc pulse. In the context of normal modes of propagation [58, 27], the formal demonstration of this follows from the normal modes orthogonality property [34]. Geometric mismatch can be partially compensated by applying a frequency shift to $h_i'(t)$, as discussed in detail in [46, 48, 47].

The idea of using a frequency shift, $\Delta\omega$, to compensate for the geometric mismatch relies on Chuprov's work [6] that for a given group of modes in a waveguide demonstrates the existence of the invariant

$$\beta = \frac{\Delta\omega}{\Delta r}\frac{R}{\omega}, \tag{6.3}$$

that defines lines of constant intensity in the frequency-range plane. For a ray with inclination χ the invariant

$$\zeta = -\beta \coth \chi = \frac{\Delta\omega}{\Delta z_i}\frac{R}{\omega}, \tag{6.4}$$

defines lines of constant intensity in the frequency-depth plane. In a layered waveguide the acoustic field is formed by a reduced number of mode groups, and for each of those β and ζ are invariant with frequency.

Song [55] used a method based on the waveguide invariant β for shifting the range of the TR focal spot. The proposed method can be readily applied in pTR for range mismatch compensation. Actually, the impact of range or depth mismatches on the acoustic field turns out to be similar, and the latter can be compensated in much the same way as the former through a properly defined invariant ζ. In [46, 48] a strategy based on the invariant ζ is developed for restoring the orthogonality property of normal modes, which is destroyed by array depth mismatch. In the context of active TR, source depth mismatch can be seen as if observing the back-propagated field at a depth different from the focal depth. In pTR this effect results in a loss of performance that can be recovered similarly to the restoration of orthogonality of normal modes. In their work, both Chuprov and Song considered only the acoustic field intensity. However, phase information is crucial when applying pTR in coherent communications, and the influence of the frequency shift in the signal phase must therefore be taken into consideration.

Considering (6.3) and (6.4) the appropriate frequency shift for mismatch compensation is given by

$$\Delta\omega = \frac{\omega}{R}(-\Delta r\beta + \Delta z_i\zeta_i + \Delta z_0\zeta_0), \tag{6.5}$$

where R is the original source-array range and ω is the mean frequency of the bandlimited IRs. The invariants ζ_i and ζ_0 are only constant, and equal, for a homogeneous sound-speed profile, otherwise they vary with sound velocity over the water column. This dependence increases with frequency as the WKB approximation becomes applicable and the perturbation of lower order modes by the sound speed variations becomes more visible. It results that when the compensation operates at low frequencies a mean value of ζ_i should be used, but when operating at high frequencies the compensation should be applied to a shorter array or considering smaller sections of the array.

Applying the frequency shift (6.5) in (6.2) it results

$$\begin{aligned} p_{TR}^{comp}(t,\Delta) &= \sum_{i=1}^{I} h_i(t,\Delta) * [h_i'^*(-t)\exp(-j\Delta\omega t)], \\ &\approx A\; p_{TR}(t - t_{\rho,\Delta}) \end{aligned} \tag{6.6}$$

were the compensation is achieved up to attenuation factor A and a time delay $t_{\rho,\Delta}$. The attenuation factor A is due to the loss of validity of the compensation through invariants in the presence of an increasing geometric mismatch. The compensation mechanism also introduces a linear phase that results in a time delay $t_{\rho,\Delta} = (\rho_\beta\Delta r - \rho_{\zeta,i}\Delta z_i - \rho_{\zeta,0}\Delta z_0)$, where ρ_β, $\rho_{\zeta,i}$ and $\rho_{\zeta,0}$ are three other invariants closely related with β, ζ_i and ζ_0. In [48] a full description of the gain factor A and of the linear phase that results in the time delay $t_{\rho,\Delta}$ is presented.

The conditions for propagation in a layered ocean are such that the field is effectively formed by a few groups of modes with consecutive indexes (that correspond to rays from the point of view of geometric acoustics) [27]. The compensation mechanism should be applied to each group independently, since only then can their phase and group velocities be approximated by a constant [35]. Despite the fact that the gain factor A causes attenuation in the matched pTR IR $p_{_{TR}}(t)$ in (6.6), the main feature of the compensation mechanism is the restoration of the modes orthogonality property, which constitutes the basis for pTR.

Replacing the mismatch pTR IR (6.2) by the compensated one (6.6) in the pTR communication system output (6.1), it results

$$y^{comp}(t) = A\ [a(t) * p_4(t)] * p_{_{TR}}(t - t_{\rho,\Delta}), \tag{6.7}$$

that resembles the pTR communication system output with no mismatch. That is the basic idea of FSpTR equalizer that in a Matched-Filter Demodulator (MFD) receiver manner applies a set of frequency shifts to the channel IR estimates (6.6) and assumes that the perfect match is obtained for the frequency shift that gives the maximum power of (6.7).

6.3 The passive time-reversal frequency shift equalizer

Figure 6.1 shows a block diagram of the pTR communication system adapted to incorporate frequency shifts for compensating geometric mismatch Δ between the probe-signal transmission IR $h'(t)$ and the IR during data transmission $h(t, \Delta)$ [49, 47]. In Figure 6.1(a) the system behaves as a matched filter (to the IR) with a set of L frequency shifts being applied to the channel IR estimates, $h_i'(t)$, after time windowing. Summing the outputs of matched filters over all array sensors yields

$$\mathsf{z}_l(t) = y_{sig,l}(t) + y_{isi,l}(t) + x_l(t), \tag{6.8}$$

where index l designates the l^{th} frequency shift $\Delta\omega_l$, $y_{sig,l}(t)$ contains the desired data-signal and $y_{isi,l}(t)$ the signal residual ISI contamination. Term $x_l(t)$ represents the pTR output noise that results from interaction between the input noises $w_i(t)$ and $u_i(t)$ and on the channel responses during transmission of probe, h_i', and data, h_i, signals (see [49] for definitions and details).

Similarly to a MFD receiver, the frequency shift described in Section 6.2 acts to equalize the overall pTR IR $\sum_{i=1}^{I} h_i'(t) * h_{i,t_0,\tau}^*(-t, \Delta)$, approximating the matched response $\sum_{i=1}^{I} h_i(t) * h_{i,t_0,\tau}^*(-t)$, where t_0 and τ are the starting time and duration of the time window, respectively. Frequency shifts do not strongly affect the power of the noise term $x_l(t)$, since their primary effect is to increase the signal power term, and thus contribute to enhance the signal-to-noise ratio (SNR). Therefore, tracking the maximum power of the pTR output $\mathsf{z}_l(t)$ gives a clear indicator of the best frequency shift taking into account the actual environmental/geometric conditions of the received signals.

In Figure 6.1(b) the L outputs of part (a), $\mathsf{z}_l(t)$, are combined, synchronized, Doppler compensated and finally used to estimate the transmitted data sequence. In the "Combining" block the $\mathsf{z}_l(t)$ are divided into N_s temporal slots, the power of each slot is computed and stored in a $L \times N_s$ matrix. The slots are then combined according to three criteria:

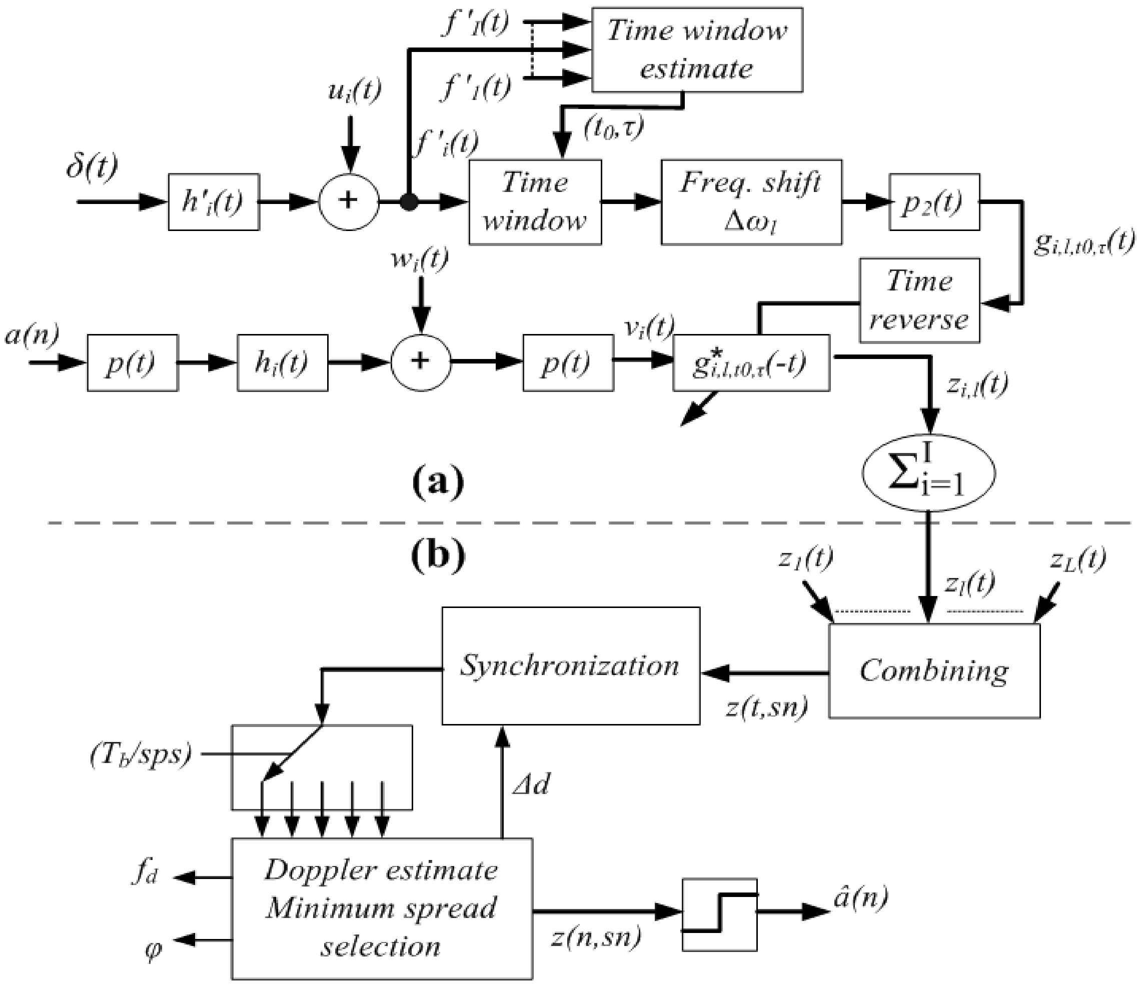

Figure 6.1: Block-diagram of the FSpTR equalizer. Part (a): the blocks in the upper path represent the probe-signal IR estimate, time windowing, and frequency shift operations. The blocks in the middle path represent data transmission and crosscorrelation with the IR estimate obtained in the upper path. Summation over the I hydrophones gives the L pTR processor outputs $\mathsf{z}_l(t)$. Part (b): the blocks depicts combining of $\mathsf{z}_l(t)$ considering the frequency shift that best compensates for geometric mismatch, Doppler compensation, synchronization, and symbol estimation.

considering that there is no frequency shift, which is the "plain pTR" case; for slot n_s select l with maximum power, which corresponds to the "FSpTR" case; find the local maxima for each slot (to be clarified in Section 6.5) and add them coherently, this will be denoted as the "FSpTR+" case. In the "Synchronization" block an initial synchronization, for the first signal slot n_s, is performed with the probe-signal sent previously to the data signal. If in the "Doppler estimate" block a requirement for Doppler compression/expansion is detected in a given slot, the next slot is re-synchronized in order to accommodate the detected Doppler compression/expansion, Δd. Such Doppler re-synchronization strategy requires that the Doppler compression/expansion of each slot should be smaller than one symbol period. The "Doppler estimate Minimum spread Selection" block operates by frac-tionating the slot into several symbol-rate-sampled (*sps*) streams. Each stream is then multiplied by a set of complex exponentials with angular frequency $2\pi f_{d,k}$. Then it is possible to identify the channel and the angular frequency with smaller constellation spread, and to estimate: 1) the Doppler frequency f_d, that is, the angular frequency which better compresses the constellation, 2) the Doppler shift Δd that results from the stream with lower constellation spread and 3) the constellation offset ϕ of the selected stream after Doppler compensation. After Doppler and offset compensation the stream with minimum constellation spread is used to feed the slicer. The slicer outputs the estimated symbol sequence, denoted by $\hat{a}(n)$.

6.4 Time-window optimization

In Figure 6.1 the time-window operation is of major importance, as it controls the length of channel IRs that will be used for pTR. Each IR typically consists of a main arrival followed by strong multipath and often preceded by weak precursor multipath. The benefits of pTR from a communications perspective are twofold; it increases the SNR and reduces the residual ISI. In both cases the amount of multipath considered in the time-window will have a strong influence. When there is no mismatch between probe-signal and data transmissions the time-window optimum length can be predicted in the "Time-window estimate" block of Figure 6.1 using the channel IR estimates required for pTR.

Residual ISI in the matched case is defined as [56],

$$ISI(t_0,\tau) = \frac{\sum_{n\neq 0} |p_{TR}(nT_b,t_0,\tau)^2|}{|p_{TR}(0,t_0,\tau)^2|} \tag{6.9}$$

where

$$p_{TR}(nT_b,t_0,\tau) = \sum_{i=1}^{I} [h_i^*(-t,t_0,\tau) * h_i(t)] * p_4(t) \Big|_{t=nT_b} \tag{6.10}$$

is the overall pTR IR affected by the time window operation, sampled at the symbol period T_b. Optimal window parameters are obtained by minimizing (6.9). In [49] it was found that the pTR output SNR is proportional to the overall pTR IR accumulated power, given by

$$\Phi^2(t_0,\tau) = \frac{|C_y(t_0,\tau)|^2}{\tau}, \tag{6.11}$$

where

$$C_y(t_0,\tau) = \sum_{i=1}^{I} \int_{t_0}^{t_0+\tau} |h_i(t)|^2 dt, \tag{6.12}$$

is the sum across hydrophones of IR energy cumulative functions. The maximum of $\Phi^2(t_0,\tau)$, will provide time window settings (such as start time t_0 and duration τ) that optimize the output SNR.

Different window settings can result from the SNR and ISI criteria, nevertheless it was shown in [49] that the output SNR criterion should be used for low input SNR, whereas better results are achieved with the ISI criterion for high input SNR. Time-window optimization based on initial channel IR estimates for the matched case loses accuracy in the presence of channel mismatch, but its validity can be extended through mismatch compensation. That is the case of the FSpTR equalizer presented here, and of the Decision-Directed Passive Phase Conjugation equalizer [14].

6.5 Real Data Application

The experimental data were acquired during the RADAR'07 sea trial that took place off the town of Setúbal, approximately 50 km south of Lisbon (Portugal), in July 2007. The environment was characterized by a water depth varying between 90 to 120 m over a 1.5 m thick silt and gravel sediment layer. During the pTR experiment the source-array range, computed with GPS data, varied between 5.3 km and 5.24 km. The receiving array was attached to a surface-suspended and freely-drifting Acoustic Oceanographic Buoy (AOB) [51]. It comprised sixteen 4 m spaced hydrophones, the depth of the top one varying between 6.07 and 6.47 m as measured by an array colocated depth sensor. The acoustic source was suspended from the research vessel NRP D. Carlos I, and its depth for the time interval of the data set processed in this work oscillates between 60 and 61.1 m.

During RADAR'07 the acoustic communication system was conceptually similar to that of figure 6.1, with a chirp signal transmitted as a probe-signal and the channel IR estimates obtained by pulse compression. This work analyzes modulated data at a carrier frequency of 12.5 kHz, using a symbol rate of 2000 baud and 2-PSK constellation. Fourth-root raised cosine signaling pulses with 50% roll-off were used such that the signal bandwidth is 3000 Hz. Each individual transmission comprised a chirp signal acting as a channel probe with 4800 Hz bandwidth centered at the carrier frequency and 0.1ms duration, followed by 0.2ms guard time and a 50s data packet. The source sequentially transmitted 4 packets with an interval of 120s. During data transmission the source-array range decreased at a variable rate (relative velocity between 0.3 and 0.05 m/s), causing variable Doppler compression of the received signals. For example, the actual duration of the first packet differs by 18 symbol intervals from the nominal packet duration.

Figure 6.2 shows the water column sound speed profile computed from the temperature profile measured by thermistors collocated with the array hydrophones. It can be seen that the temperature profile is downward refracting up to hydrophone 9, at approximately 42m depth, and then becomes nearly constant.

Figure 6.3 shows the arrival pattern estimated from the chirp signal of the first data packet. It can be seen that the wavefronts are composed of a main path followed by down and up-going multipaths. Note that the WKB approximation is valid at the acoustic frequencies used in this experiment. Low-order modes, responsible for the main arrival, strongly attenuate in the water column and do not interact with the surface. On the other hand later paths, due to high-order modes, do interact with the sea surface. From this description it is expected that multipath will have greater impact in a communications system when using the upper part of the array than when using the full array, as ISI will be stronger in the former.

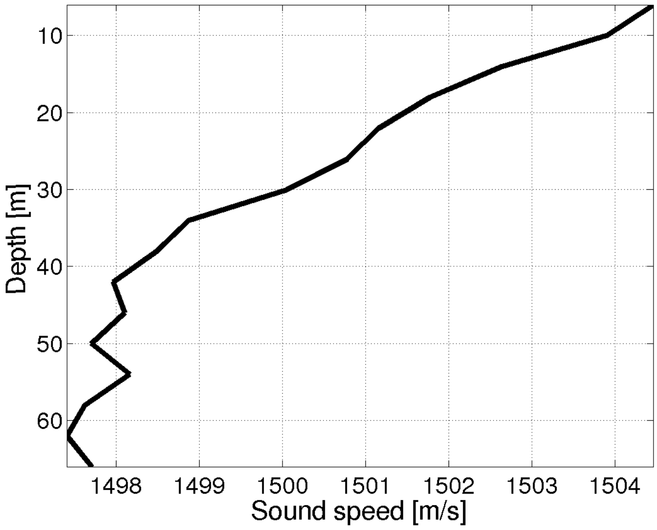

Figure 6.2: Mean sound speed profile during data transmission, during day 195 between 10:07h and 10:15h (local time).

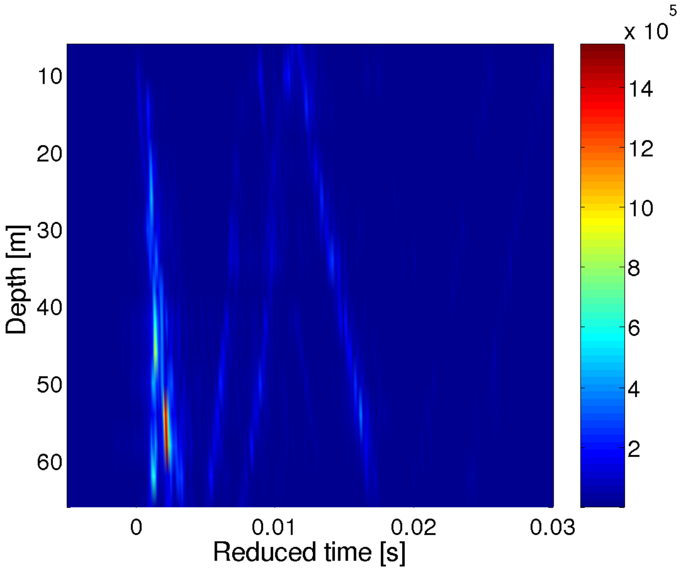

Figure 6.3: Arrival pattern estimated by pulse compression of the chirp probe-signal of the first data packet.

Figure 6.4 shows the normalized inverse of (6.9), $ISI^{-1}(t_0, \tau)$ (solid line), and the normalized $\Phi^2(t_0, \tau)$ from (6.11) (dashed line), where t_0 has been set arbitrarily before the main arrival. The channel IR estimates used to compute the arrival pattern of figure 6.3 are superimposed and plotted in figure 6.4, providing visual clues of where channel IRs are more intense, for the full 16-hydrophone array (a) and for the top 6 hydrophone array (b). The maximum of the dashed line gives the time-window length τ where the output pTR SNR is higher, whereas the solid line reveals the value of τ where residual ISI is better compensated. Figure 6.4(a) shows that for this case better results are expected with a short window covering approximately 4 symbols, while figure 6.4(b) shows that a short time-window can be used to optimize the output pTR SNR, but since there is a strong local maximum of the Φ curve (dashed line) close to the maximum of the ISI^{-1} curve (solid line) a 28 symbols time-window length is more appropriate.

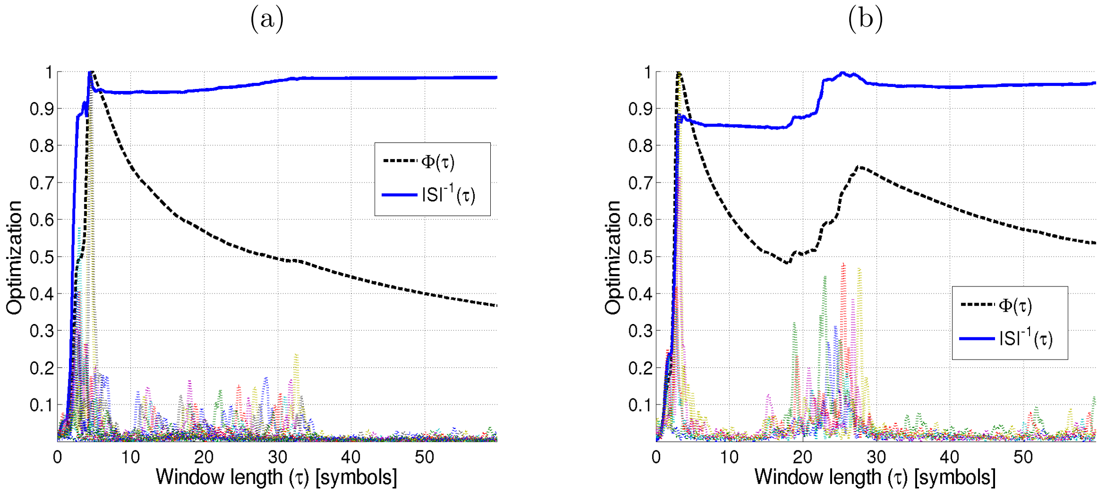

Figure 6.4: Time-window optimization with a 16-hydrophone array (a), with a 6-hydrophone array (b).

As an example of frequency shift optimization, figure 6.5 depicts the evolution of the pTR output $\mathbf{z}_l(t)$ mean power along one data packet as a function of frequency shift and time/slot number. Frequency shifts vary in the range ±600 Hz with an interval of $25Hz$. Each packet was divided into 200 time slots of 0.25 s duration each. The solid line connects the surface maxima (indicated by the stars '*') obtained for each time/slot-number. In figure 6.5(a), for the 16-hydrophone case, the same frequency shift $\Delta\omega_l$ is applied to all modes captured in the time window (t_0, τ). GPS data show that during these 50s of data transmission the source-array range decreases by approximately 11 m, which should be reflected in a mean increment of the optimal frequency shift in Figure 6.5. However, this is not visible because the frequency shift due to range decrease is masked by that due to source and array depth variations that can be observed in the up and down swing of the maximum power curve.

In Figure 6.5(b) the frequency shift $\Delta\omega_l$ is applied only to higher-order modes captured in the time window (t_0, τ) between 18 and 28 symbols of Figure 6.4(b). The compensation mechanism acts on modes that are poorly sampled by the array, resulting in spatial aliasing that degrades their orthogonality. This is clearly visible in the compensation mechanism of Figure 6.5(b) in the 6-hydrophone case when the time-window covers also the high order modes.

In figure 6.1 part (b) the "Combining" block uses the output power shown in figure 6.5

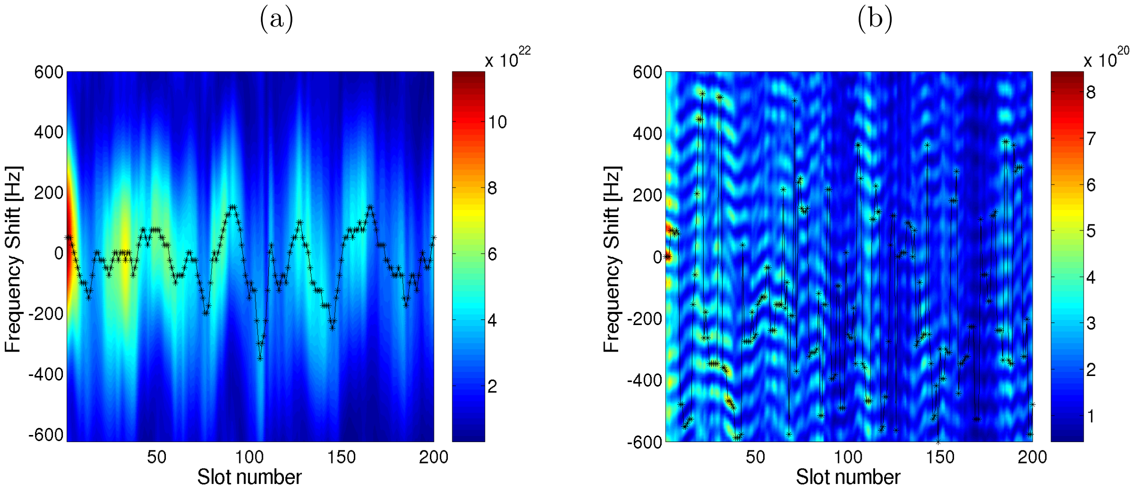

Figure 6.5: Passive time-reversal output $\mathbf{z}_l(t)$ mean power as a function of time/slot-number and applied frequency shift, for the first data packet. The $\mathbf{z}_l(t)$ mean power is computed in slots of 0.25s for a 16-hydrophone array and time-window covering the first arriving paths (a), and for a 6-hydrophone array and time window covering all paths and compensation applied only to later paths (b). The solid line connects the surface maxima ('*') for each time/slot number.

to organize the equalized data before estimating the transmitted data sequence. For "plain pTR" all time slots are assumed to have a null frequency shift, while for "FSpTR" the slots with maximum power represented in Figure 6.5 by '*' are considered. However, Figure 6.5(b) shows an additional phenomenon that consists on the spread of each maximum over a number of local maxima on the frequency axis for each time/slot number. This is clearly due to the aliasing referred above. A third processor, termed "FSpTR+", is proposed for coherently exploiting all possible local maxima by adding them together into the final result. Due to its nature "FSpTR+" should only be applied in the presence of spatial aliasing.

MSE results calculated using the demodulated sequence before slicing, $z(n, n_s)$, and the transmitted data sequence, $a(n)$, are shown in Table 6.1(Case I) for the 16-hydrophone array with a time-window that covers 4 symbols, in Table 6.1(Case II) considering a 6-hydrophone array with a time-window that covers only the first 4 symbols such that only the pTR output SNR is optimized and in Table 6.1(Case III) considering a 6-hydrophone array with the time window covering 28 symbols but with the frequency shift being applied only to the latter paths between 18 and 28 symbols. The pTR output mean power, for the first data packet of Table 6.1(Case I) and (Case III) is shown in Figures 6.5(a) and (b), respectively. In Table 6.1(Case I) and (Case II) the modal aliasing is not visible, since the time-window only captures the first arriving paths that correspond to low order modes, and only the plain pTR and FSpTR equalizers are considered. In Table 6.1(Case III) the FSpTR+ equalizer is also used, since the frequency shift compensation mechanism is applied to high order modes which are not correctly sampled by the 4 m - hydrophone spaced array.

Table 6.1: MSE table for: the 16-hydrophone array with the short time-window capture of the channel IRs first arrivals and full frequency shift compensation (Case I); the 6-hydrophone array with the short time-window capture of the channel IRs first arrivals and full frequency shift compensation (Case II); the 6-hydrophone array with full window capture of the channel IRs arrivals and the frequency shift compensation applied only to later arrivals (Case III).

	Case I		Case II		Case III		
	plain pTR	FSpTR	plain pTR	FSpTR	plain pTR	FSpTR	FSpTR+
data packet 1	-7.19dB	-7.32dB	-3.31dB	-3.56dB	0.37dB	-2.52dB	-4.16dB
data packet 2	-6.83dB	-6.50dB	-3.05dB	-1.18dB	0.30dB	-1.64dB	-3.46dB
data packet 3	-8.45dB	-8.24dB	-1.59dB	-1.82dB	-0.03dB	-3.04dB	-4.00dB
data packet 4	-10.04dB	-9.08dB	-4.04dB	-4.08dB	-1.28dB	-2.46dB	-4.85dB
mean	-8.12dB	-7.85dB	-2.99dB	-2.66dB	-0.16dB	-2.41dB	-4.11dB

Results in Table 6.1(Case I) show that there is no advantage in using FSpTR (with a mean MSE of -7.85 dB) over plain pTR (with a mean MSE of -8.12 dB), which is possibly due to the existence of different mode groups (that require independent compensation) in the time-window selection. Those different mode groups can be seen in the arrival pattern of Figure 6.3 for the first arriving paths, and manifest their existence in Figure 6.4(a) by the slope in the rising edge of the $\Phi(\tau)$ and $ISI^{-1}(\tau)$ curves. When comparing the plain pTR with the FSpTR performance in Table 6.1(Case II), a similar behavior to that of Table 6.1(Case I) is observed and similar comments apply. Comparing Table 6.1(Case I) for 16 hydrophones with Table 6.1(Case II) for 6 hydrophones with a similar time-window, the superior performance of the large array over the short one becomes clear. That is related with the TR basic assumption that the array should be densely populated over the whole water column [34], and also to the fact that in the former case there is lower multipath and the time-window is optimized for pTR output SNR and ISI, while in the latter there is a strong multipath and the time-window is only optimized for output SNR.

When compared with Table 6.1(Case III) for the plain pTR, the results of Table 6.1(Case II) reveal that the latter, when only the pTR output SNR is optimized by the time window, is clearly better than the former when the time-window tries to simultaneously optimize the pTR output SNR and the ISI. That is due to the uncompensated mismatch that affects the later paths and reveals that it is better not to include all significant paths than to leave them uncompensated. In Table 6.1(Case III) the FSpTR partially compensates the later arrivals but due to modal aliasing its performance is still worse than that of plain pTR in Table 6.1(Case II). On the other hand, in Table 6.1(Case III) the performance of FSpTR+, which coherently adds aliasing components, achieves the best performance of all 6-hydrophone cases, revealing its capacity to compensate for channel mismatch with an array that poorly samples higher order modes and does not span the entire water column.

The real data performance of the communications system using plain pTR, FSpTR and

FSpTR+ are compared with a Fractionally-Spaced Equalizer (FSE) [41] updated by the RLS algorithm. Doppler compensation/tracking is performed by the FSE itself (tracking sliding IR taps over time) and an external PLL (tracking the rotating constellation). When applied to real data special care has been taken with the selection of the number of coefficients on the FSE to ensure that it does not diverge due to an excessive number of taps or due to uncompensated Doppler. In fact the FSE spans 12 symbols in the 6-hydrophone and 7 symbols in the 16-hydrophone array. If those settings are swapped the FSE will diverge in both cases: in the 6-hydrophone array case due to uncompensated Doppler and in the 16-hydrophone array case due to an excessive number of coefficients. Nevertheless, it is interesting to observe that for the first data packet with a Doppler compression of 18 symbols the FSE remains effective even with a much smaller number of coefficients. Apparently, the FSE dynamically changes the combination of multipath replicas that it uses to generate symbol estimates as they slide through its analysis window in the course of a 50 s packet due to Doppler compression/expansion of waveforms.

Table 6.2 shows the MSE results for the FSE when using 16 and 6 hydrophone arrays. The best performance is achieved in the 16-hydrophone case with -21.45dB, although there is an unexplained performance degradation in the second and third data packets. With the 6-hydrophone array the FSE's mean MSE performance is -12.9 dB, which is clearly better than the mean value of -4.11dB achieved by FSpTR+ with 6 hydrophones and a time window that covers 28 symbols. Plain pTR and FSpTR with 16 hydrophones present mean MSEs of -8.12 and -7.85 dB, respectively, which approach the value of -12.9 dB attained by the FSE with 6 hydrophones and emphasize the pTR requirement for a long and dense array to preserve the near-orthogonality of sampled modes.

Table 6.2: MSE table for the FSE with 16 and 6 hydrophones.

	16 hydrophones	6 hydrophones
data packet 1	-20.54dB	-11.49dB
data packet 2	-14.99dB	-13.87dB
data packet 3	-13.95dB	-13.81dB
data packet 4	-21.45dB	-12.58dB
mean	-17.73dB	-12.93dB

6.6 Conclusions and Future work

Experimental results were given for time-reversed demodulation of 12.5 kHz, 2000 bits per second, binary PSK data collected during the RADAR'07 experiment. Three receiving pTR-based architectures were compared: plain pTR, FSpTR and FSpTR+ environmental equalizers. The plain pTR demodulator explores the stability of the channel IRs estimate that is only attained when only the first arriving paths of the channel IRs estimate (generated by the lower order modes) are considered by the pTR processor. Based on the waveguide invariants of the underwater layered channel the FSpTR and the FSpTR+

demodulators attempt to equalize the geometric channel variability with a frequency shift of the channel IRs estimate. The former is more appropriate for low frequency applications where mode sampling aliasing is less severe or can be controlled [47], while the latter takes advantage of the high order modes aliasing to improve its performance. Results with 50 s data packets show that an effective compensation of the channel variability can be attained, with mean MSE results of -4.1 dB with 6 hydrophones and -8.12 dB with 16 hydrophones.

The multipath spread of the channel IRs estimate considered by the pTR processor should be optimized before the arrival of the data. The probe timing optimization can be performed with a time-window that when it is too large can introduce undesired noise in the pTR processor and when it is too small can fail to include all significant multipath. Two criteria whose metric can be computed with the IRs estimate were considered: pTR output SNR optimization and pTR residual ISI optimization. The two criteria may provide different time-window results and the automatic joint-operation of those two metrics is required for a future unsupervised operation of the presented environmental equalizers.

Despite the fact that underwater coherent communication systems based on black-box equalizers [31] usually perform better than pTR-based ones [20], the latter are attractive as the ocean itself supplies the information that is needed for deconvolution. Moreover, their ability to self-adapt to the environment results in a potentially more robust system, which is in line with current efforts to incorporate environmental information into black-box equalizers [40]. The proposed environmental equalizer, as other pTR equalizers [14, 54, 20], tries to overcome the loss of performance of pTR-based systems due to environmental mismatch by adding short-term adaptability while maintaining the long-term principle of time reversal. The environmental equalizers presented here track a single parameter — a frequency shift — and provide a robust and low-complexity viable alternative to equalizers. Since the frequency shift depends on the actual environment/geometric conditions, future work will address the possibility of extracting geometric information from the adaptive frequency shift estimate.

The environmental equalizer presented in this work finds application in coherent communications in the presence of geometric mismatch, as is the case in underwater communications between underwater autonomous vehicles and/or drifting or moving receivers. Its validity is limited to layered media where waveguide invariants apply, which is the case of acoustic underwater channels and electromagnetic ionospheric channels [6].

Acknowledgments

This work was supported by Fundação para a Ciência e a Tecnologia under programs POCI, POCTI and POSI. The authors would like to thank CINTAL for the organization of RADAR'07 sea trial and NRP D. Carlos I master and crew.

Chapter 7

Conclusion

This work addresses several issues related to the implementation of an environmental-based equalizer in the specific context of underwater coherent communications.

Passive Time Reversal (pTR) is one of the variants of time reversal applicable to digital underwater communications. In pTR a probe-signal is transmitted ahead of the data-signal in order to estimate the channel impulse response for later use as a replica signal in a time reversal mirror fashion. In practice the received probe-signal is captured in a time-window and, after correlation with the transmitted probe-signal, gives a noisy estimate of the channel impulse response. Therefore, the output signal to noise ratio and the detection rate of passive time reversal will strongly depend of the starting time and on the duration of such time-window, typically these time-window should depend on the travel time and the time spread of the acoustic channel.

The influence of the time-window length in the pTR communication system is two fold: it affects the residual Inter-Symbolic Interference (ISI) and the output Signal to Noise Ratio (SNR). With a densely populated Vertical Line Array (VLA) covering a significant portion of the propagation channel, even for a short time-window, it was shown that the residual ISI tends to zero by means of the modes orthogonality property. With a realistic, sparse and limited aperture, VLA the residual ISI decreases as the time-window length increases as more paths are included in the pTR processor. Different window settings result from optimization of the pTR output SNR and the pTR residual ISI. It was shown that the output SNR criterion should be used for low input SNR, and the residual ISI criterion should be used for high input SNR. Time window optimization was made possible considering the well known ISI metric and after the derivation of a closed form expression for the pTR output SNR. In both cases the optimum time window can be accurately estimated before the data arrival using the channel IRs estimate obtained with the probe-signal. For the pTR output SNR criterion it corresponds to the time-window that gives the higher power of the overall pTR impulse response.

In most underwater acoustic experiments acoustic sources and hydrophone arrays are moored so as to provide a geometry as controllable as possible. A more operational scenario is to use moving sources and drifting acoustic receivers in which case the data exhibits continuous phase and amplitude changes due to depth and range shifts. This may be problematic when the processing of the collected acoustic data requires the use of correlation between successive received signals, e.g., in pTR where a probe-signal is sent ahead of the data-signal for post crosscorrelation. An identical problem arises when the source is placed in a continuously moving and unstable autonomous underwater vehicle. Up to now, only the range shift is usually compensated using data processing techniques, by applying an appropriate frequency shift to the received acoustic field based on the frequency/range plane invariant of the waveguide β.

In the present work a waveguide-invariant-based approach has been developed for pTR geometric mismatch compensation when the pTR operates with two subsequent IRs estimates. It was found that the waveguide invariant β can be used to approximate the horizontal wavenumber using the horizontal group slowness and in that way compensate for the source-array range mismatch. The waveguide invariant in the frequency/depth plane, ζ, shows its ability to approximate the vertical wavenumber using the horizontal group slowness and its application to the compensation of the source and array depths mismatch was addressed. Since β and ζ are invariants in the frequency/range plane and frequency/depth plane respectively it was found that the geometric mismatch compensation operates by applying a frequency shift to the former IRs estimate to compensate for the geometric mismatch between the former and latter IRs estimates. The appropriate frequency shift can be computed in a closed form using the invariants and the geometric mismatch.

When communications are required between a moving source and a moving receiver the passive time-reversal allows for the implementation of a communications system that loses performance when in presence of geometric mismatch between the probe-signal and the actual data symbols transmission. Using the pTR geometric mismatch compensation and the pTR optimization for coherent communications an environmental-based equalizer was developed. It behaves as a Matched-Filter Demodulator (MFD) in a matched-field processing fashion, where the synthetic acoustic field to be matched with the real acoustic field is given by a previous probe-signal estimate of the acoustic field and a waveguide invariant based model that uses the geometric properties of the environment to track the actual acoustic field. It results in the Frequency Shift passive Time-Reversal (FSpTR) environmental-based equalizer where the optimum frequency shift is that for which the largest pTR output power is obtained. Real data comparison, between plain pTR and the FSpTR communication systems, reveals an effective environmental mismatch compensation.

Two further improvements were made in the basic FSpTR environmental-equalizer that are related with the Doppler compression/expansion and with the use of a sparse array for pTR operation. Since the optimum frequency shift that compensates for the actual geometric mismatch is given by the maximum power of the pTR output, the symbol decision does not have to be fed back to the equalization structure and a simple Doppler compensation method can be adopted. When using a sparse array the poor spatial sampling of high order modes results in mode aliasing. Such mode aliasing is clearly visible in the FSpTR output and can be partially overcome by adding the aliasing replicas coherently.

The main objective of this thesis was to study the feasibility of using environmental-based equalizers to perform underwater coherent communications. Such an objective was attained since when compared with the plain pTR communications system the FSpTR equalizer shows its capability to compensate for the geometric mismatch between the probe and the data transmissions, however when compared with the Fractionally-Spaced Equalizer (FSE) it was found that the FSE outperforms the environmental equalizer. Even so the environmental-based equalizers are attractive because of their ability to self-adapt to the environment that potentially results in a more robust system.

7.1 Open issues

In order to operationalize the FSpTR environmental-equalizer three requirements were identified: first it must be unsupervised and simple enough to be implemented in an autonomous platform such as the AOB; second is that it must strongly reduce the number of probe signals to be sent in the pTR digital communications process in order to increase the effective data rate transfer between the source and the receiver; finally, the third requirement is that it must allow for geometric inversion, i.e., for source-array range and source and array depths estimate.

In order to have an unsupervised operation the FSpTR equalizer requires a probe timing optimization before the data arrival. Based on the channel IRs estimate two criteria with well defined metrics can be computed: for pTR output SNR optimization and for ISI optimization. Future work should address the automatic joint-operation of those two metrics in order to attain a global optimization.

The actual MFD implementation of the FSpTR equalizer requires a set of matched-filters with a dimension equal to the “number of hydrophones times the number of frequency shifts times the optimum window length”. The matched-filters output are then summed for each frequency shift in a pTR fashion, and followed by a maximum power selector. This results in a calculation load that is too large to be implemented in a low power consumption autonomous platform. However the number of matched-filters can be strongly reduced if a dynamic tracking of the frequency shift is adopted (e.g. by using a sub-set of frequency shifts in the vicinity of the previous identified optimal frequency shift).

Due to its environmental based nature, FSpTR more than being able to perform reliable underwater communications can be used to track the geometric variations during data transmission. This has not been fully explored with real data during the present work, mainly due to the absence of sufficiently high sample rate of source depth and array depth information during the experiments. Future experiments should be prepared in order to explore such possibility.

Solving an inverse problem requires a physical model, i.e., a mapping that relates a number of features that are expected to be observed given the model parameters. In its most basic form, and in the absence of model mismatch, this mapping would allow to predict the error-free values of the observable parameters. Such a physical model for the environment geometric parameters has been derived in the present thesis. A more elaborate setting based on the conditional probability density for the observables given the model parameters, accounting for inherent uncertainties of the theory due to imperfect parametrization (e.g. the environmental non-geometric properties mismatch) or to some fundamental lack of knowledge, should be addressed in future work. Such probability density and its estimation will allow for the development of a sequential algorithm that predicts the frequency shift compensation, instead of the actual FSpTR exhaustive search MFD implementation.

Appendix A

A.1 Deterministic and stochastic filters autocorrelation

This appendix recalls the autocorrelation of the response Y, of a finite impulse response filter H, to an input signal X when the input and filter autocorrelations are known and when: case 1 - H is stochastic and X is stochastic ; case 2 - H is deterministic and X is stochastic; case 3 - H is stochastic and X is deterministic. The filter output is given by the convolution

$$Y(t) \;=\; \int_{-\infty}^{+\infty} H(t-u)X(u)du, \tag{A1}$$

and the filter output autocorrelation

$$\begin{aligned} R_Y(t+t',t) &= E\{Y(t+t')Y(t)\} \\ &= \int\!\!\int E\{H(t+t'-u)H(t-v)\}E\{X(u)X(v)\}dudv \\ &= \int\!\!\int E\{X(t+t'-u)X(t-v)\}E\{H(u)H(v)\}dudv, \end{aligned} \tag{A2}$$

considering that X and H are independent, (A2) is valid for H and X deterministic or stochastic. In the following the index t_0, τ will be used to represent a signal time limited by the unit-gate function

$$\Pi_\tau(t-t_0) = \Pi_{t_0,\tau}(t) = \begin{cases} 1 & t_0 \le t < t_0+\tau \\ 0 & \text{otherwise} \end{cases}. \tag{A3}$$

Capital letters designate stochastic quantities and lower case designate deterministic quantities, thus R will represent the stochastic autocorrelation and r the deterministic autocorrelation.

In case 1 H_τ is a stochastic time limited signal (where t_0 has been dropped since in a stochastic signal the instant when the unit-gate function is applied is irrelevant), and X an unlimited WSS stochastic signal, the output filter autocorrelation as given in [15], is equal to

$$R_Y(t') = E\{r_{H,\tau}(t')\} * R_X(t'), \tag{A4}$$

where

$$E\{r_{H,\tau}(t')\} = E\left\{\int H_\tau(t+t')H_\tau(t)dt\right\}. \tag{A5}$$

Considering that the time limited stochastic process H_τ is the result of the product of a WSS process H with a rectangular window (A3)

$$E\{r_{H,\tau}(t')\} = R_H(t')\tau\Delta_\tau(t'), \tag{A6}$$

where $\tau\Delta_\tau(t')$ is the triangular function that results from the deterministic autocorrelation of the rectangular function (A3). When X and H are both white gaussian processes with autocorrelations $\sigma_X^2\delta(t')$ and $\sigma_H^2\delta(t')$ respectively the output autocorrelation will be given by

$$R_Y(t') = \sigma_X^2\sigma_H^2\tau r_\delta(t'), \tag{A7}$$

and Y is a white stochastic signal, since $r_\delta(t') = \delta(t') * \delta(t')$ is the autocorrelation of the dirac impulse.

Case 2 is a standard case where $h_{t_0,\tau}$ is a deterministic signal that results from the product of an infinite signal with time window (A3) applied in the arbitrary instant t_0, and X is an infinite stochastic signal. The output filter autocorrelation is given by

$$R_Y(t') = r_{h,t_0,\tau}(t') * R_X(t'), \tag{A8}$$

where

$$r_{h,t_0,\tau}(t') = \int h_{t_0,\tau}(t+t')h_{t_0,\tau(t)}dt \tag{A9}$$

$$= \begin{cases} \int_{t_0}^{t_0+\tau-t'} h(w+t')h(w)dw & \tau \geq t' > 0 \\ \int_{t_0}^{t_0+\tau} h(w+t')h(w)dw & t' = 0 \\ \int_{t_0-t'}^{t_0+\tau} h(w+t')h(w)dw & 0 > t' \geq -\tau \\ 0, & \text{otherwise} \end{cases} \tag{A10}$$

When $h_{t_0,\tau}$ is a deterministic signal and X is an infinite white gaussian process

$$R_Y(t') = \sigma_X^2 r_{h,t_0,\tau}(t'). \tag{A11}$$

and the filter output Y is a WSS stochastic signal.

In case 3 x is deterministic, and H_τ a time limited stochastic signal that, as in case 1, results from the product of a WSS signal with the rectangular window (A3), since the signal is WSS the moment when the window is applied is not important and t_0 can be dropped. In that case, since

$$E\{H_\tau(u)H_\tau(v)\} = R_H(u-v)[\Pi_\tau(u)\Pi_\tau(v)], \tag{A12}$$

equation (A2) becomes

$$R_Y(t+t',t) = \int\int [x(t+t'-u)x(t-v)][\Pi_\tau(u)\Pi_\tau(v)]R_H(u-v)dudv, \tag{A13}$$

if we change the independent variables

$$\begin{cases} w = t - v \\ t - u = w - z \end{cases}, \tag{A14}$$

the output autocorrelation becomes

$$R_Y(t+t',t) = \int R_H(z) A_\tau(t',t,z)dz, \tag{A15}$$

with

$$A_\tau(t',t,z) = \int [x(w-z+t')\Pi_\tau(t-w+z)][x(w)\Pi_\tau(t-w)]dw. \tag{A16}$$

Equation (A16) can be rewritten in four intervals defined by variable z

$$A_\tau(t',t,z) = \begin{cases} \int_{t-\tau}^{t+z} x(w-z+t')x(w)dw & -\tau \le z < 0 \\ \int_{t-\tau}^{t} x(w-z+t')x(w)dw & z = 0 \\ \int_{t-\tau+z}^{t} x(w-z+t')x(w)dw & 0 < z \le \tau \\ 0, & \text{otherwise} \end{cases}. \tag{A17}$$

When x is deterministic and H is a time limited white gaussian process with autocorrelation given by $\sigma_H^2 \delta(t')$ the auto-correlation of Y becomes

$$R_Y(t+t',t) = \sigma_H^2 A_\tau(t',t,z=0). \tag{A18}$$

which is seen to be non stationary.

A.2 Time windowed passive Time Reversal

Without mismatch pTR operation consists on the sum over all hydrophones of the deterministic correlation between two subsequent channel IRs (with only a time delay between them denoted by $'$). In pass-band the pTR operator is given by

$$p_{TR}(t) = \sum_{i=1}^{I} h_i(t) * h_i'(-t), \tag{A19}$$

where $p_{TR}(t)$ can be seen as the IR of the pTR operator.

In the frequency domain (where pTR is usually termed passive phase conjugation) for a perfect waveguide the same is attained by

$$\begin{aligned} P_{PC}(\omega) &= \sum_{i=1}^{I} H_i(\omega) H_i^*(\omega) \\ &= a_i^2 \sum_{n=1}^{M}\sum_{m=1}^{M} \Psi_n(z_0)\Psi_m(z_0) \frac{e^{j(\xi_n - \xi_m^*)R}}{\sqrt{\xi_n \xi_m^*}} \sum_i \Psi_n(z_i)\Psi_m(z_i) \end{aligned} \tag{A20}$$

using the modes orthogonal property (4.30) it results

$$\begin{aligned} P_{PC}(\omega) &= a_i^2 \sum_{m=1}^{M} |\Psi_m(z_0)|^2 \frac{e^{j(\xi_m - \xi_m^*)R}}{\sqrt{\xi_m \xi_m^*}} \\ &= a_i^2 \sum_{m=1}^{M} |\Psi_m(z_0)|^2 \frac{e^{-2Im(\xi_m)R}}{|\xi_m|} \\ &\approx C \end{aligned} \tag{A21}$$

where all terms have obvious notations in the normal mode formulation of the acoustic field. The modes orthogonality property was used, in a similar manner to [44] for pTR and to [34] for aTR. In (A21) the $Im(\xi_m)$ exponential is due to the loss mechanisms [27], and according to [44] acts to attenuate higher order modes. It results that $P_{PC}(\omega) \approx C$ is approximately constant over the narrowband frequencies of interest and in the time domain $p_{TR}(t)$ will be a *sinc* function convolved with a weighted dirac proportional to C.

The time windowing operation consists in multiplying the IRs $h_i(t)$ by a unit-gate function $\Pi_{t0,\tau}(t)$, given in (A3), with starting time t_0 and length τ. In an isovelocity perfect waveguide the travel time of the arriving paths is ruled by the modes group velocity that converges from zero, at the mode cutoff frequency, to the water column sound velocity as a monotonic ascending function of the frequency [[58] pp. 40]. In a real waveguide the modes group velocity oscillate with the frequency up to the Airy phase and after that behave as perfect waveguide modes [[58] pp. 128]. In the narrowband case at high frequencies the grate majority of modes has already reached the Airy phase and that makes the usual assumption that at high frequencies the underwater channel is more similar to the perfect waveguide than at low frequencies. After the Airy phase for a given frequency the group velocities are well ordered in an descending manner and that makes lower modes to present always higher group velocities [[58] pp. 40 and 128]. It results that high order modes become responsible for later arrivals and in such conditions the time window operation behaves as a mode filter. When applied to communications in a real waveguide only the IRs in the bandwidth of the signal are of interest and the previous heuristic findings are applied at the cost of ignoring the modes whose influence spreads over several arriving paths because they have not reached the airy phase.

Considering the ray mode approximation [58, 5] where at a given frequency, higher order modes are associated with later rays, the effect of a time window that eliminates later rays can be reversed to mode analysis where it will filter out higher order modes. In the following it will be considered that $Me(t_0, \tau)$ is the set of modes that have not been filtered by the time window

The influence of the time windowing operation over the pTR processor can now be considered under two aspects: when both channel IRs are time limited or when only one of them is time limited. In the first case the resulting p_{TR} and P_{PC} will be given by

$$p_{TR,2tw}(t) = \sum_{i=1}^{I} h_{i,t_0,\tau}(t) * h'_{i,t_0,\tau}(-t), \tag{A22}$$

and

$$\begin{aligned}
P_{PC,2tw}(\omega) &= \sum_{i=1}^{I} H_{i,t_0,\tau}(\omega)H^*_{i,t_0,\tau}(\omega) \\
&= a_i^2 \sum_{n=1}^{Me(t_0,\tau)} \sum_{m=1}^{Me(t_0,\tau)} \Psi_n(z_0)\Psi_m(z_0)\frac{e^{j(\xi_n-\xi_m^*)R}}{\sqrt{\xi_n\xi_m^*}} \sum_i \Psi_n(z_i)\Psi_m(z_i) \\
&= a_i^2 \sum_{m=1}^{Me(t_0,\tau)} |\Psi_m(z_0)|^2 \frac{e^{-2Im(\xi_m)R}}{|\xi_m|} \\
&\approx C' \qquad\qquad \text{(A23)}
\end{aligned}$$

respectively.

In the second case the resulting p_{TR} and P_{PC} will be given by

$$p_{TR,1tw}(t) = \sum_{i=1}^{I} h_i(t) * h'_{i,t_0,\tau}(-t), \qquad \text{(A24)}$$

and

$$\begin{aligned}
&P_{PC,1tw}(\omega) = \\
&= \sum_{i=1}^{I} H_i(\omega)H^*_{i,t_0,\tau}(\omega) \\
&= a_i^2 \sum_{n=1}^{M} \sum_{m=1}^{Me(t_0,\tau)} \Psi_n(z_0)\Psi_m(z_0)\frac{e^{j(\xi_n-\xi_m^*)R}}{\sqrt{\xi_n\xi_m^*}} \sum_i \Psi_n(z_i)\Psi_m(z_i) \\
&= C' + a_i^2 \sum_{n=Me(t_0,\tau)}^{M} \sum_{m=1}^{Me(t_0,\tau)} \Psi_n(z_0)\Psi_m(z_0)\frac{e^{j(\xi_n-\xi_m^*)R}}{\sqrt{\xi_n\xi_m^*}} \sum_i \Psi_n(z_i)\Psi_m(z_i) \\
&\approx C'' \qquad\qquad \text{(A25)}
\end{aligned}$$

respectively. As the time window increases $Me(t_0, \tau)$ converges to $M(\omega)$ and, C' and C'' converge to C.

When the TR associated assumptions are accomplished the two summations of the right-hand second term of (A25) become null due to the modes orthogonality property and $C' \equiv C''$. Since C' and C'' given by (A23) and (A25) respectively are week functions of frequency [34], for narrowband IRs $h_i(t)$, the resulting $p_{TR,\cdots}(t)$ can be approximated by a *sinc* type function with an amplitude given by the $C^{\cdots}$ coefficients. It results that the mode-reduction/time-windowing does not affect $p_{TR,\cdots}(t)$ in shape but only in amplitude.

When the TR assumptions are not fully accomplished, that is, the array do not span the entire water column and/or it is not sufficiently populated, it results that the $p_{TR}(t)$ shape becomes a distorted *sinc* and such distortion will be responsible for residual ISI in the pTR digital communications system. In such conditions $C' \neq C''$ and the residual ISI becomes dependent on the considered number of modes, $M(t_0, \tau)$, and thus on the time-window length.

Appendix B

B.1 Linear approximation of monotonic functions

Sections 4.3.3 and 4.3.4 require the computation of horizontal and vertical wavenumbers using the horizontal wavenumber inverse. Both problems can be seen as a generic linear approximation of one monotonic function, Φ_m, using another monotonic function, Π_m.

Considering the linear approximation of Φ_m using Π_m with $m = 1...M$ in the least-squares sense, it results

$$\Phi_m \approx \Phi'_m = -\varepsilon \Pi_m + \rho, \tag{B1}$$

where

$$\varepsilon = -\frac{\overline{\Phi_m \Pi_m} - \overline{\Phi_m}\;\overline{\Pi_m}}{\overline{\Pi_m^2} - \overline{\Pi_m}^2}, \tag{B2}$$

and

$$\rho = \overline{\Phi_m} + \varepsilon \overline{\Pi_m}, \tag{B3}$$

where the bar denotes the mean over m. If both functions Φ_m and Π_m are linear with m, the approximation becomes exact. When one or both functions are non-linear with different curvatures the approximation will have an error that can be reduced if instead of approximating Φ_m for $m = 1...M$ only a subset of m is considered. For the approximation of horizontal and vertical wavenumbers an effective number of modes M_e smaller than the total number of modes M will be considered. That will result in a linear approximation given by the parameters ε_e and ρ_e.

A different approximation to Φ_m using Π_m is given by computing

$$\Phi_m \approx \Phi'_m = -\varepsilon_{\mu,\nu} \Pi_m + \rho_{\mu,\nu}, \tag{B4}$$

with

$$\varepsilon_{\mu,\nu} = -\frac{\Phi_\mu - \Phi_\nu}{\Pi_\mu - \Pi_\nu}, \tag{B5}$$

and

$$\rho_{\mu,\nu} = \Phi_\nu + \varepsilon_{\mu,\nu} \Pi_\nu, \tag{B6}$$

where $m = \nu$ and $m = \mu$ are the abscissa for $\Phi_\nu = \Phi'_\nu$ and $\Phi_\mu = \Phi'_\mu$ respectively. It results that $\Phi'_m \approx \Phi_m$ with different degrees of accuracy given by the selected ν and μ.

Since (B4) represents a set of linear approximations with the only constraint that the two functions Φ_m and Φ'_m meet at two different points $m = \nu$ and $m = \mu$, it is expected that the linear least-squares approximation (B1) will coincide or be close to one of them, i.e, for each M_e there is a (μ, ν) such that $\varepsilon_e \approx \varepsilon_{\mu,\nu}$ and $\rho_e \approx \rho_{\mu,\nu}$.

B.2 Mode orthogonality in the presence of an array depth mismatch

When there is no array depth mismatch the mode orthogonality condition is given by

$$\Psi(m,n) = \int_0^D \frac{Z_m(z)Z_n(z)}{\rho(z)} dz = \delta_{m,n}, \tag{B7}$$

where D is the waveguide water column depth, $\rho(z)$ is the water density, considered to be constant and equal to 1, and z is the depth. The mode shape $Z_m(z)$ in a perfect wave guide is given by

$$Z_m(z) = \sqrt{\frac{D}{2}} \sin(\gamma_m z), \tag{B8}$$

with

$$\gamma_m = \left(m - \frac{1}{2}\right) \frac{\pi}{D}. \tag{B9}$$

Using (B8) in (B7) it results

$$\Psi(m,n) = \frac{2}{D} \int_0^D \sin(\gamma_m z) \sin(\gamma_n z) dz, \tag{B10}$$

and (B7) follows readily.

If now in (B10) there is a depth shift between the mode functions Z_m and Z_n, it results

$$\Psi(m,n,\Delta z) = \frac{2}{D} \int_0^D \sin(\gamma_m z - \gamma_m \Delta z) \sin(\gamma_n z) dz. \tag{B11}$$

Using the Euler formula, and ignoring the backward propagating modes (with m and n negative integers), (B11) becomes

$$\Psi(m,n,\Delta z) \approx \frac{-2}{4D} \left[\int_0^D \Lambda'_{m,n} dz + \int_0^D \Omega'_{m,n} dz \right], \tag{B12}$$

where

$$\begin{aligned} \Lambda'_{m,n} &= \Lambda_{m,n} \exp(-j\pi(m-1/2)\Delta z/D), \\ \Omega'_{m,n} &= \Omega_{m,n} \exp(j\pi(m-1/2)\Delta z/D), \end{aligned} \tag{B13}$$

and

$$\begin{aligned} \Lambda_{m,n} &= -\exp(j\pi(m-n)z/D), \\ \Omega_{m,n} &= -\exp(-j\pi(m-n)z/D). \end{aligned} \tag{B14}$$

Defining

$$\begin{aligned} \Psi_\Lambda(m,n) &= \int_0^D \Lambda_{m,n} dz, \\ \Psi_\Omega(m,n) &= \int_0^D \Omega_{m,n} dz, \end{aligned} \tag{B15}$$

using (B9) and the fact that the exponential terms in (B13) do not depend on z, (B12) becomes

$$\Psi(m,n,\Delta z) = \frac{-2}{4D}\left[\exp(-j\gamma_m \Delta z)\Psi_\Lambda(m,n) + \exp(j\gamma_m \Delta z)\Psi_\Omega(m,n)\right]. \tag{B16}$$

When m and n are both either odd or even, this yields

$$\Psi(m,n,\Delta z) = \frac{-2}{4D}\left[2D\delta_{m,n}\cos(-\gamma_m \Delta z)\right], \tag{B17}$$

otherwise,

$$\Psi(m,n,\Delta z) = \frac{-2}{4D}\left[\frac{-2D}{\pi}(\delta_{m,n+1} - \delta_{m,n-1})\sin(-\gamma_m \Delta z)\right]. \tag{B18}$$

From (B17) and (B18) it is obvious that the mode orthogonality has been lost. It can be partially recovered by multiplying (B16) by $2\cos(\gamma_m \Delta z)$, resulting, for m and n with the same parity,

$$\Psi(m,n,\Delta z) 2\cos(\gamma_m \Delta z) = \frac{-2}{4D}\left[2D\delta_{m,n}(1 + \cos(-2\gamma_m \Delta z))\right], \tag{B19}$$

and, for m and n with different parity,

$$\Psi(m,n,\Delta z) 2\cos(\gamma_m \Delta z) = \frac{-2}{4D}\left[\frac{-2D}{\pi}(\delta_{m,n+1} - \delta_{m,n-1})\sin(-2\gamma_m \Delta z)\right]. \tag{B20}$$

Comparing (B17) with (B19) it is clear that there is a gain in amplitude for $m = n$, and comparing (B18) with (B20) the amplitude does not change, thus enabling the partial recovery of the modes orthogonality

$$\Psi(m,n,\Delta z)\cos(\gamma_m \Delta z) \approx \Psi(m,n)\frac{(1 + \cos(-2\gamma_m \Delta z))}{2}. \tag{B21}$$

A similar result can be obtained if $\exp(\pm j\gamma_m \Delta z)$ is used instead of $2\cos(\gamma_m \Delta z)$. In that case a linear phase with Δz will appear for $m = n$, and (B21) can be generalized to

$$\Psi(m,n,\Delta z) e^{\pm j\gamma_m \Delta z} \approx \Psi(m,n)\frac{W(m,\Delta z)}{2}, \tag{B22}$$

where $|W(m,\Delta z)|$ is equal to 2 when $\Delta z = 0$ and oscillates around 1 when $\Delta z \neq 0$.

Bibliography

[1] S. J. A. Caiti, J-P. Hermand and M. Porter, editors. *Experimental Acoustic Inversion Methods for Exploration of the Shallow Water Environment.* Kluwer Academic Publishers, 2000.

[2] A. Baggeroer, W. Kuperman, and P. M. P. An overview of matched field methods in ocean acoustics. *IEEE Journal of Oceanic Engineering*, 18(4):307–338, October 1993.

[3] P. A. Baxley, H. Bucker, V. K. MacDonald, J. A. Rice, and M. B. Porter. Shallow-water acoustic communications channel modeling using three-dimensional gaussian beams. *SPAWAR Bienal Review*, (1):251–261, 2001.

[4] J. Candy, A. Meyer, A. Poggio, and B. Guidry. Time-reversal processing for an acoustic communications experiment in a highly reverberant environment. *J. Acoust. Soc. America*, 115(4):1621–1631, 2004.

[5] D. Chapman and D. D. Ellis. The group velocity of normal modes. *J. Acoust. Soc. America*, 3(74):973–979, September 1983.

[6] S. Chuprov. Interference structure of a sound field in a layered ocean. In L. Brekhovskikh and I. Andreevoi, editors, *Ocean Acoustics, Current State*, pages 71–91, Nauka, Moscow, 1982.

[7] R. Dowling. Acoustic pulse compression using passive phase-conjugate processing. *J. Acoust. Soc. America*, 95(3):1450–1458, 1994.

[8] R. Dowling and R. Jackson. Narrow-band performance of phase-conjugate arrays in dynamic random media. *J. Acoust. Soc. Am.*, 91(6):3257–3277, June 1992.

[9] G. D'Spain and W. A. Kuperman. Application of waveguide invariants to analysis of spectrograms from shallow water environments that vary in range and azimuth. *J. Acoust. Soc. America*, 106(5):2454–2468, 1999.

[10] R. P. E. Pouliquen, A.D. Kirwan, editor. *Rapid Environment Assessment*, La Spezia, Italy, 1997. NATO SACLANT Undersea Research Centre.

[11] G. Edelmann, W. Hodgkiss, S. Kim, W. Kuperman, H. Song., and T. Akal. Underwater acoustic communications using time-reversal. In *Proc. of the MTS/IEEE Oceans 2001*, pages 2231–2235, Honolulu, Hawai, USA, 5-8 November 2001.

[12] P. Felisberto, C. Lopes, and S. Jesus. An autonomous system for ocean acoustic tomography. *Sea-Technology*, 45(4):17–23, April 2004.

[13] M. Fink. Time reversal acoustics. *Sci. Amer*, 103(1):25–40, Jan 1998.

[14] J. A. Flynn, J. A. Ritcey, D. Rouseff, and W. L. J. Fox. Multichannel equalization by decision-direct passive phase conjugation: Experimental results. *IEEE J. Oceanic Eng.*, 29:824–836, 2004.

[15] W. Gardner. A new method of channel identification. *IEEE Trans. Communications*, 39:813–817, 1991.

[16] P. Gerstoft and Z. Michalopoulou. Global optimization in matched field inversion. In *Proc. of the Fourth European Conference on Underwater Acoustics (ECUA)*, pages 27–32, Rome, Italy, 1998.

[17] J. Gomes and V. Barroso. A matched field processing approach to underwater acoustic communication. In *Proc. of the MTS/IEEE Oceans 1999*, pages 991–995, Seattle, USA, 1999.

[18] J. Gomes and V. Barroso. Asymmetric underwater acoustic communication using a time-reversal mirror. In *Proc. of the MTS/IEEE Oceans 2000*, Providance, USA, 2000.

[19] J. Gomes, A. Silva, and S. Jesus. Joint passive time reversal and multichannel equalization for underwater communications. In *Proc. of the MTS/IEEE Oceans'06*, Boston, MA, USA, September 2006.

[20] J. Gomes, A. Silva, and S. Jesus. Spatial combining for passive time-reversed communications. accepted *J. Acoust. Soc. America*, March 2007.

[21] G. A. Grachev. Theory of acoustic field invariants in layered waveguide. *Acoust. Phys.*, (39):33–35, 1993.

[22] W. S. Hodgkiss, W. A. Kuperman, and D. E. Ensberg. Channel impulse response fluctuations at 6 khz in shallow water. In J. Pace, editor, *Impact of Littoral Environment Variability on Acoustic Predictions and Sonar Performance*, pages 295–302, Kluwer, September 2002.

[23] P. Hursky, M. Porter, B. Cornuelle, W. Hodgkiss, and W. Kuperman. Adjoint modelling for acoustic inversion. *J. Acoust. Soc. Am.*, 115(2):607–619, February 2004.

[24] P. Hursky, M. Porter, R. Rice, and V. McDonald. Passive phase-conjugate signaling using pulse-position modulation. In *Proc. of the MTS/IEEE Oceans 2001*, pages 2244–2249, Honolulu, Hawai, USA, 5-8 November 2001.

[25] P. Hursky, M. Porter, and M. Siderius. High-frequency (8-16 khz) model-based source localization. *J. Acoust. Soc. Am.*, 115(6):3021–3032, June 2004.

[26] R. Jackson and R. Dowling. Phase conjugation in underwater acoustics. *J. Acoust. Soc. Am.*, 89(1):171–181, January 1991.

[27] F. Jensen, W. Kuperman, M. Porter, and H. Schmidt. *Computational Ocean Acoustics.* AIP Series in Modern Acoustics and Signal Processing, New York, 1994.

[28] S. Jesus and A. Silva. Virtual time reversal in underwater acoustic communications: Results on the intifante'00 sea trial. In *Proc. of Forum Acusticum*, Sevilla, Spain, September 2002.

[29] S. Jesus and A. Silva. Time reversal and spatial diversity: issues in a time varying geometry test. In S. Porter and Kuperman, editors, *Proc. Conf. on High Frequency Ocean Acoustics*, pages 530–538, La Jolla, USA, March 2004.

[30] S. Jesus, C. Soares, A. Silva, J. Hermand, and E. Coelho. Aob-acoustic oceanographic buoy: concept and feasibility. In *Proc. of the UDT'06*, Hamburg, Germany, June 2006.

[31] D. Kilfoyle and A. Baggeroer. The state of the art in underwater acoustic telemetry. *IEEE J. Oceanic Eng.*, 25(1):4–27, 2000.

[32] J. Kim, W. Kuperman, W. S. Hodgkiss, H. Song, G. F. Edelmann, and T. Akal. Robust time reversal focusing in the ocean. *J. Acoust. Soc. America*, 114:145–157, 2003.

[33] J. Kim, H. Song, and W. Kuperman. Adaptive time-reversal mirror. *J. Acoust. Soc. America*, 109:1817–1825, 2001.

[34] W. Kuperman, W. Hodgkiss, H. C. Song, T. Akal, C. Ferla, and D. Jackson. Phase conjugation in the ocean: Experimental demonstration of an acoustic time-reversal mirror. *J. Acoust. Soc. Am.*, 103(1):25–40, January 1998.

[35] W. Kuperman, S. Kim, G. Edelmann, W. Hodgkiss, H. Song, and T. A. T. Group and phase speed analysis for predicting and mitigating the effects of fluctuations. In J. Pace, editor, *Impact of Littoral Environment Variability on Acoustic Predictions and Sonar Performance*, pages 279–286, Kluwer, September 2002.

[36] E. Lee and D. Messerschmitt. *Digital Communication.* Kluwer Academic Publishers, Massachusetts, 1994.

[37] N.Martins, C.Soares, , and S.M.Jesus. Environmental and acoustic assessment: The aob concept. *Journal of Marine Systems*, doi:10.1016/j.jmarsys.2007.02.003 2007.

[38] A. Parvulescu. Matched-signal (mess) processing by the ocean. *J. Acoust. Soc. America*, 98(2):943–960, 1995.

[39] M. Porter, P. Hursky, M. Siderius, V. McDonald, and P. Baxley. High-frequency propagation for acoustic communications. In J. Pace, editor, *Impact of Littoral Environment Variability on Acoustic Predictions and Sonar Performance*, pages 278–294, Kluwer, September 2002.

[40] J. C. Preisig. Performance analysis of adaptive equlization for coheren acoustic communications in the time-varying ocean environment. *J. Acoust. Soc. Am.*, 118(1):263–278, July 2005.

[41] J. Proakis. *Digital Communications.* McGraw-Hill, Massachusetts, 1995.

[42] D. Rouseff. Intersymbol interference in underwater acoustic communications using time-reversal signal processing. *J. Acoust. Soc. America*, 117(2):780–788, 2005.

[43] D. Rouseff, L. Fox, D. Jackson, and D. Jones. Underwater acoustic communications using passive phase conjugation. In *Proc. of the MTS/IEEE Oceans 2001*, pages 2227–2230, Honolulu, Hawai, USA, November 2001.

[44] D. Rouseff, D. Jackson, W. Fox, D. Jones, J. Ritcey, and D. Dowling. Underwater acoustic communications by passive-phase conjugation: Theory and experimental results. *J. Oceanic Engineering*, 26(4):821–831, 2001.

[45] A. Silva and S. Jesus. Underwater communications using virtual time-reversal in a variable geometry channel. In *Proc. MTS/IEEE Oceans'2002*, pages 2416–2421, Biloxi, USA, November, 2002.

[46] A. Silva, S. Jesus, and J. Gomes. Depth and range shift compensation using waveguide invariant properties. In *Proc. of the UAM'07*, Heraklion, Crete, Greece, June 2007.

[47] A. Silva, S. Jesus, and J. Gomes. Environment-based underwater communications. In *Proc. of the OCEANS'07*, Vancouver, Canada, October 2007.

[48] A. Silva, S. Jesus, and J. Gomes. Generalization of waveguide invariants and application to passive time reversal. to be submitted to *Acta Acoustica*, 2008.

[49] A. Silva, S. Jesus, and J. Gomes. Probe timing optimization for time-reversal underwater communications. To be Submitted to *IEEE J. of Oceanic Engineering*, 2008.

[50] A. Silva, S. Jesus, J. Gomes, and V. Barroso. Underwater acoustic communications using a 'virtual' electronic time-reversal mirror approach. In P. Chevret and M.Zakharia, editors, *5th European Conference on Underwater Acoustics*, pages 531–536, Lyon, France, June 2000.

[51] A. Silva, F. Zabel, and C. Martins. Acoustic oceanographic buoy telemetry system. *Sea Technology*, 47(9), September 2006.

[52] C. Soares, S. Jesus, A. Silva, and E. Coelho. Acoustic oceanographic buoy testing during the maritime rapid environmental assessment 2003 sea trial. In *Proc. European Conference on Underwater Acoustics*, Delft, The Netherlands, July 2004.

[53] C. Soares, M. Siderius, and S. Jesus. Source localization in a time-varying ocean waveguide. *J. Acoust. Soc. America*, 112(5):1879–1889, December 2002.

[54] H. Song, W. Hodgkiss, A. Kuperman, M. Stevenson, and T. Akal. Improvement of time-reversal communications using adaptive channel equalizers. *IEEE J. Ocean Eng.*, (31):487–496, 2006.

[55] H. C. Song, W. A. Kuperman, and W. S. Hodgkiss. Time-reversal mirror with variable range focusing. *J. Acoust. Soc. Am.*, 103((6)):3234–3240, June 1998.

[56] M. Stojanovic. Retrofocusing techniques for high rate acoustic communications. *J. Acoust. Soc. America*, 117(3):1173–1185, 2005.

[57] M. Stojanovic, J. Catipovic, and J. Proakis. Adaptive multichannel combining and equalization for underwater acoustic communications. *J. Acoust. Soc. America*, 94(3):1621–1631, 1993.

[58] I. Tolstoy and C. Clay. *Ocean Acoustics: Theory and experiments in underwater sound.* AIP, New York, 1966.

[59] S. Walker, P.Roux, and W. Kuperman. Data-based mode extraction with a partial water column spanning array. *J. Acoust. Soc. America*, 118(3):1518–1525, 2005.

[60] S. Walker, P.Roux, and W. Kuperman. Focal depth shifting of a time reversal mirror in a range-independent waveguide. *J. Acoust. Soc. America*, 118(3):1341–1347, 2005.

[61] K. L. Williams, D. R. Jackson, E. I. Thorsos, D. Tang, and K. B. Briggs. Spatial and temporal variability in bottom roughness: Implications to high frequency subcritical penetrations and backscatter. In J. Pace, editor, *Impact of Littoral Environment Variability on Acoustic Predictions and Sonar Performance*, pages 195–202, Kluwer, September 2002.

[62] T. C. Yang. Differences between passive-phase conjugation and decision-feedback equalizer for underwater acoustic communications. *IEEE Journal of Oceanic Engineering*, 29(2):472–487, April 2004.

Abstract

The present thesis aims at the development of an environmental-based equalizer for shallow water coherent communications. In recent years time-reversal aroused as a viable option for underwater communications since its focusing property allows for a significant signal to noise ratio enhancement and inter-symbolic interference reduction. In order to use time-reversal in an operational modem the main constraints were identified as the performance loss due to the source-vertical-line-array geometric mismatch during the data transmission and the optimization concerning the multipath spread of underwater channel impulse responses in a noisy environment.

For the time-reversal environmental geometric mismatch compensation a physical model based on waveguide invariants of the acoustic channel was developed. It makes use of the frequency/range invariant and of the frequency/depth invariant. With such a physical-model in hand an environmental-based equalizer was developed.

The multipath spread that guarantees the maximum of the signal to noise ratio is given by the time-reversal overall impulse response maximum power that can be computed using channel impulse response estimates. Such optimum signal to noise ratio results in a suboptimum inter-symbolic interference compensation nevertheless with value close to the optimum.

In parallel with the scientific objectives, the development of a surface buoy prototype – the AOB, Acoustic Oceanographic Buoy – was carried out. The AOB is an advanced sonobuoy with a long and dense acoustic/oceanographic vertical-line-array and with additional processing capabilities. The AOB was tested in six sea trials where its telemetry capabilities where successfully proven, and was used to acquire the real data used to test the developed environmental-based equalizer.

The time-reversal optimization concerning the multipath spread was validated with real data at 400 and 2000 bits per second, as well as the time-reversal environmental-base equalizer that showed a mean squared error gain of 5 dB over the non equalized time-reversal data.

Keywords: Underwater acoustic communication, matched field processing, time-reversal, waveguide invariants, environmental-based equalizer.

Resumo

Nos sistemas de comunicações acústicos actuais a informação ambiental e espacial é quase completamente ignorada. Esta tese pretende desenvolver um equalizador ambiental para comunicações coerentes em aguas pouco profundas.

Experimentações anteriores em geometria fixa, mostraram que a focalização das técnicas baseadas no espelho acústico é estável a longo termo. Aproveitando essa propriedade de focalização foi possível desenvolver um sistema de comunicações usando o espelho acústico passivo, que faz uso de uma estimativa das respostas impulsivas do canal acústico para aumentar a relação sinal ruído e para reduzir a interferência inter-simbólica dos dados enviados posteriormente.

Para usar o espelho acústico passivo num modem acústico as principais limitações encontradas foram a optimização do operador de retro focagem em função do espalhamento temporal das respostas impulsivas do canal num ambiente ruidoso, e a perda de eficiência devido às variações da geometria fonte agregado de receptores durante a transmissão dos dados.

Para a compensação da variação geométrica da configuração fonte agregado de receptores foi desenvolvido um modelo físico baseado nos invariantes do guia de ondas. Para isso foi usado o invariante no plano frequência/distância e o invariante no plano frequência/profundidade. A partir desse modelo físico foi possível desenvolver nesta tese um equalizador ambiental.

O espalhamento temporal que garante um máximo da relação sinal ruído é dado pela máxima potência da resposta impulsiva global do operador de retro focagem passiva, e essa optimização em termos de relação sinal ruído resulta numa compensação de interferência inter-simbólica sub-óptima no entanto próxima do óptimo.

Em paralelo com os objectivos científicos foi desenvolvida a bóia de superficie – AOB, *Acoustic Oceanographic Buoy*. A AOB pretende ser uma evolução da *sonobuoy* com um agregado vertical de hidrofones e termistors e com capacidade de processamento adicional. A AOB foi testada em seis campanhas de mar em que as suas capacidades de telemetria foram demonstradas com sucesso, além disso foi usada para adquirir os dados reais usados para testar o equalizador ambiental desenvolvido.

A optimização do operador de retrofocagem em relação ao espalhamento temporal associado ao equalizador ambiental foi validado com dados reais com taxas de transmissão de 400 e 2000 bits por segundo e permitiu observar uma redução de aproximadamente 5dB no erro quadrático médio entre os símbolos transmitidos e os detectados no receptor entre o espelho acústico simples e o novo equalizador ambiental.

Palavras-chave: Comunicações acústicas submarinas, processamento por ajuste de campo, espelho acústico, invariantes do guia de ondas, equalizador ambiental.

Contents

1 Introduction **1**
1.1 Rapid environmental assessment and the acoustic oceanographic buoy concept 2
1.2 Time reversal mirror and underwater communications 3
1.3 Time reversal mirror and matched-based processing 5
1.4 Communications and geometric tracking 6
1.5 Outline of the thesis 9
1.6 Contributions 9

2 The Acoustic Oceanographic Buoy Telemetry System **11**
2.1 Introduction 11
2.2 System design 12
2.3 AOB main features 14
2.4 Engineering test 15
2.5 Future developments 16

3 Probe timing optimization for time-reversal underwater communications **17**
3.1 Introduction 17
3.2 Theoretical background 19
  3.2.1 Digital communications with passive Time Reversal 20
  3.2.2 Autocorrelation of the noise terms 23
  3.2.3 Signal and noise power 25
3.3 The passive time-reversal output SNR and its maximum 26
3.4 Performance simulations in realistic channels 28
3.5 Experimental results 31
3.6 Conclusion and future work 34

4 Generalization of Waveguide Invariants and Application to Passive Time Reversal **37**
4.1 Introduction 37
4.2 The waveguide invariants 39
  4.2.1 Approximation of the horizontal wavenumbers using waveguide invariants 39

4.2.2 Approximation of the vertical wavenumbers using waveguide invariants 42
4.3 Geometric mismatch compensation in passive time reversal 44
4.3.1 Passive Time Reversal in a stationary geometry 44
4.3.2 Passive Time Reversal with Source-Array Range Shift 45
4.3.3 Passive Time Reversal with Source Depth Shift 47
4.3.4 Passive Time Reversal with Array Depth Shift 49
4.4 Simulations with a perfect waveguide 50
4.5 Extension of geometric compensation mechanisms to realistic waveguides . 52
4.6 Geometric mismatch compensation with experimental data 55
4.7 Conclusions and future work 58

5 Environmental equalizer for underwater communications 61
5.1 Introduction 61
5.2 Passive Time Reversal applied to communications 63
5.3 Passive Time Reversal geometric mismatch compensation 64
5.4 The passive time-reversal frequency shift equalizer 66
5.5 Real Data Application 67
5.6 Conclusions and Future work 69

6 Environmental equalizer for high data rate underwater communications 71
6.1 Introduction 71
6.2 Passive Time Reversal geometric mismatch compensation 74
6.3 The passive time-reversal frequency shift equalizer 76
6.4 Time-window optimization 78
6.5 Real Data Application 79
6.6 Conclusions and Future work 84

7 Conclusion 87
7.1 Open issues 89

A 91
A.1 Deterministic and stochastic filters autocorrelation 91
A.2 Time windowed passive Time Reversal 93

B 97
B.1 Linear approximation of monotonic functions 97
B.2 Mode orthogonality in the presence of an array depth mismatch 98

Bibliography 100

List of Figures

1.1 Acoustic rapid environmental assessment network 3

2.1 AOB pre-deployment set-up, during Makai Ex. sea trial 13
2.2 AOB hardware and software block diagram 13
2.3 Base Station monitor interface, with received acoustic data during the Makai Ex. sea trial 15

3.1 Block-diagram for the application of passive time reversal to digital communications. 20
3.2 Simulated depth dependent broadband arriving pattern over a realistic scenario: start time 'o', optimum window duration '*' and maximum window duration '+'. 29
3.3 Simulated pTR output SNR for the LF case (a), and for the HF case (b). . 30
3.4 Simulated performance of the proposed optimal time-window prediction method using (3.37) and (3.40) for the LF and HF cases 31
3.5 Real data vertical array estimated impulse responses: start time '0', optimum window duration '*' and maximum window duration '+'. 32
3.6 Real data performance of the proposed optimal time-window prediction method obtained in shot 9: pTR output SNR computed by using the MSE at the slicer/detector input (a) and maxima prediction by using (3.43) (b). 33
3.7 Real data performance of the proposed optimal time-window prediction method obtained in shot 7: pTR output SNR computed by using the MSE at the slicer/detector input (a) and maxima prediction by using (3.43) (b). 33
3.8 Mean analysis over all shots for the real data performance of the proposed optimal time-window prediction method: pTR output SNR output computed by using the shot-mean MSE at the slicer/detector input (a) and shot-mean of the maxima prediction by using (3.43) (b). 34

4.1 Normalized product $\Lambda_{\beta,m}$ (4.16) (dotted line), and its least-squares approximation (4.17) for an effective number of modes $M_e = M/2$ (circles). 42
4.2 Normalized product $\Lambda_{\zeta,m}$ (4.26) (dotted line), and its least-squares approximation (4.27) for an effective number of modes $M_e = M/2$ (circles). 44

4.3 Frequency shift source-array range mismatch compensation given by the pTR acoustic field $P_{PC}(\cdot;\Delta r,\Delta\omega)$ of (4.34); (a) normalized magnitude, (b) unwrapped phase. 51

4.4 Frequency shift source depth mismatch compensation given by the pTR acoustic field $P_{PC}(\cdot;\Delta z_0,\Delta\omega)$ of (4.51); (a) normalized magnitude, (b) unwrapped phase. 52

4.5 Frequency shift array depth mismatch compensation given by the pTR acoustic field $P_{PC}(\cdot;\Delta z_i,\Delta\omega)$ of (4.57); (a) normalized magnitude, (b) unwrapped phase. 53

4.6 Arrival pattern of the non mismatch IR estimate. 56

4.7 The surface represents the normalized magnitude of $P_{pc}(\cdot;\Delta,\Delta\omega)$, when the nominal IR is at $t = 40$s and considering the IRs limited to two arriving paths. The solid line traces the maxima of the surface over time. The dashed line represents the expected behavior if there is only range mismatch. 57

4.8 Power spectrum of the slice of P_{pc} along the maximum line of Figure 4.7 (solid line), and power spectrum of the source depth time series (‘*’). 58

4.9 The same as Figure 4.7 considering the IRs limited to three arriving paths. 58

5.1 Block-diagram of the FSpTR equalizer. The blocks in the upper path represent the probe-signal IRs estimate, time windowing, and frequency shift operations. The blokes in the middle path represent data transmission and crosscorrelation with the IRs estimate obtained in the upper path. Summation over the I hydrophones gives the L pTR processor outputs $\mathrm{z}_l(t)$. The blokes path below represent the selection of $\mathrm{z}_l(t)$ with the frequency shift that best compensates for geometric mismatch between probe and data transmissions, and the transmitted symbols estimation. 67

5.2 Passive time-reversal output mean magnitude $\mathbf{z}_l(t)$ as a function of time and applied frequency shift, computed by slots of 0.5 s. The solid line traces the maximum of the surface. 69

5.3 Mean squared error between the estimated and transmitted data symbols for plain pTR (black line) and FSpTR (red dashed line). 70

6.1 Block-diagram of the FSpTR equalizer. Part (a): the blocks in the upper path represent the probe-signal IR estimate, time windowing, and frequency shift operations. The blocks in the middle path represent data transmission and crosscorrelation with the IR estimate obtained in the upper path. Summation over the I hydrophones gives the L pTR processor outputs $\mathrm{z}_l(t)$. Part (b): the blocks depicts combining of $\mathrm{z}_l(t)$ considering the frequency shift that best compensates for geometric mismatch, Doppler compensation, synchronization, and symbol estimation. 77

6.2 Mean sound speed profile during data transmission, during day 195 between 10:07h and 10:15h (local time). 80

6.3 Arrival pattern estimated by pulse compression of the chirp probe-signal of the first data packet. 80
6.4 Time-window optimization with a 16-hydrophone array (a), with a 6-hydrophone array (b). 81
6.5 Passive time-reversal output $\mathbf{z}_l(t)$ mean power as a function of time/slot-number and applied frequency shift, for the first data packet. The $\mathbf{z}_l(t)$ mean power is computed in slots of 0.25s for a 16-hydrophone array and time-window covering the first arriving paths (a), and for a 6-hydrophone array and time window covering all paths and compensation applied only to later paths (b). The solid line connects the surface maxima ('*') for each time/slot number. 82

List of Tables

6.1 MSE table for: the 16-hydrophone array with the short time-window capture of the channel IRs first arrivals and full frequency shift compensation (Case I); the 6-hydrophone array with the short time-window capture of the channel IRs first arrivals and full frequency shift compensation (Case II); the 6-hydrophone array with full window capture of the channel IRs arrivals and the frequency shift compensation applied only to later arrivals (Case III). 83
6.2 MSE table for the FSE with 16 and 6 hydrophones. 84

Chapter 1

Introduction

Evolution occurs when new solutions are found for previously identified needs that - when solved - reveal new needs, prompting a search for new solutions. That is what happens, when after underwater communications, tomographic inversion and source localization in shallow waters were made possible through acoustic means, the need for Acoustic Rapid Environmental Assessment (A-REA) that motivates the development of free-drifting, light and easy to deploy acoustic Vertical Line Arrays (VLA) evolves, and in turn necessitates new solutions for computationally less demanding underwater communications algorithms and channel geometric tracking. The present work has been developed in the described context where, in order to answer the requirements of A-REA, the light 'Oceanographic Acoustic Buoy (AOB)' VLA has been developed and due to its specific characteristics a new environmental-based underwater communications algorithm has been developed. That makes the present thesis two fold: at first a technological development is proposed with the implementation of the AOB; and second a more challenging scientific objective is attained with the development of an environmental-based equalizer for underwater communications in shallow waters where the waveguide approach is valid.

The aim of this work is to incorporate into the receiver equipment some awareness of the environmental and spatial configuration of the acoustic link that is almost totally lacking in current underwater modems. Having these capabilities built into the receiver would be very appealing for a number of reasons. Firstly, it would provide a clear picture of the difficulties of the acoustic link involved in a given spatial configuration. Secondly, it could provide useful oceanographic information about the environment at no extra cost. Thirdly, it would provide useful localization information to be incorporated into navigation systems, e.g. of an Autonomous Underwater Vehicle (AUV).

The option for the development of an environmental-based equalizer relies on the basic idea that although the underwater channel Impulse Responses (IRs) change quite rapidly, which makes computation requirements quite demanding for current adaptive equalizers, the non-geometric physical properties of the propagation environment change slowly. That is revealed by the medium-term stability of tomographic inversions and of Time-Reversal Mirror (TRM) experiments [34]. The robustness of TRM to the non-geometric environmental changes and its applicability to underwater communications motivate its use as the starting point for the environmental-based equalizer. With reference to the environmental geometric parameters - source-array range, source depth and array depth - their variability should be tracked and used to compensate for the loss of performance that they impose on the Time-Reversal (TR) communications system. That is made possible by the simple physical relations given by the use of waveguide invariants that allow for the establishment of relations between the geometric variations and an appropriate frequency shift of the acoustic field.

1.1 Rapid environmental assessment and the acoustic oceanographic buoy concept

In the past few years Rapid Environment Assessment (REA), in shallow water, has become one of the most challenging topics in ocean acoustics [10], mostly because acoustic means provide the tools for the survey of an unknown region with minimal human intervention.

The REA concept involves the integration of acoustic and non-acoustic systems for collecting environmental information as well as the short notice dissemination of the acquired information to an operational command. REA has been developed in the military context where information that include meteorology, oceanography, hydrography, geography, mine reconnaissance, and many others can all be relevant in affecting the operation of marine and supported ground forces. REA methods applied to shallow water areas are also seen as promising techniques for civil and scientific environment monitoring systems. The coastal transition zone is a very sensitive region subject to a great deal of human activity that interferes with the marine system. It is a region of significant fishing and of intense ship traffic, in particular cargo vessels and tankers. Comprehensive knowledge of the dynamics and structure of this system would have strong importance in coastal management and prevention in the case of natural or man made hazards. Such knowledge is also important for the protection of maritime structures (bridges, ports, seashore lines), and the monitoring and study of complex ocean and coastal processes such as beach erosion, sediment transport, surface and internal tide propagation and currents.

In the context of REA, the use of acoustic means is usually termed Acoustic REA (A-REA) [10] and can be applied for submarine localization, mine detection, tomographic and bottom inversion. Acoustic means also provide the necessary framework for a fast and easy deployment of an underwater communication network (see figure 1.1) where the underwater nodes (e.g. oceanographic sensors, autonomous underwater vehicles, benthic labs, telemetry buoys) communicate with each other by using acoustic modems and consequently no cables are required. The use of acoustic equipment provides an unmanned and inexpensive manner of doing high-resolution surveys, and allows for remote data collection in a large area.

Figure 1.1 shows the scenario for one of the currently most promising A-REA concepts, that is, the use of a field of air-dropped 'advanced' sonobuoys, to receive signals from controlled sound sources such as Autonomous Underwater Vehicles (AUV), or other

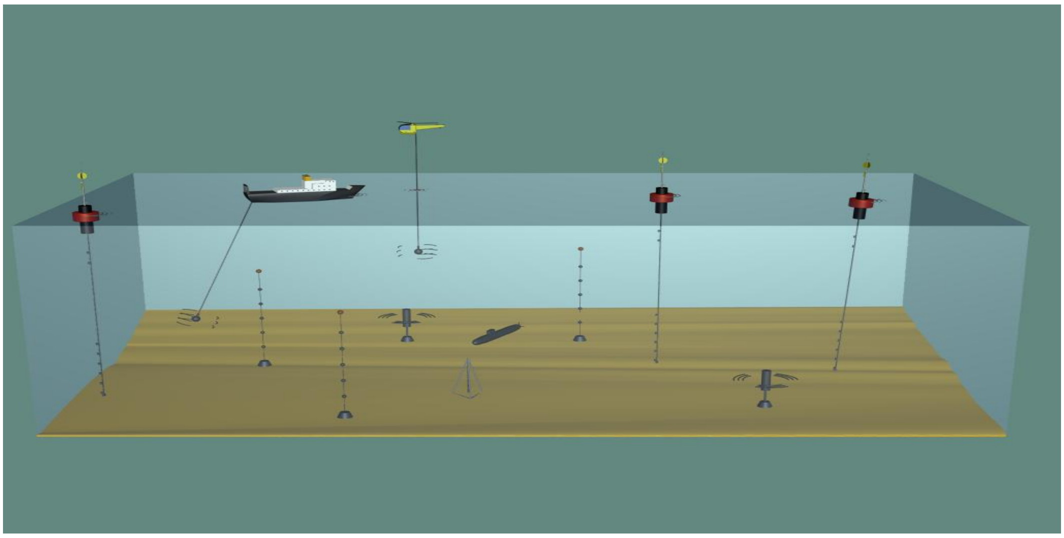

Figure 1.1: Acoustic rapid environmental assessment network

sources of opportunity. The collected information, radio transmitted to an aircraft, ship or land-based station, is processed to determine the AUV localization, water column and bottom acoustic properties. The collected information also comprises other AUV collected data e.g. imaging and mine reconnaissance. As any REA operation is likely to be performed in a crisis area – both for operational reasons and in order to have a fast uploading of the data – the collected information should be pre-processed in-situ in order to reduce the amount of data to be sent. To meet those requirements, in this work, the 'advanced' sonobuoy concept is implemented in the Oceanographic Acoustic Buoy (AOB): a telemetry buoy that meets the traditional sonobuoys characteristics of small size and weight, but with the advanced characteristics of having a sufficiently dense array of hydrophones and thermistors, a self localizing GPS system, high processing capability, a high throughput radio data link, and a large data storage capacity. The two last characteristics make it possible for REA to require a short-time presence of manned devices (helicopters, aircrafts or ships) in the operational scenario, since the AOB provides the means for the storage of the slow data acquisition and a rapid radio-link up-load. The development of such a telemetry buoy poses a significant technological challenge since usual systems with analogous capabilities are too large and too heavy (more than 300Kg). Examples of those are the ULVA/RDAS [12] and the ACDS systems (National Research Laboratory, USA).

Nevertheless the usefulness of the AOB concept depends on the development of reliable underwater communication and inversion methods suitable to be implemented on the AOB and that is the main objective of this thesis.

1.2 Time reversal mirror and underwater communications

Underwater acoustic channels exhibit time-varying severe multipath due to sound reflections on the sea surface and bottom, which is widely regarded as the dominant environmental influence on the performance of acoustic communications systems. The time variability of the multipath structure is due to the variability of the geometric characteristics of the environment (source-receiver range, source depth and receiver depth) and to the variability of the non-geometric characteristics like internal waves, internal turbulence, tidal flows, surface waves and variable sound speed profile. An experiment conduced in the island of Elba by Kuperman et. al. in 1997 [34] revealed a great immunity of Time-Reversal (TR) to the non-geometric environment properties variation and motivate its use as the starting point of the methods to be developed in the present work.

In several recent papers [38, 26, 34, 4] TR was shown to efficiently focalize a received signal, in time and space, at the source position in the presence of an unknown environment. It makes use of a VLA that collects the signal transmitted by the source and an array of transducers collocated with the VLA that retransmits a time reversed version of the received signals. Such experiments show the capability of the acoustic channel to deconvolve itself. The same concept can be applied in a slightly different way by using only a source and a VLA. In such a case, before the signal focalization, the source must transmit a probe signal that by pulse compression will generate in the receiver an estimate of the channel Impulse Responses (IRs). Those estimates will then be used as a synthetic acoustic channel in order to implement the TR [50]. Such technique is termed Passive Phase Conjugation (PPC) [7] in the frequency domain or passive TR (pTR) in the time domain. The ability of pTR to produce a time focus suggests its attractiveness for use in underwater communications. In fact, the time focalization property of the pTR is equivalent to deconvolve the severe multipath introduced by the channel and that results in a low complexity communications system. In fact the pTR processor instead of trying to eliminate the multipath, will operate coherently on it in order to improve the time focalization. Unfortunately due to the acoustic channel variability such focalization does not hold in time, moreover acoustic focalization fluctuations are greater at higher frequencies due to the smaller focal size, where its usage is mostly interesting for digital communications. Recent works [62, 56] made a performance comparison between pTR and the multichannel decision-feedback equalizer (DFE) [57] both using a common framework concluding that for a small number of hydrophones the DFE outperforms PPC, as the number of receivers increase, the bit error rate of both processors approaches zero. The nature of the methods is different: DFE is a signal processing method to which the nature of the channel is irrelevant; on the other hand PPC uses the physics of propagation to deconvolve the channel. The main difference is that the former is adaptive and the latter is not, that means that an estimation error in the DFE can be compensated as opposed to what happens in pTR. The problem can be overcome by shortening the time period between probe signals, but that will impose a serious reduction of the effective symbol rate. A second solution is to use an adaptive algorithm to track the IRs from the initial probe-signal IRs estimate: with such solution the estimated IRs are represented by a set of coefficients with given statistical properties. A third alternative is to use a low-complexity equalizer to compensate for the residual ISI, where the equalizer coefficients represents weights to the estimated IRs. A performance comparison of the previous solutions is presented in [20]. A fourth approach, is to use a physical-based model to develop a pTR equalizer. Such approach suggests that environmental properties of the acoustic channel can be estimated jointly with the data signals. Although the physical-based equalizer has already been suggested by several authors [32, 42, 23], an effective way of carrying it out has not yet been proposed. In fact, that is the main topic of this thesis. In order to develop the basis for an environmental-based pTR equalizer the matched field methods present a framework already endowed with experience and expertise.

1.3 Time reversal mirror and matched-based processing

The key component of ocean Matched-Based Processing (MBP)[1] techniques [2] is an algorithm that generates field predictions from a set of model parameters and that allow to infer physical parameters of the ocean itself. The traditional MBP approach is to compare (e.g. correlate) the acoustic field generated by the ocean (true environment data vector) with the acoustic field generated by a reliable acoustic model over all possible parameter space, and then find which one is closer to the true environment data vector. The concept of TRM can be considered as an alternative representation of the classical MBP with the main difference that in the former the ocean is used to match with itself, while in the later the ocean is matched with a synthetic acoustic field. Despite their similarities Jesus [29], has shown that for the same amount of model mismatch, MBP will have a better performance than TR. Such result encourage the use of computational model-based methods to implement the pTR equalizer.

Unfortunately MBP with an environmental-parameters exhaustive search approach would lead to huge number of comparisons unless a reduced parameter space by a priori knowledge of the possible values of the environment parameters is used. Fortunately fast environmental-parameters global search methods were developed, genetic algorithms [53] and simulated annealing [16] are two global optimization methods that provide the framework for such an approach. Although excellent results are attained when trying to invert tomographic parameters, and its ability to deal with the non-linearity of the acoustic field, the convergence of the algorithms doesn't follow a steepest descendent of the mismatch error, rather it converges *somehow* statistically to the minimum by using a smaller amount of comparisons than the traditional MBP approach. That is a strong disadvantage when trying to apply it to communication algorithms. Recently a new approach has been proposed using a MBP adaptive formulation, the adjoint of the acoustic model. In such a technique the mismatch between the model predictions and the measured observations results in a residual field – by means of adjoint modelling [23] – such residual is backpropagated in order to locate which of the model properties need to be adjusted. Because of

---

[1] In the present work the term matched-based processing means the inversion of any physical parameter that influences the underwater acoustic propagation (e.g. matched-field inversion for geoacoustic parameters, matched-field tomography for water column parameters and matched-field processing for geometric parameters)

the non-linearity of the acoustic models, up to now the algorithms based in the adjoint model approach are developed using a local linear approximation and the gradient of the ambiguity surface. The disadvantages of the global methods when compared to the local ones are only practical and technical, in fact the local methods are not able to “see” the large number of local extrema of the ambiguity surface, and so they require a closer to the solution starting point.

MBP has now been widely demonstrated for performing source localization, detection and tomographic inversion in ocean waveguides, but most of the processing approaches become increasingly sensitive to fluctuations or uncertainties as the frequency increases. In fact the shallow water environment is quite dynamic. In addition to the background internal wave field, rapid water temperature fluctuations generated by internal tides have a substantial impact on high frequency acoustic propagation. Recent works [25, 23, 39, 22, 61] that study the environment's influence over high frequencies and compare the results with predictions made by models attain encouraging results, but the idea that new models are required to operate MBP at high frequencies still holds [3], or at least new MBP techniques should be made as insensitive as possible to modelling mismatch at high frequency.

In order to compensate for the geometric mismatch between the actual and previous acoustic field a *partial*[2] acoustic model that is able to track the pTR acoustic field will be developed . The proposed approach can be seen as MBP since pTR by itself is a matched-based processor where the actual acoustic field matches with an estimated version of the acoustic field at a different time. It is assumed, at least in a short time interval, that pTR is insensitive to non-geometric mismatch between the actual and the previous acoustic field.

Up to now, underwater digital communications and source localization are treated as two different topics by the scientific community. By using physics-based models and the pTR processor a different approach is proposed where the problem of performing geometric source and array tracking and communications in real time are treated as a joint problem.

1.4 Communications and geometric tracking

In this section two problems will be addressed, the first one will be a communication system based on pTR, and the second will be the tracking of the source and array locations.

One of the most challenging applications of underwater acoustics is when applied to autonomous underwater vehicles (AUVs) *in situ* real-time monitoring. In that case, a localization system is required to have a mapping of the survey and a high data rate acoustic communication up-loading link is required for real data transfer. In what concerns the communication system, performance constraints arise from the available SNR and ISI. SNR depends of the underwater noise power and of a compromise between the available power for communications and the increasing need for autonomy. ISI depends of the

---

[2] *partial* - means that the model can track the acoustic field but can not determine it.

underwater acoustic channel impulse response that changes quite rapidly due to the AUV's continuous movement or drift.

One of the key components that enables the real-time exchange of data between the AUV and a fixed or drifting station is a reliable up-loading high speed acoustic communication link (from the AUV to the station). In order to implement such an up-loading link and due to constraints on the AUV's power, only one AUV-projector is allowed, but an array of receivers can be placed in the receiving station. In such a configuration the pTR technique, presented in [50] can be applied, the main difference between that implementation and other pTR [7, 43] is the clear adoption of the digital modulation pulse shape as the probe signal of the channel. In fact, pTR requires a probe-signal to be transmitted ahead of the data-signal in order to estimate the channel IR (Green's function). The Green's function estimate is then used to perform a synthetic reverse channel, inside a digital signal processor. One of the most critical aspects of the pTR method is the channel IRs (Green's functions) estimate. It can be done from the probe-signal by simply correlating the received channel distorted probe-signal with the transmitted one, in which case the result will be an estimation of the channel impulse response. The probe-signal can be a M-sequence, a chirp, the convolution between the chirp and the pulse shape or the pulse shape adopted in the data digital modulation. The first three are high power signals with a large time bandwidth product, so, they allow for a better channel impulse response estimation; the latter is a low power signal and can be seen as a better choice when AUV power requirements are critical.

In order to be used in a digital computer, the estimated IRs must be approximated by a finite impulse response filter: that means that it must be captured in a finite time window. Typically, the onset and the duration of this time window should depend on the time dispersion of the acoustic channel which, in turn, depends on the physical channel properties and on the experiment geometry. Empirical reasoning would suggest that if a short time window fails to include all significant multipath it will result in an imperfect retrofocusing, while a too long time window will reduce the efficiency of the communication system by introducing additional noise in the pTR operation. That problem was addressed in [18, 11, 45] though no attempt for optimization has been proposed.

When there is a geometric mismatch between the probe-signal transmission and the data transmission the pTR communications system performance degrades quite rapidly. The proposed solution has to meet three requirements: first it must be simple enough to be implemented in an autonomous platform such as the AOB; second is that it must strongly reduce the number of probe signals to be sent in the pTR digital communications process in order to increase the effective data rate transfer between the source and the receiver; finally, the third requirement is that it must allow for geometric inversion, i.e., for source-array range and source and array depths estimate. In the present work a first step is carried on in order to integrate the three requirements in a single solution. It consists in developing an adaptive pTR-based communication system that track the channel IR variability assuming that in a short time period is manly due to the geometric mismatch between the probe and data transmissions. The proposed solution is based on the Chuprov's waveguide-invariant theory [6, 21] that states that the geometric mismatches, i.e., the source-array range and the source and array depths variations result in a frequency shift of an original channel Green's function. Such system it would be conceptually low complexity since only one parameter – the frequency shift – has to be tracked, it increases the effective error rate since it compensates for the channel variability, and it allows for the geometric inversion since the appropriate the frequency shift is closely related with the geometric variations.

The waveguide-invariant theory has been widely used in tomographic inversion and characterization. In recent work such property has been used to change the TRM focus range [55, 33], and to increase the period of stable focusing in a non-stationary environment [32]. In stratified environments wheakle range dependent and a constant sound speed profile (SSP), the lines of constant sound intensity lead to a constant slope between certain parameters of the waveguide [21, 35]. The invariant, denoted by β, characterizes the relation between range and frequency as

$$\delta\omega = \frac{\beta\omega}{R}\delta r, \tag{1.1}$$

where R is the horizontal range and ω is the angular frequency, δr and $\delta\omega$ denote the range and frequency shifts. At this point it is important to mention that parameter β is a weak function of frequency [9, 42], and although most of the experiments that confirm such fact have been carried up to 3.5 kHz, a similar behavior is anticipated at higher frequencies. This states the usefulness of the waveguide invariant in our narrow-band data communication application. Since β is invariant in the frequency/range plane it can be used for the compensation of the range mismatch between the probe and the data transmission in the pTR communications system. In a similar manner there exists an invariant ζ in the frequency/depth plane that can be use to compensate for the source and array depths mismatches. It results that using the waveguide invariants the channel geometric variability can be modelled by a frequency shift.

The basic idea of the TRM focal range shift approach [55] is that the focus can be placed at different ranges by increasing or decreasing the carrier frequency of the time-reversed signal to be retransmitted back to the channel. When applied to the pTR the idea is slightly different, in that case the channel that has been used to estimate the IR is different from the channel that was used to transmit the data sequence. So, the requirement is to adjust the synthetic channel estimated by the probe-signal, to the true one that exists during the data transmission by means of a frequency shift. The overall system operates as a matched-filter where the actual received acoustic field matches with the frequency shifted initial channel IRs estimate, where the appropriate frequency shift is given by a waveguide invariant model.

1.5 Outline of the thesis

This thesis was divided into five main chapters where Chapters 2-6 has been intensionally written as papers.

Chapter 2 describes the AOB system design, where the main system features will be addressed and its integration in an A-REA network is explained. In the end the operation of the AOB during the MakaiEx sea trial off Hawaii in 2005 is presented.

Chapter 3 addresses the underwater communications pTR system optimization as a function of the IRs estimate time window capture. A closed form expression for the pTR output SNR as a function of the time window is obtained. When the noise power dominates over the Inter-Symbolic Interference (ISI) it is found that the optimal time window does not depend on the noise level but only on the multipath structure of the underwater channel, and is given by a closed form expression that can be computed previously to the data arrival. Demonstrative results are presented using simulations and real data acquired during the INTIFANTE'00 sea trial off the west coast of Portugal in 2000.

Chapter 4 presents a re-interpretation of the waveguide invariant β and its application to compute an approximation of the horizontal wavenumber using the horizontal group slowness. A similar formulation is used to compute a vertical wavenumber approximation using the waveguide invariant ζ. The influence of the geometric mismatch between the probe-signal and the data transmission in the pTR operator is explained and compensation strategies using the invariants β and ζ are presented. Real data acquired during the MREA'04 sea trial are used as a demonstrative example of the effectiveness of the compensation mechanism.

Chapter 5 integrates the communication system developed in Chapter 3 and the pTR geometric mismatch compensation developed in Chapter 4 resulting in the environmental-equalizer 'Frequency Shift passive Time Reversal (FSpTR)'. Performance comparison between plain pTR and FSpTR communication systems, with low data rate signals (400 baud at 3.5 kHz band), is performed using real data acquired during the MREA'04 sea trial.

Chapter 6 applies the FSpTR environmental-equalizer to binary PSK signals at a data rate of 2000 baud with a carrier frequency of 12.5 kHz. A performance comparison between the Fractionally-Spaced Equalizer and the environmental-equalizer with real data acquired during the RADAR'07 sea trial is presented.

Chapter 7 summarizes the main results and discusses directions for future research.

1.6 Contributions

The following topics reported in this thesis represent original contributions:

1. [Chapter 3] A closed form expression for the autocorrelation of the output of a filter when the filter IR is a time limited stochastic signal and the input is a deterministic signal.

2. [Chapter 3] A closed form expression for the pTR output SNR when applied to underwater communications is derived.
3. [Chapter 3] A closed form expression for the determination of the optimum time window length for the IR estimates step of the pTR processor when applied to underwater communications is derived.
4. [Chapter 4] The waveguide invariants β and ζ are applied to the geometric mismatch compensation of the pTR processor.
5. [Chapter 5 and 6] The environmental-based equalizer is successfully applied to real data.

Chapter 2

The Acoustic Oceanographic Buoy Telemetry System

An Advanced Sonobuoy that Meets Acoustic Rapid Environmental Assessment Requirements

2.1 Introduction

In the past few years Rapid Environmental Assessment (REA), applied to shallow waters, has become one of the most challenging topics in ocean acoustics. The REA concept evolved after the cold war when the outset of regional conflicts shifted the potential operational areas from open ocean towards littoral areas, and has been identified by NATO as a new warfare requirement. REA must provide detailed and accurate information, in near real time, in order to prepare the maritime forces deployment into highly variable coastal waters that are not well known. More recently REA has become a promising technique for civil and scientific environment monitoring. Such an interest arises because the coastal transition zone is a region of significant fishing effort and of intense shiping traffic. The rapid knowledge of the dynamics and structure of coastal zones would assume strong importance in the case of natural or man made hazards. Because of the short time required for REA applications, the main topics of REA have been identified as rapid data collection, data synthesis and assessment, and dissemination of assessed products to action groups [10].

In the context of REA, the data synthesis and assessment requires the use of dynamic models for nowcast and forecast [37] that are fed with data acquired by the recording equipment. Data collection can be attained by using space/airborne sensors e.g. for marine wind, large scale currents and shallow water bathymetry; traditional oceanographic sensors like CTDs, wave height and ADCPs; passive and/or active acoustic e.g. for submarine localization, mine detection, tomography and bottom inversion. Acoustic means also provide the necessary framework for a fast and easy deployment of an underwater communication network where the underwater nodes (e.g.: oceanographic sensors, autonomous underwater vehicles, benthic labs, telemetry buoys) communicate with each other using acoustic modems and consequently no cables are required. The use of acoustic equipment is usually termed as Acoustic REA (AREA), it provides an unmanned and inexpensive manner of doing high-resolution surveys, and allows for remote data collection in a large area [10].

Currently one of the most promising AREA concepts is the use of a field of air-dropped 'advanced' sonobuoys, as an interface between an underwater wireless Acoustic Network (AcN), and an air Radio Network (RaN). The underwater AcN nodes are responsible for data collection. The air RaN nodes (satellites, aircrafts, vessels ...) are responsible for raw data storage and relay over local or world distributed data processing groups, for near real-time data synthesis and assessment. The 'advanced' sonobuoy field is responsible for the upload (from the AcN to the air RaN) of the acquired data; and for the download (from air RaN to the underwater AcN) of control and operation instructions. The 'advanced' sonobuoy field integrates simultaneously the air RaN and the underwater AcN, and that results in a single seamless network. Moreover, the 'advanced' sonobuoys can be used as an intermediate step for acquired data pre-processing and data fusion, through which data reduction can be attained. Such data reduction implies shorter data uploading, an important requisite for REA operations in a hostile area where the long time presence of air RaN nodes can compromise the mission success. Hostile area operations suggest that the 'advanced' sonobuoy field must integrate a network where nodes can be added or suppressed at any time, performing reduced operations even with a single 'advanced' sonobuoy.

The Acoustic Oceanographic Buoy (AOB) telemetry system aims to meet the 'advanced' sonobuoy characteristics. It integrates the air RaN by using a standard 'IEEE 802.11' WLAN configuration, and the underwater AcN by using a hydrophone array and an acoustic source. The first AOB prototype was tested during the Maritime Rapid Environmental Assessment sea trials in 2003 [52], and in 2004 [30]. The present version of the AOB (see figure 2.1) was tested, from 15th of September to 2nd of October 2005, during the MakaiEx sea trial off Kauai Island, Hawaii, USA, in the context of the High Frequency Initiative promoted by HLS Research Inc, San Diego, USA.

In the following, the AOB design will be described, the main system features will be addressed, the MakaiEx AOB engineering test will be presented and future developments will be pointed out.

2.2 System design

The physical characteristics of the AOB, in terms of height (1.2m), diameter (16cm), weight (40kg) and autonomy (12 hours) tend to those of a standard sonobuoy. However, the AOB presents advanced capabilities, which include: stand-alone or network operation; local data storage; dedicated signal-processing; GPS timing and localization; real-time data transmission and relaying. In this section the AOB hardware and software (see figure 2.2) is briefly presented and the main characteristics of the 'base station', an air RaN node, will be given.

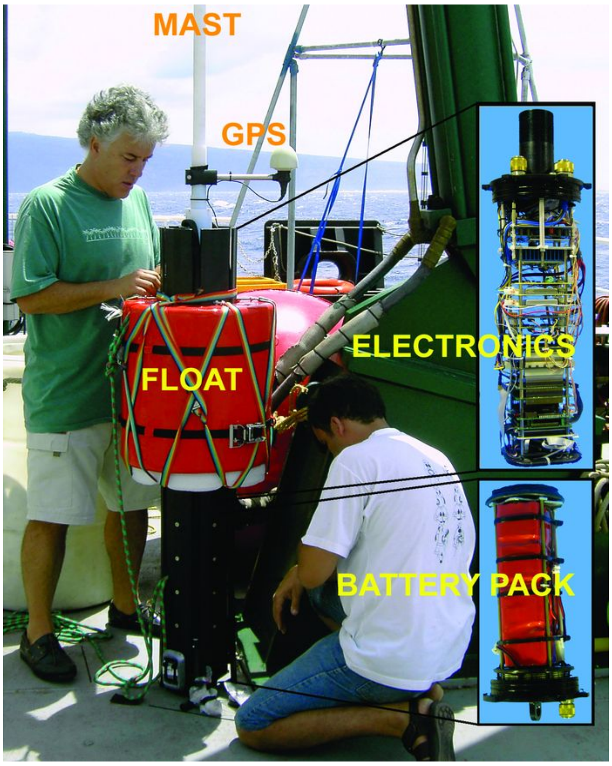

Figure 2.1: AOB pre-deployment set-up, during Makai Ex. sea trial

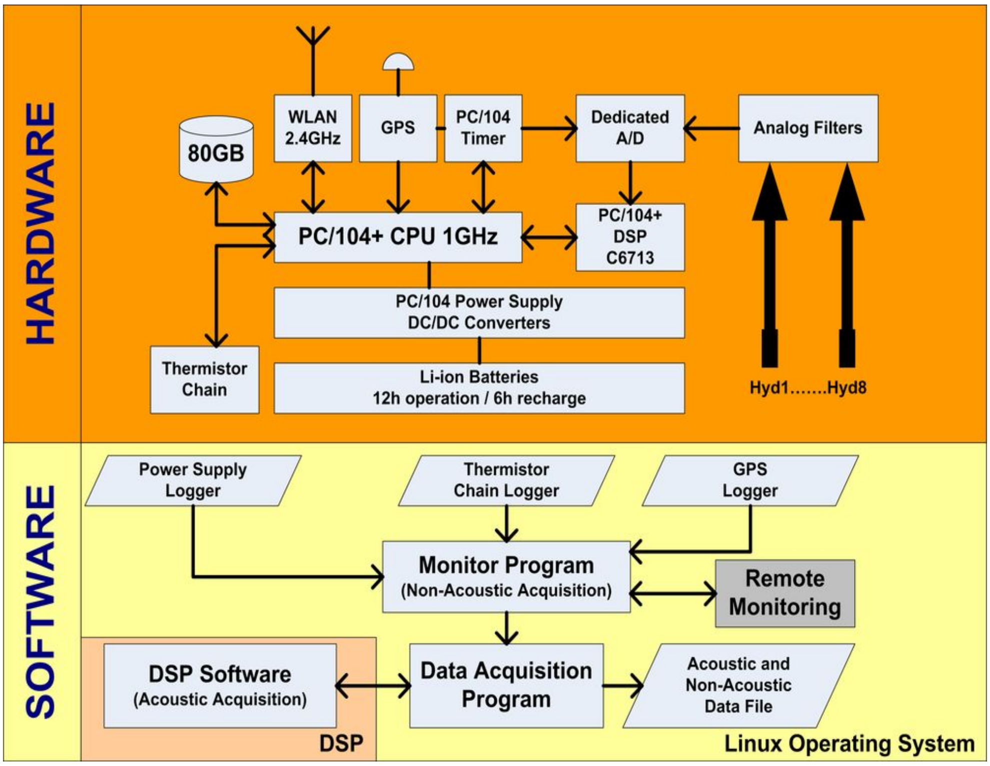

Figure 2.2: AOB hardware and software block diagram

The hardware system is contained within a PC/104 computer/electronics stack with standard purchased and inhouse developed boards. The core is a fan-less CPU board which takes care of all the system management. A 120 Gbytes hard drive allows for in situ data storage. Due to its standard WLAN transceiver the AOB is easily integrable with other similar systems to form a flexible network, and to perform online high speed data transmissions. A GPS receiver is responsible for timing and positioning information. An external data logger with 16 thermistors is responsible for the water column temperature sampling. The acoustic data acquisition system includes 8 hydrophones, 42dB pre-amplifiers, 15kHz anti-aliasing filters, signal conditioning circuitry and a dedicated acquisition board. A real time GPS synchronized timer provides the acquisition board with an accurate clock sampling signal and absolute time marking, a must for tomographic applications. The TMS320C6713 DSP board gives the AOB strong signal processing capabilities that allow for in situ data processing tasks.

All software applications were specifically developed for the AOB which runs the Linux operating system. The software is divided into various modules, each running independently. Modules include: GPS position logging; power supply control and monitoring; thermistors chain non-acoustic data acquisition; real-time remote monitoring; and the main acoustic data acquisition program which configures acquisition and stores data on the local disk. The modules exchange information through the use of TCP/IP network sockets which also allows real-time remote monitoring of buoy position and acquired data.

The 'base station' (see figure 2.3) that monitors the AOBs and manages the AOB WLAN network is portable and is comprised of a notebook and one external antenna, allowing for a reliable connection up to 10 km. The user is presented with a visual output of the 'base station' and AOB trajectories on-top of a bathymetric map, the state of the various equipments inside the buoy and the display of acquired signals. When deployed, operation requirements can be remotely modified, changes can be performed at any time and include parameters such as data acquisition rate, begin and end time for each acquisition cycle, and other options.

2.3 AOB main features

The AOB is a reusable system with reduced maintenance. Aboard, only two maintenance operations have to be performed: recharging batteries and downloading acquired data. Both are done by simply unplugging one connector, and plugging two connectors: one for recharging the batteries, and the other for external power supply and a fast ethernet link. The AOB is light enough in order to be deployed by hand from a ship, and robust enough to be deployed by air from an aircraft or to operate under rough sea conditions. At sea, the AOB is a salt-water-plug and play system designed to operate in free drifting mode, self time synchronized and locatable with great precision at all times.

Due to its DSP facility, the AOB is suitable for performing distributed digital signal processing tasks. When used in Matched Field Tomography (MFT), in the frequency

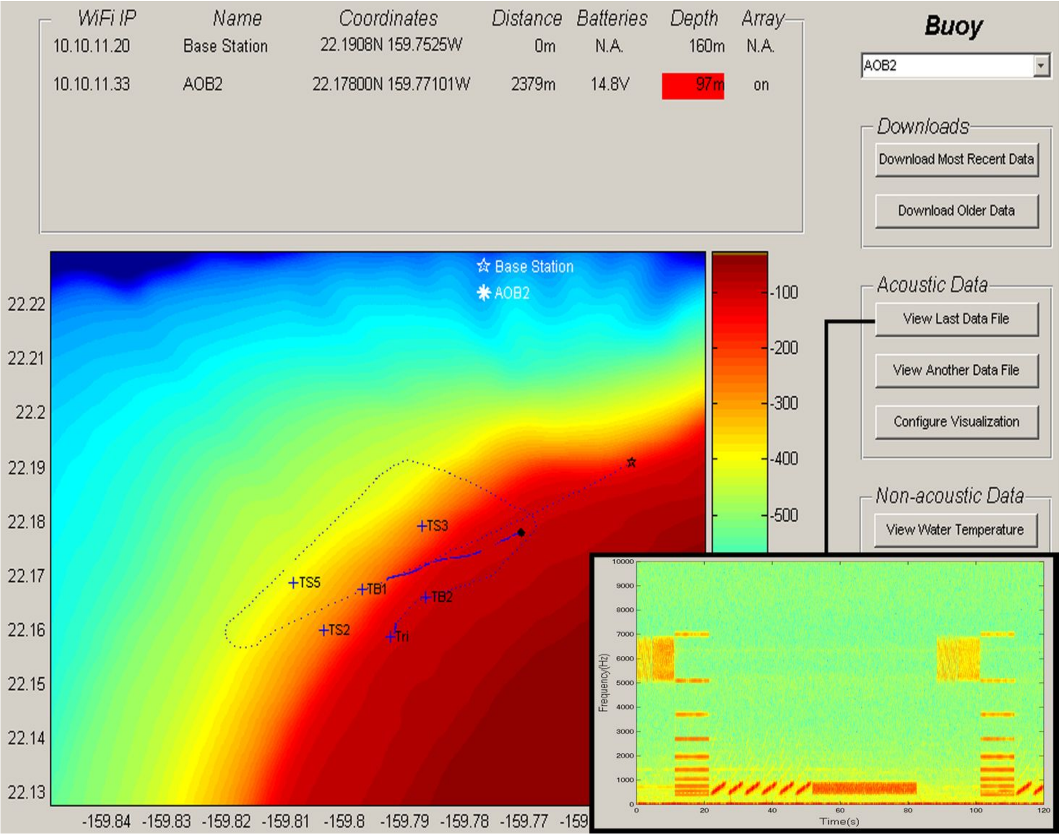

WiFi IP	Name	Coordinates	Distance	Batteries	Depth	Array
10.10.11.20	Base Station	22.1908N 159.7525W	0m	N.A.	160m	N.A.
10.10.11.33	AOB2	22.17800N 159.77101W	2379m	14.8V	97m	on

Figure 2.3: Base Station monitor interface, with received acoustic data during the Makai Ex. sea trial

domain, the AOB can pre-process the acoustic data. This can be performed by computing Fourier transforms of the acquired raw data, compute cross-covariance matrix estimates, and then just send to the base station the data concerning the frequencies of interest for posterior MFT operation. Such a distributed processing technique is advantageous when the propagated signals are either broadband or tones, in particular for the latter since only few frequency bins contain useful information. When used in non-coherent underwater acoustic data communications the DSP processing capabilities allow for the implementation of a full demodulation system. It is also suitable for the implementation of simple array processing passive localization algorithms.

2.4 Engineering test

The first engineering test of the present AOB version, in its stand-alone mode, took place during the MakaiEx sea trial [4]. Three deployments were initially planed but six were done since it was realized that the AOB was an easy system to deploy and recover. The AOB was in a free drifting configuration during five of the deployments; remote monitoring of the buoy was useful to know the status in terms of positioning and battery charge. There was one deployment where the AOB was tethered to the ship. This was not the initial planned setup and the rough sea conditions at the time showed that the AOB construction was robust and functional even when under strain. During MakaiEx the AOB participated in a wide spectrum of scientific experiments. In the first five deploys, 8-14 kHz acoustic transmissions where acquired with the main objectives of high-resolution tomography and understanding of the acoustic-environment interaction at high frequency and its influence on underwater communications. In the last deployment acoustic transmissions ranging from 500 Hz to 14 kHz where acquired in order to performs field calibration using inversion algorithms at high and low frequency.

2.5 Future developments

The AOB is now fully operational in its stand-alone mode, and the developing team is looking to future developments. A current project is the replacement of the sensor array by a robust and light array with 16 hydrophones, thermistors, pressure and other user defined sensors; and an acoustic source for control/communication operations over the underwater nodes.

An AOB network-mode engineering test, with 3 AOBs, is now under preparation and is scheduled to take place in October 2006. After that, as well as supporting the University of Algarve Signal Processing Laboratory (SiPLAB) research activities, the AOB's will be operated as a service to the international underwater research community.

Acknowledgments

The AOB system was developed under the NUACE (POSI/CPS/47824/2002) and RADAR (POCTI/CTA/47719/2002) projects supported by the FCT - Foundation for Science and Technology (Portugal). Special thanks are due to Prof. Sergio de Jesus for promoting and heading the AOB project.

Chapter 3

Probe timing optimization for time-reversal underwater communications

Abstract: Passive time reversal is one of the variants of time reversal applicable to digital underwater communications. In passive time reversal a probe-signal is transmitted ahead of the data-signal in order to estimate the channel impulse response for later use as a replica signal in a time reversal mirror fashion. In practice the received probe-signal must be captured in a time-window and, after correlation with the transmitted probe-signal, give a noisy estimation of the channel impulse response. Therefore, the output signal to noise ratio (SNR) and the detection rate of passive time reversal will strongly depend on the starting time and duration of such time-window. Typically the beginning and the duration of that time-window should depend on the travel time and the dispersion of the acoustic channel. Heuristic reasoning would suggest that if a short time-window fails to include all significant multipath it will result in imperfect focusing, while a too long time-window will reduce the efficiency of the communication system by introducing additional noise in the passive time reversal system. That problem clearly calls for an optimization. In order to bring the time reversal capabilities to a practical modem the time-window automatic optimization engineering problem must be solved. In this paper, the maximization of the passive time reversal output SNR relative to the probe time-window is derived in closed form. Theoretical results are found to be in full agreement with simulations and with results obtained on experimental data taken during the INTIFANTE'00 sea trial.

3.1 Introduction

In the past few years coherent modulation techniques for fast and reliable shallow water acoustic communication have triggered a number of theoretic developments, simulations and field experiments. To that end multichannel adaptive equalization methods [57], although quite computationally demanding, currently provide the most popular framework. Recently, active and passive Time Reversal (a-pTR) [26, 7] appeared as a viable alternative for simple and robust underwater coherent communications [50, 18, 43]. Active Time Reversal (aTR) takes advantage of the acoustic channel mode orthogonality and reciprocity properties and matches the ocean response with itself in a much similar way to Matched Field Processing (MFP)[29]. Like aTR, passive Time Reversal (pTR) relies on mode orthogonality but instead of the reciprocity property, uses an estimate of the underwater channel Green's function to perform a virtual ocean response match inside the computer, in a MFP fashion. Despite its simplicity, a-pTR applied to high frequency underwater communications presents a lower performance than multichannel equalization [45, 62, 56]. That is due to the Time Reversal Mirror (TRM) requirement for a long and dense array [34], without which residual Inter-Symbol Interference (ISI) is always present due to poor sampling of the high-order modes and subsequent orthogonality property violation.

One of the most critical aspects of the a-pTR methods is the channel Green's function estimation, which is typically obtained by simply correlating the received channel distorted probe-signal with the transmitted one, resulting in a noisy version of the channel Impulse Response (IR). In practice the probe-signal can be a M-sequence, a chirp, or the pulse shape adopted in the data digital modulation. In any case, and since the underwater channel is quite time variable, probe-signals must be frequently transmitted in order to maintain the a-pTR performance at an acceptable level. A significantly different technique is to adaptively estimate the channel Green's function by using the data communication signal [19], in a similar manner to that used in the multichannel equalizer [57] with, however, the difference that the IR must be estimated instead of its inverse. As in the multichannel equalizer, such technique is computationally very demanding when compared with the probe-signal based Green's function estimation which in turns presents the major drawback of losing validity due to channel fading.

Figure 3.1 shows a block diagram of the pTR application adopted in the sequel, where the received probe-signal $f_i'(t)$ is the channel IR estimate that is simply obtained as the channel noise contaminated response to a dirac impulse (upper path in the block diagram). For later use the estimated IR must be approximated by a FIR filter, which means that it must be captured in a finite time-window (see Figure 3.1). The time windowed estimated IR, $g_{i,t0,\tau}(t)$, is them used as a matched filter with the received data signal $v_i(t)$ (lower path in the block diagram). Typically, the start time and the duration of such time-window should depend on the time dispersion of the acoustic channel which, in turn, depends on the physical channel properties and on the experiment geometry. Heuristic reasoning would suggest that if a short time-window fails to include all significant multipath it will result in an imperfect retrofocusing, while a too long time-window will reduce the efficiency of the communication system and introduce additional noise in the pTR operation [18, 45, 11]. In a pTR communications system that adaptively estimates the channel IRs [19, 47] the *a priori* time-window optimization is also relevant since it anticipates the optimum number of coefficients that should be used to track the channel IRs.

The time-window probe-signal capture optimization is an important issue since it will affect the pTR communications system performance, its output Signal-to-Noise Ratio (SNR) and thus the detection error rate. For a well designed pTR Vertical Line Array

(VLA) [1] that is able to reduce the residual ISI to an acceptable level, the time-window optimization can be transformed in to a problem of pTR output SNR maximization, that can be solved after establishing signal and noise power time-window dependence. The a-pTR output SNR have been addressed by several authors [56, 4], including heuristic characterizations of time-window dependence [18, 45, 11] though optimization was not attempted.

It will be shown that the optimal pTR output SNR occurs when the time-windowed pTR overall IR has maximum power, while the optimal time-window for ISI tends to occur when the full length of the pTR overall IR is considered. Since in shallow water the IRs can extend over hundreds of milliseconds it turns out that the time-window for ISI optimization can be made impractical. Moreover, it will be shown that the time-window that gives an optimum Mean Square Error (MSE), between the transmitted and estimated symbols sequence, can be predicted by the pTR output SNR when in presence of a low input SNR, and by the ISI when in presence of a high input SNR.

In Section 3.2 signal and noise terms of the pTR communication system are identified and their means, autocorrelations and powers are derived. In Section 3.3 a closed form expression for the pTR output SNR as a function of the time-window is obtained and strategies for its optimization are proposed. In particular, it is found that the optimal time-window does not depend on the input noise level but only on the multipath structure of the underwater acoustic channel. Section 3.4 presents the results obtained in simulation using realistic underwater acoustic propagation models. In Section 3.5 the proposed optimization method will be applied to real data acquired during the INTIFANTE'00 sea trial. Conclusions and future work are presented in Section 3.6

3.2 Theoretical background

The objective of this Section is to set up the theoretical background for analysing the implications of probe-signal windowing operation in pTR performance when applied to digital communications in the presence of acoustic noise. An 'ideal' pTR where the TRM basic principle associated assumptions [2] are fulfilled will be considered.

The pTR communications system in the presence of a noisy environment involves the filtering of deterministic or stochastic signals by deterministic or stochastic IRs resulting in noise terms whose output statistical characteristics are required for the computation of the pTR output SNR. In Appendix A.1 the autocorrelation of those noise terms is derived in closed form. In Appendix A.2, for a perfect waveguide the time-window operation mode-filtering relation will be established and applied to time-windowed pTR.

---

[1] i.e., with a sufficiently large number of hydrophones spanning almost whole the water column

[2] *i.e.*, that there is a sufficiently large number of hydrophones, the vertical array is spanning the whole water column and the propagation environment is time-invariant.

3.2.1 Digital communications with passive Time Reversal

Figure 3.1 shows the baseband equivalent of the source-channel-receiver representation of the pTR processor for one hydrophone. In a first step (upper path in Figure 3.1) a duly time windowed and phase conjugated channel IR estimate is computed. In a second step (lower path in Figure 3.1) the deconvolution of the transmitted data sequence a_n distorted by the underwater channel is accomplished using the estimated channel IR computed in the first step. In that figure, the transmitting and receiving filter, $p(t)$, is a fourth-root raised cosine pulse [3]. In the sequel

$$p_m(t) = \underbrace{p(t) * ... * p(t)}_{\text{m times}}, \tag{3.1}$$

represents the m-times self-convolution of $p(t)$ such that $p_4(t)$ is the raised-cosine pulse shape function. In the IR estimation step, $p_2(t)$ is used as a narrowband filter resulting in a square-root raised cosine shape. In the second step $p(t)$ is used as the transmitting pulse shape for the data sequence that, in conjunction with $p(t)$ in the receiver side, results in a received data sequence square-root raised cosine pulse shaped, distorted with the baseband equivalent channel IR $h_i(t)$. With such configuration, in presence of a non-distortive channel (that is $h_i(t) = h_i'(t) = \delta(t)$) and with a sufficiently large time-window, one can guarantee a raised cosine pulse shape for the data sequence in the pTR output signal $z(t)$.

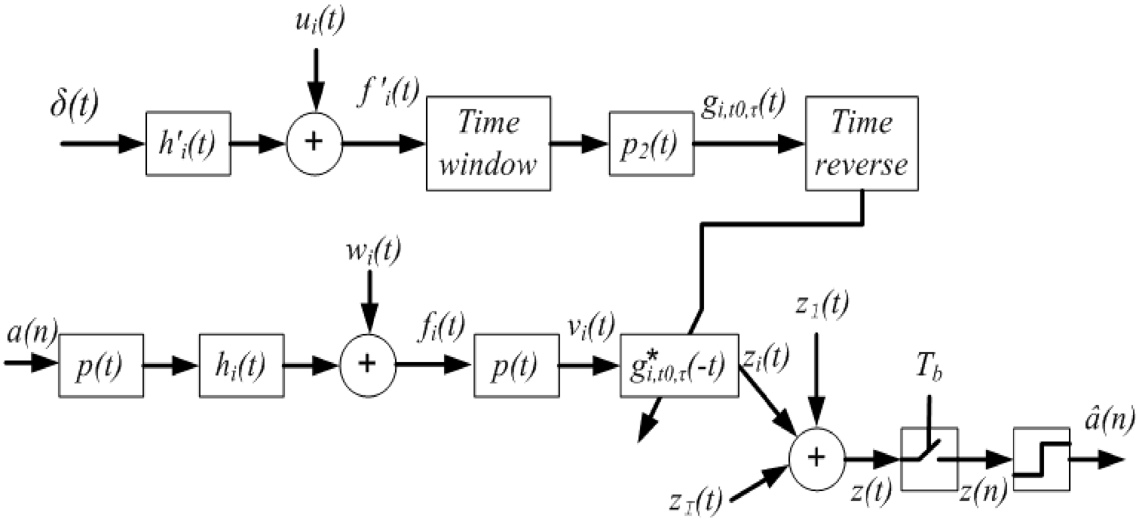

Figure 3.1: Block-diagram for the application of passive time reversal to digital communications.

Let us assume that the transmitted signal is Pulse Amplitude Modulated (PAM) written as

$$s(t) = a(t) * p(t), \tag{3.2}$$

---

[3] for notation convenience it is assumed that $p(t)$ is the inverse Fourier transform of $\sqrt[4]{P_4(f)}$, where $P_4(f)$ is a raised cosine pulse in the frequency domain.

with

$$a(t) = \sum_{n=-\infty}^{+\infty} a_n \delta(t - nT_b), \tag{3.3}$$

where a_n is a zero mean symbol sequence assumed to be white with power σ_a^2, and T_b is the symbol duration.

Assuming the acoustic channel as a time-invariant linear system with impulse response $h_i(t)$, the received data-signal at hydrophone i is given by

$$v_i(t) = h_i(t) * a(t) * p_2(t) + w_i(t) * p(t), \tag{3.4}$$

where $w_i(t)$ is an additive zero mean white noise with power σ_w^2, assumed to be uncorrelated with the signal and from sensor to sensor. When the probe-signal is a dirac impulse the received probe (upper path in Figure 3.1) is written as

$$f_i'(t) = h_i'(t) + u_i(t) \tag{3.5}$$

where $u_i(t)$ is the channel additive noise sequence with the same properties as $w_i(t)$ and independent from it, $h_i'(t)$ is the same channel impulse response as $h_i(t)$ (no environment/geometry mismatch case) and the $'$ denotes that there is an unspecified time delay between the two impulse responses (IRs).

The time-window operator multiplies the input signal with a unit-gate function of length τ and starting point t_0 (A3), thus

$$f_{i,t_0,\tau}'(t) = \begin{cases} f_i'(t) & t \in [t_0, t_0 + \tau] \\ 0 & \text{elsewhere} \end{cases}. \tag{3.6}$$

The narrowband time-limited IR estimate is then obtained as

$$g_{i,t_0,\tau}(t) = f_{i,t_0,\tau}'(t) * p_2(t). \tag{3.7}$$

Finally, the time limited IR estimation is phase conjugated or, equivalently in the time domain, time-reversed and conjugated. The pTR output for channel i is therefore

$$z_i(t) = g_{i,t_0,\tau}^*(-t) * v_i(t) \tag{3.8}$$

where $v_i(t)$ is given by (3.4). Replacing (3.3), (3.4) and (3.7) in (3.8) and summing over the hydrophone index i, the pTR output signal can be written as

$$z(t) = y(t) + x1(t) + x2(t) + x3(t), \tag{3.9}$$

where $y(t)$ contains the desired data-signal contaminated with ISI and the other three terms are noise disturbances, defined as

$$\begin{aligned} y(t) &= \sum_{n=-\infty}^{+\infty} a_n c(t - nT_b) \\ x1(t) &= \sum_{n=-\infty}^{+\infty} a_n e(t - nT_b) \\ x2(t) &= p_3(t) * \sum_{i=1}^{I} h^*_{i,t0,\tau}(-t) * w_i(t) \\ x3(t) &= p_3(t) * \sum_{i=1}^{I} u^*_{i,t0,\tau}(-t) * w_i(t), \end{aligned} \tag{3.10}$$

where

$$\begin{aligned} c(t) &= p_4(t) * \sum_{i=1}^{I} h_i(t) * h^*_{i,t0,\tau}(-t) \\ e(t) &= p_4(t) * \sum_{i=1}^{I} h_i(t) * u^*_{i,t0,\tau}(-t). \end{aligned} \tag{3.11}$$

The next logic step will be to derive the pTR output SNR using (3.9) and proceed to its maximization relative to the time-window parameters t_0 and τ, respectively start time and duration. Before doing so, and in order to motivate this optimization procedure, Figures 3.2 and 3.5 anticipate the results obtained, respectively in simulation (Section 3.4) and with real data (Section 3.5). Figures 3.2 and 3.5 shows the depth dependent IRs for a reduced time scale where the sign 'o' indicates the time-window starting instant t_0, sign '*' indicates the optimum time-window duration, the one that guarantees the pTR best performance $t_0 + \tau_{opt}$ as derived from the optimization of the output SNR, and sign '+' indicate the maximum time-window duration considered in the analysis, $t_0 + \tau_{max}$. Close inspection in Figure 3.5, for the real data noise contaminated IR estimates, reveals that as the time-window increases, more IR paths are included in $h_{i,t_0,\tau}(t)$ and simultaneously more noise power is included in $u_{i,t_0,\tau}(t)$. Those two factors will affect the pTR performance in opposite directions, resulting in an optimum time-window that does not include all the arriving paths ('*' signs). It should be noted however that, in order for the system to operate as a pTR, the time windowing operation must contain at least the main arrivals of the channel IRs. When operating with a vertical line array this can be done by using the same time-window for all hydrophones since at long ranges, greater than a few water depths, the main arrivals approximate plane waves. Under those conditions t_0 must be set before the main arrivals and τ must include the first arriving paths. In order to proceed to the output SNR maximization one needs to first derive the various noise cross terms that will appear in the SNR expression denominator.

3.2.2 Autocorrelation of the noise terms

In order to obtain a closed form expression for the pTR SNR output it is important to characterize each noise disturbance $x1\ldots3$ individually, namely by determining their mean and variance. Their mean is easily calculated since the additive noise is zero mean, then $E\{x1\ldots3(t)\}=0$. The variance can be obtained as the value of the autocorrelation function at the origin after demonstrating that the noise terms are zero-mean Wide Sense Stationary (WSS).

The autocorrelation function of $x3(t)$ can be obtained considering that the autocorrelation of the convolution is equal to the convolution of the autocorrelations and that the autocorrelation of a sum is the sum of the autocorrelation plus the cross correlated terms that will be zero for independent summation terms. Assuming the independence of noise from sensor to sensor, and (A7), the autocorrelation of $x3$ will be

$$\begin{aligned}
R_{x3}(t+t',t) &= E\{x3(t+t')x3(t)\} \\
&= r_{p_3}(t')*\sigma_w^2\sigma_u^2\tau I r_\delta(t') \\
&= r_{p_3}(t')\sigma_w^2\sigma_u^2\tau I \\
&= R_{x3}(t'), \qquad (3.12)
\end{aligned}$$

where σ_w^2 and σ_u^2 are the noise variances of $w(t)$ and $u(t)$ respectively, τ is the window length, I is the number of hydrophones, $r_{p_3}(t')$ is the autocorrelation of $p_3(t)$ and $r_\delta(t')$ is the autocorrelation of $\delta(t)$. In order to compute its variance it is important to note that $x3(t)$ is a WSS stochastic signal.

For $x2(t)$ the autocorrelation can be computed considering (A7) and (A11) for each hydrophone i,

$$\begin{aligned}
R_{x2,i}(t+t',t) &= E\{x2_i(t+t')x2_i(t)\} \\
&= r_{p_3}(t')*r_{h,i,t_0,\tau}(t')*\sigma_w^2\delta(t') \\
&= r_{p_3}(t')*r_{h,i,t_0,\tau}(t')\sigma_w^2 \\
&= R_{x2,i}(t'). \qquad (3.13)
\end{aligned}$$

Thus, since the autocorrelation of the sum over the entire array is the sum of the autocorrelations given by (3.13) plus the cross-correlation terms that are null due to the noise independence from sensor to sensor, the autocorrelation of $x2(t)$ is given by

$$R_{x2}(t')=r_{p_3}(t')*\sigma_w^2\sum_{i=1}^{I}r_{h,i,t_0,\tau}(t'). \qquad (3.14)$$

This equation can be further simplified considering that for a well positioned time-window that covers the main arrival paths of $h_i(t)$, according to the TRM basic principle associated assumptions, and considering (A10)

$$\sum_{i=1}^{I}r_{h,i,t_0,\tau}(t')\approx C_{x2}(t_0,\tau)\delta(t'), \qquad (3.15)$$

with the time-window dependent coefficient

$$C_{x2}(t_0,\tau) \approx \sum_{i=1}^{I} \int_{t_0}^{t_0+\tau} h_i(t)h_i^*(t)dt, \tag{3.16}$$

where $C_{x2}(\cdot)$ is a baseband version of C' from (A23).

Thus the autocorrelation of $x2(t)$ is approximately equal to

$$\begin{aligned} R_{x2}(t') &\approx r_{p_3}(t') * \sigma_w^2 C_{x2}(t_0,\tau)\delta(t') \\ &\approx r_{p_3}(t')\sigma_w^2 C_{x2}(t_0,\tau), \end{aligned} \tag{3.17}$$

which means that $x2$ is also a WSS stochastic signal.

In (3.15) it was considered that IRs bandwidth is large enough in order to attain convergence of the *sinc* function to an impulse (see Appendix A.2). Nevertheless such assumption can be relaxed since in (3.17) the *sinc* convolution with $r_{p_3}(t')$ behaves as an identity in the signal bandwidth. In the following, with no loss of generality, the *sinc* will be ignored when similar operations to (3.15) appear.

For the autocorrelation of $x1(t)$, the signal will be considered as the convolution of two continuous stochastic signals

$$x1(t) = a(t) * e(t), \tag{3.18}$$

where $a(t)$ and $e(t)$ are respectively given in (3.3) and (3.11). The autocorrelation of $e(t)$ is obtained by applying (A18) to the summation terms $h_i(t) * u^*_{i,t0,\tau}(-t)$, and by applying (A2)

$$\begin{aligned} R_e(t+t',t) &= \int\int r_{p_4}(t'-\gamma)\sigma_u^2 C_{x1}(\gamma,\nu,\tau)d\nu d\gamma \\ &= \sigma_u^2 \int r_{p_4}(t'-\gamma) \int C_{x1}(\gamma,\nu,\tau)d\nu d\gamma, \end{aligned} \tag{3.19}$$

where $C_{x1}(\cdot,\cdot,\cdot)$ is a summation of terms analogous to $A_\tau(\cdot,\cdot,z=0)$ given in (A17), that is

$$C_{x1}(t',t,\tau) = \sum_{i=1}^{I} \int_{t-\tau}^{t} h_i(\lambda+t')h_i^*(\lambda)d\lambda. \tag{3.20}$$

In (3.19) the integral of (3.20) is given by

$$\begin{aligned} \int_{-\infty}^{+\infty} C_{x1}(t',t,\tau)dt &= \int_{-\infty}^{+\infty} \sum_{i=1}^{I} \int_{t-\tau}^{t} h_i(\alpha+t')h_i(\alpha)d\alpha dt \\ &= \sum_{i=1}^{I} \int_{-\infty}^{+\infty} \int_{-\infty}^{+\infty} h_i(\alpha+t')h_i(\alpha)\Pi_{t-\tau,\tau}(\alpha)d\alpha dt \\ &= \sum_{i=1}^{I} \int_{-\infty}^{+\infty} h_i(\alpha+t')h_i(\alpha) \int_{-\infty}^{+\infty} \Pi_{t-\tau,\tau}(\alpha)dtd\alpha \\ &= \tau \sum_{i=1}^{I} \int_{-\infty}^{+\infty} h_i(\alpha+t')h_i(\alpha)d\alpha \\ &\approx \tau C_h \delta(t'), \end{aligned} \tag{3.21}$$

where $\Pi_{t-\tau,\tau}(\alpha)$ is an unit-gate sliding window, similar to (A3) with constant area equal to τ, and

$$C_h = \sum_{i=1}^{I} \int h_i(t) h_i^*(t) dt, \tag{3.22}$$

considering analogous assumptions as those for $x2(t)$. In (3.22) C_h is a baseband version of C in (A21). The autocorrelation of $e(t)$ will be given by

$$R_e(t+t', t) = R_e(t') = r_{p_4}(t')\sigma_u^2 \tau C_h, \tag{3.23}$$

where $e(t)$ becomes a WSS stochastic signal.

The PAM signal $a(t)$ is a cyclostationary signal [36, 41] given by (3.3), but here the strategy used in [36] will be adopted whereby $a(t)$ is changed to $a(t) = \sum_{n=-\infty}^{+\infty} a_n \delta(t + \Theta - nT_b)$, where Θ is an unknown timing phase that reflects the fact that the origin of the time axis is arbitrary. By considering that Θ is uniformly distributed over the interval $[0, T_b[$, $a(t)$ becomes WSS with autocorrelation given by

$$R_a(t') = \frac{\sigma_a^2}{T_b} r_\delta(t'), \tag{3.24}$$

where $r_\delta(t')$ is the autocorrelation of the dirac impulse. Finally, the autocorrelation of $x_1(t)$ can be seen as the convolution of the autocorrelations of $e(t)$ and $a(t)$, and is given by

$$R_{x1}(t') = r_{p_4}(t') \frac{\sigma_a^2}{T_b} \sigma_u^2 C_h \tau, \tag{3.25}$$

where one can see that $x_1(t)$ is also WSS.

3.2.3 Signal and noise power

In order to compute the pTR output SNR (SNR_{out}) the signal and the noise terms power must be obtained. Since we have already computed the noise terms autocorrelation and shown that they are zero mean WSS processes, their power can be easily computed by considering its variance equal to the autocorrelation at the origin

$$\sigma_{x3}^2(\tau) = R_{x3}(0) = r_{p_3}(0)\sigma_w^2 \sigma_u^2 \tau I, \tag{3.26}$$

$$\sigma_{x2}^2(t_0, \tau) = R_{x2}(0) = r_{p_3}(0)\sigma_w^2 C_{x2}(t_0, \tau), \tag{3.27}$$

$$\sigma_{x1}^2(\tau) = R_{x1}(0) = r_{p_4}(0) \frac{\sigma_a^2}{T_b} \sigma_u^2 C_h \tau. \tag{3.28}$$

In (3.9) the PAM data-signal has pulse shape $c(t)$ given by (3.11), and considering similar assumptions to those underlying (3.24) its power is

$$\sigma_y^2(t_0, \tau) = \frac{\sigma_a^2}{T_b} [C_y(t_0, \tau)]^2 r_{p_4}(0), \tag{3.29}$$

where $C_y(t_0,\tau)$ is computed in a similar manner to $C_{x2}(t_0,\tau)$ and becomes

$$\begin{aligned} C_y(t_0,\tau)\delta(t') &\approx \sum_{i=1}^{I}\int_{-\infty}^{\infty} h_i(t+t')h^*_{i,t_0,\tau}(t)dt \\ &\approx \sum_{i=1}^{I}\int_{t_0}^{t_0+\tau} h_i(t+t')h^*_i(t)dt. \end{aligned} \tag{3.30}$$

Under those conditions $[C_y(t_0,\tau)]^2$ is the autocorrelation at the origin of $C_y(t_0,\tau)\delta(t')$, and $C_y(.)$ is a baseband version of C'' in (A25).

In the above equations the time-window dependent factors $C_.(.)$ that affects the signal and noise power terms are equivalent to TRM gains at the focal point for different configurations of the channel IRs (limited and/or unlimited). These constants are related with each other and it is important to note that when TRM associated assumptions are fulfilled C_{x2} is equal to C_y and as τ increases they both converge to C_h.

3.3 The passive time-reversal output SNR and its maximum

The pTR communication system firstly recombines energy as a matched filter, whose function is to maximize the SNR in each hydrophone and then sums all z_i signals (see Figure 3.1) to further reduce SNR and to reduce the ISI [56]. Considering that the array structure is adapted to the propagation environment such that the residual ISI is considered negligible the time-windowing optimization can be obtained from a closed form expression for the pTR output SNR.

The pTR communication system signal and noise power terms have already been found in (3.26), (3.27), (3.28) and (3.29). Since $x1$, $x2$ and $x3$ are zero mean independent random terms the variance of the sum is simply the sum of the variances and the pTR output SNR will be given by

$$SNR_{o,ideal}(t_0,\tau) = \frac{\sigma^2_y(t_0,\tau)}{\sigma^2_{x3}(\tau)+\sigma^2_{x2}(t_0,\tau)+\sigma^2_{x1}(\tau)}, \tag{3.31}$$

where its dependence on the window length, τ, and starting time t_0 is perfectly clear. Such pTR output SNR is ideal in the sense that it considers that there is no residual ISI.

After the pTR, the data frame detection can be made, as in Figure 3.1, in two steps: by sampling the pTR output signal $z(t)$ at the symbol period, T_b, that will result in the sampled signal $z(nT_b)$ corrupted by noise and ISI, followed by a slicer/detector that estimates the transmitted symbols. The full elimination of the ISI can only be attained if the pTR associated assumptions are fulfilled and, as deduced in Appendix A.2, can be attained even for a short time window. In a real scenario the array does not densely cover the entire water column and the overall pTR IR becomes a dirac-pulse corrupted with residual multipath that in the pTR communication system results in residual ISI.

For digital communications purpose the residual ISI should be considered as a corruption term similar to a noise term and can be incorporated in the SNR_{out} of (3.31) in a similar manner of equation (33) of [56]. Despite the influence of the residual multipath over the noise terms the pTR output SNR in presence of ISI can be approximated by

$$SNR_{o,isi}(t_0,\tau) \approx \frac{\sigma_y^2(t_0,\tau)}{\sigma_y^2(t_0,\tau)[ISI(t_0,\tau)] + \sigma_{x3}^2(\tau) + \sigma_{x2}^2(t_0,\tau) + \sigma_{x1}^2(\tau)}, \tag{3.32}$$

where the ISI is given by the ratio between the power of the multipath spread of the pTR overall IR at the symbol rate and its main path power,

$$ISI(t_0,\tau) = \frac{\sum_{n\neq 0} |p_{TR}(nT_b, t_0, \tau)^2|}{|p_{TR}(0, t_0, \tau)^2|} \tag{3.33}$$

where

$$p_{TR}(nT_b, t_0, \tau) = \sum_{i=1}^{I} [h_i^*(-t, t_0, \tau) * h_i(t)] * p_4(t)\Bigg|_{t=nT_b} \tag{3.34}$$

is the baseband version of the pTR IR (A24) affected by the time window operation and sampled at the symbol rate $1/T_b$.

The pTR output SNR in presence of ISI given by (3.32) can also be computed considering the MSE between the transmitted symbols and the detector input $\overline{|a(n) - z(n)|^2}$ (see Figure 3.1) as in [56, 41]

$$SNR_{o,mse}(t_0,\tau) = \frac{1}{MSE(t_0,\tau)} - 1. \tag{3.35}$$

When the noise power dominates over the ISI $SNR_{o,mse}(t_0,\tau) \approx SNR_{o,ideal}(t_0,\tau)$, but when ISI dominates $SNR_{o,mse}(t_0,\tau) \approx ISI^{-1}(t_0,\tau)$ while the $SNR_{o,ideal}$ increases as the input noise power decreases. In spite of the differences between the $SNR_{o,ideal}$ given in (3.31) and $SNR_{o,mse}$ given in (3.35), when in presence of a well designed array that ensures $ISI^{-1} > SNR_{o,ideal}$ at the pTR output, their maxima occur for the same time-window duration, which will be clarified in Section 3.4. Window parameters for optimal detection can therefore be predicted from the pTR output SNR given in (3.31).

Equation (3.31) can be simplified since in (3.27) and (3.28) $C_{x2}(t_0,\tau) \ll \tau C_h$, $\sigma_w^2 = \sigma_u^2$, $\sigma_a^2/T_b \gg 1$, and $r_{p_4}(0) > r_{p_3}(0)$, such that $\sigma_{x2}^2(t_0,\tau) \ll \sigma_{x1}^2(t_0,\tau)$. Then (3.31) reduces to

$$SNR_{o,ideal}(t_0,\tau) \approx \frac{\sigma_y^2(t_0,\tau)}{\sigma_{x3}^2(\tau) + \sigma_{x1}^2(\tau)}, \tag{3.36}$$

and the approximation improves as τ increases, and more channel IR paths are included in the time-window.

For values of $\tau > 0$ one can define

$$\Phi(t_0,\tau) = \frac{C_y(t_0,\tau)}{\tau^{\frac{1}{2}}}, \tag{3.37}$$

where $C_y(t_0,\tau)$ can be computed from (3.30) as

$$C_y(t_0,\tau) = \sum_{i=1}^{I} \int_{t_0}^{t_0+\tau} |h_i(t)|^2 dt, \tag{3.38}$$

that is the summation of the energy cumulative functions of the channels IRs at all hydrophones. Using (3.37) in (3.36) it results that

$$\frac{SNR_{out}(t_0,\tau)}{\Phi^2(t_0,\tau)} = \frac{(\sigma_a^2/T_b)r_{p4}(0)}{\sigma_w^2\sigma_u^2 I r_{p3}(0) + (\sigma_a^2/T_b)\sigma_u^2 C_h r_{p4}(0)}. \tag{3.39}$$

Since the right term of the equation is constant with τ, $SNR_{out}(t_0,\tau)$ and $|\Phi(t_0,\tau)|^2$ have the same shape and the optimum τ that yields the global maximum for $SNR_{out}(t_0,\tau)$ is given by

$$\tau_{opt} = \arg\max(\Phi(t_0,\tau)). \tag{3.40}$$

where, with no loss of generality, the time-window starting point t_0 was considered to be chosen arbitrarily before the main path arrivals of the $h_i(t)$ IRs. Equations (3.37) and (3.40) state the remarkable result that the time-window that ensure the pTR maximum output SNR does not depend on the input noise power, and that it only depends on the channel IRs (see (3.38)). Since $C_y(t_0,\tau)$ can be seen as the overall pTR IR, $\Phi^2(t_0,\tau)$ represents its power and τ_{opt} the time-window length that guarantees an higher power of the pTR operator.

In a real situation $C_y(t_0,\tau)$ is not available since only a noisy version of $h_i(t)$ can be estimated in the pTR processor. An estimate of $\hat{C}_y(t_0,\tau)$ can be computed as

$$\begin{aligned}\hat{C}_y(t_0,\tau) &= \sum_{i=1}^{I}\int_{t_0}^{t_0+\tau} E\{|h_i(t)+u_i(t)|^2\}dt \\ &= C_y(t_0,\tau) + \sigma_u^2 I\tau, \end{aligned} \tag{3.41}$$

it results that

$$C_y(t_0,\tau) = \hat{C}_y(t_0,\tau) - \sigma_u^2 I\tau \tag{3.42}$$

where here $h_i(t) + u_i(t)$ is considered to be a narrowband estimate of the channel IRs. Replacing (3.42) in (3.37) yields an estimate of the optimal τ for real data

$$\begin{aligned}\hat{\Phi}(t_0,\tau) &= \frac{\hat{C}_y(t_0,\tau) - \sigma_u^2 I\tau}{\tau^{\frac{1}{2}}} \\ \hat{\tau}_{opt} &= \arg\max\hat{\Phi}(t_0,\tau) \end{aligned} \tag{3.43}$$

A good estimate of $\hat{C}_y(t_0,\tau)$ should be used in (3.42) if good results using real data are expected. It will be seen in Section 3.5 that when estimating $\hat{C}_y(t_0,\tau)$ with a single realization the estimate $\hat{\Phi}(t_0,\tau)$ becomes sensitive to noise, but using an average of (3.42) realizations improves the quality of results.

3.4 Performance simulations in realistic channels

The simulation scenario comprises a range independent acoustic channel with 100 m depth, over a 1.5 m thick silt sub-bottom and a gravel like bottom. The arrival pattern computed with the Bellhop ray/beam model [27], for a source depth of 60m and a source-array range of 1.5km, can be seen in Figure 3.2, where the multipath spans over 100 ms, as usual with a higher concentration of energy in the first arrivals. The beginning of the time-window was chosen manually just before the first arriving path, and is represented by a vertical line of 'o' in Figure 3.2 where the '+' indicates the maximum time-window length considered in the analysis, and '*' the optimum time-window length for pTR output SNR optimization as described below.

Two cases were considered:

1. The Low Frequency (LF) case that comprises a 16-hydrophone-4-meter-spaced VLA with the first hydrophone placed at 30m, the transmitted data signal is a 2-PSK PAM signal with a 50% rolloff fourth-root raised-cosine pulse shape, the carrier frequency is of 1600Hz, and the data rate is 300 bits/s.

2. The High Frequency (HF) case that comprises a 8-hydrophone-8-meter-spaced Vertical Line Array (VLA) with the first hydrophone placed at 30m, the transmitted data signal is a 2-PSK PAM signal with a 50% rolloff fourth-root raised-cosine pulse shape, the carrier frequency is of 10kHz, and the data rate is 2000 bits/s.

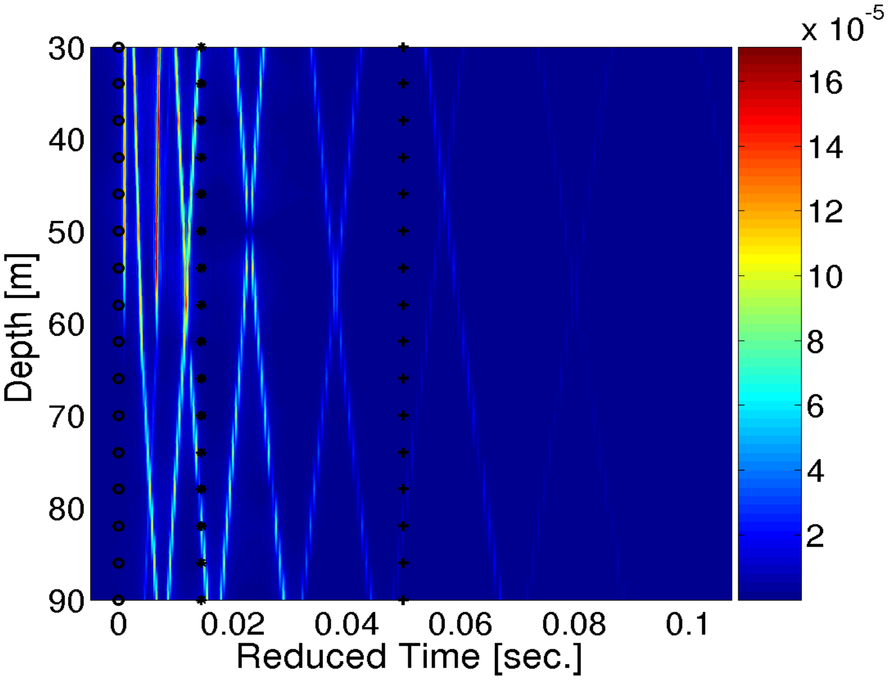

Figure 3.2: Simulated depth dependent broadband arriving pattern over a realistic scenario: start time 'o', optimum window duration '*' and maximum window duration '+'.

For the LF case a low pTR residual ISI is expected due to the low symbol rate and the high number of hydrophones. In opposition an high pTR residual ISI will be expected in the HF case. For each of the two cases Monte Carlo runs under low and high input SNR will be conducted.

Figure 3.3 shows the pTR output SNR (in dB) as a function of window length parameterized by the input SNR ($\mathrm{SNR}_{\mathrm{in}}$), for the LF case (a) and the HF case (b). In each case, pTR output SNR results are shown via Monte-Carlo simulation with the MSE-based form (3.35) (‘□’), using the ideal pTR closed form expression (3.31) (‘∇’), and for the residual ISI given by the inverse of (3.32) (‘o’).

For low residual ISI in LF case Figure 3.3(a) shows that for a $SNR_{in} \approx -25$ dB good agreement is obtained between the ideal pTR and MSE curves. For high $SNR_{in} \approx -10$ dB the residual ISI of the TR operator becomes dominant and leads to saturation of SNR_{mse}. For high residual ISI, in the HF case, Figure 3.3(b) shows that for a low $SNR_{in} \approx -25$ dB good agreement in shape is obtained between the ideal pTR and MSE curves a better agreement would be obtained if instead of the SNR_{out} given by (3.31) the SNR_{out} given by (3.32) was used, nevertheless the agreement in shape its enough for the optimum time window length prediction. For high $SNR_{in} \approx -10$ dB the residual ISI of the TR operator becomes dominant and leads to saturation of SNR_{mse}.

The overall SNR gain of the pTR is given by the array number of elements that is approximately 12dB (for 16-hydrophone, LF case) and 9dB (for 8-hydrophone, HF case), the time-window length SNR and ISI improvement. In what concerns the ISI as the time-window includes more paths its tendency is to reduce as it can be observed in the enhancement of the $SNR_{o,isi} = ISI^{-1}$ curve of Figure 3.3(b), nevertheless in Figure 3.3(a) shows that the ISI^{-1} curve present a local maximum at 6ms and the global maximum at 30ms revealing that such tendency behave nonlinearly with the time-windowed multipath structure of the channel.

As previously mentioned for the low SNR_{in} case the optimum time-window is ruled by the $SNR_{o,ideal} \approx SNR_{o,mse}$ curves, their maxima reveal that the optimum time-window length would be 15ms, approximately 5 symbols for the LF case, and 13.5ms, approximately 27 symbols for the HF case. In the high SNR_{in} case the optimum time-window is ruled by the ISI and the $SNR_{o,mse}$ curve is maximum when the $SNR_{o,isi}$ is maximum.

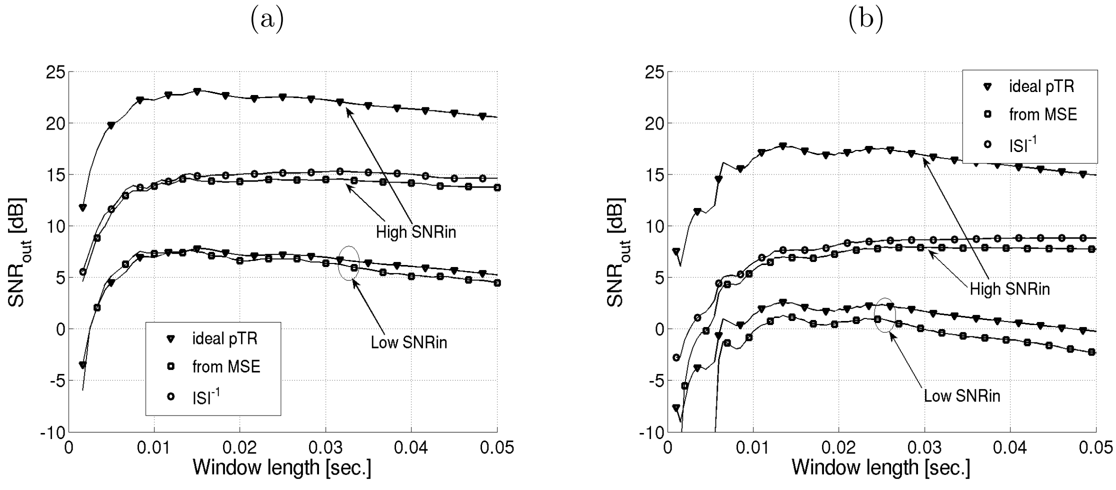

Figure 3.3: Simulated pTR output SNR for the LF case (a), and for the HF case (b).

Figure 3.4 shows the behavior of $\Phi(t_0, \tau)$ (3.37) versus time-window length for the LF and the HF cases. It can be seen that, as predicted by the theoretical derivation, the maxima clearly coincide with those of $SNR_{o,ideal}$ in Figure 3.3 both for the LF case with $\tau_{opt} = 15$ms and the HF case with $\tau_{opt} = 13.5$ms. More than detecting the optimum time window when the SNR dominates over the ISI the $\Phi(t_0, \tau)$ curve shape agrees well with the $SNR_{o,ideal}$ and $SNR_{o,mse}$ curves shape.

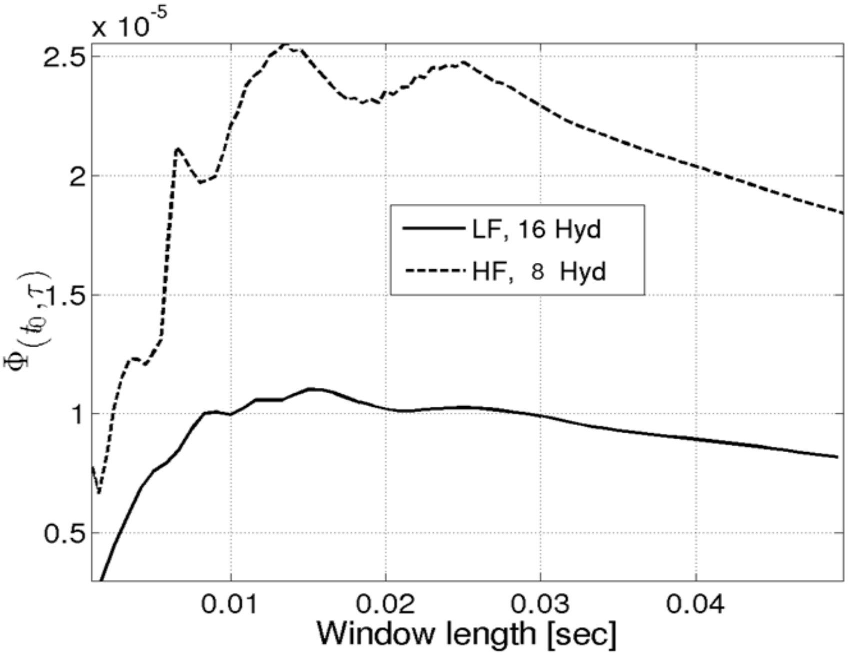

Figure 3.4: Simulated performance of the proposed optimal time-window prediction method using (3.37) and (3.40) for the LF and HF cases

3.5 Experimental results

The experimental data were acquired during the INTIFANTE'00 sea trial that took place off the town of Setúbal, approximately 50km south of Lisbon (Portugal) in October 2000 [28]. This paper concentrates on the Binary Phase Shift Keying data collection. The scenario was similar to that used in Section 3.4 with the main differences being that with real data there are noise corruption and geometric/environment mismatch between the probe-signal and the data transmissions. The acoustic source was suspended from the free drifting oceanographic vessel - NRP D. Carlos I - at a nominal depth of 60 m. The receiver was a surface suspended 16-equispaced-hydrophone vertical line array spanning nominal depths between 31 an 91 m. The source range distance was approximately 1420 m ± 100 m. Nine sequential transmissions (in the following referred to as shot 1 to 9) will be considered, each one composed of a probe-signal transmitted 0.5 seconds before a 5 second PSK data stream, with a repetition rate of 7 seconds.

During the INTIFANTE'00 sea trial the pTR based data communications system was similar to that of Figure 3.1, with the $p_2(t)$ narrowband filter of the IR estimation operation (path above in Figure 3.1) distributed between the transmitter and the receiver, i.e., the transmitted probe-signal was a fourth-root raised-cosine pulse, $p_1(t)$, and IR estimates were obtained by pulse compression at the receiver side (see [45] for details).

The estimated arrival pattern for shot 9 can be seen in Figure 3.5. This Figure shows a number of arrival paths that are not as well defined as in the simulations due to noise corruption. Such noise corruption will, obviously, affect the proposed time-window optimization method given by equation (3.43) since $\hat{C}_y(t_0, \tau)$ in (3.41) has to be computed from a single realization of $|h_i(t) + u_i(t)|^2$. In (3.43) the noise variance σ_u^2 was calculated considering the mean noise variance for all hydrophones.

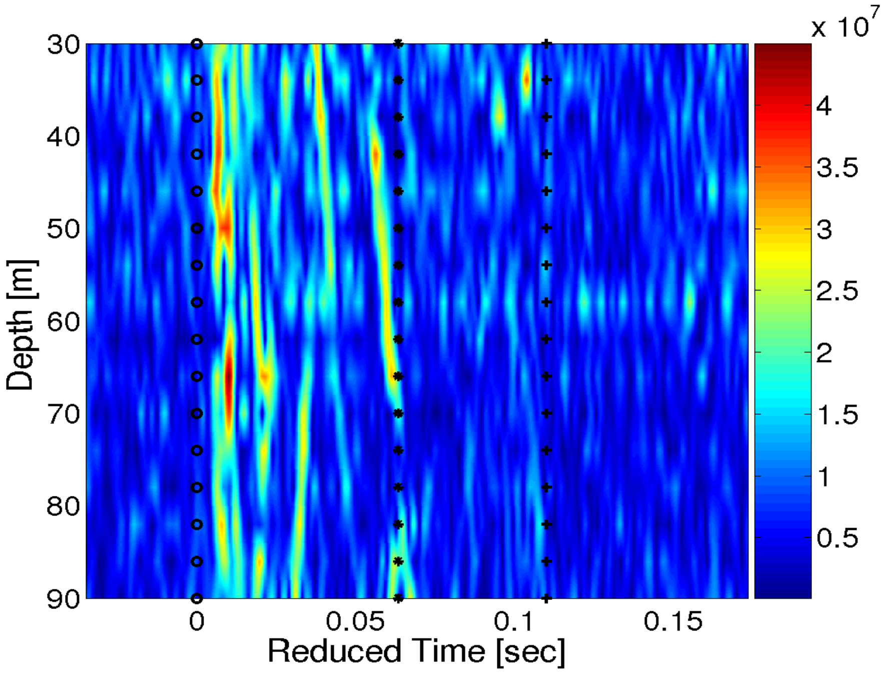

Figure 3.5: Real data vertical array estimated impulse responses: start time '0', optimum window duration '*' and maximum window duration '+'.

Figure 3.6(a) shows the pTR output SNR computed via the MSE at the detector input with (3.35), for the first 3 seconds of data during shot 9. One can see a progressive degradation in performance due to geometric/environmental mismatch in IRs between the probe-signal and data-signal transmissions. Such loss of performance affects primarily larger time windows since those include the later arrivals that are usually considered more prone to fading. Despite this channel variability, Figure 3.6(b) shows that the predicted pTR output SNR maxima, given by the local maxima of $\hat{\Phi}(t_0, \tau)$, are in a good agrement with the true local maxima in the first-second curve of Figure 3.6(a). Although the maxima location are well predicted the first and the second maxima are interchanged.

Figure 3.7 shows analogous results for shot 7. Figure 3.7(a) shows that, although this case presents a pTR output SNR maxima location almost constant during the three seconds of data only the first maximum is clearly predicted by the $\hat{\Phi}(t_0, \tau)$ curve in Figure 3.7(b).

Figures 3.6 and 3.7 present two extreme cases in the pTR output SNR maxima detec-

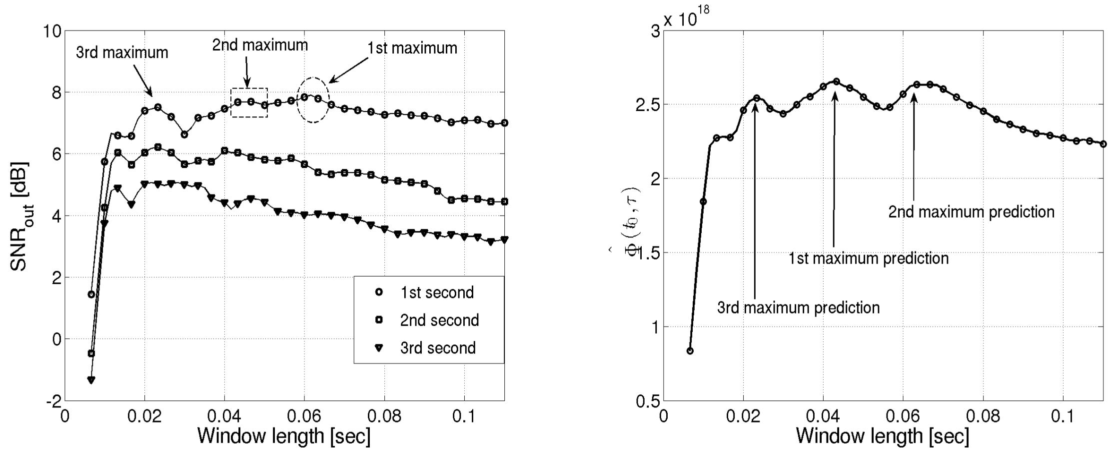
(a) (b)

Figure 3.6: Real data performance of the proposed optimal time-window prediction method obtained in shot 9: pTR output SNR computed by using the MSE at the slicer/detector input (a) and maxima prediction by using (3.43) (b).

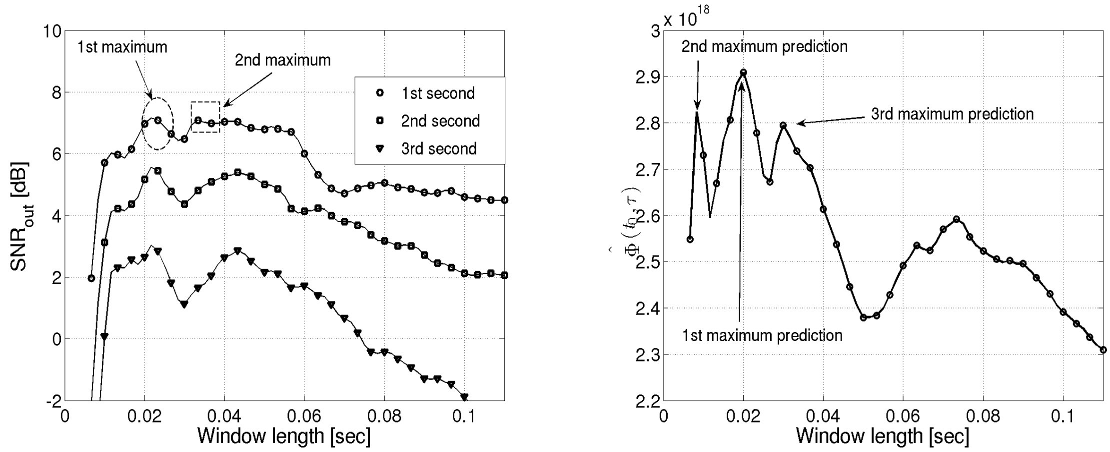
(a) (b)

Figure 3.7: Real data performance of the proposed optimal time-window prediction method obtained in shot 7: pTR output SNR computed by using the MSE at the slicer/detector input (a) and maxima prediction by using (3.43) (b).

tion: in the former the global maximum is predicted to be the second true maximum but a reasonable shape agreement is observed between $\hat{\Phi}(t_0, \tau)$ and the first-second SNR_{out} curves; while in the latter the global maxima is well predicted but a different shape are observed for the two curves. Typically the other shots present an intermediate behavior between shot 7 and 9.

To verify the robustness of the proposed optimization technique a mean analysis over the first second of data using all nine shots is presented in Figure 3.8. The continuous line shows the mean pTR SNR_{out} that partially eliminates the fake (noise-induced) paths and the later path arrivals that are more sensitive to fading. The dashed line shows the mean of $\hat{\Phi}(t_0, \tau)$ over all shots. One can see that these two curves are in excellent agreement and display an almost constant ratio, such that the same maxima locations are predicted. That suggests that pTR performance optimization is affected by channel noise that will introduce a fake path structure. The problem can be overcome by enhanced IR estimation using large time-bandwidth product probe-signal or by averaging a number of closely time spaced probe-signals sent before the data stream.

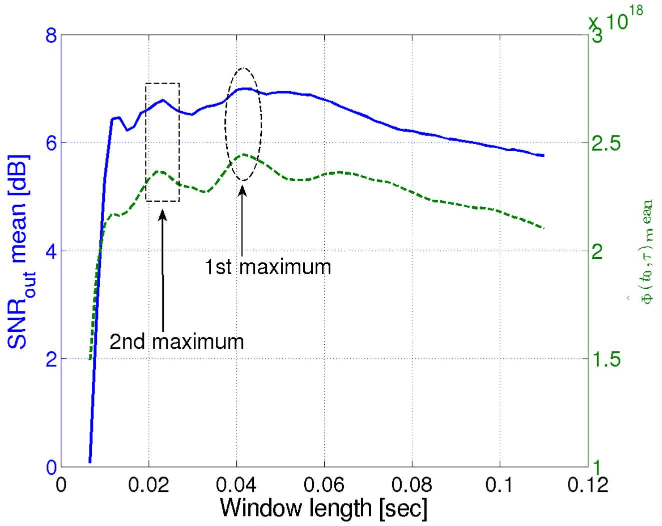

Figure 3.8: Mean analysis over all shots for the real data performance of the proposed optimal time-window prediction method: pTR output SNR output computed by using the shot-mean MSE at the slicer/detector input (a) and shot-mean of the maxima prediction by using (3.43) (b).

Due to the good agrement between the $\hat{\Phi}(t_0, \tau)$ and $SNR_{o,mse}$ curves one can state that the VLA used during the experiment is well design for the ISI reduction required to satisfy the condition that the pTR output SNR dominates over the ISI.

3.6 Conclusion and future work

The problem of time-window optimization when operating a pTR with a VLA for underwater communications was considered. It was found that the optimum time-window simultaneously guarantees higher pTR output SNR and lower MSE at the slicer/detector input, concerning the use of a well design VLA for the environmental conditions to provide a sufficiently low ISI at the pTR output, in order to satisfy the condition that the pTR output SNR should dominate over the ISI. Time window optimization was made possible by the derivation of a closed-form expression for the pTR output SNR (3.31). Such expression allowed the derivation of (3.40) that clearly states that the optimum time-window depends only on the channel IRs and is not dependent on the data signal or noise level. Simulation results confirm and gauge for the theoretic foresight.

When applied to real data the channel IRs are not available and noisy estimates must be used. Even with heavily noise corrupted IRs the developed technique presents a good fit with the pTR output SNR and its global maximum being closely predicted in most of the shots. Noise-related problems in IRs estimation are mainly due (in real data) to the use of low power probe-signals (fourth-root raised cosine pulse). The usage of high power probe-signals such as chirp signals or M-sequences should be addressed in future experiments. Despite its quality, it was found that the optimum time-window loses validity after only a few seconds due to geometric/environment variability. Future developments should address the problem of using the proposed time-window optimization with adaptive pTR-based equalizers.

Although it was developed for pTR, the time-window optimization method can also be applied to aTR by considering that in the latter case the noise term $x3$ does not exist and $x2$ and $x1$ (3.10) are slightly different (see [18]).

Acknowledgments

The authors would like to thank the NATO Undersea Research Centre (NURC) for the loan of the acoustic sound source, the support of Enrico Muzzi and the NRP D. Carlos I crew during the INTIFANTE'00 sea trial. This work was financed by FCT, Portugal, under NUACE project, contract POSI/CPS/47824/2002, ATOMS project, contract POCTI/P/MAR/15296/1999, and the Portuguese Ministry of Defense under the LOCAPASS project.

Chapter 4

Generalization of Waveguide Invariants and Application to Passive Time Reversal

---

Abstract: In most underwater acoustic experiments acoustic sources and hydrophone arrays are moored so as to provide a geometry as controllable as possible. A more operational approach is to use moving sources and drifting acoustic receivers in which case the data exhibits continuous phase and amplitude changes due to depth and range shifts. This may be problematic when the processing of the collected acoustic data requires the use of correlation between successive received signals, e.g., in passive time reversal where a probe-signal is sent ahead of the data for post crosscorrelation. This paper demonstrates that in the passive time reversal context the source-array range, the array and source depth mismatches that occurs during data transmission can be compensated using an appropriate frequency shift of the received probe-signal pressure field. Acoustic simulations and real data collected during the MREA'04 experiment show that the frequency translation required for the geometric mismatch compensation can be computed using invariant properties of the waveguide, and thus provide a potential for substantial processing signal to noise ratio gain in underwater communications between moving platforms.

4.1 Introduction

Active Time reversal (aTR) has been shown to produce temporally and spatially focused acoustic signals in a stationary environment. Such focusing capabilities are a consequence of the time reversal invariance of the linear lossless wave equation describing acoustic propagation in the ocean environment [34] and one of its major goals is the development of underwater coherent communication techniques since focusing is similar to undoing the multipath structure of the channel [17, 11]. Passive Time Reversal (pTR), originally referred to as Passive Phase Conjugation (PPC) [8], is a synthetic version of aTR where a probe-signal is transmitted ahead of the data-signal in order to provide an estimate of the underwater channel Impulse Responses (IRs). Time focusing is then performed at the array side by simply convolving a time reversed version of the estimated IRs with the incoming data-signal [50, 24, 43]. In the presence of a moving source and a free drifting array, there exist three major sources of mismatch: the source-array range shift, the source depth shift and the array depth shift. Due to those geometric mismatches pTR rapidly loses its time focusing capability [29, 45] and up to now there has been no attempt to incorporate a geometric tracking in pTR in order to attain long-term focusing.

For aTR, previous work by Song el al. [55] addresses the focal spot range shift problem using a frequency translation of the array received acoustic field. The technique can be readily applied in pTR, making it possible to perform source-array range tracking. It is based on the β waveguide invariant [21] and only accounts for shifting in range of the focal spot intensity. In what concerns the focal spot depth shift in aTR a different strategy was proposed by Walker [60]. In Walker's work a depth shift of the focal spot has been achieved, but contrarily to the source-array range shift proposed by Song it is not based in simple waveguide invariant properties, and its implementation for the pTR source depth shift compensation in real time does not look straightforward.

In [46] the authors presented preliminary simulations and real data results suggesting that similarly to source-array range shift compensation, source depth shift and array depth shift compensation could be performed by a frequency shift of the acoustic field. It was found that for narrowband signals with a center frequency of 3.6 kHz, frequency shift compensation performs well in the vicinity of the geometric canonical values. Moreover, it was found that associated with the intensity geometric mismatch compensation there is an approximately linear phase. In the present paper the theoretical proof for such compensation capability is given for the source-array range shift, for the array depth and source depth shifts.

The source-array range compensation depends on the waveguide invariant β that relates the modal horizontal phase velocity with the horizontal group velocity. The invariant β summarizes in a single parameter the dispersive characteristics of the acoustic field in a waveguide. In fact, it has been shown by Chuprov [6, 21] that the lines of constant sound intensity, constant rate of change of the phase velocity along the waveguide, and constant envelope group delay have constant slope β in the frequency/range plane. In this paper by using a perfect waveguide a different interpretation of the invariant is given in order to explicitly derive an approximation of the horizontal wavenumber by using the group slowness. Such reinterpretation of β is then used for range shift compensation of the pressure field in intensity and phase by simply using an appropriate frequency shift. Using a similar approach it was found that the vertical wave number can also be approximated by considering a frequency invariant ζ that relates the vertical phase velocity with the horizontal group velocity, which allows for the compensation of source and array depth shifts in pTR applications. The invariants β and ζ has been originally derived by Chuprov [6] taking in consideration only the sound pressure field intensity. The reinterpretation presented in this work allows for the use of the invariants for pressure field intensity and phase compensation when using pTR in a geometric mismatch environment.

When applied to underwater communications the proposed geometric mismatch compensation method provides a longer stability of a pTR communications system by increasing the elapsed time between probe-signal transmissions, but also makes it possible to estimate source and receiving array depth oscillations, and source-receiver range variations, under the form of an environmental equalizer [47].

Section 4.2 explains how the invariant β and ζ can be used to compute an approximation to the horizontal and vertical wave numbers respectively, using the horizontal group slowness. Section 4.3 explains the influence of the geometric mismatch over the pTR in a perfect waveguide and finds compensation strategies using a frequency shift that can be computed with the invariants β and ζ. Section 4.5 heuristically extends the findings to realistic environments, by taking into consideration the WKB approximation and the Pekeris waveguide. Section 4.6 uses real data, narrowband signals centered at 3.6 kHz, with geometric mismatch to demonstrate the usefulness of the new findings, and shows that longer stability of the pTR processor can be attained at least up to a range mismatch of 25 m, and a source depth mismatch and an array depth mismatch of about 0.7 m. Section 4.7 summarizes the compensation procedure and describes possible applications.

4.2 The waveguide invariants

In this section it will be shown that the horizontal wavenumber k_m and the vertical wavenumber γ_m can be computed by a linear approximation of the horizontal group slowness and that such approximation is made possible by the frequency invariants β and ζ, respectively. These results will be obtained for the perfect waveguide and extended heuristically to the Pekeris waveguide and to the WKB approximation in Section 4.5

The derivation draws upon generic results proposed in Appendix B.1, where it is shown that one monotonic function Φ can be linearly approximated by another monotonic function Π using a least-squares approximation or by setting one point of the two functions to the same position and then rotating one of the functions until it fits the other at a different point. The later provides a connection with the current waveguide invariant theory and the former becomes more useful in the context of the pTR geometric mismatch compensation proposed in this paper. The former strategy is a particular case of the latter and ensures smaller approximation error.

4.2.1 Approximation of the horizontal wavenumbers using waveguide invariants

The two strategies of Appendix B.1 can be applied to the approximation of horizontal wavenumbers by their reciprocals by setting $\Phi_m = k_m$ and $\Pi_m = k_m^{-1}$. Using (B4) it results that k_m can be approximated by k'_m with

$$k'_m = -\beta'_{\mu,\nu} k_m^{-1} + \rho'_{\beta,\mu,\nu}, \tag{4.1}$$

where $m = \mu$ and $m = \nu$ are the modes where k_m and k'_m coincide,

$$\beta'_{\mu,\nu} = -\frac{k_\mu - k_\nu}{\frac{1}{k_\mu} - \frac{1}{k_\nu}}, \tag{4.2}$$

and

$$\rho'_{\beta,\mu,\nu} = k_\nu + \beta'_{\mu,\nu}\frac{1}{k_\nu}. \tag{4.3}$$

In a perfect waveguide the horizontal wavenumber is given by

$$k_m = \sqrt{\frac{\omega^2}{c^2} - \gamma_m^2}, \tag{4.4}$$

where γ_m is the vertical wavenumber (which, in a range independent waveguide, is frequency independent). Using (4.4) the horizontal group slowness becomes

$$\frac{1}{u_{h,m}} = \frac{dk_m}{d\omega} = \frac{\omega}{c^2}\frac{1}{k_m}, \tag{4.5}$$

and the horizontal phase slowness

$$\frac{1}{v_{h,m}} = \frac{k_m}{\omega}. \tag{4.6}$$

Multiplying and dividing the fist term of the right hand side of (4.1) by $(\omega/c)^2$, multiplying and dividing the second term by ω, and considering the phase and the group slowness equations for the perfect waveguide (4.5) and (4.6), respectively, it results

$$k'_m = -\beta_{\mu,\nu}\omega\frac{dk_m}{d\omega} + \omega\rho_{\beta,\mu,\nu}, \tag{4.7}$$

where

$$\beta_{\mu,\nu} = -\frac{\frac{k_\mu}{\omega} - \frac{k_\nu}{\omega}}{\frac{\omega}{c^2}\frac{1}{k_\mu} - \frac{\omega}{c^2}\frac{1}{k_\nu}} = -\frac{\frac{1}{v_{h,\mu}} - \frac{1}{v_{h,\nu}}}{\frac{1}{u_{h,\mu}} - \frac{1}{u_{h,\nu}}}, \tag{4.8}$$

and

$$\rho_{\beta,\mu,\nu} = \frac{1}{v_{h,\nu}} + \beta_{\mu,\nu}\frac{1}{u_{h,\mu}}. \tag{4.9}$$

Since (4.7) can be rewritten as

$$\frac{k_m}{\omega} \approx -\beta_{\mu,\nu}\frac{dk_m}{d\omega} + \rho_{\beta,\mu,\nu}, \tag{4.10}$$

it corresponds to linearly approximate the horizontal phase slowness using the horizontal group slowness [35] [1], and $\beta_{\mu,\nu}$ is usually termed waveguide invariant [21] [6]. Here it will be re-termed as horizontal waveguide invariant since it relates the horizontal phase slowness with the horizontal group slowness.

In a similar manner the approximation can be done considering the least-squares form (B1), that can be applied by considering all modes or just a subset M_e of the propagating modes M, resulting in

$$k'_m = -\beta_e\omega\frac{dk_m}{d\omega} + \omega\rho_{\beta,e}, \tag{4.11}$$

---

[1] Figure 1 of reference [35] shows that there is an approximately linear relation between phase speed and group speed. A case with two groups of modes that result in a dual slope linear relation is presented.

where

$$\beta_e = -\frac{\overline{k_m k_m^{-1}} - \overline{k_m}\;\overline{k_m^{-1}}}{\overline{(k_m^{-1})^2} - \overline{k_m^{-1}}^2}\,\frac{c^2}{\omega^2}, \tag{4.12}$$

and

$$\rho_{\beta,e} = \overline{\frac{1}{v_{h,m}}} + \beta_e \overline{\frac{1}{u_{h,m}}}, \tag{4.13}$$

where the bar represents the mean over the assumed subset of modes M_e

Since (4.7) represents a set of linear approximations to k_m it is expected that the approximation in the least-squares error sense (4.11) equals or is close to one of them. In other words, there should exist an effective number of modes M_e and a pair (μ, ν) where $\beta_e \approx \beta_{\mu,\nu}$ and $\rho_{\beta,e} \approx \rho_{\beta,\mu,\nu}$. The approximation using an effective number of modes $M_e < M$ is plausible since in a real situation the waveguide itself filters the higher order modes or, at least, strongly attenuates them. Such filtering corresponds, in the ray mode analogy, to eliminating rays with steeper angles.

In order to develop signal processing techniques that make use of the horizontal wavenumber approximation k'_m it is important to demonstrate the frequency invariance of β_e and $\rho_{\beta,e}$. To establish that property the following auxiliary normalized product will be used

$$\Gamma_{\beta,m} = \frac{k_m k_m}{\gamma_m^2 + k_m^2}, \tag{4.14}$$

where $(\gamma_m^2 + k_m^2) = (\omega/c)^2$ is the wavenumber absolute value.

In the ray mode analogy it is considered by Tolstoy ([58] pp. 102) that the ray solution to the wave equation defines an infinite number of angles corresponding to the angles of incidence. The mode solution defines a finite number of angles that correspond to the rays that reinforce each other. So, in a perfect waveguide each mode is associated to an angle from the horizontal $\pm\theta_m$ that corresponds to an angle of incidence $\left(\frac{\pi}{2} - \theta_m\right)$. In such context the horizontal and the vertical wavenumbers can be defined as

$$\begin{aligned} k_m &= \frac{\omega}{c}\cos\theta_m, \\ \gamma_m &= \frac{\omega}{c}\sin\theta_m, \end{aligned} \tag{4.15}$$

where c represents the waveguide sound speed (assumed isovelocity). By using (4.15), product (4.14) becomes

$$\Gamma_{\beta,m} = \Gamma_\beta(\theta_m) = \cos^2(\theta_m) \tag{4.16}$$

where $\theta_m \in]0, \pi/2[$. Figure 4.1 shows the product $\Gamma_{\beta,m}$ as a function of θ_m (dotted curve). As the frequency increases the angles θ_m shift to the left and new angles, that correspond to new modes/rays, are included every $\omega_{0,m} = (c/D)m\pi$ ([58] pp. 99), where $\omega_{0,m}$ is the mode m cutoff frequency. Although θ_m changes with frequency, for a sufficiently high number of propagating modes M the shape of $\Gamma_{\beta,m}$ remains unchanged, in particular for small values of m where θ_m is densely populated. That means that the shape of $\Gamma_{\beta,m}$ becomes invariant with increasing frequency.

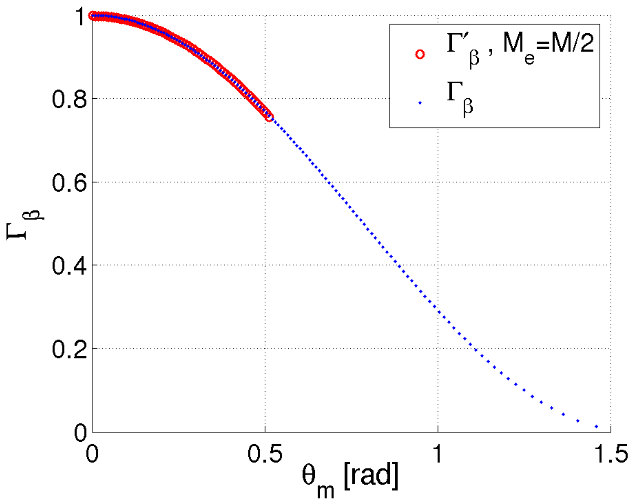

Figure 4.1: Normalized product $\Lambda_{\beta,m}$ (4.16) (dotted line), and its least-squares approximation (4.17) for an effective number of modes $M_e = M/2$ (circles).

Product (4.14) can be approximated by $\Gamma'_{\beta,m}$ with

$$\begin{aligned} \Gamma'_{\beta,m} &= \frac{k'_m k_m}{\gamma_m^2 + k_m^2}, \\ \Gamma'_{\beta}(\theta_m) &= -\beta_e + \rho_{\beta,e}\, c \cos\theta_m, \end{aligned} \tag{4.17}$$

where k'_m is given by (4.11). This is shown by the circles in Figure 4.1 for $M_e = M/2$ corresponding to $\theta_m \in]0, \pi/6[$. Since the $\Gamma_{\beta,m}$ shape is invariant with frequency its approximation $\Gamma'_\beta(\theta_m)$ will be almost invariant, and that makes β_e and $\rho_{\beta,e}$ also almost frequency invariant. In fact as the frequency increases M_e increases and β_e and $\rho_{\beta,e}$ oscillate around a frequency independent mean value with an amplitude that decreases with frequency.

4.2.2 Approximation of the vertical wavenumbers using waveguide invariants

The approximation of the vertical wavenumber using the horizontal wavenumber inverse is analogous to the approximation of the horizontal wavenumber of Section 4.2.1 and is straightforward considering the two linear approximation strategies of Appendix B.1 with $\Phi_m = \gamma_m$ and $\Pi_m = k_m^{-1}$.

Considering the vertical phase slowness

$$\frac{1}{v_{v,m}} = \frac{\gamma_m}{\omega}, \tag{4.18}$$

and the horizontal group slowness for the perfect waveguide (4.5), it results that γ_m can be approximated by γ'_m

$$\gamma'_m = -\zeta_{\mu,\nu}\omega\frac{dk_m}{d\omega} + \omega\rho_{\zeta,\mu,\nu}, \tag{4.19}$$

where

$$\zeta_{\mu,\nu} = -\frac{\frac{\gamma_\mu}{\omega} - \frac{\gamma_\nu}{\omega}}{\frac{\omega}{c^2}\frac{1}{k_\mu} - \frac{\omega}{c^2}\frac{1}{k_\nu}} = -\frac{\frac{1}{v_{v,\mu}} - \frac{1}{v_{v,\nu}}}{\frac{1}{u_{h,\mu}} - \frac{1}{u_{h,\nu}}}, \tag{4.20}$$

and

$$\rho_{\zeta,\mu,\nu} = \frac{1}{v_{v,\nu}} + \zeta_{\mu,\nu}\frac{1}{u_{h,\mu}}, \tag{4.21}$$

where (4.20) defines a constant that will be called vertical waveguide invariant and its invariance with the frequency will be shown at the end of this section.

Similarly to the k_m approximation in the least-squares sense, the approximation can be done considering the least-squares form (B1), yielding

$$\gamma'_m = -\zeta_e \omega \frac{dk_m}{d\omega} + \omega \rho_{\zeta,e}, \tag{4.22}$$

where

$$\zeta_e = -\frac{\overline{\gamma_m k_m^{-1}} - \overline{\gamma_m}\;\overline{k_m^{-1}}}{\overline{(k_m^{-1})^2} - \overline{k_m^{-1}}^2}\,\frac{c^2}{\omega^2}, \tag{4.23}$$

and

$$\rho_{\zeta,e} = \overline{\frac{1}{v_{v,m}}} + \zeta_e \overline{\frac{1}{u_{h,m}}}. \tag{4.24}$$

Since (4.19) represents a set of linear approximations to γ_m it is expected that the approximation in the least-squares sense (4.22) will be close to one of them, that is, there is an effective number of modes M_e and one pair (μ, ν) such that $\zeta_e \approx \zeta_{\mu,\nu}$ and $\rho_{\zeta,e} \approx \rho_{\zeta,\mu,\nu}$.

In order to develop signal processing techniques that make use of the horizontal wavenumber approximation γ'_m with wideband signals it is important to demonstrate the frequency invariance of ζ_e and $\rho_{\zeta,e}$. Such frequency invariance is better understood by considering the normalized product

$$\Gamma_{\zeta,m} = \frac{\gamma_m k_m}{\gamma_m^2 + k_m^2}. \tag{4.25}$$

Considering the ray mode analogy ([58] pp. 102) and k_m and γ_m given by (4.15), product (4.25) becomes

$$\Gamma_{\zeta,m} = \Gamma_\zeta(\theta_m) = \frac{1}{2}\sin(2\theta_m), \tag{4.26}$$

where $\theta_m \in]0, \pi/2[$. It can be approximated by $\Gamma'_{\zeta,m}$, defined as

$$\begin{aligned} \Gamma'_{\zeta,m} &= \frac{\gamma'_m k_m}{\gamma_m^2 + k_m^2} \\ \Gamma'_\zeta(\theta_m) &= -\zeta_e + \rho_{\zeta,e}\, c\cos\theta_m. \end{aligned} \tag{4.27}$$

Figure 4.2 shows the product $\Gamma_{\zeta,m}$ as a function of θ_m (dotted line). The maximum of Γ_ζ is always at $M/\sqrt{2}$ that corresponds to $\theta_{M/\sqrt{(2)}} \approx \pi/4$. In Figure 4.2 the circles represent the approximation to Γ_ζ with $M_e = M/2$ that correspond to $\theta_m \in]0, \pi/6[$.

It is clear from Figures 4.1 and 4.2 that the approximation γ'_m is poorer than k'_m, nevertheless in both cases the approximation quality can be enhanced by applying the

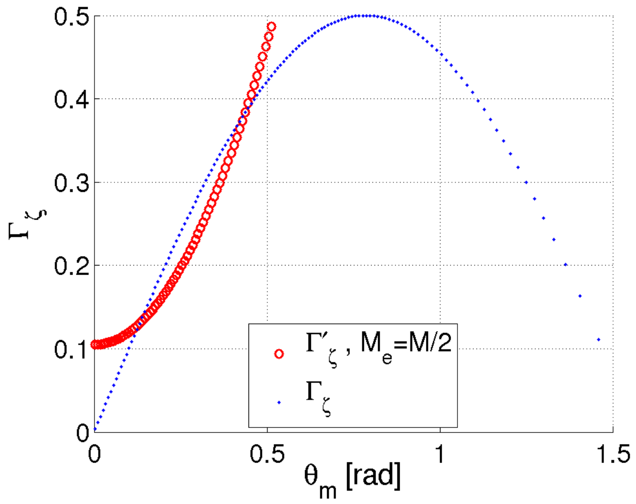

Figure 4.2: Normalized product $\Lambda_{\zeta,m}$ (4.26) (dotted line), and its least-squares approximation (4.27) for an effective number of modes $M_e = M/2$ (circles).

approximation to a small number of modes M_e or by applying the approximation in small sets of modes, resulting in different values of the waveguide invariants for each set. Still similar arguments as those used in Figure 4.1 demonstrate that ζ_e and $\rho_{\zeta,e}$ are also nearly invariant with frequency.

4.3 Geometric mismatch compensation in passive time reversal

This section establishes how the geometric mismatch (source-array range, source depth and array depth mismatch) and the frequency shift affect the pTR output in a perfect waveguide. The usefulness of the approximations to k_m and γ_m developed in Section 4.2 for geometric mismatch compensation will then arise naturally.

4.3.1 Passive Time Reversal in a stationary geometry

The behavior of pTR in a stationary environment was originally defined in [26] and refined by several authors, and it will be repeated here only for the definition of terms and for further formal understanding of how geometric mismatch affects pTR performance.

The pressure field received by each hydrophone of a Vertical Line Array (VLA) from a monochromatic point source is given by the *Green's* function

$$G_\omega(R, z_0, z_i) = \frac{-j}{\rho\sqrt{8\pi R}} e^{-j\frac{\pi}{4}} \sum_{m=1}^{M} \frac{Z_m(z_i) Z_m(z_0)}{\sqrt{k_m}} e^{ik_m R}, \tag{4.28}$$

where R represents the range between the source and the VLA, z_0 the source depth, z_i the array hydrophones depth, ρ the water density considered to be unitary constant over the water column, Z_m is the depth dependent mode shape and k_m is the horizontal wavenumber.

When the pTR processor is implemented in a stationary environment a first signal (index m) is sent from the source to the array and then the received pressure field is correlated with a second transmission (index n). The resulting pressure field in the frequency domain is given by

$$\begin{aligned} P_{pc}(R, z_0, z_i, \omega) &= \sum_{i=1}^{I} G_\omega(R, z_0, z_i) G_\omega^*(R, z_0, z_i) \\ &= \frac{1}{\rho^2 8\pi R} \sum_{m=1}^{M} \sum_{n=1}^{M} \frac{Z_m(z_0) Z_n(z_0)}{\sqrt{k_m k_n}} \Psi(m,n) e^{j(k_m R - k_n R)}, \end{aligned} \tag{4.29}$$

where, according to the basic assumptions of aTR [2], the mode orthogonality property can be applied, such that

$$\Psi(m,n) = \sum_{i=1}^{I} Z_m(z_i) Z_n(z_i) \approx \delta_{m,n}. \tag{4.30}$$

Due to (4.30) the two summations in (4.29) can be replaced by a single one, the exponential vanishes, and the pTR pressure field in the frequency domain becomes approximately constant

$$P_{pc}(\cdot) = \frac{1}{\rho^2 8\pi R} \sum_{m=1}^{M} \frac{|Z_m(z_0)|^2}{|k_m|}. \tag{4.31}$$

In the following the problem of performance loss of pTR with variable geometry will be addressed and compensation strategies will be proposed. Since pTR performs the crosscorrelation between the first and a second received signal, it will be considered that the geometric mismatch affects the second received signal (index n) while the compensation strategies will be implemented in the first received signal (index m).

4.3.2 Passive Time Reversal with Source-Array Range Shift

If there is a source-array range shift $\Delta r = r - R$ (where r is the new range) between the first and the second transmissions the resulting pTR pressure field is given by

$$\begin{aligned} P_{pc}(\cdot; \Delta r) &= \sum_{i} G_\omega(R + \Delta r, z_0, z_i) G_\omega^*(R, z_0, z_i) \\ &= \frac{1}{\rho^2 8\pi R} \sum_{m=1}^{M} \frac{|Z_m(z_0)|^2}{|k_m|} e^{j(k_m(R+\Delta r) - k_m R)}, \end{aligned} \tag{4.32}$$

where Δr is small enough in order to be considered negligible in the denominator. The argument of the complex exponential in (4.32) is no longer null and this is responsible for a loss of performance of pTR.

---

[2] *i.e.*, that there is a sufficiently large number of hydrophones, the vertical array is spanning the whole water column and the propagation environment is time-invariant.

Song et al [55] developed a waveguide invariant based method [21] to perform range shift of the aTR focal spot whose application to pTR range shift compensation is straightforward. As originally proposed this method only emphasizes the pressure field intensity, and a different interpretation of the compensation mechanism is given here to account for the phase effect over the frequency domain pressure field, that results in a delay in the time domain. According to [55] the source-array range distortion over the pTR can be compensated by applying a frequency shift $\Delta\omega$ to the first received pressure field (index m) in (4.32), i.e.,

$$G_{\omega+\Delta\omega}(R, z_0, z_i) = \frac{-j}{\rho\sqrt{8\pi R}} e^{-j\frac{\pi}{4}} \sum_{m=1}^{M} \frac{Z_m(z_i)Z_m(z_0)}{\sqrt{k_m}} e^{ik_m(\omega+\Delta\omega)R}, \tag{4.33}$$

where under the adiabatic condition the only quantity that is considered to be frequency dependent is the horizontal wavenumber k_m in the argument of the complex exponential (the frequency shift in the k_m placed in the denominator is negligible). Using (4.33) in (4.32) results in

$$\begin{aligned} P_{pc}(\cdot; \Delta r, \Delta\omega) &= \sum_i G_\omega(R + \Delta r, z_0, z_i) G^*_{\omega+\Delta\omega}(R, z_0, z_i) \\ &= \frac{1}{\rho^2 8\pi R} \sum_{m=1}^{M} \frac{|Z_m(z_0)|^2}{|k_m|} e^{j(k_m(R+\Delta r) - k_m^\dagger R)}, \end{aligned} \tag{4.34}$$

where $k_m^\dagger = k_m(\omega + \Delta\omega)$. Considering the first order Taylor approximation for the frequency shift horizontal wavenumber

$$\begin{aligned} k_m^\dagger &= k_m + \frac{dk_m}{d\omega}\Delta\omega \\ &= k_m + \frac{1}{u_m(\omega)}\Delta\omega, \end{aligned} \tag{4.35}$$

where u_m is the horizontal group velocity. Replacing (4.35) in (4.34) yields

$$P_{pc}(\cdot; \Delta r, \Delta\omega) = \frac{1}{\rho^2 8\pi R} \sum_{m=1}^{M} \frac{|Z_m(z_0)|^2}{|k_m|} e^{jk_m\Delta r} e^{-j\frac{dk_m}{d\omega}\Delta\omega R}. \tag{4.36}$$

The frequency shift $\Delta\omega$ used in [55] to perform a range shift of the aTR focal spot can be adapted here to compensate for the pTR range shift Δr, and is given by

$$\Delta\omega = -\frac{\omega}{R}\Delta r\beta. \tag{4.37}$$

where β is the horizontal waveguide invariant that can be chosen from a set of possible values (4.8) or given by (4.12). In the following the second option will be considered.

As previously mentioned, in [55] only the aTR focal spot intensity was considered, and no attempt was made to understand the range shift influence over the aTR focal spot phase. When applying the same strategy to compensate for pTR range mismatch, namely for underwater communications, the argument of the exponential term in (4.34) should be approximately linear with frequency and range shift (to avoid signal distortion). That is made possible by using (4.11) and (4.37) in the exponential term (4.36)

$$k_m \Delta r + \frac{dk_m}{d\omega}\omega\beta_e\Delta r \approx \omega\rho_{\beta,e}\Delta r, \tag{4.38}$$

where β_e and $\rho_{\beta,e}$ are given by (4.12) and (4.13) respectively. Finally replacing (4.38) in (4.36) results in

$$P_{pc}(\cdot;\Delta r,\Delta\omega) \approx \frac{e^{j\rho_{\beta,e}\omega\Delta r}}{\rho^2 8\pi R}\sum_{m=1}^{M}\frac{|Z_m(z_0)|^2}{|k_m|}. \tag{4.39}$$

When compared with (4.31), it is clear that, except for a harmless linear phase term, the source-array range mismatch has been compensated in (4.39).

4.3.3 Passive Time Reversal with Source Depth Shift

If there is a source depth shift Δz_0 between the first and second transmissions the pTR pressure field becomes

$$\begin{aligned} P_{pc}(.;\Delta z_0) &= \sum_i^I G_\omega(R, z_0+\Delta z_0, z_i)G_\omega^*(R, z_0, z_i) \\ &= \frac{1}{8\pi R}\sum_{m=1}^{M}\sum_{n=1}^{M}\frac{Z_m(z_0)Z_n(z_0+\Delta z_0)}{\rho}\sum_i \frac{Z_n(z_i)Z_m(z_i)}{\rho}\frac{e^{j(k_mR-k_nR)}}{\sqrt{k_mk_n}} \\ &= \frac{1}{\rho 8\pi R}\sum_{m=1}^{M}\left[\frac{Z_m(z_0)Z_m(z_0+\Delta z_0)}{\rho}\right]\frac{1}{|k_m|}, \end{aligned} \tag{4.40}$$

where the term in $[\cdot]$ is responsible for a loss of performance of pTR.

In a perfect waveguide with no source depth mismatch, $\rho = 1$, and considering the full set of modes,

$$\sum_{m=1}^{M}\frac{Z_m(z_0)Z_m(z)}{\rho} \approx \begin{cases} \frac{D}{2}\frac{M}{2} & \text{if } z = z_0 \\ 0 & \text{if } z \neq z_0 \end{cases}, \tag{4.41}$$

which means that even with a small depth mismatch $\Delta z_0 = z - z_0$ the pTR performance strongly degrades, since (4.41) results in a weighted dirac in depth [3].

Applying to pTR the basic idea of Walker [60] for aTR focal spot depth shift, the term in $[\cdot]$ can be written as

$$\sum_{m=1}^{M}\left[\frac{Z_m(z_0)Z_m(z_0+\Delta z_0)}{\rho}\right] = \sum_{m=1}^{M}\left[\frac{Z_m(z_0)Z_m(z_0)}{\rho}\left\{\frac{Z_m(z_0+\Delta z_0)}{Z_m(z_0)}\right\}\right]. \tag{4.42}$$

This implies that a compensation of the source depth shift can be achieved by applying the inverse of the term in $\{\cdot\}$ to (4.40). The method proposed in [60] requires the explicit computation of $Z_m(z)$ using, e.g., the data-based mode extraction method proposed in

---

[3] it should be mentioned that in a real scenario the weighted dirac is replaced by a pulse with a main lobe, that originates a slower performance degradation with the depth mismatch, when compared with the theoretical case.

[59] that requires the collection of data at several ranges. Although the basic idea is the same, the compensation method presented here does not require the explicit computation of Z_m; instead, by using a frequency shift of the acoustic field, an approximation to the inverse of the term in $\{\cdot\}$ is computed implicitly.

It was found that in a perfect waveguide the source depth mismatch compensation can be partially achieved multiplying by $\cos(\gamma_m \Delta z_0)$ the left term of (4.42) [4], that is

$$\sum_{m=1}^{M} Z_m(z_0) Z_m(z_0 + \Delta z_0) \cos(\gamma_m \Delta z_0). \tag{4.43}$$

For the perfect waveguide mode shape (4.43) can be rewritten as

$$\frac{D}{2} \sum_{m=1}^{M} \sin(\gamma_m z_0) \sin(\gamma_m z_0 + \gamma_m \Delta z_0) \cos(\gamma_m \Delta z_0), \tag{4.44}$$

that, by trivial trigonometric manipulation, becomes

$$\frac{D}{2} \sum_{m=1}^{M} \frac{1}{4} \left[1 + \cos(2\gamma_m \Delta z_0) - \cos(2\gamma_m z_0) - \cos(2\gamma_m z_0 + 2\gamma_m \Delta z_0)\right]. \tag{4.45}$$

The sum of oscillating terms in (4.45) is approximately zero except for $\Delta z_0 = 0$ due to $\cos(2\gamma_m \Delta z_0)$, and the term 1 is responsible for the compensation. It results that

$$\sum_{m=1}^{M} Z_m(z_0) Z_m(z_0 + \Delta z_0) \cos(\gamma_m \Delta z_0) \approx \begin{cases} \frac{D}{2} \frac{M}{2} & \text{if } \Delta z_0 = 0 \\ \frac{D}{2} \frac{M}{4} & \text{if } \Delta z_0 \neq 0 \end{cases}. \tag{4.46}$$

Comparing (4.41) and (4.46) it is clear that under depth mismatch the compensation can restore half the magnitude of (4.41). Similarly $\exp(j\gamma_m \Delta z_0)$ (the negative exponential is also a viable choice) can be used for compensation instead of $\cos(\gamma_m \Delta z_0)$, in which case one must consider an additional imaginary component that will be responsible for the presence of a linear phase[5] with Δz_0

$$\sum_{m=1}^{M} Z_m(z_0) Z_m(z_0 + \Delta z_0) e^{j\gamma_m \Delta z_0} \approx \sum_{m=1}^{M} Z_m(z_0) Z_m(z_0) \frac{V(\Delta z_0)}{2}, \tag{4.47}$$

where $|V(\Delta z_0)| \approx 2$ for $\Delta z_0 = 0$ and $|V(\Delta z_0)| \approx 1$ for $\Delta z_0 \neq 0$.

In [34] it is considered that for aTR (4.41) can be applied approximately by assuming that the k_m's are nearly constant over the interval of the contributing modes and can be replaced by their mean $\overline{|k_m|}$. Here, in a similar manner (4.47) is used for the compensated pTR and results in the source depth shift compensated pTR pressure field given by

$$P_{pc}^{comp}(\cdot; \Delta z_0) \approx \frac{1}{\rho^2 8\pi R} \sum_{m=1}^{M} \frac{|Z_m(z_0)|^2}{\overline{|k_m|}} \frac{V(\Delta z_0)}{2}. \tag{4.48}$$

---

[4] the choice of $\cos(\gamma_m \Delta z_0)$ was made in aTR context and further adapted to pTR by considering an analogy with the demodulation of a single-side-band modulation using a double-side-band demodulator.

[5] in a real scenario due to the previously mentioned replacement of the weighted dirac in (4.41) by a pulse with a main lobe, it results that the linear phase with Δz_0 becomes a dual-slope linear phase (one inside the lobe and the other outside), that can be observed in Figure 4.4 for simulated data.

As previously, a frequency shift is used to implicitly perform the compensation based on the product by $\exp(j\gamma_m \Delta z_0)$. Considering the approximation to the vertical wavenumber using the horizontal group slowness (4.22), in a similar manner to the compensation of the source-array range mismatch (4.38) one can write

$$\gamma_m \Delta z_0 \approx -\frac{dk_m}{d\omega}\omega\zeta_0\Delta z_0 + \rho_{\zeta,0}\omega\Delta z_0, \tag{4.49}$$

where ζ_0 is given by (4.23) and $\rho_{\zeta,0}$ is given by (4.24). Taking

$$\Delta\omega = \frac{\omega}{R}\Delta z_0 \zeta_0, \tag{4.50}$$

in the first-order Taylor expansion (4.35), results in the compensated field

$$\begin{aligned} P_{pc}(\cdot; \Delta z_0, \Delta\omega) &= \sum_i G_\omega(R, z_0 + \Delta z_0, z_i) G^*_{\omega+\Delta\omega}(R, z_0, z_i) \\ &= \frac{1}{\rho^2 8\pi R} \sum_{m=1}^{M} \frac{Z_m(z_0 + \Delta z_0) Z_m(z_0)}{|k_m|} e^{-j\frac{dk_m}{d\omega}\Delta\omega R} \\ &\approx \frac{V(\Delta z_0)}{2} \frac{e^{-j\rho_{\zeta,0}\omega\Delta z_0}}{\rho^2 8\pi R} \sum_{m=1}^{M} \frac{|Z_m(z_0)|^2}{|k_m|}. \end{aligned} \tag{4.51}$$

When compared with (4.31) it is clear that, at the cost of an attenuation and a harmless linear phase term the source depth mismatch pTR acoustic field becomes partially compensated.

4.3.4 Passive Time Reversal with Array Depth Shift

If there is an array depth shift Δz_i between the first and the second transmissions the mismatched pTR pressure field becomes

$$\begin{aligned} P_{pc}(.; \Delta z_i) &= \sum_i^I G_\omega(R, z_0, z_i + \Delta z_i) G^*_\omega(R, z_0, z_i) \\ &= \frac{1}{\rho^2 8\pi R} \sum_{m=1}^{M} \sum_{n=1}^{M} \frac{Z_m(z_0) Z_n(z_0)}{\sqrt{k_m k_n}} \sum_i Z_n(z_i + \Delta z_i) Z_m(z_i) e^{j(k_m R - k_n R)} \\ &= \frac{1}{\rho^2 8\pi R} \sum_{m=1}^{M} \sum_{n=1}^{M} \frac{Z_m(z_0) Z_n(z_0)}{\sqrt{k_m k_n}} \Psi(m, n, \Delta z_i) e^{j(k_m R - k_n R)}. \end{aligned} \tag{4.52}$$

Unlike $\Psi(m, n)$ in (4.29) and (4.30) in (4.52) $\Psi(m, n, \Delta z_i)$, is no longer an impulse and the two summations $\sum_{m=1}^{M} \sum_{n=1}^{M}(.)$ cannot be replaced by a single one. Instead they must be replaced by $\sum_{m=n}^{M}(.) + \sum_{m\neq n}^{M}(.)$, where the cross terms will be responsible for a loss of performance of the pTR processor.

Appendix B.2 studies the effect of the array depth mismatch over the mode orthogonality property, and proposes a compensation strategy that partially recovers it in the presence of array depth mismatch. It results that partial compensation can be achieved using (B22) in (4.52)

$$\begin{aligned} P_{pc}^{comp}(.;\Delta z_i) &\approx \frac{1}{\rho^2 8\pi R}\sum_{m=1}^{M}\sum_{n=1}^{M}\frac{Z_m(z_0)Z_n(z_0)}{\sqrt{k_m k_n}}\Psi(m,n,\Delta z_i)e^{j\gamma_m\Delta z_i}e^{j(k_m R-k_n R)} \\ &\approx \frac{1}{\rho^2 8\pi R}\sum_{m=1}^{M}\sum_{n=1}^{M}\frac{Z_m(z_0)Z_n(z_0)}{\sqrt{k_m k_n}}\Psi(m,n)\frac{W(m,\Delta z_i)}{2}e^{j(k_m R-k_n R)} \end{aligned} \quad (4.53)$$

In (4.53) the summation $\sum_{m=1}^{M}\sum_{n=1}^{M}(.)$ can be replaced by $\sum_{m=n}^{M}[W(m,\Delta z_i),(.)]$, and the resulting pTR pressure field will be given by

$$P_{pc}^{comp}(.;\Delta z_i) \approx \frac{1}{\rho^2 8\pi R}\sum_{m=1}^{M}\frac{|Z_m(z_0)|^2}{|k_m|}\frac{W(m,\Delta z_i)}{2}. \quad (4.54)$$

As in (4.48) a frequency shift implicitly introduces the required factor $\exp(j\gamma_m\Delta z_i)$ (note that $\exp(-j\gamma_m\Delta z_i)$ is also a viable choice since in appendix B.2 the compensation is originally attained by $\cos(\gamma_m\Delta z_i)$). Considering the approximation to the vertical wavenumber using the horizontal group slowness (4.22), one can write, similarly to (4.49),

$$\gamma_m\Delta z_0 \approx -\frac{dk_m}{d\omega}\omega\zeta_i\Delta z_i + \rho_{\zeta,i}\omega\Delta z_i, \quad (4.55)$$

where ζ_i is given by (4.23) and $\rho_{\zeta,i}$ is given by (4.24). Considering the first order Taylor expansion (4.35) and

$$\Delta\omega = \frac{\omega}{R}\Delta z_i\zeta_i, \quad (4.56)$$

yields the compensated field

$$\begin{aligned} P_{pc}(\cdot;\Delta z_i,\Delta\omega) &= \sum_i G_\omega(R,z_0,z_i+\Delta z_i)G^*_{\omega+\Delta\omega}(R,z_0,z_i) \\ &= \frac{1}{\rho^2 8\pi R}\sum_{m=1}^{M}\frac{|Z_m(z_0)|^2}{|k_m|}\Psi(m,n,\Delta z_i)e^{-j\frac{dk_m}{d\omega}\Delta\omega R} \\ &\approx \frac{e^{-j\rho_{\zeta,i}\omega\Delta z_i}}{\rho^2 8\pi R}\sum_{m=1}^{M}\frac{|Z_m(z_0)|^2}{|k_m|}\frac{W(m,\Delta z_i)}{2}, \end{aligned} \quad (4.57)$$

that resembles (4.51), and similar comments apply.

4.4 Simulations with a perfect waveguide

In order to illustrate the behavior of the geometric mismatch frequency shift compensation mechanism, simulations were conducted for a perfect waveguide with $D = 100$m water column depth, $c = 1500$m/s, frequency $f = 1$kHz, nominal source-array range $R = 1$km, nominal source depth $z_0 = 50$m and a vertical line array of 81 hydrophones, 1m spaced, centered in the water column.

Results for the source-array range mismatch compensation given by the pTR acoustic field $P_{PC}(\cdot;\Delta r,\Delta\omega)$ of (4.34), source depth mismatch compensation given by $P_{PC}(\cdot;\Delta z_0,\Delta\omega)$

of (4.51), and array depth mismatch compensation given by $P_{PC}(\cdot; \Delta z_i, \Delta\omega)$ of (4.57), are shown in Figures 4.3, 4.4 and 4.5, respectively. The blue dashed line shows the behavior of pTR under the geometric mismatch $\Delta \equiv (\Delta r, \Delta z_0, \Delta z_i)$ with no compensation, $\Delta\omega = 0$ where $\Delta\omega = 2\pi\Delta f$. The continuous line shows the maxima of the surface $|P_{PC}(\cdot; \Delta, \Delta\omega)|$ in (a) and the respective phase in (b). The red dot-dashed line represents the pTR acoustic field with the proposed compensation mechanism given by (4.37), (4.50) and (4.56) for source-array range, source depth and array depth mismatches, respectively. In all three cases the waveguide invariants β_e, $\zeta_{e,0}$, $\zeta_{e,i}$, $\rho_{\beta,e}$, $\rho_{\zeta,e,0}$ and $\rho_{\zeta,e,i}$ were computed for an effective number of modes $M_e = M/2$.

Figure 4.3(a) shows the pTR acoustic field magnitude $|P_{PC}(\cdot; \Delta r, \Delta\omega)|$ of (4.34) where it is clear that the compensation $\Delta\omega$ behaves linearly with the mismatch Δr with an invariant $\beta_e \approx 0.88$ given by (4.12). For each Δr the frequency shift for which the maximum magnitude is attained almost equals (4.37), and provides a strong gain when compared with the no compensation case given by the dashed line. Figure 4.3(b) shows the unwrapped phase of (4.36) for the three cases described before. Except for the $\max(P_{PC})$ case the others exhibit a linear trend with Δr that, for the proposed frequency shift compensation mechanism, is controlled by $\rho_{\beta,e}$ given by (4.13).

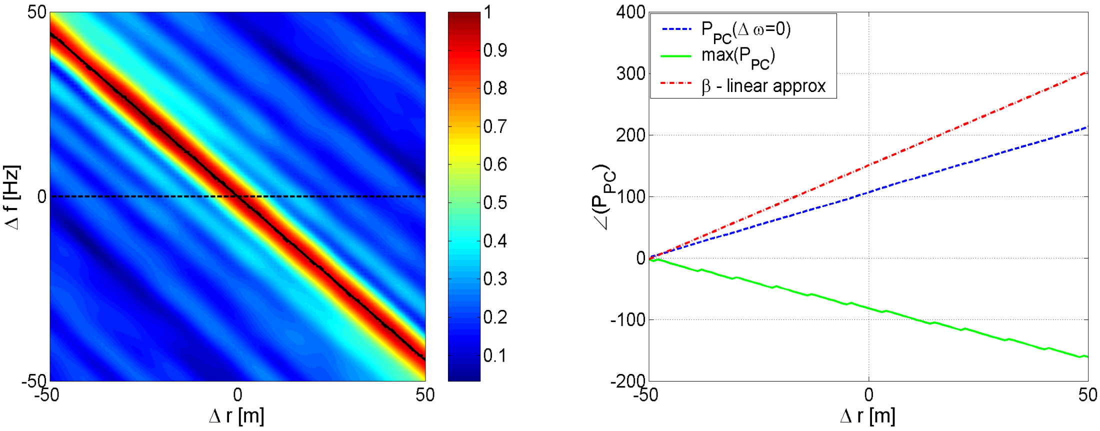
(a) (b)

Figure 4.3: Frequency shift source-array range mismatch compensation given by the pTR acoustic field $P_{PC}(\cdot; \Delta r, \Delta\omega)$ of (4.34); (a) normalized magnitude, (b) unwrapped phase.

Figure 4.4(a) shows the magnitude of (4.51) where an almost symmetric behavior with Δf is observed since the compensation can be done either with $\exp(j\gamma_m \Delta z_0)$ or $\exp(-j\gamma_m \Delta z_0)$ (recall that compensation is originally attained using $\cos(\gamma_m \Delta z_0)$ and that the positive and the negative exponentials are both easy to implement alternative choices). This near symmetry causes the maximum to toggle between positive and negative values of the frequency shift. Considering only one side of the symmetry it can be observed that the compensation $\Delta\omega$ behaves almost linearly with the mismatch Δz_0 with a invariant $\zeta_{e,0} \approx 3.14$ given by (4.23) (such linearity becomes a weaker approximation for high frequencies and high source depth mismatches). Figure 4.4(a) shows that the frequency shift compensation maximum ($\max(P_{PC})$) attain a stronger magnitude than the non-compensated case ($P_{PC}(\Delta\omega = 0)$) when the main lobe, which can be seen in the center of the figure, reaches one half of the maximum value given for $\Delta z_0 = 0$ as predicted by (4.46).

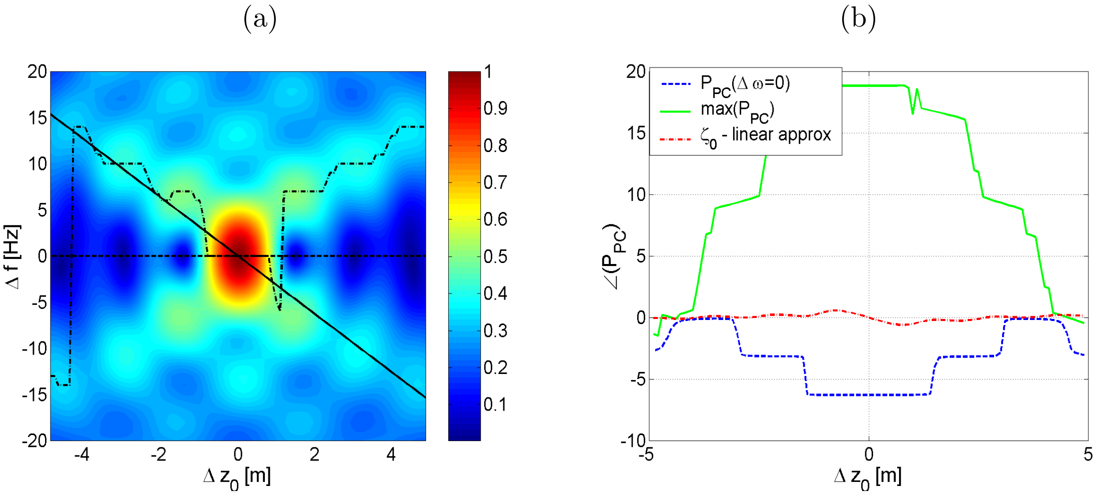

Figure 4.4: Frequency shift source depth mismatch compensation given by the pTR acoustic field $P_{PC}(\cdot; \Delta z_0, \Delta\omega)$ of (4.51); (a) normalized magnitude, (b) unwrapped phase.

Figure 4.4(b) shows the phase of (4.51) for the three cases described above. An almost linear trend with Δz_0 is observed only for the proposed compensation mechanism (dot-dashed line) that is controlled by $\rho_{\zeta,e}$ and the phase of $V(\Delta z_0)$ as given by (4.51) (in fact a detailed observation shows a tenuous two slope linear phase with one slope inside the $|P_{PC}(\cdot; \Delta z_0, \Delta\omega)|$ main lobe and a different one outside).

Figure 4.5 shows the simulation behavior of the array depth mismatch frequency shift compensation mechanism for a perfect waveguide similar to the one used for Figures 4.3 and 4.4. The behavior is quite similar to the one observed for the source depth mismatch compensation case and similar comments apply, with the main difference being that now $W(m, \Delta z_i)$ plays the role of $V(\Delta z_0)$. Note that the invariant $\zeta_{e,i} = \zeta_{e,0} \approx 3.14$ are both given by (4.23) and are equal due to the fact that the Sound Speed Profile (SSP) is constant over the water column, which makes the vertical wavenumber γ_m depth independent. Additional comments when in the presence of a depth dependent SSP will be given in Sections 4.5 and 4.6.

4.5 Extension of geometric compensation mechanisms to realistic waveguides

The intrinsic behavior of the geometric mismatch compensation mechanism in a perfect waveguide can be further extended to more realistic waveguides by considering the Pekeris waveguide and the WKB approximation. In a Pekeris waveguide the high order modes become leaky due to the presence of the half space and at sufficiently larger range they have

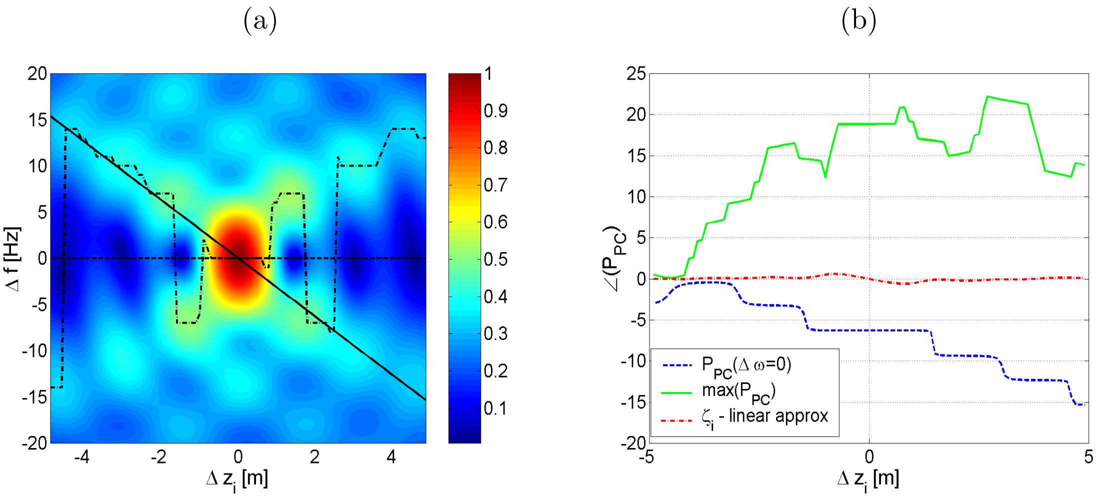

Figure 4.5: Frequency shift array depth mismatch compensation given by the pTR acoustic field $P_{PC}(\cdot;\Delta z_i,\Delta\omega)$ of (4.57); (a) normalized magnitude, (b) unwrapped phase.

no contribution to the received acoustic field [27]. That means that in a real waveguide the mode limitation required to improve the k'_m to k_m approximation (4.11) and γ'_m to γ_m approximation (4.22) is performed up to a certain point by the waveguide itself.

Although the WKB approximation is usually applied in deep water, some insight into the behavior of the modes in a waveguide with a depth-dependent SSP can be obtained. In [5] it is shown that under the WKB approximation the group slowness is given by

$$\frac{dk_m}{d\omega} = \frac{\omega}{k_m}\frac{\int \frac{1}{\rho(z)c^2(z)} Z_m^2(z)dz}{\int \frac{1}{\rho(z)} Z_m^2(z)dz} \tag{4.58}$$

where $\rho(z)$ and $c(z)$ are the depth-dependent water density and SSP, respectively, and the ratio of integrals in the right hand side is a constant. Using the WKB horizontal group slowness (4.58) instead of the perfect waveguide horizontal group slowness (4.5) the approximations (4.11) and (4.22) are still valid. Heuristically, this suggests that the genesis of the range shift compensation mechanism under the WKB approximation with a depth-dependent SSP remains unchanged.

Regarding the use of $\exp(\pm j\gamma_m\Delta z)$ to compensate for the source depth shift and array depth shift, the following should be considered. The WKB approximation reveals that in the presence of a ducted SSP [58, 5] the mode shape is no longer ruled by a constant vertical wavenumber, γ_m, but by a depth-dependent $\gamma_m(z)$. Under the WKB approximation the mode shape between the points where it vanishes, that is, between the ray turning points in the ray mode analogy, is given by

$$Z_m(z) = A_m(z)\sin\Upsilon_m(z), \tag{4.59}$$

where $A_m(z)$ is a slowly-varying amplitude

$$A_m(z) = \gamma_m^{-1/2}(z) = \left[\frac{\omega^2}{c^2(z)} - k_m^2\right]^{-1/4}, \tag{4.60}$$

the WKB phase is

$$\Upsilon_m(z) = \Upsilon_a + \int_a^z \gamma_m(z')dz', \tag{4.61}$$

where a is the upper mode vanishing depth (or the equivalent ray turning depth) and the depth dependent vertical wavenumber is

$$\gamma_m^2(z) = \frac{\omega^2}{c^2(z)} - k_m^2, \tag{4.62}$$

where k_m is the depth-independent horizontal wavenumber. In presence of a depth shift Δz one can compute the new vertical wavenumber $\gamma_m(z+\Delta z)$ using the nominal $\gamma_m(z)$ and the sound speed at z and $z+\Delta z$

$$\gamma_m^2(z+\Delta z) = \frac{\omega^2}{c^2(z)}\sigma_c(z,\Delta z) + \gamma_m^2(z), \tag{4.63}$$

where

$$\sigma_c(z,\Delta z) = \frac{c^2(z) - c^2(z+\Delta z)}{c^2(z+\Delta z)}. \tag{4.64}$$

Replacing (4.62) in (4.63) results in

$$\gamma_m^2(z+\Delta z) = \frac{\omega^2}{c^2(z)}(\sigma_c(z,\Delta z)+1) - k_m^2, \tag{4.65}$$

where $\sigma_c(z,\Delta z) \approx 0$ and $\gamma_m^2(z+\Delta z) \approx \gamma_m^2(z)$ if the sound speed varies slowly with depth. In the presence of a depth shift Δz the WKB phase (4.61) becomes

$$\Upsilon_m(z+\Delta z) = \Upsilon_a + \int_a^z \gamma_m(z')dz' + \int_z^{z+\Delta z} \gamma_m(z')dz', \tag{4.66}$$

and, since $\sigma_c(z,\Delta z)+1 \approx 1$ for a slowly-varying SSP , with small Δz, the third term of (4.66) becomes

$$\int_z^{z+\Delta z} \gamma_m(z')dz' \approx \gamma_m(z)\Delta z, \tag{4.67}$$

and the mode shape $Z_m(z)$ becomes

$$Z_m(z+\Delta z) \approx A_m(z)\sin\left[\Upsilon_m(z) + \gamma_m(z)\Delta z\right]. \tag{4.68}$$

Note the similarity to the mode shape in a perfect waveguide, given by $Z_m(z+\Delta z) = \sin(\gamma_m z + \gamma_m \Delta z)$.

Considering now that a real waveguide is a Pekeris waveguide with a WKB approximation such that the mode shape in the water column is given by the WKB approximation, but near the boundaries the mode vanishing locations (ray turning points) are given by the boundaries of the waveguide as in the Pekeris waveguide, the $\Psi(m,n,\Delta z_i)$ function of (B11) becomes

$$\Psi(m,n,\Delta z_i) = \Xi \int_0^D \sin[\Upsilon_m(z) + \gamma_m(z)\Delta z_i)]\sin(\Upsilon_n(z))dz, \tag{4.69}$$

where the assumed constant Ξ is a function of water depth D and $A_m(z)$ of (4.60). The latter is a slowly-varying function of z and assumed constant within the water column.

Comparing (B11) for the perfect waveguide with (4.69) for the more realistic case based on the Pekeris waveguide with the WKB approximation, one can see that the distortion is similar, the main difference being that for (4.69) the vertical wavenumber is depth dependent. Such dependence suggests that a short array placed in the middle of the water column must be used in order to consider $\gamma_m(z) \approx \overline{\gamma_m(z)}$, or that for large vertical arrays the compensation should be applied in small array sections.

4.6 Geometric mismatch compensation with experimental data

The experimental data were collected during the MREA'04 sea trial that took place off the town of Setúbal, approximately 50km from Lisbon (Portugal) in April 2004. The acoustic source was suspended from the NRV Alliance at a nominal depth of 70m, the receiving VLA was surface-suspended from the free-drifting Acoustic Oceanographic Buoy (AOB) [30] and comprised two sections. The upper section with two hydrophones at nominal depths of 10 and 15m and the lower section with six hydrophones at nominal depths of 55, 60, 65, 70, 75 and 80m (in the following only the lower section will be used). The pTR experiment data processed in this section were acquired at a close range between 0.6 and 0.8km to the south of the acoustic source in a constant up slope region with a water column depth varying between 90 and 110m, at an almost constant source-array relative speed of about 0.6m/s. The environment was characterized by a thermocline of approximately 20m over a downward refracting SSP over a 1.5m silt bottom and a gravel sub-bottom. The surface-suspended AOB was affected by a wave height of approximately 0.63m with frequency between 0.43 and 0.4Hz, as measured with a costal monitoring buoy placed in the area of the experiment. The source depth was measured at a sampling rate of 1 second with 10cm resolution and oscillates between 71.64 and 72.24m. The power spectral density of the source depth data reveals the presence of one main component at 0.1Hz.

The transmission set processed here corresponds to modulated data at a carrier frequency of 3.6kHz, using a 400 baud symbol rate with 2-PSK constellation and fourth-root raised cosine signaling pulses with 100% roll-off, such that the signal bandwidth is 800Hz. Each individual transmission comprises a single PAM signaling pulse acting as a channel probe with symmetric guard intervals and a total duration of 1s, followed by a 20s data packet. The source transmits four packets with a total duration of 84s.

Before any geometric mismatch compensation the data were synchronized, Doppler compensated and channel identification was performed independently for each hydrophone using the exponentially-windowed RLS algorithm (see [19] and [20] for details). Each data packet provides a set of 400 IR estimates at intervals of 0.05s, where the first 9 estimates were rejected. The proposed pTR geometric mismatch compensation is then applied to

78.2s of data (collected during 83s) that corresponds to 1564 IR estimates with the IR estimate number 782 being used as the nominal IR. This results in a setup where the source-array range mismatch $\Delta r = r - R$ starts at negative values and then gradually increases up to the 1564 IR estimate.

Figure 4.6 shows the arriving pattern of the lower sections of the array for the middle IR estimate where four relevant paths are clearly identified.

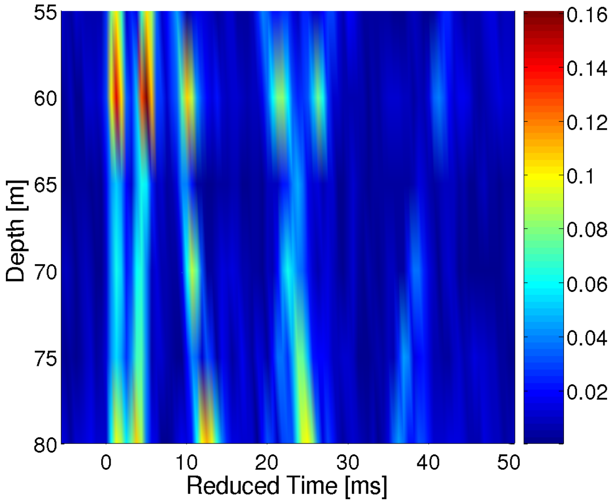

Figure 4.6: Arrival pattern of the non mismatch IR estimate.

Applying the proposed frequency shift geometric mismatch compensation strategy to the pTR operator, with only the first two paths of Figure 4.6, the surface of Figure 4.7 is obtained. Since the range mismatch changes from negative to positive values, crossing zero at about $40s$ (that corresponds to the nominal IR), it is expected that the frequency shift which compensates for the range mismatch varies from positive to negative values as in Figure 4.3(a) for the simulation in a perfect waveguide. This is confirmed in Figure 4.7 that shows a patch of pTR maxima ranging from a frequency shift mean value of about -90 up to 90Hz. The dashed line represents the expected frequency shift obtained with (4.37) by considering the range shift obtained from the NRV Alliance and AOB real-time GPS data, the data carrier frequency ($f_c = 3.6$kHz) and a horizontal waveguide invariant $\beta = 0.81$. The β value was computed from an approximation for constant slope range-dependent environments with constant sound speed derived by D'Spain [9]. In such conditions the invariant β depends of the water column depths at the source and receiver location and varies slowly with the source-receiver range. Originally, β was proposed to be the ratio between the source and the array position water-column depths, $\beta \approx D(S)/D(VLA)$. When applied in the present context (with the compensation mechanism applied in the reversed field) it should be considered that pTR implements a synthetic aTR with a virtual transmitting/receiving array at the VLA location and a virtual receiver at the source location. It results that the β invariant as a function of range is approximately given by

$$\beta \approx \frac{D(VLA)}{D(S)}. \tag{4.70}$$

Although the dashed line is just an approximation, Figure 4.7 confirms that (4.37) produces a good fit to the actual path of maximum magnitude (solid line). This similarity suggests that the frequency shift compensation is dominated by the range mismatch.

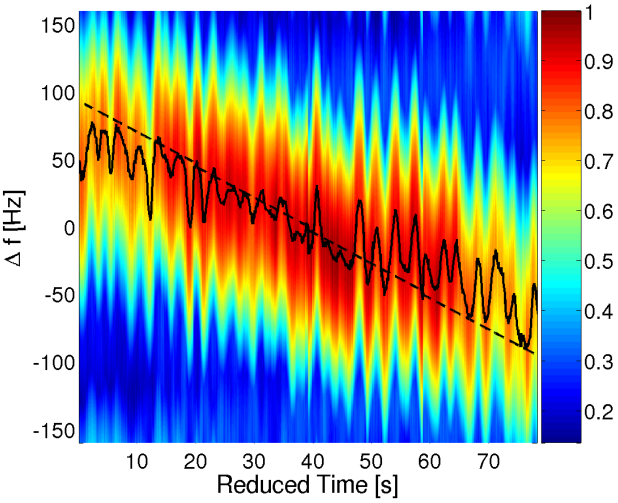

Figure 4.7: The surface represents the normalized magnitude of $P_{pc}(\cdot;\Delta,\Delta\omega)$, when the nominal IR is at $t = 40$s and considering the IRs limited to two arriving paths. The solid line traces the maxima of the surface over time. The dashed line represents the expected behavior if there is only range mismatch.

Figure 4.8 shows the power spectral density of the slice of $P_{pc}(\cdot;\Delta,\Delta\omega)$ along the maximum line of Figure 4.7, where three main components are identifiable at approximately 0.21, 0.3 and 0.4Hz (the first maximum at 0.012Hz is due to the 83s data packet length). Superimposed on the $P_{pc}(\cdot;\Delta,\Delta\omega)$ along the maximum line power spectrum, with '*', one can see the power spectrum of the source depth time series during the same data packet. Both curves display a similar behavior, despite a displacement in frequency. This fact, together with the array depth oscillation induced by the 0.4Hz surface waves allow us to speculate that the swing of the $P_{pc}(\cdot;\Delta,\Delta\omega)$ along the maximum line curve in Figure 4.7 is due to source and array depth oscillations. Nevertheless, no definitive conclusions can be attained since no accurate *in situ* source and array depth measurements with fast enough sampling rate are available.

It is interesting to observe that the symmetric ducts of the source and array depth compensations in the ideal waveguide of Figures 4.4(a) and 4.5(a) vanish in Figure 4.7. That is due to the presence of a depth-dependent SSP that causes the vertical wavenumber $\gamma_m(z)$ to become depth dependent as well.

Figure 4.9 is similar to Figure 4.7, but was computed with the first three paths of Figure 4.6. The main difference between these two figures is the appearance of two more P_{PC} maximum patches almost parallel to the original one. Those patches do not have

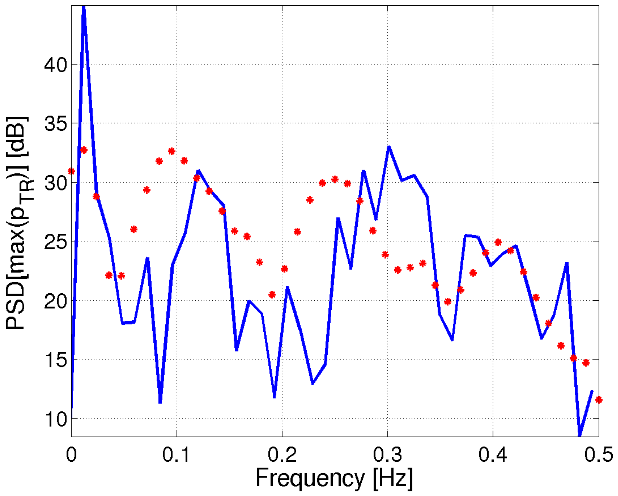

Figure 4.8: Power spectrum of the slice of P_{pc} along the maximum line of Figure 4.7 (solid line), and power spectrum of the source depth time series (‘*’).

the same nature as the symmetric patches of the source and array depth compensations in an ideal waveguide (see Figures 4.4 and 4.5). They originate from aliasing due to poor spatial sampling of the high-order modes in the 5m spaced hydrophone array.

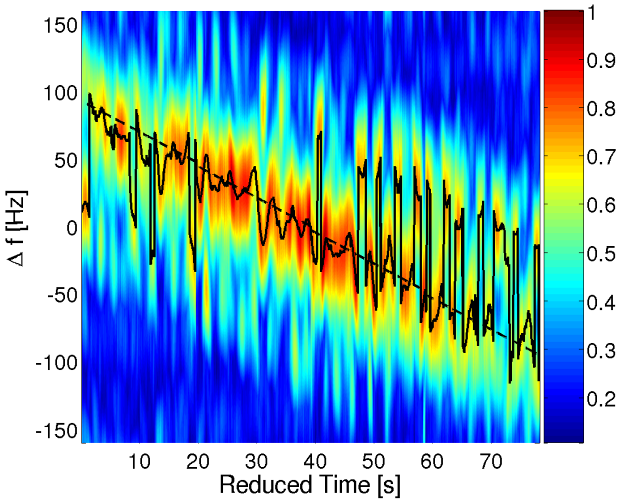

Figure 4.9: The same as Figure 4.7 considering the IRs limited to three arriving paths.

4.7 Conclusions and future work

An analytical model based waveguide invariant approach has been developed for pTR geometric mismatch compensation in shallow water. It was found that the horizontal waveguide invariant β can be used to approximate the horizontal wavenumber using the group slowness, and that the waveguide invariant ζ can be used to approximate the vertical wavenumber. By analogy with the invariance of β in the frequency/range plane, ζ would be invariant in the frequency/depth plane. After theoretically establishing the effect of geometric mismatch over the pTR operation for a perfect waveguide, it was found that an appropriate frequency shift calculated using the invariants can then be used for compensation during the pTR operation. The compensation method was extended heuristically to realistic waveguides and its usefulness was shown with real data.

In the present paper the invariance of ζ in the frequency/depth plane was not completely demonstrated, mainly due to the absence of appropriate real data. Future experiments should be designed in order to overcome this problem, by providing sufficiently high sample rate measurements of the source and array depths.

The proposed compensation method is potentially useful, e.g., in underwater communication systems based on pTR, where the presence of uncompensated geometric mismatch between the probe-signal and actual data transmissions degrades the performance. In fact, an underwater communication system, based on the developed geometric mismatch compensation, is proposed in [47]. It results in a environmental equalizer that uses a relatively small number of coefficients to deconvolve the cannel multipath, unlike most current equalizers.

Acknowledgments

This work was supported by Fundação para a Ciência e a Tecnologia under programs POCI, POCTI and POSI. The authors would like to thank the NATO Undersea Research Centre for the organization of MREA'04 sea trial, NRV Alliance master and personnel and the scientist in charge Emanuel F. Coelho, and to Orlando C. Rodrigez for the useful conversations about the waveguide invariants.

Chapter 5

Environmental equalizer for underwater communications

Abstract: This paper presents an environmental-based equalization algorithm for underwater communications. This algorithm is based on the passive time-reversal (pTR) and waveguide invariant properties of ocean channels. Passive time-reversal allows for the implementation of a simple communications system, but it loses performance in the presence of geometric mismatch between the probe-signal and the actual data symbols transmission. The waveguide invariant properties state that geometric mismatches, both in depth and range, can be partially compensated by applying an appropriate frequency shift in the passive time-reversal operator. Results with binary PSK data at a carrier frequency of 3.6 kHz, collected during the MREA'04 sea trial, show that the Mean Square Error (MSE) between the transmitted and the received data symbols remains stable at least to a range mismatch of about 37.5 m in the presence of source depth and an array depth oscillations of approximately 0.7 m. In such conditions, when comparing the proposed pTR equalizer with plain pTR, an overall gain of approximately 4.11 dB in output MSE is achieved.

5.1 Introduction

In recent years Time Reversal (TR) has received particular attention from the scientific community. After practical demonstration of its spatial-temporal focusing capabilities in the ocean [34] several applications of active TR (aTR), from tomography to communications, were suggested [34, 26]. Passive TR uses a receive-only array, and a probe-signal is transmitted ahead of the data for channel Impulse Response (IR) estimation. The IR estimate is then used as a synthetic channel for temporal focusing of the data signal, which is equivalent to the deconvolution of the multipath generated by the real channel.

When applied to underwater coherent communications the achieved TR focus is not perfect due to errors on the IR estimate and the time variability of the channel, resulting in uncompensated intersymbol interference (ISI) [45]. That problem is even more relevant in communications with a moving source and/or receiver. In that case it is intuitive that a rapid degradation of passive TR temporal focusing will occur due to the increasing mismatch between the assumed and actual channels. In order to guarantee longer stability of the focal spot, three solutions are usually proposed: one is to transmit probe-signals more frequently; another is to use an adaptive algorithm to track the IR from the initial probe signal IR estimation; and finally a third alternative is to use a low-complexity equalizer with only one coefficient per channel. A performance comparison between those adaptive pTR variants is presented in [20]. The major inconvenient of the first method is that frequent transmission of probe-signals reduces the overall transmission rate. In the second the channel estimates are represented by a large number of coefficients that have to be adapted. The third case seems to be the best compromise between complexity and efficiency. In this paper a different approach is proposed by considering that the environment mismatch between the probe-signal and data transmission is mainly due to the geometric properties (source-array range, source depth and array depth), and that the knowledge of such mismatch can be used to compensate for the overall pTR IR mismatch between the probe-signal and actual data transmissions.

A physics-based algorithm for pTR equalization based on the waveguide invariant properties of the shallow water channel is proposed. The waveguide invariant property β [6, 21] has been applied to change the aTR range focus in [55], and to interpret a model for performance prediction of a time-reversal communication system [42]. In [48] the waveguide invariant ζ in conjunction with β, allows for the compensation of pTR geometric mismatch. Through those waveguide invariants, changes on geometric features of the acoustic channel, such as source-receiver range, source depth and array depth, can be compensated by a frequency shift in the estimated IRs during probe-signal transmission. The resulting Frequency Shift pTR (FSpTR) equalizer will increase the pTR output power, resulting in lower MSE. A physics-based equalizer for underwater communications that is able to detect the transmitted data sequence and to simultaneously estimate the source-array range, source depth and array depth is thus obtained.

The reliability of the physics-based waveguide invariant pTR equalizer is demonstrated using experimental data obtained during the MREA'04 sea trial, where binary PSK signals at a data rate of 400 bits per second were transmitted with a carrier frequency of 3.6 kHz. Results obtained with FSpTR, after Doppler compensation of the received signals, show a long-term compensation of channel mismatch, with the MSE remaining stable up to a source-array range mismatch of about 37.5 m in the presence of source depth variations between 71.6 m and 72.3 m and array depth oscillations of approximately 0.63 m. In such conditions, when comparing FSpTR with plain pTR, an overall gain of approximately 4.11 dB in output MSE is achieved.

The paper is organized as follows: Section 5.2 recalls the use of pTR in underwater communications; in Section 5.3 the pTR geometric mismatch compensation using frequency shifts is presented; Section 5.4 develops the FSpTR equalizer, which is applied to real data in section 5.5; Section 5.6 summarizes the main results, draws some conclusions, and suggests future research.

5.2 Passive Time Reversal applied to communications

The basic setup for applying pTR to communications consists in a point source that sends information to a Vertical Line Array (VLA). The procedure starts by sending a short probe-signal, waiting for the channel to clear of multipath arrivals, and then sending the data stream. Considering the noiseless case, the received probe and the data are processed in a TR fashion and it results that the pTR output, in its baseband version [49], is given by

$$y(t) = [a(t) * p_4(t)] * p_{TR}(t, \Delta), \tag{5.1}$$

where $*$ represents convolution, $[a(t) * p_4(t)]$ is the transmitted signal with raised-cosine shaped symbols; $p_{TR}(t, \Delta)$ is the resulting pTR IR acoustic field given by

$$p_{TR}(t, \Delta) = \sum_{i=1}^{I} h_i(t, \Delta) * h_i'^*(-t), \tag{5.2}$$

where the upper $*$ represents conjugation, i is the hydrophones index, $h_i'(t)$ represents the channel IRs during probe transmission, $h_i(t, \Delta)$ is the channel IRs during data transmission, and Δ represents a possible mismatch between h_i' and h_i.

In a shallow water waveguide and at a range greater than a few water depths the acoustic field generated by a monochromatic point source at the i^{th} hydrophone of a VLA is given by the so-called *Green's* function

$$G_\omega(r, z_0, z_i) = \frac{-j}{\rho\sqrt{8\pi R}} e^{-j\frac{\pi}{4}} \sum_{n=1}^{M} \frac{Z_m(z_i) Z_m(z_0)}{\sqrt{k_m}} e^{jk_m R}, \tag{5.3}$$

where m is the mode number, M is the total number of propagating modes, ρ is the (constant) water density, R is the source-array range, Z_m is the m^{th} mode shape, z_0 is the source depth, z_i is the i-hydrophone depth, and k_m is the m^{th} mode horizontal wavenumber. In a range independent environment and under the adiabatic condition k_m and M are the only quantities in (5.3) that depend on frequency ω. In the frequency domain the synthetic pTR IR acoustic field (5.2) in a stationary environment (considering Δ to be negligible) is given by [44]

$$\begin{aligned} P_{pc}(R, z_0, z_i, \omega) &= \sum_{i=1}^{I} G_\omega(R, z_0, z_i) G_\omega^*(R, z_0, z_i) \\ &= \frac{1}{\rho^2 8\pi R} \sum_{m=1}^{M} \sum_{n=1}^{M} \frac{Z_m(z_0) Z_n(z_0)}{\sqrt{k_m k_n}} \sum_{i=1}^{I} Z_m(z_i) Z_n(z_i) e^{j(k_m R - k_n R)} \\ &= \frac{1}{\rho^2 8\pi R} \sum_{m=1}^{M} \frac{|Z_m(z_0)|^2}{|k_m|}, \end{aligned} \tag{5.4}$$

where, for simplicity, it was considered that $Z_m(\cdot)$ and k_m are real quantities, which amounts to ignoring the leaky modes and considering the loss mechanisms to be negligible [27]. Additionally, in (5.4) it was considered that the array spans the entire water column and that hydrophones depth sampling is sufficiently dense to fulfil the modal orthogonality property.

Since k_m in the denominator of (5.4) is a weak function of frequency, $P_{pc}(\cdot)$ is approximately constant. Thus the in time domain $p_{TR}(\cdot)$ given by (5.2) can be approximated by a dirac pulse under convolution with the bandlimited transmitted sequence.

5.3 Passive Time Reversal geometric mismatch compensation

When there is a geometric mismatch Δ (Δr for source-array range, Δz_0 for source depth, Δz_i for array depth, or any combination of those) between the probe and data transmissions it can be shown [48] that the mismatch in one of them can be compensated by applying a frequency shift $\Delta\omega$ to the other, and (5.4) becomes

$$\begin{aligned} P_{pc}(\cdot, \Delta\omega; \Delta r, \Delta z_0, \Delta z_i) &= \sum_i^I G_\omega(R+\Delta r, z_0+\Delta z_0, z_i+\Delta z_i) G^*_{\omega+\Delta\omega}(R, z_0, z_i) \\ &= \frac{1}{\rho^2 8\pi R} \sum_{m=1}^M \sum_{n=1}^M \frac{Z_m(z_0) Z_n(z_0+\Delta z_0)}{\sqrt{k_m k_n}} \sum Z_m(z_i) Z_n(z_i+\Delta z_i) \\ &\quad e^{j(k_m^\dagger R - k_n(R+\Delta r))}, \end{aligned} \tag{5.5}$$

where $k_m^\dagger = k_m(\omega+\Delta\omega)$, the influence of the frequency shift on the horizontal wavenumber k_m placed in the denominator of (5.5) is neglected and the range shift is considered to be small enough so that $R \approx \sqrt{R(R+\Delta r)}$ in the denominator. In (5.5) it is relevant that the source-array range shift Δr perturbs the exponential term, the array depth shift Δz_i perturbs the modes orthogonality and the source depth shift Δz_0 perturbs the gain that is related with the focal spot depth in aTR (see [48] for details). A full discussion of this perturbation mechanism is presented in [48] and [46]. From this discussion it turns out that the frequency shift $\Delta\omega$ used in (5.5) can be computed as

$$\Delta\omega = \frac{\omega}{R}(-\Delta r\beta + \Delta z_i \zeta_i + \Delta z_0 \zeta_0), \tag{5.6}$$

and is applied in (5.5) by considering the first order Taylor expansion

$$k_m(\omega+\Delta\omega) \approx k_m(\omega) + \frac{dk_m(\omega)}{d\omega}\Delta\omega, \tag{5.7}$$

where the derivative of k_m with respect to ω represents the horizontal group slowness. In (5.6) β, ζ_i and ζ_0 are the waveguide invariants related to Δr, Δz_i and Δz_0, respectively. Since ζ_i and ζ_0 have a similar nature, in the following ζ will be used to represent both.

The invariant β is a well-known invariant in the frequency/range plane [6, 21] and is selected from a set of values

$$\beta_{mn} = \frac{\frac{1}{v_{h,n}} - \frac{1}{v_{h,m}}}{\frac{1}{u_{h,n}} - \frac{1}{u_{h,m}}}, \tag{5.8}$$

where $v_{h,m} = \omega/k_m$ is the horizontal phase velocity and $u_{h,m}$ is the horizontal group velocity of mode m. The selection of β from the β_{mn} set must take in consideration the best linear approximation in the least-squares sense of the horizontal wavenumber k_m using the horizontal group slowness for a limited number of of modes $M_e < M$, that is,

$$k_m \approx -\frac{dk_m}{d\omega}\omega\beta + \omega\rho_\beta, \tag{5.9}$$

where β represents the slope of the approximation and ρ_β its offset. The invariant ρ_β is closely related with β and is selected in a set of values

$$\rho_{\beta,mn} = \frac{1}{v_{h,m}} + \beta_{mn}\frac{1}{u_{h,m}}. \tag{5.10}$$

With the approximation of k_m (5.9) the compensation of the range mismatch is straightforward since the range mismatch Δr and the frequency shift compensation $\Delta\omega$ given by (5.6) both affect (5.5) in the exponential term. Such compensation can be applied to narrowband signals since β and ρ_β are invariant with frequency, in a similar manner to the focal intensity range shift for aTR proposed in [55].

The ζ waveguide invariants used for source depth Δz_0 and array depth Δz_i compensation have been used in [48] in a similar manner to β, but for the approximation of the vertical wavenumber γ_m using the horizontal group slowness

$$\gamma_m \approx -\frac{dk_m}{d\omega}\omega\zeta + \omega\rho_\zeta, \tag{5.11}$$

ζ is selected from a set of values

$$\zeta_{mn} = \frac{\frac{1}{v_{v,n}} - \frac{1}{v_{v,m}}}{\frac{1}{u_{h,n}} - \frac{1}{u_{h,m}}}, \tag{5.12}$$

where $v_{v,m} = \omega/\gamma_m$ is the vertical phase velocity, and ρ_ζ is selected in the set

$$\rho_{\zeta,mn} = \frac{1}{v_{v,m}} + \zeta_{mn}\frac{1}{u_{h,m}}. \tag{5.13}$$

The application of (5.11) in (5.5) for the source depth mismatch Δz_0 and array depth mismatch Δz_i compensation was made possible after establishing that they can be partially compensated using $\exp(j\gamma_m\Delta z_0)$ and $\exp(j\gamma_m\Delta z_i)$ respectively (see [48] for details). That is, for source depth mismatch Δz_0 compensation

$$\sum_{m=1}^{M} Z_m(z_0)Z_m(z_0+\Delta z_0)e^{j\gamma_m\Delta z_0} \approx \sum_{m=1}^{M} Z_m(z_0)Z_m(z_0)\frac{V(\Delta z_0)}{2}, \tag{5.14}$$

where $|V(\Delta z_0)| \approx 2$ for small values of Δz_0 and $|V(\Delta z_0)| \approx 1$ for higher values of Δz_0. For the array depth mismatch Δz_i compensation

$$\sum_{i=1}^{I} Z_m(z_i)Z_n(z_i+\Delta z_i)e^{j\gamma_m\Delta z_i} \approx \sum_{i=1}^{I} Z_m(z_i)Z_n(z_i)\frac{W(m,\Delta z_i)}{2}, \tag{5.15}$$

where $|W(m, \Delta z_i)| \approx 2$ for small values of Δz_i and $|W(m, \Delta z_i)|$ oscillates around 1 for higher values of Δz_i.

With the approximation of γ_m (5.11) and the compensation mechanisms (5.14) and (5.15) the compensation of the source and array depth mismatches is straightforward since the mismatch can be compensated by a complex exponential of γ_m and the frequency shift compensation $\Delta\omega$, given by (5.6), affects (5.5) in an exponential factor. Such compensation can be applied to narrowband signals since ζ and ρ_ζ are invariant with frequency.

As previously suggested for the invariant β, the ζ compensation mechanism has better performance when considering an effective number of modes $M_e < M$. The selection of β in (5.8) and ζ in (5.12) for optimal compensation depends on M_e. Such dependence suggests that the compensation mechanism can be further optimized by considering its application to smaller groups of modes instead of a single group of modes from $m = 1, .., M_e$, resulting in different values of β and ζ for each group. That was previously proposed in [55] and [35] for the waveguide invariant β.

In a waveguide with a depth-dependent sound-speed profile the vertical wavenumber as well as phase velocity become depth dependent. In the present paper it is assumed that such dependence is small enough so that ζ_i can be calculated from the mean phase velocity, $\overline{v_{v,m}(z_i)}$, over the array. Since ζ_0 is computed for the nominal source depth z_0 in a real situation it will be expected that $\zeta_i \neq \zeta_0$.

5.4 The passive time-reversal frequency shift equalizer

Figure 5.1 shows the pTR system adapted to incorporate a frequency shift that compensates for the geometric mismatch Δ between the IR for probe-signal transmission $h'(t)$ and the IR during data transmission $h(t)$. It behaves as a matched filter (to the IR) demodulator with a set of L frequency shifts being applied to the channel IR $h'(t)$ estimate after time windowing, where the optimal frequency shift is selected based on the "Maximum power selection" block with the $\mathsf{z}_l(t)$ power being computed in time slots. In Figure 5.1 the pTR output signal can be written as

$$\mathsf{z}_l(t) = y_l(t) + x1_l(t) + x2_l(t) + x3_l(t), \tag{5.16}$$

where index l designates frequency shift $\Delta\omega_l$, $y_l(t)$ contains the desired data-signal contaminated with ISI and the other three terms are noise disturbances (see [49] for definitions and details).

The overall Signal to Noise Ratio (SNR) is the ratio between the power of the signal term $y_l(t)$ and a sum of the variances of the noise disturbances $x1_l(t)$, $x2_l(t)$ and $x3_l(t)$. Considering the signal and noise powers given by (3.26-29) of [49] it can be shown that the effect of the frequency shift compensation on the channel IR $h'(t)$ estimate is higher on the signal variance term than on the noise variances, contributing to SNR enhancement. Therefore, tracking the maximum power of the pTR output $\mathsf{z}_l(t)$ gives a clear indicator of the best frequency shift taking into account the actual environmental/geometric conditions

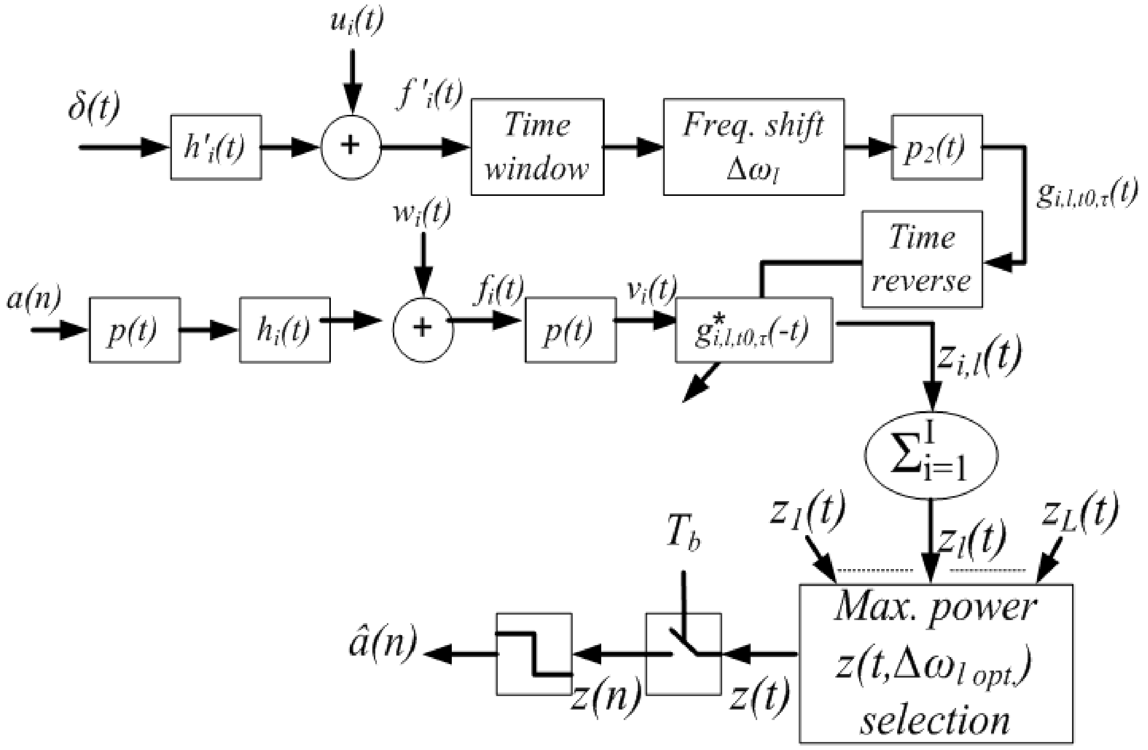

Figure 5.1: Block-diagram of the FSpTR equalizer. The blocks in the upper path represent the probe-signal IRs estimate, time windowing, and frequency shift operations. The blokes in the middle path represent data transmission and crosscorrelation with the IRs estimate obtained in the upper path. Summation over the I hydrophones gives the L pTR processor outputs $\mathsf{z}_l(t)$. The blokes path below represent the selection of $\mathsf{z}_l(t)$ with the frequency shift that best compensates for geometric mismatch between probe and data transmissions, and the transmitted symbols estimation.

of the signals being received. That results in the FSpTR system that equalizes the real pTR IR $\sum_{i=1}^{I} h_i(t) * h'^{*}_{i,t_0,\tau}(-t)$ (where the $'$ indicates that there is a geometric mismatch Δ between h_i and $h'^{*}_{i,t_0,\tau}$) with the non mismatched pTR IR $\sum_{i=1}^{I} h_i(t) * h^{*}_{i,t_0,\tau}(-t)$, where t_0 and τ are the starting time and duration of the time window, respectively.

5.5 Real Data Application

The experimental data were acquired during the MREA'04 sea trial that took place off the town of Setúbal, approximately 50km south of Lisbon (Portugal), in April 2004. The pTR experiment started at a close range of 0.6km to the south of the receiving array (in a gently up sloping region) and the source progressively opened range to the southeast up to 2km (with a progressive slope reduction up to range independence). The environment was characterized by a water column depth ranging between 90 to 110 m over a 1.5 m silt bottom and gravel layer. The receiving array was free drifting in a surface suspended Acoustic Oceanographic Buoy (AOB) [51], which was found to oscillate vertically due to the surface waves with amplitude of approximately 0.63m and frequency between 0.43 and

0.4Hz, as measured by a wave rider buoy placed in the area of the experiment. The acoustic source was suspended from the NRV Alliance, its depth was measured at a sampling rate of 1 s with a 10 cm resolution depth sensor. In the data set processed in this paper it oscillates with a main component of 0.1 Hz, between 71.64 and 72.24 m.

During the MREA'04 sea trial the pTR based data communications conceptual system was similar to that of Figure 5.1, with the $p_2(t)$ narrowband filter of the IR estimation operation (path above in Figure 5.1) distributed between the transmitter and the receiver, i.e., the transmitted probe-signal was a fourth-root raised-cosine pulse and IR estimates were obtained by correlating the received probe-signal with the transmitted one (see [45] for details).

This paper analyzes modulated data at a carrier frequency of 3.6 kHz, using a symbol rate of 400 baud and 2-PSK constellation. Fourth-root raised cosine signaling pulses with 100% roll-off were used such that the signal bandwidth is 800 Hz. Each individual transmission comprises a single truncated PAM signaling pulse acting as a channel probe with symmetric guard intervals for a total duration of 1 s, followed by a 20 s data packet. The source sequentially transmits 4 packets for a total duration of 84 s. In order to demonstrate the long-term stability of the proposed FSpTR compensation mechanism only the third channel probe pulse was used in the pTR operation of Figure 5.1 to estimate the transmitted symbols in the four data packets. The data was preprocessed using the Doppler compensation method as proposed in [20].

Since the sound speed profile is composed of a thermocline of approximately 20 m and 1512 m/s over a down refracting sound speed up to approximately 1505 m/s near the bottom two different modal structures have been observed by the top two hydrophones and by the six bottom hydrophones [35] [48]. Those two modal structures are expected to have different invariants [35], and for the purpose of showing the usefulness of the waveguide invariant frequency shift in underwater communications with pTR in a geometric variable environment, only the six hydrophones below the thermocline were considered.

The system of Figure 5.1 requires the use of a time window whose optimum length τ_{opt}, in a non geometric mismatch case, has been found in [49]. The time window initial point t_0 is set to an arbitrary point before the first arrival and the time window length τ is set to a value higher that the optimum in order to allow for a better behavior of the compensation mechanism in presence of geometric mismatch. In the ray mode analogy [58] later arrivals are related with higher modes, making the time window operate as a mode filter.

By considering the same frequency shift $\Delta\omega_l$ to be applied to all modes captured in the time window (t_0, τ) in the system of Figure 5.1 the surface of Figure 5.2 results. The surface represents the pTR output power $\sigma_z^2(t)$, computed in time slots of 0.5 s, as a function of time and frequency shift and the blank spaces represent the the elapsed time between the data slots. The solid line traces the maximum of the surface as a function of time, and the '*' indicates the time instant where the channel probe used in the pTR processor was received. GPS data, acquired during the experiment, shows that during the 80 s of data transmission the source-array range increases by about 50 m, which can be clearly seen in Figure 5.2 as a mean decrement of optimal frequency shift from about 150 Hz to about -50 Hz with 0 Hz at the channel probe location. Oscillations around the mean increment seem to be mainly due to the other geometric mismatches (array depth and source depth), but no definitive conclusions can be drawn since there is no ground truth information about array or source depth variations.

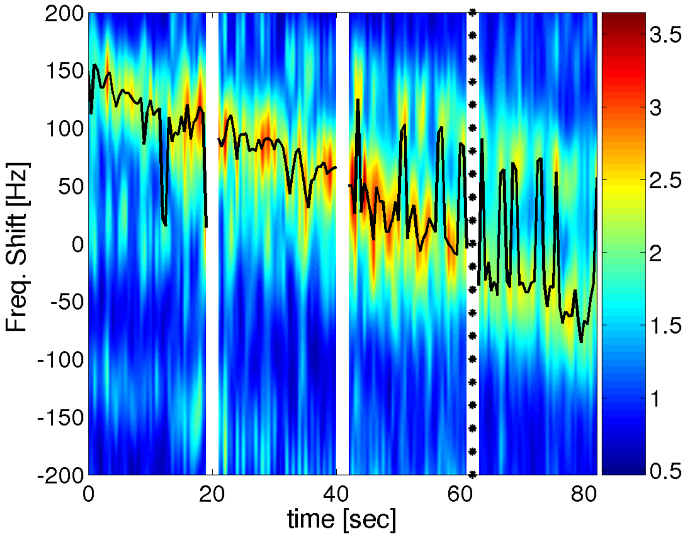

Figure 5.2: Passive time-reversal output mean magnitude $\mathbf{z}_l(t)$ as a function of time and applied frequency shift, computed by slots of 0.5 s. The solid line traces the maximum of the surface.

Figure 5.3 shows the MSE between the estimated and transmitted bit sequences, computed in slots of 0.5 seconds, for plain pTR with no compensation (solid line) and for pTR with compensation (red dashed line). The solid line initially shows a strong degradation in the uncompensated pTR that progressively reduces when approaching $t = 60$ s. Compensated results (red dashed line) maintain the MSE at approximately the same level, resulting in a strong gain. In the first 20 s that gain is about 5.55 dB, in the second 20 s it is about 5.7 dB, in the third 20 s is about it 1.64 dB and in last 20 s it is about 1.53 dB, for an overall gain of about 4.11 dB. It is remarkable that such results were obtained with a range mismatch up to about 37.5 m with source depth varying between 71.6 m and 72.3 m and an array depth oscillation of approximately 0.63 m.

5.6 Conclusions and Future work

Experimental results were given for time-reversed demodulation of 3.6 kHz binary PSK data collected during the MREA'04 experiment. Two receiving architectures were compared: plain pTR and pTR with frequency shift for geometric mismatch compensation - FSpTR. By itself, pTR suffers a significant performance penalty due to geometric mismatch during data transmission, resulting in acceptable results only in a 20 s window

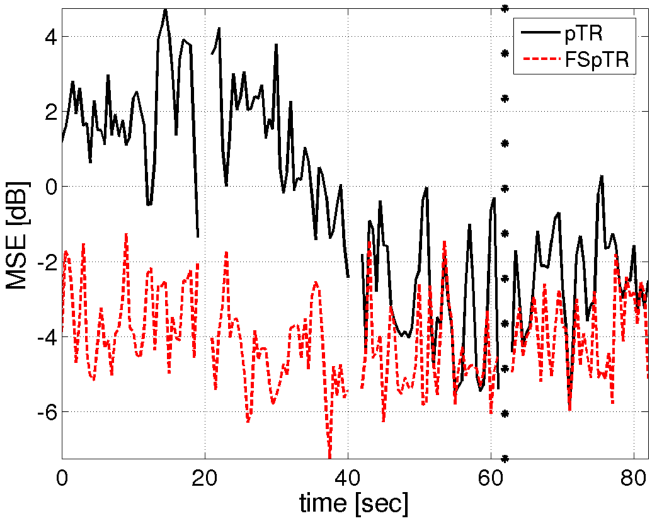

Figure 5.3: Mean squared error between the estimated and transmitted data symbols for plain pTR (black line) and FSpTR (red dashed line).

around the channel probe location. FSpTR presents a longer stability that was shown to be effective for up to 60 s from the channel probe location. Moreover, FSpTR presents a gain of 1.5 dB over pTR even for short-term mismatch. Future work should address a comparison between FSpTR and other adaptive pTR systems [20].

Due to its environmental based nature, FSpTR can be used not only to attain reliable underwater communications, but also to track the geometric variations during data transmission considering a previous estimation of the waveguide invariants β, ζ_i and ζ_0. Future experiments should be planned in order to explore such possibility.

In the present paper the Doppler compensation has been performed off-line prior to the equalization process. Future work should address its inclusion in the equalizer processor. In what concerns symbol synchronization, an heuristic method that chooses the minimal spread of the constellation prior to the slicing, was adopted.

Acknowledgments

This work was supported by Fundação para a Ciência e a Tecnologia under programs POCI, POCTI and POSI. The authors would like to thank the NATO Undersea Research Centre for the organization of MREA'04 sea trial, NRV Alliance master and personnel and the scientist in charge Emanuel F. Coelho.

Chapter 6

Environmental equalizer for high data rate underwater communications

---

Abstract: Equalizers are used in underwater coherent communications to track channel impulse responses and compensate for intersymbol interference due to multipath. Such equalizers are based on black-box channel models which conceptually ignore the fact that IR variability is caused by fluctuations of environmental parameters. Environmental-based equalization as presented in this work is based on passive time-reversal and waveguide invariant properties of ocean channels. Passive time-reversal allows for the implementation of a simplified communication system, but its primary cause of performance degradation is the presence of geometric mismatch between the probe-signal and the actual data transmission. This problem is addressed here through waveguide invariance, which states that geometric mismatches, both in depth and range, can be partially compensated by applying an appropriate frequency shift in the passive time-reversal operator. Results with 2000 baud binary PSK signaling at a carrier frequency of 12.5 kHz, collected during the RADAR'07 sea trial with a moving source and a free drifting receiver array, show that the Mean-Square Error (MSE) between transmitted and estimated data symbols reduces to -4 and -8 dB in the presence of strong and mild multipath, respectively.

6.1 Introduction

Underwater acoustic communication channels present serious limitations for attaining even modest data rates that are trivially achieved in terrestrial wireless radio channels. Common causes are the significant delay spread that induces multipath and hence strong frequency selectivity; the available bandwidth is limited and increasing the frequency also increases the attenuation; and the low propagation speed of sound causes significant Doppler even with low source-receiver relative speeds.

In order to overcome such drawbacks the most widely-used solutions for coherent communications are based on equalizers similar to those adopted in terrestrial communications. Operational difficulties, such as problems of convergence of adaptive algorithms, occur due to specific characteristics of the underwater channel (high variability of the channel Impulse Responses (IRs), high number of coefficients that depend on the channel delay spread and can vary from a few to hundreds of symbols, strong Doppler).

Despite the high spread and high variability of underwater channel IRs it is well known, from tomographic and inversion experiments, that the physical characteristics of the environment vary quite slowly [1]. This suggests that an equalizer based on environmental change tracking and matched-field processing (i.e. a full inversion equalizer) would be more robust and stable than standard equalizers. Unfortunately, the strong nonlinearity of inversion and tomographic methods and their high computational load (when compared with the required speed for high data-rate acoustic communication) makes full inversion equalization impractical.

Considering that a communication system usually transmits information in packets whose duration does not exceeds a few tens of seconds, it is possible to identify geometric environmental characteristics[1], as being those that have first order impact on the variability of IRs during packet transmission. Chuprov's work [6] on the invariant properties of layered media establishes a linear relation between group and phase velocities in the vicinity of a canonic point, from which local frequency/range and frequency/depth invariants follow.

The first attempts at underwater communication using environmental information [17, 50, 24, 43] relied on basic properties of Time-Reversal (TR) in underwater channels [38, 26, 8, 34, 13]. A particular type of TR — passive Time-Reversal (pTR), also termed Passive Phase Conjugation (PPC) [26] in the frequency domain —, uses a receive-only array, with a probe-signal transmitted ahead of the data for IR estimation. The received probes are then used as a synthetic channel for temporal focusing of the data, which effectively deconvolves the multipath generated by the real channel.

When applied to field data, the achieved TR focus is not perfect due to errors in IR estimates and the time variability of the channel, resulting in uncompensated intersymbol interference (ISI) [45]. That problem is even more relevant in communications with a moving source and/or receiver, in which case one would expect a rapid degradation of pTR temporal focusing due to the increasing mismatch between assumed and actual channels. In order to ensure longer stability of the focal spot, three solutions have been proposed in the literature: one is to use an adaptive algorithm to track the IRs throughout data packets [14]; another solution is to use a single-channel equalizer after TR [54]; and finally a third alternative is to use a low-complexity equalizer with only one coefficient per channel [20]. A performance comparison between adaptive pTR variants is presented in [20]. In the first method, channel estimates are represented by a large number of coefficients that need to be adapted, thus leading to relatively complex equalizers. The second and third methods offer a better compromise between complexity and efficiency. The approach taken in this work

---

[1] geometric characteristics are source-receiver range, as well as source, receiver and water column depths. Non-geometric characteristics include sound-speed profile, sediment and bottom properties, salinity, and water density.

stems from those but goes one step further by considering that the environment mismatch between the probe-signal and data transmissions is mainly due to geometric disparities, knowledge of which can then be used to compensate for the overall IR mismatch.

A physics-based algorithm for pTR equalization based on waveguide invariants of shallow water channels is proposed. The waveguide invariant β [6, 21] has been previously applied to change the range focus in active time reversal (aTR) [55], and to develop a model for performance prediction of a time-reversal communication system [42]. In [48] the waveguide invariant allowed for the compensation of pTR geometric mismatch, as it was shown that the impact of changes on geometric features can be compensated by a simple frequency shift of estimated IRs acquired during probe-signal transmission. In [47] such mismatch compensation method was applied to underwater communications in the 3.5 kHz frequency band. The resulting environmental equalizer, termed Frequency Shift pTR (FSpTR), increased the pTR output power and reduced the Mean-Square Error (MSE).

In this work the FSpTR equalizer is applied in a frequency band around 12.5 kHz. Signal propagation is substantially different from the one reported in [47], with a significant number of undersampled high order modes resulting in strong modal aliasing, while a strategy to overcome this effect is proposed. Moreover, the environmental equalizer does not require symbol decisions to be fed back to the processing structure, as the performance criterion is based on output power. This has the added benefit of allowing simple Doppler compensation methods to be used at the equalizer output.

Probe timing optimization is another important issue in pTR-based communications. Heuristic reasoning suggests that if the observation window fails to include all significant multipaths, pTR operation will result in imperfect retrofocusing, while an overly long window will degrade the performance by introducing undesired noise [18, 45, 11]. In [49] it was shown that a metric can be defined in order to optimize the pTR communications system with respect to the time-window length. In this work it will be shown that the same approach can be extended to the pTR environmental equalizer.

The reliability of the physics-based waveguide invariant pTR equalizer is demonstrated using experimental data obtained during the RADAR'07 sea trial, where binary PSK signals at a data rate of 2000 bits per second were transmitted with a carrier frequency of 12.5 kHz. FSpTR features long-term compensation of channel mismatch (up to 50 seconds), its output MSE remaining stable even in the presence of geometric mismatches. Results show that the environmental equalizer achieves almost error-free decoding, with -4 dB of MSE using a short array of 6 hydrophones, and -8 dB using 16 hydrophones.

A performance comparison between the Fractionally-Spaced Equalizer (FSE) and the environmental equalizer is presented. It is found that the FSE outperforms the environmental equalizer. Nevertheless, it should be stressed that for proper operation the FSE requires crucial human intervention for selecting the number of coefficients and forgetting factor, while the probe timing optimization of pTR environmental equalizers depends on well-defined metrics that can possibly be used for unsupervised operation.

This work is organized as follows: section 6.2 recalls the use of pTR in underwater communications and the geometric mismatch compensation of pTR using frequency shifts; section 6.3 presents the FSpTR equalizer and describes its operation; section 6.4 addresses probe timing optimization; the FSpTR is applied to real data in section 6.5; section 6.6 summarizes the main results, draws some conclusions, and suggests future research.

6.2 Passive Time Reversal geometric mismatch compensation

The basic setup for applying pTR to communications consists in a point source that sends information to a Vertical Line Array (VLA). The procedure starts by sending a short probe-signal, waiting for the channel to clear of multipath arrivals, and then sending the data stream. In the noiseless case, the pTR output after the received probe and data are processed is given by [49]

$$y(t) = [a(t) * p_4(t)] * p_{TR}(t, \Delta), \tag{6.1}$$

where $*$ represents convolution, $[a(t)*p_4(t)]$ is the transmitted amplitude/phase-modulated signal with raised-cosine shaped symbols; $p_{TR}(t, \Delta)$ is the resulting pTR IR acoustic field given by

$$p_{TR}(t, \Delta) = \sum_{i=1}^{I} h_i(t, \Delta) * h_i'^*(-t), \tag{6.2}$$

where the superscript $*$ denotes complex conjugation, i is the hydrophone index, $h_i'(t)$ represents the channel IR during probe transmission, $h_i(t, \Delta)$ is the IR during data transmission, and $\Delta \equiv (\Delta r, \Delta z_i, \Delta z_0)$ represents a possible mismatch between h_i' and h_i (where Δr is the source-array range mismatch, Δz_i is the array depth mismatch, and Δz_0 the source depth mismatch). If there is no mismatch and the array densely samples the whole water column the overall time domain pTR IR given by (6.2) for $\Delta \equiv 0$ can be approximated by a bandlimited sinc pulse. In the context of normal modes of propagation [58, 27], the formal demonstration of this follows from the normal modes orthogonality property [34]. Geometric mismatch can be partially compensated by applying a frequency shift to $h_i'(t)$, as discussed in detail in [46, 48, 47].

The idea of using a frequency shift, $\Delta\omega$, to compensate for the geometric mismatch relies on Chuprov's work [6] that for a given group of modes in a waveguide demonstrates the existence of the invariant

$$\beta = \frac{\Delta\omega}{\Delta r}\frac{R}{\omega}, \tag{6.3}$$

that defines lines of constant intensity in the frequency-range plane. For a ray with inclination χ the invariant

$$\zeta = -\beta \coth\chi = \frac{\Delta\omega}{\Delta z_i}\frac{R}{\omega}, \tag{6.4}$$

defines lines of constant intensity in the frequency-depth plane. In a layered waveguide the acoustic field is formed by a reduced number of mode groups, and for each of those β and ζ are invariant with frequency.

Song [55] used a method based on the waveguide invariant β for shifting the range of the TR focal spot. The proposed method can be readily applied in pTR for range mismatch compensation. Actually, the impact of range or depth mismatches on the acoustic field turns out to be similar, and the latter can be compensated in much the same way as the former through a properly defined invariant ζ. In [46, 48] a strategy based on the invariant ζ is developed for restoring the orthogonality property of normal modes, which is destroyed by array depth mismatch. In the context of active TR, source depth mismatch can be seen as if observing the back-propagated field at a depth different from the focal depth. In pTR this effect results in a loss of performance that can be recovered similarly to the restoration of orthogonality of normal modes. In their work, both Chuprov and Song considered only the acoustic field intensity. However, phase information is crucial when applying pTR in coherent communications, and the influence of the frequency shift in the signal phase must therefore be taken into consideration.

Considering (6.3) and (6.4) the appropriate frequency shift for mismatch compensation is given by

$$\Delta\omega = \frac{\omega}{R}(-\Delta r\beta + \Delta z_i\zeta_i + \Delta z_0\zeta_0), \tag{6.5}$$

where R is the original source-array range and ω is the mean frequency of the bandlimited IRs. The invariants ζ_i and ζ_0 are only constant, and equal, for a homogeneous sound-speed profile, otherwise they vary with sound velocity over the water column. This dependence increases with frequency as the WKB approximation becomes applicable and the perturbation of lower order modes by the sound speed variations becomes more visible. It results that when the compensation operates at low frequencies a mean value of ζ_i should be used, but when operating at high frequencies the compensation should be applied to a shorter array or considering smaller sections of the array.

Applying the frequency shift (6.5) in (6.2) it results

$$\begin{aligned} p_{TR}^{comp}(t,\Delta) &= \sum_{i=1}^{I} h_i(t,\Delta) * [h_i'^*(-t)\exp(-j\Delta\omega t)], \\ &\approx A\; p_{TR}(t - t_{\rho,\Delta}) \end{aligned} \tag{6.6}$$

were the compensation is achieved up to attenuation factor A and a time delay $t_{\rho,\Delta}$. The attenuation factor A is due to the loss of validity of the compensation through invariants in the presence of an increasing geometric mismatch. The compensation mechanism also introduces a linear phase that results in a time delay $t_{\rho,\Delta} = (\rho_\beta\Delta r - \rho_{\zeta,i}\Delta z_i - \rho_{\zeta,0}\Delta z_0)$, where ρ_β, $\rho_{\zeta,i}$ and $\rho_{\zeta,0}$ are three other invariants closely related with β, ζ_i and ζ_0. In [48] a full description of the gain factor A and of the linear phase that results in the time delay $t_{\rho,\Delta}$ is presented.

The conditions for propagation in a layered ocean are such that the field is effectively formed by a few groups of modes with consecutive indexes (that correspond to rays from the point of view of geometric acoustics) [27]. The compensation mechanism should be applied to each group independently, since only then can their phase and group velocities be approximated by a constant [35]. Despite the fact that the gain factor A causes attenuation in the matched pTR IR $p_{_{TR}}(t)$ in (6.6), the main feature of the compensation mechanism is the restoration of the modes orthogonality property, which constitutes the basis for pTR.

Replacing the mismatch pTR IR (6.2) by the compensated one (6.6) in the pTR communication system output (6.1), it results

$$y^{comp}(t) = A\ [a(t) * p_4(t)] * p_{_{TR}}(t - t_{\rho,\Delta}), \tag{6.7}$$

that resembles the pTR communication system output with no mismatch. That is the basic idea of FSpTR equalizer that in a Matched-Filter Demodulator (MFD) receiver manner applies a set of frequency shifts to the channel IR estimates (6.6) and assumes that the perfect match is obtained for the frequency shift that gives the maximum power of (6.7).

6.3 The passive time-reversal frequency shift equalizer

Figure 6.1 shows a block diagram of the pTR communication system adapted to incorporate frequency shifts for compensating geometric mismatch Δ between the probe-signal transmission IR $h'(t)$ and the IR during data transmission $h(t, \Delta)$ [49, 47]. In Figure 6.1(a) the system behaves as a matched filter (to the IR) with a set of L frequency shifts being applied to the channel IR estimates, $h'_i(t)$, after time windowing. Summing the outputs of matched filters over all array sensors yields

$$\mathsf{z}_l(t) = y_{sig,l}(t) + y_{isi,l}(t) + x_l(t), \tag{6.8}$$

where index l designates the l^{th} frequency shift $\Delta\omega_l$, $y_{sig,l}(t)$ contains the desired data-signal and $y_{isi,l}(t)$ the signal residual ISI contamination. Term $x_l(t)$ represents the pTR output noise that results from interaction between the input noises $w_i(t)$ and $u_i(t)$ and on the channel responses during transmission of probe, h'_i, and data, h_i, signals (see [49] for definitions and details).

Similarly to a MFD receiver, the frequency shift described in Section 6.2 acts to equalize the overall pTR IR $\sum_{i=1}^{I} h'_i(t) * h^*_{i,t_0,\tau}(-t, \Delta)$, approximating the matched response $\sum_{i=1}^{I} h_i(t) * h^*_{i,t_0,\tau}(-t)$, where t_0 and τ are the starting time and duration of the time window, respectively. Frequency shifts do not strongly affect the power of the noise term $x_l(t)$, since their primary effect is to increase the signal power term, and thus contribute to enhance the signal-to-noise ratio (SNR). Therefore, tracking the maximum power of the pTR output $\mathsf{z}_l(t)$ gives a clear indicator of the best frequency shift taking into account the actual environmental/geometric conditions of the received signals.

In Figure 6.1(b) the L outputs of part (a), $\mathsf{z}_l(t)$, are combined, synchronized, Doppler compensated and finally used to estimate the transmitted data sequence. In the "Combining" block the $\mathsf{z}_l(t)$ are divided into N_s temporal slots, the power of each slot is computed and stored in a $L \times N_s$ matrix. The slots are then combined according to three criteria:

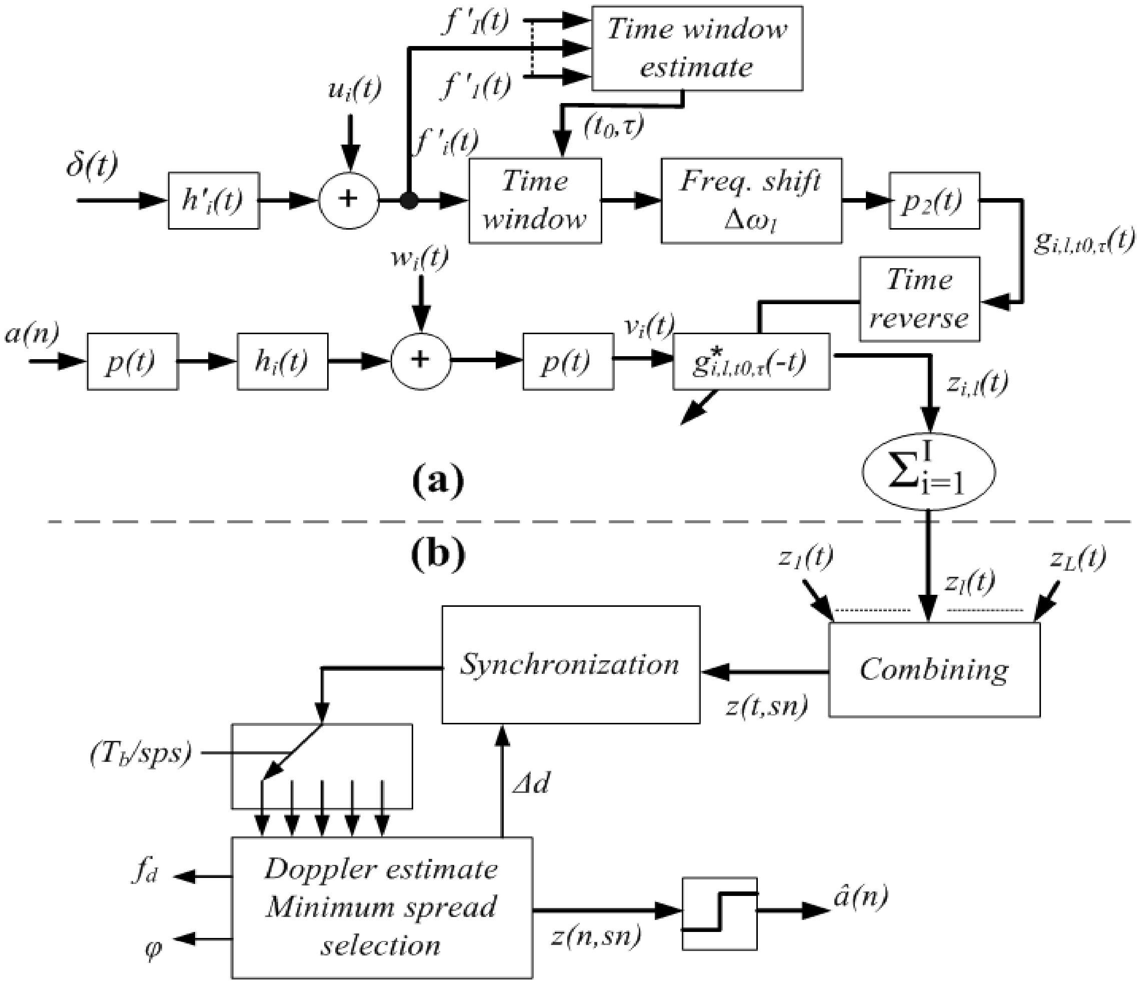

Figure 6.1: Block-diagram of the FSpTR equalizer. Part (a): the blocks in the upper path represent the probe-signal IR estimate, time windowing, and frequency shift operations. The blocks in the middle path represent data transmission and crosscorrelation with the IR estimate obtained in the upper path. Summation over the I hydrophones gives the L pTR processor outputs $\mathsf{z}_l(t)$. Part (b): the blocks depicts combining of $\mathsf{z}_l(t)$ considering the frequency shift that best compensates for geometric mismatch, Doppler compensation, synchronization, and symbol estimation.

considering that there is no frequency shift, which is the "plain pTR" case; for slot n_s select l with maximum power, which corresponds to the "FSpTR" case; find the local maxima for each slot (to be clarified in Section 6.5) and add them coherently, this will be denoted as the "FSpTR+" case. In the "Synchronization" block an initial synchronization, for the first signal slot n_s, is performed with the probe-signal sent previously to the data signal. If in the "Doppler estimate" block a requirement for Doppler compression/expansion is detected in a given slot, the next slot is re-synchronized in order to accommodate the detected Doppler compression/expansion, Δd. Such Doppler re-synchronization strategy requires that the Doppler compression/expansion of each slot should be smaller than one symbol period. The "Doppler estimate Minimum spread Selection" block operates by frac-tionating the slot into several symbol-rate-sampled (sps) streams. Each stream is then multiplied by a set of complex exponentials with angular frequency $2\pi f_{d,k}$. Then it is possible to identify the channel and the angular frequency with smaller constellation spread, and to estimate: 1) the Doppler frequency f_d, that is, the angular frequency which better compresses the constellation, 2) the Doppler shift Δd that results from the stream with lower constellation spread and 3) the constellation offset ϕ of the selected stream after Doppler compensation. After Doppler and offset compensation the stream with minimum constellation spread is used to feed the slicer. The slicer outputs the estimated symbol sequence, denoted by $\hat{a}(n)$.

6.4 Time-window optimization

In Figure 6.1 the time-window operation is of major importance, as it controls the length of channel IRs that will be used for pTR. Each IR typically consists of a main arrival followed by strong multipath and often preceded by weak precursor multipath. The benefits of pTR from a communications perspective are twofold; it increases the SNR and reduces the residual ISI. In both cases the amount of multipath considered in the time-window will have a strong influence. When there is no mismatch between probe-signal and data transmissions the time-window optimum length can be predicted in the “Time-window estimate” block of Figure 6.1 using the channel IR estimates required for pTR.

Residual ISI in the matched case is defined as [56],

$$ISI(t_0,\tau) = \frac{\sum_{n\neq 0} |p_{TR}(nT_b,t_0,\tau)^2|}{|p_{TR}(0,t_0,\tau)^2|} \tag{6.9}$$

where

$$p_{TR}(nT_b,t_0,\tau) = \sum_{i=1}^{I} [h_i^*(-t,t_0,\tau) * h_i(t)] * p_4(t)\Big|_{t=nT_b} \tag{6.10}$$

is the overall pTR IR affected by the time window operation, sampled at the symbol period T_b. Optimal window parameters are obtained by minimizing (6.9). In [49] it was found that the pTR output SNR is proportional to the overall pTR IR accumulated power, given by

$$\Phi^2(t_0,\tau) = \frac{|C_y(t_0,\tau)|^2}{\tau}, \tag{6.11}$$

where

$$C_y(t_0,\tau) = \sum_{i=1}^{I} \int_{t_0}^{t_0+\tau} |h_i(t)|^2 dt, \tag{6.12}$$

is the sum across hydrophones of IR energy cumulative functions. The maximum of $\Phi^2(t_0,\tau)$, will provide time window settings (such as start time t_0 and duration τ) that optimize the output SNR.

Different window settings can result from the SNR and ISI criteria, nevertheless it was shown in [49] that the output SNR criterion should be used for low input SNR, whereas better results are achieved with the ISI criterion for high input SNR. Time-window optimization based on initial channel IR estimates for the matched case loses accuracy in the presence of channel mismatch, but its validity can be extended through mismatch compensation. That is the case of the FSpTR equalizer presented here, and of the Decision-Directed Passive Phase Conjugation equalizer [14].

6.5 Real Data Application

The experimental data were acquired during the RADAR'07 sea trial that took place off the town of Setúbal, approximately 50 km south of Lisbon (Portugal), in July 2007. The environment was characterized by a water depth varying between 90 to 120 m over a 1.5 m thick silt and gravel sediment layer. During the pTR experiment the source-array range, computed with GPS data, varied between 5.3 km and 5.24 km. The receiving array was attached to a surface-suspended and freely-drifting Acoustic Oceanographic Buoy (AOB) [51]. It comprised sixteen 4 m spaced hydrophones, the depth of the top one varying between 6.07 and 6.47 m as measured by an array colocated depth sensor. The acoustic source was suspended from the research vessel NRP D. Carlos I, and its depth for the time interval of the data set processed in this work oscillates between 60 and 61.1 m.

During RADAR'07 the acoustic communication system was conceptually similar to that of figure 6.1, with a chirp signal transmitted as a probe-signal and the channel IR estimates obtained by pulse compression. This work analyzes modulated data at a carrier frequency of 12.5 kHz, using a symbol rate of 2000 baud and 2-PSK constellation. Fourth-root raised cosine signaling pulses with 50% roll-off were used such that the signal bandwidth is 3000 Hz. Each individual transmission comprised a chirp signal acting as a channel probe with 4800 Hz bandwidth centered at the carrier frequency and 0.1ms duration, followed by 0.2ms guard time and a 50s data packet. The source sequentially transmitted 4 packets with an interval of 120s. During data transmission the source-array range decreased at a variable rate (relative velocity between 0.3 and 0.05 m/s), causing variable Doppler compression of the received signals. For example, the actual duration of the first packet differs by 18 symbol intervals from the nominal packet duration.

Figure 6.2 shows the water column sound speed profile computed from the temperature profile measured by thermistors collocated with the array hydrophones. It can be seen that the temperature profile is downward refracting up to hydrophone 9, at approximately 42m depth, and then becomes nearly constant.

Figure 6.3 shows the arrival pattern estimated from the chirp signal of the first data packet. It can be seen that the wavefronts are composed of a main path followed by down and up-going multipaths. Note that the WKB approximation is valid at the acoustic frequencies used in this experiment. Low-order modes, responsible for the main arrival, strongly attenuate in the water column and do not interact with the surface. On the other hand later paths, due to high-order modes, do interact with the sea surface. From this description it is expected that multipath will have greater impact in a communications system when using the upper part of the array than when using the full array, as ISI will be stronger in the former.

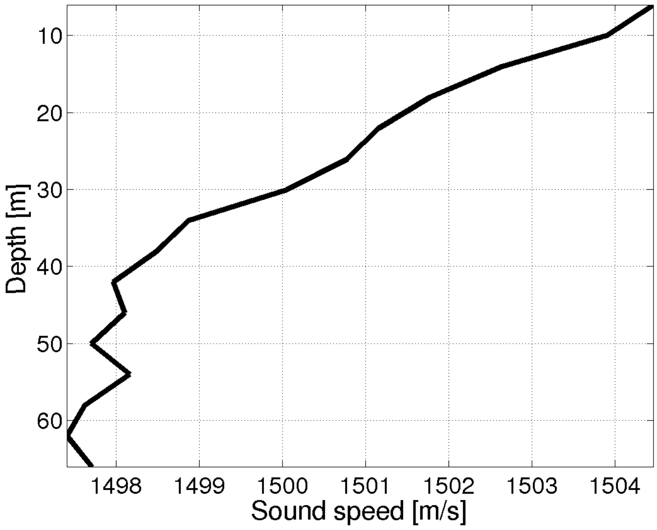

Figure 6.2: Mean sound speed profile during data transmission, during day 195 between 10:07h and 10:15h (local time).

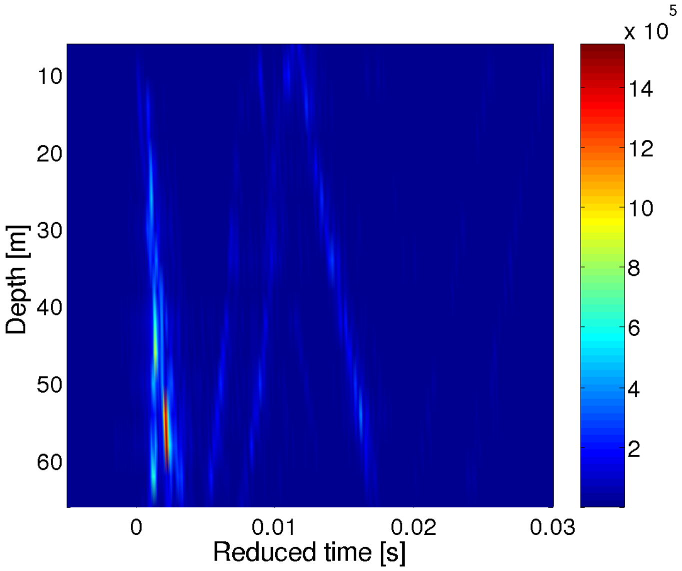

Figure 6.3: Arrival pattern estimated by pulse compression of the chirp probe-signal of the first data packet.

Figure 6.4 shows the normalized inverse of (6.9), $ISI^{-1}(t_0, \tau)$ (solid line), and the normalized $\Phi^2(t_0, \tau)$ from (6.11) (dashed line), where t_0 has been set arbitrarily before the main arrival. The channel IR estimates used to compute the arrival pattern of figure 6.3 are superimposed and plotted in figure 6.4, providing visual clues of where channel IRs are more intense, for the full 16-hydrophone array (a) and for the top 6 hydrophone array (b). The maximum of the dashed line gives the time-window length τ where the output pTR SNR is higher, whereas the solid line reveals the value of τ where residual ISI is better compensated. Figure 6.4(a) shows that for this case better results are expected with a short window covering approximately 4 symbols, while figure 6.4(b) shows that a short time-window can be used to optimize the output pTR SNR, but since there is a strong local maximum of the Φ curve (dashed line) close to the maximum of the ISI^{-1} curve (solid line) a 28 symbols time-window length is more appropriate.

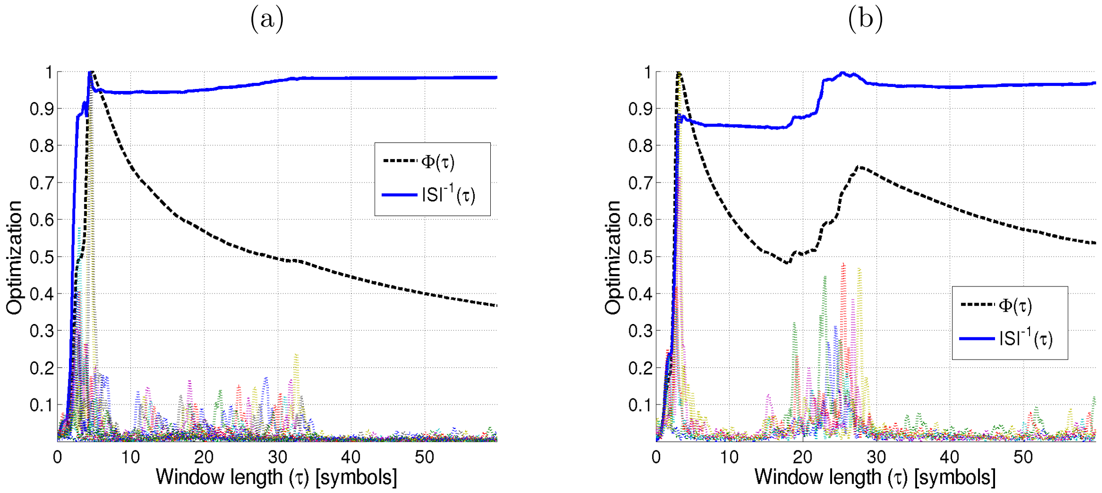

Figure 6.4: Time-window optimization with a 16-hydrophone array (a), with a 6-hydrophone array (b).

As an example of frequency shift optimization, figure 6.5 depicts the evolution of the pTR output $\mathbf{z}_l(t)$ mean power along one data packet as a function of frequency shift and time/slot number. Frequency shifts vary in the range ±600 Hz with an interval of $25Hz$. Each packet was divided into 200 time slots of 0.25 s duration each. The solid line connects the surface maxima (indicated by the stars '*') obtained for each time/slot-number. In figure 6.5(a), for the 16-hydrophone case, the same frequency shift $\Delta\omega_l$ is applied to all modes captured in the time window (t_0, τ). GPS data show that during these 50s of data transmission the source-array range decreases by approximately 11 m, which should be reflected in a mean increment of the optimal frequency shift in Figure 6.5. However, this is not visible because the frequency shift due to range decrease is masked by that due to source and array depth variations that can be observed in the up and down swing of the maximum power curve.

In Figure 6.5(b) the frequency shift $\Delta\omega_l$ is applied only to higher-order modes captured in the time window (t_0, τ) between 18 and 28 symbols of Figure 6.4(b). The compensation mechanism acts on modes that are poorly sampled by the array, resulting in spatial aliasing that degrades their orthogonality. This is clearly visible in the compensation mechanism of Figure 6.5(b) in the 6-hydrophone case when the time-window covers also the high order modes.

In figure 6.1 part (b) the "Combining" block uses the output power shown in figure 6.5

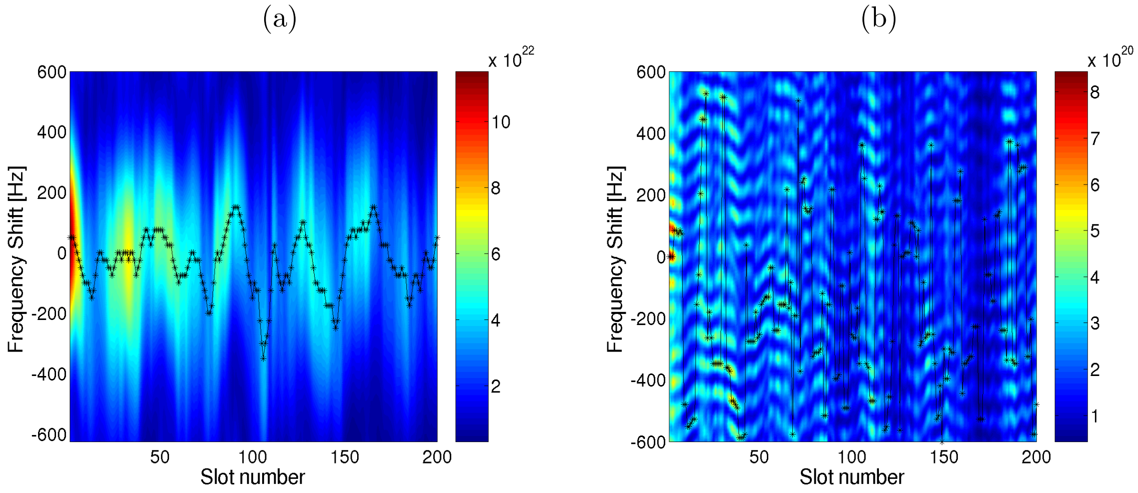

Figure 6.5: Passive time-reversal output $\mathbf{z}_l(t)$ mean power as a function of time/slot-number and applied frequency shift, for the first data packet. The $\mathbf{z}_l(t)$ mean power is computed in slots of 0.25s for a 16-hydrophone array and time-window covering the first arriving paths (a), and for a 6-hydrophone array and time window covering all paths and compensation applied only to later paths (b). The solid line connects the surface maxima ('*') for each time/slot number.

to organize the equalized data before estimating the transmitted data sequence. For "plain pTR" all time slots are assumed to have a null frequency shift, while for "FSpTR" the slots with maximum power represented in Figure 6.5 by '*' are considered. However, Figure 6.5(b) shows an additional phenomenon that consists on the spread of each maximum over a number of local maxima on the frequency axis for each time/slot number. This is clearly due to the aliasing referred above. A third processor, termed "FSpTR+", is proposed for coherently exploiting all possible local maxima by adding them together into the final result. Due to its nature "FSpTR+" should only be applied in the presence of spatial aliasing.

MSE results calculated using the demodulated sequence before slicing, $z(n, n_s)$, and the transmitted data sequence, $a(n)$, are shown in Table 6.1(Case I) for the 16-hydrophone array with a time-window that covers 4 symbols, in Table 6.1(Case II) considering a 6-hydrophone array with a time-window that covers only the first 4 symbols such that only the pTR output SNR is optimized and in Table 6.1(Case III) considering a 6-hydrophone array with the time window covering 28 symbols but with the frequency shift being applied only to the latter paths between 18 and 28 symbols. The pTR output mean power, for the first data packet of Table 6.1(Case I) and (Case III) is shown in Figures 6.5(a) and (b), respectively. In Table 6.1(Case I) and (Case II) the modal aliasing is not visible, since the time-window only captures the first arriving paths that correspond to low order modes, and only the plain pTR and FSpTR equalizers are considered. In Table 6.1(Case III) the FSpTR+ equalizer is also used, since the frequency shift compensation mechanism is applied to high order modes which are not correctly sampled by the 4 m - hydrophone spaced array.

Table 6.1: MSE table for: the 16-hydrophone array with the short time-window capture of the channel IRs first arrivals and full frequency shift compensation (Case I); the 6-hydrophone array with the short time-window capture of the channel IRs first arrivals and full frequency shift compensation (Case II); the 6-hydrophone array with full window capture of the channel IRs arrivals and the frequency shift compensation applied only to later arrivals (Case III).

	Case I		Case II		Case III		
	plain pTR	FSpTR	plain pTR	FSpTR	plain pTR	FSpTR	FSpTR+
data packet 1	-7.19dB	-7.32dB	-3.31dB	-3.56dB	0.37dB	-2.52dB	-4.16dB
data packet 2	-6.83dB	-6.50dB	-3.05dB	-1.18dB	0.30dB	-1.64dB	-3.46dB
data packet 3	-8.45dB	-8.24dB	-1.59dB	-1.82dB	-0.03dB	-3.04dB	-4.00dB
data packet 4	-10.04dB	-9.08dB	-4.04dB	-4.08dB	-1.28dB	-2.46dB	-4.85dB
mean	-8.12dB	-7.85dB	-2.99dB	-2.66dB	-0.16dB	-2.41dB	-4.11dB

Results in Table 6.1(Case I) show that there is no advantage in using FSpTR (with a mean MSE of -7.85 dB) over plain pTR (with a mean MSE of -8.12 dB), which is possibly due to the existence of different mode groups (that require independent compensation) in the time-window selection. Those different mode groups can be seen in the arrival pattern of Figure 6.3 for the first arriving paths, and manifest their existence in Figure 6.4(a) by the slope in the rising edge of the $\Phi(\tau)$ and $ISI^{-1}(\tau)$ curves. When comparing the plain pTR with the FSpTR performance in Table 6.1(Case II), a similar behavior to that of Table 6.1(Case I) is observed and similar comments apply. Comparing Table 6.1(Case I) for 16 hydrophones with Table 6.1(Case II) for 6 hydrophones with a similar time-window, the superior performance of the large array over the short one becomes clear. That is related with the TR basic assumption that the array should be densely populated over the whole water column [34], and also to the fact that in the former case there is lower multipath and the time-window is optimized for pTR output SNR and ISI, while in the latter there is a strong multipath and the time-window is only optimized for output SNR.

When compared with Table 6.1(Case III) for the plain pTR, the results of Table 6.1(Case II) reveal that the latter, when only the pTR output SNR is optimized by the time window, is clearly better than the former when the time-window tries to simultaneously optimize the pTR output SNR and the ISI. That is due to the uncompensated mismatch that affects the later paths and reveals that it is better not to include all significant paths than to leave them uncompensated. In Table 6.1(Case III) the FSpTR partially compensates the later arrivals but due to modal aliasing its performance is still worse than that of plain pTR in Table 6.1(Case II). On the other hand, in Table 6.1(Case III) the performance of FSpTR+, which coherently adds aliasing components, achieves the best performance of all 6-hydrophone cases, revealing its capacity to compensate for channel mismatch with an array that poorly samples higher order modes and does not span the entire water column.

The real data performance of the communications system using plain pTR, FSpTR and

FSpTR+ are compared with a Fractionally-Spaced Equalizer (FSE) [41] updated by the RLS algorithm. Doppler compensation/tracking is performed by the FSE itself (tracking sliding IR taps over time) and an external PLL (tracking the rotating constellation). When applied to real data special care has been taken with the selection of the number of coefficients on the FSE to ensure that it does not diverge due to an excessive number of taps or due to uncompensated Doppler. In fact the FSE spans 12 symbols in the 6-hydrophone and 7 symbols in the 16-hydrophone array. If those settings are swapped the FSE will diverge in both cases: in the 6-hydrophone array case due to uncompensated Doppler and in the 16-hydrophone array case due to an excessive number of coefficients. Nevertheless, it is interesting to observe that for the first data packet with a Doppler compression of 18 symbols the FSE remains effective even with a much smaller number of coefficients. Apparently, the FSE dynamically changes the combination of multipath replicas that it uses to generate symbol estimates as they slide through its analysis window in the course of a 50 s packet due to Doppler compression/expansion of waveforms.

Table 6.2 shows the MSE results for the FSE when using 16 and 6 hydrophone arrays. The best performance is achieved in the 16-hydrophone case with -21.45dB, although there is an unexplained performance degradation in the second and third data packets. With the 6-hydrophone array the FSE's mean MSE performance is -12.9 dB, which is clearly better than the mean value of -4.11dB achieved by FSpTR+ with 6 hydrophones and a time window that covers 28 symbols. Plain pTR and FSpTR with 16 hydrophones present mean MSEs of -8.12 and -7.85 dB, respectively, which approach the value of -12.9 dB attained by the FSE with 6 hydrophones and emphasize the pTR requirement for a long and dense array to preserve the near-orthogonality of sampled modes.

Table 6.2: MSE table for the FSE with 16 and 6 hydrophones.

	16 hydrophones	6 hydrophones
data packet 1	-20.54dB	-11.49dB
data packet 2	-14.99dB	-13.87dB
data packet 3	-13.95dB	-13.81dB
data packet 4	-21.45dB	-12.58dB
mean	-17.73dB	-12.93dB

6.6 Conclusions and Future work

Experimental results were given for time-reversed demodulation of 12.5 kHz, 2000 bits per second, binary PSK data collected during the RADAR'07 experiment. Three receiving pTR-based architectures were compared: plain pTR, FSpTR and FSpTR+ environmental equalizers. The plain pTR demodulator explores the stability of the channel IRs estimate that is only attained when only the first arriving paths of the channel IRs estimate (generated by the lower order modes) are considered by the pTR processor. Based on the waveguide invariants of the underwater layered channel the FSpTR and the FSpTR+

demodulators attempt to equalize the geometric channel variability with a frequency shift of the channel IRs estimate. The former is more appropriate for low frequency applications where mode sampling aliasing is less severe or can be controlled [47], while the latter takes advantage of the high order modes aliasing to improve its performance. Results with 50 s data packets show that an effective compensation of the channel variability can be attained, with mean MSE results of -4.1 dB with 6 hydrophones and -8.12 dB with 16 hydrophones.

The multipath spread of the channel IRs estimate considered by the pTR processor should be optimized before the arrival of the data. The probe timing optimization can be performed with a time-window that when it is too large can introduce undesired noise in the pTR processor and when it is too small can fail to include all significant multipath. Two criteria whose metric can be computed with the IRs estimate were considered: pTR output SNR optimization and pTR residual ISI optimization. The two criteria may provide different time-window results and the automatic joint-operation of those two metrics is required for a future unsupervised operation of the presented environmental equalizers.

Despite the fact that underwater coherent communication systems based on black-box equalizers [31] usually perform better than pTR-based ones [20], the latter are attractive as the ocean itself supplies the information that is needed for deconvolution. Moreover, their ability to self-adapt to the environment results in a potentially more robust system, which is in line with current efforts to incorporate environmental information into black-box equalizers [40]. The proposed environmental equalizer, as other pTR equalizers [14, 54, 20], tries to overcome the loss of performance of pTR-based systems due to environmental mismatch by adding short-term adaptability while maintaining the long-term principle of time reversal. The environmental equalizers presented here track a single parameter — a frequency shift — and provide a robust and low-complexity viable alternative to equalizers. Since the frequency shift depends on the actual environment/geometric conditions, future work will address the possibility of extracting geometric information from the adaptive frequency shift estimate.

The environmental equalizer presented in this work finds application in coherent communications in the presence of geometric mismatch, as is the case in underwater communications between underwater autonomous vehicles and/or drifting or moving receivers. Its validity is limited to layered media where waveguide invariants apply, which is the case of acoustic underwater channels and electromagnetic ionospheric channels [6].

Acknowledgments

This work was supported by Fundação para a Ciência e a Tecnologia under programs POCI, POCTI and POSI. The authors would like to thank CINTAL for the organization of RADAR'07 sea trial and NRP D. Carlos I master and crew.

Chapter 7

Conclusion

This work addresses several issues related to the implementation of an environmental-based equalizer in the specific context of underwater coherent communications.

Passive Time Reversal (pTR) is one of the variants of time reversal applicable to digital underwater communications. In pTR a probe-signal is transmitted ahead of the data-signal in order to estimate the channel impulse response for later use as a replica signal in a time reversal mirror fashion. In practice the received probe-signal must be captured in a time-window and, after correlation with the transmitted probe-signal, gives a noisy estimate of the channel impulse response. Therefore, the output signal to noise ratio and the detection rate of passive time reversal will strongly depend of the starting time and on the duration of such time-window, typically these time-window should depend on the travel time and the time spread of the acoustic channel.

The influence of the time-window length in the pTR communication system is two fold: it affects the residual Inter-Symbolic Interference (ISI) and the output Signal to Noise Ratio (SNR). With a densely populated Vertical Line Array (VLA) covering a significant portion of the propagation channel, even for a short time-window, it was shown that the residual ISI tend to reduces to zero by means of the modes orthogonality property. With a realistic VLA the residual ISI tends to reduce as the time-window length increases and more paths are included in the pTR processor. Different window settings can result from the pTR output SNR and the pTR residual ISI optimizations, it was shown that the output SNR criterion should be used for low input SNR, and the residual ISI criterion should be used for high input SNR. The time window optimization was made possible considering the well known ISI metric and after the derivation of a closed form expression for the pTR output SNR. In both cases the optimum time window can be accurately estimated previously to the data arrival using the channel IRs estimate obtained with the probe-signal. For the pTR output SNR criterion it corresponds to the time-window that gives the higher power of the overall pTR impulse response.

In most underwater acoustic experiments acoustic sources and hydrophone arrays are moored so as to provide a geometry as controllable as possible. A more operational approach is to use moving sources and drifting acoustic receivers in which case the data exhibits continuous phase and amplitude changes due to depth and range shifts. This may be problematic when the processing of the collected acoustic data requires the use of correlation between successive received signals, e.g., in pTR where a probe-signal is sent ahead of the data-signal for post crosscorrelation. An identical problem arises when the source is placed in a continuously moving and unstable autonomous underwater vehicle. Up to now, only the range shift is usually compensated using data processing techniques, for example, by applying an appropriate frequency shift to the received acoustic field based on the slope invariant of the waveguide β.

In the present work a waveguide-invariant-based approach has been developed for the pTR geometric mismatch compensation when the pTR operates with two subsequent IRs estimate. It was found that the waveguide invariant β can be used to approximate the horizontal wavenumber using the horizontal group slowness and in that way to compensate for the source-array range mismatch. The waveguide invariant ζ shows its ability to approximate the vertical wavenumber using the horizontal group slowness and its application to the compensation of the source and array depths mismatch was addressed. Since β and ζ are invariants in the frequency/range plane and frequency/depth plane respectively it was found that the geometric mismatch compensation operates by applying a frequency shift to one of the IRs estimate to compensate for the geometric mismatch of the other IRs estimate. The appropriate frequency shift can be computed in a closed form using the invariants and the geometric mismatch.

When communications are required between a moving source and a moving receiver the passive time-reversal allows for the implementation of a communications system that loses performance when in presence of geometric mismatch between the probe-signal and the actual data symbols transmission. The waveguide invariant properties states that the geometric mismatches can be partially compensated by applying an appropriate frequency shift in the passive time-reversal operator.

Using the pTR geometric mismatch compensation and the pTR optimization for coherent communications an environmental-based equalizer was developed. It behaves as a Matched-Filter Demodulator (MFD) in a matched-field processing fashion, where the synthetic acoustic field to be matched with the real acoustic field is given by a previous probe-signal estimate of the acoustic field and a waveguide invariant based model that uses the geometric properties of the environment to track the actual acoustic field. It results in the Frequency Shift passive Time-Reversal (FSpTR) environmental-based equalizer where the optimum frequency shift selection is given by the higher pTR output power. Real data comparison between plain pTR communications system and the FSpTR reveals an effective environmental mismatch compensation.

Two further improvements has been made in the basic FSpTR environmental-equalizer that are related with the Doppler compression/expansion and with the use of a sparse array for pTR operation. Since the optimum frequency shift that compensates for the actual geometric mismatch is given by the maximum power of the pTR output, the symbol decision does not have to be fed back to the equalization structure and a simple Doppler compensation method can be adopted. When using a sparse array the poor spatial sampling of high order modes results in mode aliasing. Such mode aliasing is clearly visible in the FSpTR output and can be partially overcome by adding the aliasing replicas coherently.

The main objective of this thesis was to study the feasibility of using environmental-based equalizers to perform underwater coherent communications. Such an objective was attained since when compared with the plain pTR communications system the FSpTR equalizer shows its capability to compensate for the geometric mismatch between the probe and the data transmissions, however when compared with the Fractionally-Spaced Equalizer (FSE) it was found that the FSE outperforms the environmental equalizer. Even so the environmental-based equalizers are attractive because of there ability to self-adapt to the environment that results potentially in a more robust system.

7.1 Open issues

In order to operationalize the FSpTR environmental-equalizer three requirements were identified at the beginning of the present thesis: first it must be unsupervised and simple enough to be implemented in an autonomous platform such as the AOB; second is that it must strongly reduce the number of probe signals to be sent in the pTR digital communications process in order to increase the effective data rate transfer between the source and the receiver; finally, the third requirement is that it must allow for geometric inversion, i.e., for source-array range and source and array depths estimate. In the present work a first step is carried on in order to integrate the three requirements in a single solution but future work is required for its full implementation.

In order to have an unsupervised operation the FSpTR equalizer requires a probe timing optimization before the data arriving. Based on the channel IRs estimate two criteria with well defined metrics can be computed: for pTR output SNR optimization and for ISI optimization. Future work should address the automatic joint-operation of those two metrics in order to attain a global optimization.

The actual MFD implementation of the FSpTR equalizer requires a set of “number of hydrophones times number of frequency shifts” matched-filters with length given by the optimum time-window. The matched-filters output are then summed for each frequency shift in a pTR fashion, and followed by a maximum power selector. It results a huge number of matched-filters that is not suitable to be implemented in a low power consumption autonomous platform. However the number of matched-filters can be strongly reduced if a dynamic tracking of the frequency shift is adopted (e.g. by using a sub-set of frequency shifts in the vicinity of the previous identified optimal frequency shift).

Due to its environmental based nature, FSpTR more than being able to perform reliable underwater communications can be used to track the geometric variations during data transmission. This has not been fully explored with real data during the present work, mainly due to the absence of sufficiently high sample rate of source depth and array depth information during the experiments. Future experiments should be prepared in order to explore such possibility.

Solving an inverse problem requires a physical theory, i.e., a mapping that calculates a number of features that are expected to be observed given the model parameters. In its most basic form this means to predict the error-free values of the observable parameters that would correspond to a given model. Such a physical model for the environment geometric parameters has been derived in the present thesis. A more elaborate setting based on the conditional probability density for the observables given the model parameters, that accounts for inherent uncertainties of the theory due to imperfect parametrization (e.g. the environmental non-geometric properties mismatch) or to some fundamental lack of knowledge, should be addressed in future work. Such probability density and its estimation will allow for the development of a sequential algorithm that predicts the frequency shift compensation, instead of the actual FSpTR MFD demodulator.

Appendix A

A.1 Deterministic and stochastic filters autocorrelation

This appendix recalls the autocorrelation of the response Y, of a finite impulse response filter H, to an input signal X when the input and filter autocorrelations are known and when: case 1 - H is stochastic and X is stochastic ; case 2 - H is deterministic and X is stochastic; case 3 - H is stochastic and X is deterministic. The filter output is given by the convolution

$$Y(t) \;=\; \int_{-\infty}^{+\infty} H(t-u)X(u)du, \tag{A1}$$

and the filter output autocorrelation

$$\begin{aligned} R_Y(t+t',t) &= E\{Y(t+t')Y(t)\} \\ &= \int\int E\{H(t+t'-u)H(t-v)\}E\{X(u)X(v)\}dudv \\ &= \int\int E\{X(t+t'-u)X(t-v)\}E\{H(u)H(v)\}dudv, \end{aligned} \tag{A2}$$

considering that X and H are independent, (A2) is valid for H and X deterministic or stochastic. In the following the index t_0, τ will be used to represent a signal time limited by the unit-gate function

$$\Pi_\tau(t-t_0) = \Pi_{t_0,\tau}(t) = \begin{cases} 1 & t_0 \le t < t_0+\tau \\ 0 & \text{otherwise} \end{cases}. \tag{A3}$$

Capital letters designate stochastic quantities and lower case designate deterministic quantities, thus R will represent the stochastic autocorrelation and r the deterministic autocorrelation.

In case 1 H_τ is a stochastic time limited signal (where t_0 has been dropped since in a stochastic signal the instant when the unit-gate function is applied is irrelevant), and X an unlimited WSS stochastic signal, the output filter autocorrelation as given in [15], is equal to

$$R_Y(t') = E\{r_{H,\tau}(t')\} * R_X(t'), \tag{A4}$$

where

$$E\{r_{H,\tau}(t')\} = E\left\{\int H_\tau(t+t')H_\tau(t)dt\right\}. \tag{A5}$$

Considering that the time limited stochastic process H_τ is the result of the product of a WSS process H with a rectangular window (A3)

$$E\{r_{H,\tau}(t')\} = R_H(t')\tau\Delta_\tau(t'), \tag{A6}$$

where $\tau\Delta_\tau(t')$ is the triangular function that results from the deterministic autocorrelation of the rectangular function (A3). When X and H are both white gaussian processes with autocorrelations $\sigma_X^2\delta(t')$ and $\sigma_H^2\delta(t')$ respectively the output autocorrelation will be given by

$$R_Y(t') = \sigma_X^2\sigma_H^2\tau r_\delta(t'), \tag{A7}$$

and Y is a white stochastic signal, since $r_\delta(t') = \delta(t') * \delta(t')$ is the autocorrelation of the dirac impulse.

Case 2 is a standard case where $h_{t_0,\tau}$ is a deterministic signal that results from the product of an infinite signal with time window (A3) applied in the arbitrary instant t_0, and X is an infinite stochastic signal. The output filter autocorrelation is given by

$$R_Y(t') = r_{h,t_0,\tau}(t') * R_X(t'), \tag{A8}$$

where

$$r_{h,t_0,\tau}(t') = \int h_{t_0,\tau}(t+t')h_{t_0,\tau(t)}dt \tag{A9}$$

$$= \begin{cases} \int_{t_0}^{t_0+\tau-t'} h(w+t')h(w)dw & \tau \geq t' > 0 \\ \int_{t_0}^{t_0+\tau} h(w+t')h(w)dw & t' = 0 \\ \int_{t_0-t'}^{t_0+\tau} h(w+t')h(w)dw & 0 > t' \geq -\tau \\ 0, & \text{otherwise} \end{cases} \tag{A10}$$

When $h_{t_0,\tau}$ is a deterministic signal and X is an infinite white gaussian process

$$R_Y(t') = \sigma_X^2 r_{h,t_0,\tau}(t'). \tag{A11}$$

and the filter output Y is a WSS stochastic signal.

In case 3 x is deterministic, and H_τ a time limited stochastic signal that, as in case 1, results from the product of a WSS signal with the rectangular window (A3), since the signal is WSS the moment when the window is applied is not important and t_0 can be dropped. In that case, since

$$E\{H_\tau(u)H_\tau(v)\} = R_H(u-v)[\Pi_\tau(u)\Pi_\tau(v)], \tag{A12}$$

equation (A2) becomes

$$R_Y(t+t',t) = \int\int [x(t+t'-u)x(t-v)][\Pi_\tau(u)\Pi_\tau(v)]R_H(u-v)dudv, \tag{A13}$$

if we change the independent variables

$$\begin{cases} w = t - v \\ t - u = w - z \end{cases}, \tag{A14}$$

the output autocorrelation becomes

$$R_Y(t+t',t) = \int R_H(z) A_\tau(t',t,z)dz, \tag{A15}$$

with

$$A_\tau(t',t,z) = \int [x(w-z+t')\Pi_\tau(t-w+z)][x(w)\Pi_\tau(t-w)]dw. \tag{A16}$$

Equation (A16) can be rewritten in four intervals defined by variable z

$$A_\tau(t',t,z) = \begin{cases} \int_{t-\tau}^{t+z} x(w-z+t')x(w)dw & -\tau \le z < 0 \\ \int_{t-\tau}^{t} x(w-z+t')x(w)dw & z = 0 \\ \int_{t-\tau+z}^{t} x(w-z+t')x(w)dw & 0 < z \le \tau \\ 0, & \text{otherwise} \end{cases}. \tag{A17}$$

When x is deterministic and H is a time limited white gaussian process with autocorrelation given by $\sigma_H^2\delta(t')$ the auto-correlation of Y becomes

$$R_Y(t+t',t) = \sigma_H^2 A_\tau(t',t,z=0). \tag{A18}$$

which is seen to be non stationary.

A.2 Time windowed passive Time Reversal

Without mismatch pTR operation consists on the sum over all hydrophones of the deterministic correlation between two subsequent channel IRs (with only a time delay between them denoted by $'$). In pass-band the pTR operator is given by

$$p_{TR}(t) = \sum_{i=1}^{I} h_i(t) * h'_i(-t), \tag{A19}$$

where $p_{TR}(t)$ can be seen as the IR of the pTR operator.

In the frequency domain (where pTR is usually termed passive phase conjugation) for a perfect waveguide the same is attained by

$$\begin{aligned} P_{PC}(\omega) &= \sum_{i=1}^{I} H_i(\omega)H_i^*(\omega) \\ &= a_i^2 \sum_{n=1}^{M}\sum_{m=1}^{M} \Psi_n(z_0)\Psi_m(z_0)\frac{e^{j(\xi_n-\xi_m^*)R}}{\sqrt{\xi_n\xi_m^*}} \sum_i \Psi_n(z_i)\Psi_m(z_i) \end{aligned} \tag{A20}$$

using the modes orthogonal property (4.30) it results

$$\begin{aligned} P_{PC}(\omega) &= a_i^2 \sum_{m=1}^{M} |\Psi_m(z_0)|^2 \frac{e^{j(\xi_m-\xi_m^*)R}}{\sqrt{\xi_m\xi_m^*}} \\ &= a_i^2 \sum_{m=1}^{M} |\Psi_m(z_0)|^2 \frac{e^{-2Im(\xi_m)R}}{|\xi_m|} \\ &\approx C \end{aligned} \tag{A21}$$

where all terms have obvious notations in the normal mode formulation of the acoustic field. The modes orthogonality property was used, in a similar manner to [44] for pTR and to [34] for aTR. In (A21) the $Im(\xi_m)$ exponential is due to the loss mechanisms [27], and according to [44] acts to attenuate higher order modes. It results that $P_{PC}(\omega) \approx C$ is approximately constant over the narrowband frequencies of interest and in the time domain $p_{TR}(t)$ will be a *sinc* function convolved with a weighted dirac proportional to C.

The time windowing operation consists in multiplying the IRs $h_i(t)$ by a unit-gate function $\Pi_{t0,\tau}(t)$, given in (A3), with starting time t_0 and length τ. In an isovelocity perfect waveguide the travel time of the arriving paths is ruled by the modes group velocity that converges from zero, at the mode cutoff frequency, to the water column sound velocity as a monotonic ascending function of the frequency [[58] pp. 40]. In a real waveguide the modes group velocity oscillate with the frequency up to the Airy phase and after that behave as perfect waveguide modes [[58] pp. 128]. In the narrowband case at high frequencies the grate majority of modes has already reached the Airy phase and that makes the usual assumption that at high frequencies the underwater channel is more similar to the perfect waveguide than at low frequencies. After the Airy phase for a given frequency the group velocities are well ordered in an descending manner and that makes lower modes to present always higher group velocities [[58] pp. 40 and 128]. It results that high order modes become responsible for later arrivals and in such conditions the time window operation behaves as a mode filter. When applied to communications in a real waveguide only the IRs in the bandwidth of the signal are of interest and the previous heuristic findings are applied at the cost of ignoring the modes whose influence spreads over several arriving paths because they have not reached the airy phase.

Considering the ray mode approximation [58, 5] where at a given frequency, higher order modes are associated with later rays, the effect of a time window that eliminates later rays can be reversed to mode analysis where it will filter out higher order modes. In the following it will be considered that $Me(t_0, \tau)$ is the set of modes that have not been filtered by the time window

The influence of the time windowing operation over the pTR processor can now be considered under two aspects: when both channel IRs are time limited or when only one of them is time limited. In the first case the resulting p_{TR} and P_{PC} will be given by

$$p_{TR,2tw}(t) = \sum_{i=1}^{I} h_{i,t_0,\tau}(t) * h'_{i,t_0,\tau}(-t), \tag{A22}$$

and

$$\begin{aligned} P_{PC,2tw}(\omega) &= \sum_{i=1}^{I} H_{i,t_0,\tau}(\omega) H^*_{i,t_0,\tau}(\omega) \\ &= a_i^2 \sum_{n=1}^{Me(t_0,\tau)} \sum_{m=1}^{Me(t_0,\tau)} \Psi_n(z_0)\Psi_m(z_0) \frac{e^{j(\xi_n - \xi_m^*)R}}{\sqrt{\xi_n \xi_m^*}} \sum_i \Psi_n(z_i)\Psi_m(z_i) \\ &= a_i^2 \sum_{m=1}^{Me(t_0,\tau)} |\Psi_m(z_0)|^2 \frac{e^{-2Im(\xi_m)R}}{|\xi_m|} \\ &\approx C' \end{aligned} \qquad \text{(A23)}$$

respectively.

In the second case the resulting p_{TR} and P_{PC} will be given by

$$p_{TR,1tw}(t) = \sum_{i=1}^{I} h_i(t) * h'_{i,t_0,\tau}(-t), \qquad \text{(A24)}$$

and

$$\begin{aligned} &P_{PC,1tw}(\omega) = \\ &= \sum_{i=1}^{I} H_i(\omega) H^*_{i,t_0,\tau}(\omega) \\ &= a_i^2 \sum_{n=1}^{M} \sum_{m=1}^{Me(t_0,\tau)} \Psi_n(z_0)\Psi_m(z_0) \frac{e^{j(\xi_n - \xi_m^*)R}}{\sqrt{\xi_n \xi_m^*}} \sum_i \Psi_n(z_i)\Psi_m(z_i) \\ &= C' + a_i^2 \sum_{n=Me(t_0,\tau)}^{M} \sum_{m=1}^{Me(t_0,\tau)} \Psi_n(z_0)\Psi_m(z_0) \frac{e^{j(\xi_n - \xi_m^*)R}}{\sqrt{\xi_n \xi_m^*}} \sum_i \Psi_n(z_i)\Psi_m(z_i) \\ &\approx C'' \end{aligned} \qquad \text{(A25)}$$

respectively. As the time window increases $Me(t_0, \tau)$ converges to $M(\omega)$ and, C' and C'' converge to C.

When the TR associated assumptions are accomplished the two summations of the right-hand second term of (A25) become null due to the modes orthogonality property and $C' \equiv C''$. Since C' and C'' given by (A23) and (A25) respectively are week functions of frequency [34], for narrowband IRs $h_i(t)$, the resulting $p_{TR,\cdots}(t)$ can be approximated by a *sinc* type function with an amplitude given by the $C^{\cdots}$ coefficients. It results that the mode-reduction/time-windowing does not affect $p_{TR,\cdots}(t)$ in shape but only in amplitude.

When the TR assumptions are not fully accomplished, that is, the array do not span the entire water column and/or it is not sufficiently populated, it results that the $p_{TR}(t)$ shape becomes a distorted *sinc* and such distortion will be responsible for residual ISI in the pTR digital communications system. In such conditions $C' \neq C''$ and the residual ISI becomes dependent on the considered number of modes, $M(t_0, \tau)$, and thus on the time-window length.

Appendix B

B.1 Linear approximation of monotonic functions

Sections 4.3.3 and 4.3.4 require the computation of horizontal and vertical wavenumbers using the horizontal wavenumber inverse. Both problems can be seen as a generic linear approximation of one monotonic function, Φ_m, using another monotonic function, Π_m.

Considering the linear approximation of Φ_m using Π_m with $m = 1...M$ in the least-squares sense, it results

$$\Phi_m \approx \Phi'_m = -\varepsilon \Pi_m + \rho, \tag{B1}$$

where

$$\varepsilon = -\frac{\overline{\Phi_m \Pi_m} - \overline{\Phi_m}\;\overline{\Pi_m}}{\overline{\Pi_m^2} - \overline{\Pi_m}^2}, \tag{B2}$$

and

$$\rho = \overline{\Phi_m} + \varepsilon \overline{\Pi_m}, \tag{B3}$$

where the bar denotes the mean over m. If both functions Φ_m and Π_m are linear with m, the approximation becomes exact. When one or both functions are non-linear with different curvatures the approximation will have an error that can be reduced if instead of approximating Φ_m for $m = 1...M$ only a subset of m is considered. For the approximation of horizontal and vertical wavenumbers an effective number of modes M_e smaller than the total number of modes M will be considered. That will result in a linear approximation given by the parameters ε_e and ρ_e.

A different approximation to Φ_m using Π_m is given by computing

$$\Phi_m \approx \Phi'_m = -\varepsilon_{\mu,\nu} \Pi_m + \rho_{\mu,\nu}, \tag{B4}$$

with

$$\varepsilon_{\mu,\nu} = -\frac{\Phi_\mu - \Phi_\nu}{\Pi_\mu - \Pi_\nu}, \tag{B5}$$

and

$$\rho_{\mu,\nu} = \Phi_\nu + \varepsilon_{\mu,\nu} \Pi_\nu, \tag{B6}$$

where $m = \nu$ and $m = \mu$ are the abscissa for $\Phi_\nu = \Phi'_\nu$ and $\Phi_\mu = \Phi'_\mu$ respectively. It results that $\Phi'_m \approx \Phi_m$ with different degrees of accuracy given by the selected ν and μ.

Since (B4) represents a set of linear approximations with the only constraint that the two functions Φ_m and Φ'_m meet at two different points $m = \nu$ and $m = \mu$, it is expected that the linear least-squares approximation (B1) will coincide or be close to one of them, i.e, for each M_e there is a (μ, ν) such that $\varepsilon_e \approx \varepsilon_{\mu,\nu}$ and $\rho_e \approx \rho_{\mu,\nu}$.

B.2 Mode orthogonality in the presence of an array depth mismatch

When there is no array depth mismatch the mode orthogonality condition is given by

$$\Psi(m,n) = \int_0^D \frac{Z_m(z)Z_n(z)}{\rho(z)} dz = \delta_{m,n}, \tag{B7}$$

where D is the waveguide water column depth, $\rho(z)$ is the water density, considered to be constant and equal to 1, and z is the depth. The mode shape $Z_m(z)$ in a perfect wave guide is given by

$$Z_m(z) = \sqrt{\frac{D}{2}} \sin(\gamma_m z), \tag{B8}$$

with

$$\gamma_m = \left(m - \frac{1}{2}\right)\frac{\pi}{D}. \tag{B9}$$

Using (B8) in (B7) it results

$$\Psi(m,n) = \frac{2}{D}\int_0^D \sin(\gamma_m z)\sin(\gamma_n z) dz, \tag{B10}$$

and (B7) follows readily.

If now in (B10) there is a depth shift between the mode functions Z_m and Z_n, it results

$$\Psi(m,n,\Delta z) = \frac{2}{D}\int_0^D \sin(\gamma_m z - \gamma_m \Delta z)\sin(\gamma_n z) dz. \tag{B11}$$

Using the Euler formula, and ignoring the backward propagating modes (with m and n negative integers), (B11) becomes

$$\Psi(m,n,\Delta z) \approx \frac{-2}{4D}\left[\int_0^D \Lambda'_{m,n} dz + \int_0^D \Omega'_{m,n} dz\right], \tag{B12}$$

where

$$\begin{aligned} \Lambda'_{m,n} &= \Lambda_{m,n}\exp(-j\pi(m-1/2)\Delta z/D), \\ \Omega'_{m,n} &= \Omega_{m,n}\exp(j\pi(m-1/2)\Delta z/D), \end{aligned} \tag{B13}$$

and

$$\begin{aligned} \Lambda_{m,n} &= -\exp(j\pi(m-n)z/D), \\ \Omega_{m,n} &= -\exp(-j\pi(m-n)z/D). \end{aligned} \tag{B14}$$

Defining

$$\begin{aligned} \Psi_\Lambda(m,n) &= \int_0^D \Lambda_{m,n} dz, \\ \Psi_\Omega(m,n) &= \int_0^D \Omega_{m,n} dz, \end{aligned} \tag{B15}$$

using (B9) and the fact that the exponential terms in (B13) do not depend on z, (B12) becomes

$$\Psi(m,n,\Delta z) = \frac{-2}{4D}\left[\exp(-j\gamma_m \Delta z)\Psi_\Lambda(m,n) + \exp(j\gamma_m \Delta z)\Psi_\Omega(m,n)\right]. \tag{B16}$$

When m and n are both either odd or even, this yields

$$\Psi(m,n,\Delta z) = \frac{-2}{4D}\left[2D\delta_{m,n}\cos(-\gamma_m \Delta z)\right], \tag{B17}$$

otherwise,

$$\Psi(m,n,\Delta z) = \frac{-2}{4D}\left[\frac{-2D}{\pi}(\delta_{m,n+1} - \delta_{m,n-1})\sin(-\gamma_m \Delta z)\right]. \tag{B18}$$

From (B17) and (B18) it is obvious that the mode orthogonality has been lost. It can be partially recovered by multiplying (B16) by $2\cos(\gamma_m \Delta z)$, resulting, for m and n with the same parity,

$$\Psi(m,n,\Delta z)2\cos(\gamma_m \Delta z) = \frac{-2}{4D}\left[2D\delta_{m,n}(1+\cos(-2\gamma_m \Delta z))\right], \tag{B19}$$

and, for m and n with different parity,

$$\Psi(m,n,\Delta z)2\cos(\gamma_m \Delta z) = \frac{-2}{4D}\left[\frac{-2D}{\pi}(\delta_{m,n+1} - \delta_{m,n-1})\sin(-2\gamma_m \Delta z)\right]. \tag{B20}$$

Comparing (B17) with (B19) it is clear that there is a gain in amplitude for $m = n$, and comparing (B18) with (B20) the amplitude does not change, thus enabling the partial recovery of the modes orthogonality

$$\Psi(m,n,\Delta z)\cos(\gamma_m \Delta z) \approx \Psi(m,n)\frac{(1+\cos(-2\gamma_m \Delta z))}{2}. \tag{B21}$$

A similar result can be obtained if $\exp(\pm j\gamma_m \Delta z)$ is used instead of $2\cos(\gamma_m \Delta z)$. In that case a linear phase with Δz will appear for $m = n$, and (B21) can be generalized to

$$\Psi(m,n,\Delta z)e^{\pm j\gamma_m \Delta z} \approx \Psi(m,n)\frac{W(m,\Delta z)}{2}, \tag{B22}$$

where $|W(m,\Delta z)|$ is equal to 2 when $\Delta z = 0$ and oscillates around 1 when $\Delta z \neq 0$.

Bibliography

[1] S. J. A. Caiti, J-P. Hermand and M. Porter, editors. *Experimental Acoustic Inversion Methods for Exploration of the Shallow Water Environment.* Kluwer Academic Publishers, 2000.

[2] A. Baggeroer, W. Kuperman, and P. M. P. An overview of matched field methods in ocean acoustics. *IEEE Journal of Oceanic Engineering*, 18(4):307–338, October 1993.

[3] P. A. Baxley, H. Bucker, V. K. MacDonald, J. A. Rice, and M. B. Porter. Shallow-water acoustic communications channel modeling using three-dimensional gaussian beams. *SPAWAR Bienal Review*, (1):251–261, 2001.

[4] J. Candy, A. Meyer, A. Poggio, and B. Guidry. Time-reversal processing for an acoustic communications experiment in a highly reverberant environment. *J. Acoust. Soc. America*, 115(4):1621–1631, 2004.

[5] D. Chapman and D. D. Ellis. The group velocity of normal modes. *J. Acoust. Soc. America*, 3(74):973–979, September 1983.

[6] S. Chuprov. Interference structure of a sound field in a layered ocean. In L. Brekhovskikh and I. Andreevoi, editors, *Ocean Acoustics, Current State*, pages 71–91, Nauka, Moscow, 1982.

[7] R. Dowling. Acoustic pulse compression using passive phase-conjugate processing. *J. Acoust. Soc. America*, 95(3):1450–1458, 1994.

[8] R. Dowling and R. Jackson. Narrow-band performance of phase-conjugate arrays in dynamic random media. *J. Acoust. Soc. Am.*, 91(6):3257–3277, June 1992.

[9] G. D'Spain and W. A. Kuperman. Application of waveguide invariants to analysis of spectrograms from shallow water environments that vary in range and azimuth. *J. Acoust. Soc. America*, 106(5):2454–2468, 1999.

[10] R. P. E. Pouliquen, A.D. Kirwan, editor. *Rapid Environment Assessment*, La Spezia, Italy, 1997. NATO SACLANT Undersea Research Centre.

[11] G. Edelmann, W. Hodgkiss, S. Kim, W. Kuperman, H. Song., and T. Akal. Underwater acoustic communications using time-reversal. In *Proc. of the MTS/IEEE Oceans 2001*, pages 2231–2235, Honolulu, Hawai, USA, 5-8 November 2001.

[12] P. Felisberto, C. Lopes, and S. Jesus. An autonomous system for ocean acoustic tomography. *Sea-Technology*, 45(4):17–23, April 2004.

[13] M. Fink. Time reversal acoustics. *Sci. Amer*, 103(1):25–40, Jan 1998.

[14] J. A. Flynn, J. A. Ritcey, D. Rouseff, and W. L. J. Fox. Multichannel equalization by decision-direct passive phase conjugation: Experimental results. *IEEE J. Oceanic Eng.*, 29:824–836, 2004.

[15] W. Gardner. A new method of channel identification. *IEEE Trans. Communications*, 39:813–817, 1991.

[16] P. Gerstoft and Z. Michalopoulou. Global optimization in matched field inversion. In *Proc. of the Fourth European Conference on Underwater Acoustics (ECUA)*, pages 27–32, Rome, Italy, 1998.

[17] J. Gomes and V. Barroso. A matched field processing approach to underwater acoustic communication. In *Proc. of the MTS/IEEE Oceans 1999*, pages 991–995, Seattle, USA, 1999.

[18] J. Gomes and V. Barroso. Asymmetric underwater acoustic communication using a time-reversal mirror. In *Proc. of the MTS/IEEE Oceans 2000*, Providance, USA, 2000.

[19] J. Gomes, A. Silva, and S. Jesus. Joint passive time reversal and multichannel equalization for underwater communications. In *Proc. of the MTS/IEEE Oceans'06*, Boston, MA, USA, September 2006.

[20] J. Gomes, A. Silva, and S. Jesus. Spatial combining for passive time-reversed communications. accepted *J. Acoust. Soc. America*, March 2007.

[21] G. A. Grachev. Theory of acoustic field invariants in layered waveguide. *Acoust. Phys.*, (39):33–35, 1993.

[22] W. S. Hodgkiss, W. A. Kuperman, and D. E. Ensberg. Channel impulse response fluctuations at 6 khz in shallow water. In J. Pace, editor, *Impact of Littoral Environment Variability on Acoustic Predictions and Sonar Performance*, pages 295–302, Kluwer, September 2002.

[23] P. Hursky, M. Porter, B. Cornuelle, W. Hodgkiss, and W. Kuperman. Adjoint modelling for acoustic inversion. *J. Acoust. Soc. Am.*, 115(2):607–619, February 2004.

[24] P. Hursky, M. Porter, R. Rice, and V. McDonald. Passive phase-conjugate signaling using pulse-position modulation. In *Proc. of the MTS/IEEE Oceans 2001*, pages 2244–2249, Honolulu, Hawai, USA, 5-8 November 2001.

[25] P. Hursky, M. Porter, and M. Siderius. High-frequency (8-16 khz) model-based source localization. *J. Acoust. Soc. Am.*, 115(6):3021–3032, June 2004.

[26] R. Jackson and R. Dowling. Phase conjugation in underwater acoustics. *J. Acoust. Soc. Am.*, 89(1):171–181, January 1991.

[27] F. Jensen, W. Kuperman, M. Porter, and H. Schmidt. *Computational Ocean Acoustics.* AIP Series in Modern Acoustics and Signal Processing, New York, 1994.

[28] S. Jesus and A. Silva. Virtual time reversal in underwater acoustic communications: Results on the intifante'00 sea trial. In *Proc. of Forum Acusticum*, Sevilla, Spain, September 2002.

[29] S. Jesus and A. Silva. Time reversal and spatial diversity: issues in a time varying geometry test. In S. Porter and Kuperman, editors, *Proc. Conf. on High Frequency Ocean Acoustics*, pages 530–538, La Jolla, USA, March 2004.

[30] S. Jesus, C. Soares, A. Silva, J. Hermand, and E. Coelho. Aob-acoustic oceanographic buoy: concept and feasibility. In *Proc. of the UDT'06*, Hamburg, Germany, June 2006.

[31] D. Kilfoyle and A. Baggeroer. The state of the art in underwater acoustic telemetry. *IEEE J. Oceanic Eng.*, 25(1):4–27, 2000.

[32] J. Kim, W. Kuperman, W. S. Hodgkiss, H. Song, G. F. Edelmann, and T. Akal. Robust time reversal focusing in the ocean. *J. Acoust. Soc. America*, 114:145–157, 2003.

[33] J. Kim, H. Song, and W. Kuperman. Adaptive time-reversal mirror. *J. Acoust. Soc. America*, 109:1817–1825, 2001.

[34] W. Kuperman, W. Hodgkiss, H. C. Song, T. Akal, C. Ferla, and D. Jackson. Phase conjugation in the ocean: Experimental demonstration of an acoustic time-reversal mirror. *J. Acoust. Soc. Am.*, 103(1):25–40, January 1998.

[35] W. Kuperman, S. Kim, G. Edelmann, W. Hodgkiss, H. Song, and T. A. T. Group and phase speed analysis for predicting and mitigating the effects of fluctuations. In J. Pace, editor, *Impact of Littoral Environment Variability on Acoustic Predictions and Sonar Performance*, pages 279–286, Kluwer, September 2002.

[36] E. Lee and D. Messerschmitt. *Digital Communication.* Kluwer Academic Publishers, Massachusetts, 1994.

[37] N.Martins, C.Soares, , and S.M.Jesus. Environmental and acoustic assessment: The aob concept. *Journal of Marine Systems*, doi:10.1016/j.jmarsys.2007.02.003 2007.

[38] A. Parvulescu. Matched-signal (mess) processing by the ocean. *J. Acoust. Soc. America*, 98(2):943–960, 1995.

[39] M. Porter, P. Hursky, M. Siderius, V. McDonald, and P. Baxley. High-frequency propagation for acoustic communications. In J. Pace, editor, *Impact of Littoral Environment Variability on Acoustic Predictions and Sonar Performance*, pages 278–294, Kluwer, September 2002.

[40] J. C. Preisig. Performance analysis of adaptive equlization for coheren acoustic communications in the time-varying ocean environment. *J. Acoust. Soc. Am.*, 118(1):263–278, July 2005.

[41] J. Proakis. *Digital Communications*. McGraw-Hill, Massachusetts, 1995.

[42] D. Rouseff. Intersymbol interference in underwater acoustic communications using time-reversal signal processing. *J. Acoust. Soc. America*, 117(2):780–788, 2005.

[43] D. Rouseff, L. Fox, D. Jackson, and D. Jones. Underwater acoustic communications using passive phase conjugation. In *Proc. of the MTS/IEEE Oceans 2001*, pages 2227–2230, Honolulu, Hawai, USA, November 2001.

[44] D. Rouseff, D. Jackson, W. Fox, D. Jones, J. Ritcey, and D. Dowling. Underwater acoustic communications by passive-phase conjugation: Theory and experimental results. *J. Oceanic Engineering*, 26(4):821–831, 2001.

[45] A. Silva and S. Jesus. Underwater communications using virtual time-reversal in a variable geometry channel. In *Proc. MTS/IEEE Oceans'2002*, pages 2416–2421, Biloxi, USA, November, 2002.

[46] A. Silva, S. Jesus, and J. Gomes. Depth and range shift compensation using waveguide invariant properties. In *Proc. of the UAM'07*, Heraklion, Crete, Greece, June 2007.

[47] A. Silva, S. Jesus, and J. Gomes. Environment-based underwater communications. In *Proc. of the OCEANS'07*, Vancouver, Canada, October 2007.

[48] A. Silva, S. Jesus, and J. Gomes. Generalization of waveguide invariants and application to passive time reversal. to be submitted to *Acta Acoustica*, 2008.

[49] A. Silva, S. Jesus, and J. Gomes. Probe timing optimization for time-reversal underwater communications. To be Submitted to *IEEE J. of Oceanic Engineering*, 2008.

[50] A. Silva, S. Jesus, J. Gomes, and V. Barroso. Underwater acoustic communications using a 'virtual' electronic time-reversal mirror approach. In P. Chevret and M.Zakharia, editors, *5th European Conference on Underwater Acoustics*, pages 531–536, Lyon, France, June 2000.

[51] A. Silva, F. Zabel, and C. Martins. Acoustic oceanographic buoy telemetry system. *Sea Technology*, 47(9), September 2006.

[52] C. Soares, S. Jesus, A. Silva, and E. Coelho. Acoustic oceanographic buoy testing during the maritime rapid environmental assessment 2003 sea trial. In *Proc. European Conference on Underwater Acoustics*, Delft, The Netherlands, July 2004.

[53] C. Soares, M. Siderius, and S. Jesus. Source localization in a time-varying ocean waveguide. *J. Acoust. Soc. America*, 112(5):1879–1889, December 2002.

[54] H. Song, W. Hodgkiss, A. Kuperman, M. Stevenson, and T. Akal. Improvement of time-reversal communications using adaptive channel equalizers. *IEEE J. Ocean Eng.*, (31):487–496, 2006.

[55] H. C. Song, W. A. Kuperman, and W. S. Hodgkiss. Time-reversal mirror with variable range focusing. *J. Acoust. Soc. Am.*, 103((6)):3234–3240, June 1998.

[56] M. Stojanovic. Retrofocusing techniques for high rate acoustic communications. *J. Acoust. Soc. America*, 117(3):1173–1185, 2005.

[57] M. Stojanovic, J. Catipovic, and J. Proakis. Adaptive multichannel combining and equalization for underwater acoustic communications. *J. Acoust. Soc. America*, 94(3):1621–1631, 1993.

[58] I. Tolstoy and C. Clay. *Ocean Acoustics: Theory and experiments in underwater sound.* AIP, New York, 1966.

[59] S. Walker, P.Roux, and W. Kuperman. Data-based mode extraction with a partial water column spanning array. *J. Acoust. Soc. America*, 118(3):1518–1525, 2005.

[60] S. Walker, P.Roux, and W. Kuperman. Focal depth shifting of a time reversal mirror in a range-independent waveguide. *J. Acoust. Soc. America*, 118(3):1341–1347, 2005.

[61] K. L. Williams, D. R. Jackson, E. I. Thorsos, D. Tang, and K. B. Briggs. Spatial and temporal variability in bottom roughness: Implications to high frequency subcritical penetrations and backscatter. In J. Pace, editor, *Impact of Littoral Environment Variability on Acoustic Predictions and Sonar Performance*, pages 195–202, Kluwer, September 2002.

[62] T. C. Yang. Differences between passive-phase conjugation and decision-feedback equalizer for underwater acoustic communications. *IEEE Journal of Oceanic Engineering*, 29(2):472–487, April 2004.